



An experimental investigation of the fracture behaviour of particulate toughened epoxies

Thesis submitted for the degree of Doctor of Philosophy

(Edited version for online publication)

Stephen Jones

Department of Mechanical Engineering

The University of Sheffield

July 2013

Version notes:

To comply with British copyright legislation, the figures in this thesis that are subject to copyright have been removed in this electronically published version. Permission for online publication of these figures was not sought. An unedited hard copy of this thesis, as submitted and examined, is available from The University of Sheffield library.

Stephen Jones, 17/07/13

Abstract

The addition of thermoplastic particles in the interlaminar region of a carbon-epoxy composite is known to generally improve mode I and mode II fracture toughnesses and also improve damage tolerance. However, the mechanisms of toughening are poorly understood. Most studies so far have selected one interlaminar toughening particle (ILTP) and studied the effect of particle size and/or spatial distribution. A missing link in the continued development of interlaminar toughened systems is study into the effect of the particle material and interface. Whilst matrix mode I toughness is a good indication of composite mode I toughness, no such relationship has previously been established or investigated for mode II. This work focuses on measuring fracture parameters in bulk, particulate toughened epoxy resins using an experimental approach.

Digital image correlation tools were used to determine displacement fields around the crack tip at a small scale, in both standard, pure mode I specimens and mixed-mode I/II specimens for five resin formulations, four with ILTP and one without. Mixed-mode stress intensity factors and the non-singular T -stress were extracted from the displacement fields using the Williams' crack tip stress solutions. The T -stress term governs crack path stability and it was found that this term can be used successfully to differentiate between the crack path behaviour at fracture of the different materials studied. A new methodology was developed to determine an apparent mode II toughness for resins and this parameter was found to be directly proportional to the composite mode II toughness. This is believed to be the first time a relationship has been established between the mode II performance of particulate toughened resins and their composites.

The novel parameters developed here allow inference of mode II composite behaviour from resin tests. Therefore this work is a significant boost to the continued development of interlaminar toughened composites.

Acknowledgements

I would like to firstly thank my tireless supervisor Rachel Tomlinson for the dedication and continued support, above and beyond what could possibly be imagined. Without you this work could not have happened. Thanks also to my other supervisors Alma Hodzic and John Yates for their support and help.

I would like to thank all the people who helped me throughout this project. Han Tai and Dave Asquith, thank you for all the help in getting the project started and for all the tips and tricks that have helped all the way to the end. Thank you Mohammed Zanganeh; without the tools you made this project would look very different. To Magda, thanks for all the experimental help, advice and support and Bill, thanks for all the encouragement and Panos, thanks for the last figure to go in this thesis!

Richard Kay, thanks for your unlimited patience in machining countless specimens and grips, and for dealing with all the work I've lumbered you with over the last three years.

I would like to thank my adopted research group, the Composite Systems Innovation Centre, for the stimulating discussion and for making my time here fun; Alon, Ioannis, Sophia, Nithian, Zurina, AnVan, Teddy, Mulyadi, Ghayth, Khaled, Diyar and everybody else, many thanks.

I would like to thank the Department of Mechanical Engineering and Cytec Engineered Materials for seeing the potential of the project and continuing to fund me and embracing the ever-changing directions the project took. I would specifically like to thank all the people I have worked with at CEM including Vincent Aerts, Steve Ward, Peter Mills, Emiliano Frulloni, Judith Elder, and the many others who all have offered consistent interest and support.

Lastly I'd like to thank my friends Jack (proof-reader extraordinaire), Skye, David and David for putting up with me, but most of all, Libby for making me happy.

Contents

Abstract.....	1
<i>Acknowledgements</i>	3
Contents.....	4
Nomenclature	8
Subscripts	9
Glossary.....	9
Chapter 1: Introduction	12
1.1 Motivation for the research.....	12
1.2 Objectives and Strategy	14
1.3 Layout of the thesis.....	15
Chapter 2: Interlaminar fracture	16
2.1 Introduction	16
2.2 Composite definitions.....	17
2.3 Crack and fracture definitions.....	17
2.4 Epoxy toughening systems.....	19
2.4.1 Early efforts: Rubber and particulate toughening.....	20
2.4.2 Nanoscale reinforcement and toughening.....	21
2.4.3 The addition of thermoplastic	23
2.4.4 Interlaminar toughening.....	23
2.4.5 Relationships between resin and composite fracture performance.....	28
2.5 Crack paths and directional stability; the <i>T</i> -stress	29
2.6 Fracture testing of polymeric materials: A concise review.....	33
2.6.1 Introduction	33
2.6.2 Pure mode I tests.....	33
2.6.3 Mode II test methods in composites.....	37
2.6.3.1 End-notched beam bending specimens.....	37
2.6.4 Mode II and mixed-mode I/II loading of bulk materials.....	37
2.6.4.3 Compact shear type specimens	38
2.6.4.4 Arcan-type specimens	39
2.6.4.5 Four point bend mixed-mode and mode II specimens	42
2.6.4.6 Other mixed-mode specimens	44

2.6.4.7	Requirements and conclusions	45
2.7	Micromechanics of interlaminar shear cracks	48
2.7.1	GIIc in composites	48
2.8	Conclusions	51
	Chapter 3: Experimental mechanics techniques	52
3.1	Introduction	52
3.2	An introduction to full-field measurement techniques.....	52
3.2.1	Photoelasticity	52
3.2.2	Electronic speckle pattern interferometry (ESPI).....	53
3.2.3	Thermoelastic stress analysis	54
3.3	An introduction to digital image correlation	54
3.3.1	Speckle pattern analysis	60
3.4	Mixed mode fracture testing: Parameter extraction and DIC studies	64
3.5	Concluding remarks	68
	Chapter 4: Meso-scale mode I fracture studies.....	69
4.1	Introduction	69
4.1.1	Materials.....	70
4.2	Meso-scale compact tension tests	71
4.2.1	Specimen thickness preparation	73
4.2.2	Introducing a starter crack	74
4.2.3	DIC speckle pattern.....	76
4.2.4	Mechanical arrangement	78
4.3	Optical arrangement.....	80
4.3.1	DIC calibration	82
4.4	Data acquisition and loading details.....	84
4.5	DIC algorithms.....	85
	Chapter 5: Mode I: Results, analysis and discussion	90
5.1	Introduction	90
5.1.1	Determining critical load values	90
5.2	Classical load cell results.....	92
5.2.1	Checking the validity of the LEFM assumptions.....	94
5.3	Extraction of fracture parameters from DIC displacement fields	95

5.3.1	Region of data collection	97
5.3.2	Crack tip location	103
5.3.3	Young's modulus correction	106
5.3.4	Strain-offset correction	109
5.3.5	Stress intensity factor results	111
5.3.6	Crack growth in specimens.....	115
5.3.7	Measuring K _{Ic} with DICITAC	117
5.4	<i>T</i> -stress.....	118
5.4.1	<i>T</i> -stress correction	119
5.4.2	Corrected <i>T</i> -stress values	121
5.4.3	Determining T/σ_0	124
5.5	Comments on the validity and accuracy of the <i>T</i> -stress results.....	125
5.6	Error analysis.....	132
5.6.1	Out of plane displacement: Poisson contraction	132
5.6.2	Out of plane displacement: Rigid body motion.....	133
5.6.3	Errors induced by DIC algorithms.....	135
5.7	DICITAC-induced inaccuracies	139
5.8	Initial fractographic analysis	142
5.9	Concluding remarks	144
Chapter 6: Mixed-mode (I/II) experiments.....		147
6.1	Introduction	147
6.2	Specimens and grip design	149
6.3	Specimen preparation.....	154
6.4	Experimental arrangement.....	156
6.5	Digital image correlation.....	158
6.6	Extraction of fracture parameters	159
Chapter 7: Mixed-mode results and discussion: Stress intensity factors.....		160
7.1	Introduction	160
7.2	Stress intensity factors.....	160
7.2.1	Stress intensity values with increased loading	160
7.2.2	Critical values.....	168
7.2.2.1	Comments on the pure mode II specimens.....	177

7.2.3	Linear regression in K _{IQ} and K _{IIQ}	177
7.2.4	Using K _{II} /K _I instead of loading angle	179
7.3	Determining K _{IIc} using an elliptical model for mixed-mode failure	183
7.3.1	K _{IIc} : Material property or ‘apparent’ value?	188
7.4	Comparing mode II failure in composites with the resin tests	189
7.5	Concluding remarks	190
Chapter 8: Mixed-mode results and discussion: Crack kinking		192
8.1	Kink angle measurement	192
8.2	Using kink angle as an indicator of K _{II} /K _I	194
8.3	Failure criteria	197
8.3.1	Maximum tangential stress criterion	197
8.3.2	Minimum strain energy density criterion	197
8.3.3	Comparing the failure criteria	198
8.3.4	Comparing kink behaviour with strain map data	199
Concluding Remarks		204
Chapter 9: Mixed-mode results and discussion: The T-stress		205
9.1	Introduction	205
9.2	Critical T-stress values	207
9.2.1	T-stress quantifying material-induced crack-tip geometry	211
9.3	Concluding remarks	214
Chapter 10: Conclusions		215
10.1	Conclusions	215
10.2	Recommendations for future work	215
Chapter 11: Appendix		220
11.1	Theoretical K and T-stress values for specimen 00-F5-06	220
11.2	Details and data from tensile tests	221
11.3	Calculation of load-based SIFs from tabulated shape functions	222
11.4	Additional details of G _{IIc} tests	222
11.5	Out of plane (z) displacement fields measured using DIC	222
References		224

Nomenclature

a	Crack length	m
E	Young's modulus	Pa
F	Load	N
G	Energy release rate	J/m ²
K	Stress intensity factor	Pa√m
Q	Load at failure	N
t	Thickness	M
T	T -stress	Pa
u, v, w	Displacement in x,y,z directions respectively	m
w	(Effective) specimen width	m
W	Absolute specimen width	m
Y	Geometric shape function	
α	Crack length to width ratio, a/w	-
β	Mode mixity	°
β_T	Biaxiality ratio	
ε	Strain	-
θ	Kink angle	°
κ	Bulk modulus	Pa
ν	Poisson's ratio	-
σ	Stress	Pa
σ_{xy}	Shear stress in xy direction	Pa
σ_y	Yield stress	Pa
σ_{UTS}	Ultimate tensile strength	Pa
τ_{xy}	Shear stress in xy, (interchangeable with σ_{xy})	Pa
ϕ	Loading angle	°

Subscripts

- I* Mode I (tensile opening)
- II* Mode II (in-plane shear)
- III* Mode III (out-of-plane shear)
- c* Critical material property
- Q* At the point of failure (i.e. load *Q*)

Glossary

3PB	Three-Point Bend flexure test/specimen used for mode I toughness measurement (or flexural modulus measurement).
4PB	Four-point bend test/specimen
Arcan	A type of mixed-mode (I/II) or mode II specimen named after its creator
CAI	Compression After Impact; a strength measurement used in composites to determine material damage tolerance. Specimens are impacted with a specified energy impact and the damaged specimens (typically plates with central impact damage) are subjected to compression until failure. Also CSAI; compressive strength after impact.
CFRP	Carbon-Fibre Reinforced Plastic (typically epoxy however other polymers, including thermoplastics, may be used).
CT	Compact Tension fracture test/specimen for mode I loading; see BS ISO 13586 [1].
Cure	To 'set' a thermoset by subjecting it to cross-linking temperature
DCB	Double Cantilever Beam test/specimen; used for mode I toughness testing (especially in laminar composites).
DIC	Digital Image Correlation
Epoxy	Strictly a thermoset polymer with epoxide functional groups, or its monomer in resin form. However, the term is used here more generally to refer to epoxies blended with thermoplastics or other chemicals to achieve improved performance.
ENF	'End-Notched Flexure', an interlaminar (mode II) shear specimen
FEA	Finite Element Analysis
ILTP	Interlaminar Toughening Particles

LEFM	Linear Elastic Fracture Mechanics
Microscale	Dimensions of the order 10^{-6} m
Nanoscale	Dimensions of the order 10^{-9} m
SIF	Stress intensity factor
Thermoplastic	Polymer that can melt and recrystallise
Thermoset	Polymer whose chemical arrangement is fixed once cured; will not melt.
UTS	Ultimate Tensile Strength

Chapter 1.

Introduction

Improving the toughness of composite materials is of huge commercial and engineering importance. Composites are now widely used in a variety of critical applications; for example, the Boeing 787 is 53% by weight composite material, much of which are carbon-epoxy composite components [2]. These composites are used throughout the primary structure of the aircraft and thus are completely relied upon for structural integrity. Likewise, the future Airbus A350-XWB is designed with a similarly high composite percentage by weight [3]. Due to the difficulties in detecting and also repairing damage, designing composite systems with sufficient toughness is paramount.

Aerospace composite materials typically consist of layers (plies) of either unidirectional tows or woven yarns embedded in a matrix of polymeric resin. The high strength and stiffness of the closely aligned fibres gives composite materials huge stiffness and strength at a much lower weight than engineering alloys. The comparatively low stiffness resin matrix allows loads to be distributed between individual fibres, and also protects the fibres from environmental corrosion and mechanical damage.

It is desirable to make composites with as high a proportion of load-bearing fibres relative to the low stiffness resin as possible. This proportion is referred to as the 'volume fraction'. Whilst composites can be produced by applying wet resin to dry fibres, by hand or by an infusion process, the preferred method of composite 'layup' in the aerospace industry is by 'prepreg' layup; layering sheets of fibres, supplied pre-impregnated with a carefully controlled amount of resin, either by hand or by an automated robotic tape layup process. The prepreg method typically allows composites of 60-70% volume fraction to be produced, close to the maximum theoretical figure for round fibres. Wet layup by skilled persons typically allows 30-50% volume fraction. For thermosetting resins, parts are then cured by subjecting them to the resin cure temperature, thus crosslinking the polymer and fixing the

fibres in position. Applying pressure to the surface of the part by vacuum and if possible, high pressures in an autoclave, reduces air-bubbles and removes unnecessary resin resulting in better parts. Prepreg layup is widely acknowledged as creating the most consistent and repeatable composites with the best material properties, with minimal mess.

A wide variety of fibre and matrix materials can be used. However, the ease of workability, relatively low cure temperature, reasonable working temperatures, good environmental resistance and acceptable cost, combined with excellent mechanical properties makes carbon-epoxy composites the most widely used in high strength structural parts.

1.1 Motivation for the research

Interlaminar toughening, especially by thermoplastic particulate interlayers, is of significant current industrial interest. It has been established that creating an interlaminar region with thermoplastic particles results in large improvements in toughness of the order of 100+% improvements in critical shear strain energy release rate (mode II toughness) G_{IIc} [4, 5]. Despite the use of thermoplastic interlayer toughening in some of the newest aerospace carbon fibre composite systems, the understanding of exactly how the interlaminar toughening particles (ILTP) improve toughness is not complete.

This study aims to use modern experimental mechanics techniques and understanding of fracture mechanics to learn more about how the particles in particulate toughened resins interact with cracks. Through studying the interaction between cracks and both unmodified and particulate toughened resins, a framework for improving resin toughness can be created.

Whilst interlaminar toughening generally improves mode I toughness in composites, the primary reason for it is to improve mode II toughness. Mode II behaviour in composites is currently less well understood than mode I behaviour but the effect of improving toughness is very real and tangible. Improving mode II composite

toughness is strongly related to improved damage tolerance; higher G_{IIc} performance has strongly linked to higher Compressive Strength After Impact (CAI) and is used in various failure criteria for design calculations [6] Whilst much work has been carried out on the toughening mechanisms and toughening methods of epoxies and other polymers used as composite matrices, little work has been directly aimed at toughening mechanisms in cracks subjected to in-plane shear (i.e. mode II) components. Studies aiming to improve resistance to shear fracture in polymers are absent in the literature. This is a strange situation considering improvement in resin mode I toughness are strongly related to improvement in mode I toughness in their respective composites, yet resin mode I toughness has limited effect on composite mode II toughness.

This work aims to further develop the understanding of the behaviour of cracks in toughened polymers under mode II loading. This knowledge will in turn aid the understanding of composite fracture. The ability to link resin behaviours with composite behaviours is invaluable in the development of new composite systems. When developing a composite system, it is intuitively understood that, for example, stiffer fibres can be expected to result in a stiffer composite. Likewise, a tougher matrix can be expected to result in a tougher composite. The reality is more subtle and complex. It is established that for consistent conditions; i.e. identical fibre, layup and matrix-fibre interfacial behaviour, that this is indeed the case for mode I. There are some properties that are more difficult to 'transfer' from resin to properties in a composite system, yet formulations are typically tested at a bulk resin level before being made into a composite system.

The mode I resin toughness has very limited relation to the mode II composite performance. Attempts have been made to link mode II polymer fracture behaviour to composite behaviour before but have been unsuccessful [7, 8]. Careful studies using experimental mechanics techniques have not previously been carried out.

A significant aim of this project is to identify methods of measuring the right resin properties so that composite systems can be developed quicker, in a more focused way, and the best toughening strategies identified without needing to produce rolls

of prepreg with a costly trial-and-error approach. An important part of this process will be identifying the 'right resin properties'.

In addition to the above material-driven objectives, this study aims to further develop the application of experimental mechanics measurement techniques. The tools and methodologies to be used are fairly well established but not widely used in material analysis. Their use so far has mostly been in metallic materials where displacements, strains and stresses are all magnitudes larger at failure (thus easier to measure) than in polymers, with phenomena occurring over much larger distances. Their previous use in measuring critical values (i.e. at the point of failure) is minimal. Few *T*-stress measurements have been directly measured from real specimens and so there is currently little understanding of the natural variation in these values due to inherent specimen and loading imperfection. Comprehensive measurement system evaluations of stress-intensity factor determining tools are currently absent from the literature. Testing numerous specimens will allow the examination of levels of accuracy, optimal data-collection windows, and the effect of different variables such as crack-tip definition. Applying experimental tools and methodologies to small-scale problems such as fracture in epoxies is hoped to improve the field of quantitative experimental mechanics and take these methodologies further.

1.2 Objectives and Strategy

The objectives of this project can be summarised thus:

- Use experimental mechanics to investigate the fracture behaviour of ILTP toughened bulk resin materials, compared with a non-particle toughened system
- Investigate the shear-fracture behaviour of the resin formulations
- Compare the resin shear-fracture behaviour with the performance of composites of the toughened resin systems
- Identify, if any, measurable link between the shear fracture performance of bulk resin and composite system
- Investigate the *T*-stress as a fracture parameter of interest

The strategy to complete these objectives will be:

- Implement the current University of Sheffield stress intensity measurement system, DICITAC, to study the relatively short length scale fracture behaviour of the formulations
- Investigate pure mode I performance of the systems using standard specimen types and comprehensively benchmark the DICITAC system against theoretical load-based measurements
- Develop a test capable of loading the formulations in predominantly mode II (in-plane shear) and measuring the stress intensity factors and the T -stress directly using the experimental mechanics approach
- Investigate the possibility of distinguishing between different formulations using the T -stress as a quantitative measure of resistance to crack kinking, identified as a potential mechanism of interest

1.3 Layout of the thesis

The thesis begins with a study of the structure of the carbon-epoxy composite in chapter 2, with attention paid especially to cracks, fracture toughness and methods of improving toughness. This is followed by a study of experimental mechanics techniques in chapter 3, focusing on measuring and quantifying fracture phenomena with Digital Image Correlation (DIC). Rather than include a separated and disjointed literature review, studies relevant to this project are introduced and discussed alongside other background and discussion in these two chapters.

The experimentation chapters of this thesis are split into two sections. First, the mode I behaviour of the materials is measured (chapter 4) and discussed (chapter 5), with an emphasis on comparing measured values with theory. Chapters 6-7 extend the techniques established in chapters 4 and 5 into mixed-mode (I/II) fracture. Again the study is split into two chapters, one for the experimental methodology – chapter 6 – and another for the subsequent presentation of results and discussion in chapter 7. The thesis concludes with the overall findings of the study, comments on limitations and suggested work for the future in chapter 8.

Chapter 2.

Interlaminar fracture

2.1 Introduction

This chapter contains an examination of the structure of tough carbon-epoxy composite materials. It begins with an explanation of a typical composite and an introduction to the nature of cracks in the composite in sections 2.2-2.3.

The development of a variety of toughening approaches are introduced and examined. Different toughening approaches and the typical, observed mechanisms of toughening are presented and discussed in section 2.4, cumulating in a critical examination of current generation interlaminar toughening. Whilst this study does not directly focus on developing new toughened resins, an appreciation of the methods by which epoxies have been toughened is essential to understand how to observe and measure fracture behaviour. This section concludes with an analysis on work carried out to link understanding of bulk matrix materials with their performance in composite structures.

Section 2.6 covers a review of the fracture mechanics understanding of cracks in relatively brittle (compared with metallic materials used for aerospace applications) bulk and laminar composite materials under pure mode I, pure mode II and mixed-mode loadings. The Williams crack tip stress solutions are examined and the nature and significance of the non-singular T -stress is discussed. Methods of measuring toughness values are examined and assessed.

The chapter culminates in section 2.7 with a discussion on crack behaviour in interlaminar shear fracture events, combining knowledge from the other sections in this chapter.

2.2 Composite definitions

A carbon-fibre – epoxy matrix composite is a lamina structure of layers of fibres, typically of alternating direction. The fibres in each layer can either lay aligned parallel to each other (unidirectional) or are woven into typically orthotropic mats with a variety of different weaves. Layers are typically arranged in different directions, often (but not exclusively) at ± 0 , 90 and 45° orientations. Layers are usually arranged symmetrically about the centre-plane to prevent warping when cured due to the residual stresses caused by the cure process being unbalanced.

Typically there is close to no gap between plies, however the introduction of a thickness of resin between the plies can improve toughness. Sometimes, in interlaminar toughened composites, an interlaminar region is created only in the centre plane. In figure 2.1, interlaminar regions between each of four plies are illustrated. The nature of the interlaminar region is explored in detail in section 2.7.

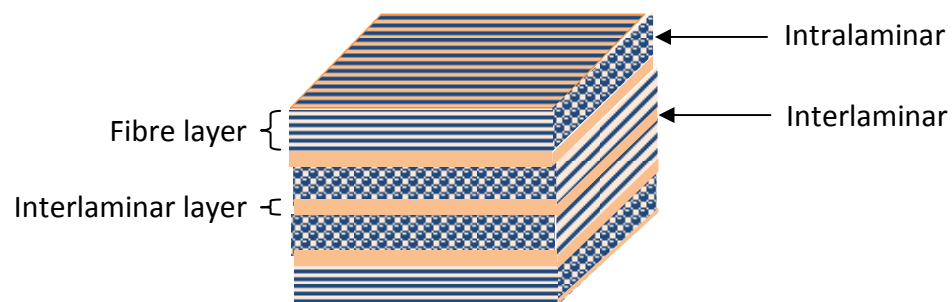


Figure 2.1 - Illustrating the layered structure of a composite. The material illustrated is a 4-ply composite made from unidirectional fibres in a $(0,90)_s$ arrangement. Note the non-zero interlaminar gap thickness present in an interlaminar toughened composite.

2.3 Crack and fracture definitions

Cracks are separated into three different modes; modes I, II and III. These modes separate the nature of crack loading into three directional modes; mode I represents tensile opening of a crack, mode II represents in-plane shear (sliding), and mode III

represents out-of-plane shear (tearing). These three modes are illustrated in figure 2.2.

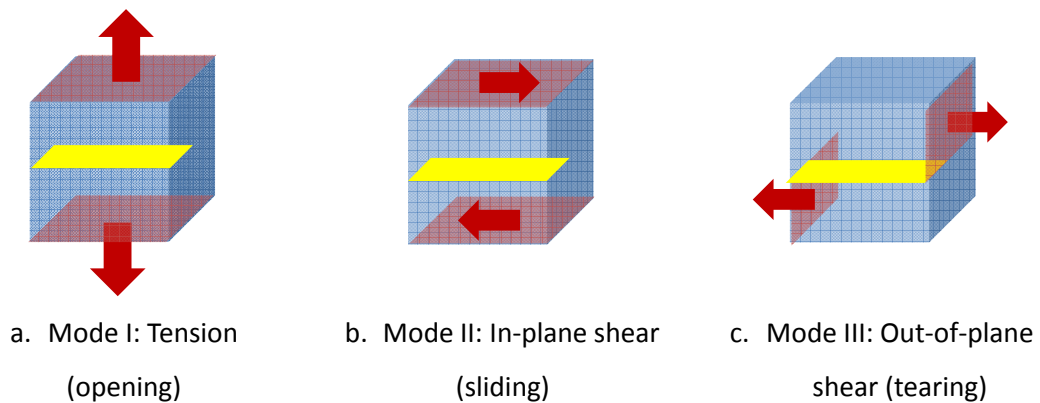


Figure 2.2 - Illustrating the three modes of fracture

‘Toughness’ is the material property which quantifies the resistance to fracture in a material. It is measured in either the energy-based terms of G , the energy-release rate (the sum of the energy released as new surfaces are formed, and by plasticity processes) at which fracture occurs, or as a stress intensity factor K , again at the point at which fracture occurs. Toughness of a material typically differs significantly between the three different modes. Mode II toughness is generally significantly higher, especially in polymers, than mode I toughness [9].

The three different loading (and failure) modes are subject to the principles of superposition. When cracks are subject to components in two or three directions this is termed ‘mixed-mode’.

Brittle materials are defined as those whose fracture process involves little to no energy absorption by plasticity, whilst ductile materials plastically deform substantially. In polymers and other amorphous materials, plasticity does not occur with the same dislocation and slip-based microstructural behaviour as in metals. Instead shear-yielding or crazing processes occur. However, the effect of these irreversible strain energy-absorption processes can be viewed as analogous to true plasticity processes [9]. Whilst the materials under study in this work are, from a fracture mechanics perspective, of a brittle type, it is emphasised that they are extremely tough aerospace epoxies and use of the term ‘brittleness’ does not imply these are low-toughness materials.

In composites (and more generally in bulk brittle materials) defining toughnesses in modes II and III can be complicated. In some materials, the resistance of a crack to fail with a shear mechanism, under shear loading is so great that the crack will 'kink', and redirect sharply toward the lower toughness pure mode I direction, literally the path of least resistance.

2.4 Epoxy toughening systems

When carbon-epoxy systems are developed, typically the resin matrix material is developed and tested before being incorporated into a composite system. Incremental improvements cannot be automatically assumed to transfer to composite performance, and indeed, a major aim of this project is to develop a method of predicting composite mode II fracture performance from resin performance. However, many properties do 'scale' from resin to composite, provided an appropriate interface between resin and fibre exists.

There are numerous properties of significant interest, including the most obvious mechanical properties such as stiffness, strength, strain-to-failure, toughness and damage tolerance. In addition to the direct mechanical properties, thermomechanical properties, resistance to solvents or other harsh environments such as hot and wet conditions, thermal and electrical conductivity are all important. A further layer of important properties are related to the manufacture process; viscosity, cure temperature (or less traditional cure regimes for out-of-autoclave processes), and handling properties when in a prepreg form are all also important considerations. Improvements in one property often come at the cost of degradation in another property and so a holistic process is required.

If formulations and tests can be performed at a resin level then the time and cost of developing new composite systems is reduced. The mechanistic relationship between resin fracture behaviour and composite fracture behaviour is not well characterised or understood and any work that improves knowledge in this area is of great benefit.

2.4.1 Early efforts: Rubber and particulate toughening

The addition of liquid elastomer particles to improve fracture resistance was common in the early 1970s before the toughening mechanisms were understood [10]. Early papers attributed the substantial increase in toughness to many different mechanisms including crack-pinning, particle cavitation and crazing. It was not until the mid 1980s that the fracture mechanisms were thoroughly studied and the theories that form current understandings were postulated [11], showing an increase in shear yielding/plasticity being most responsible for toughening with some additional toughness caused by particle bridging. Their diagrammatic representation of the considered toughening mechanisms is reproduced in figure 2.3.

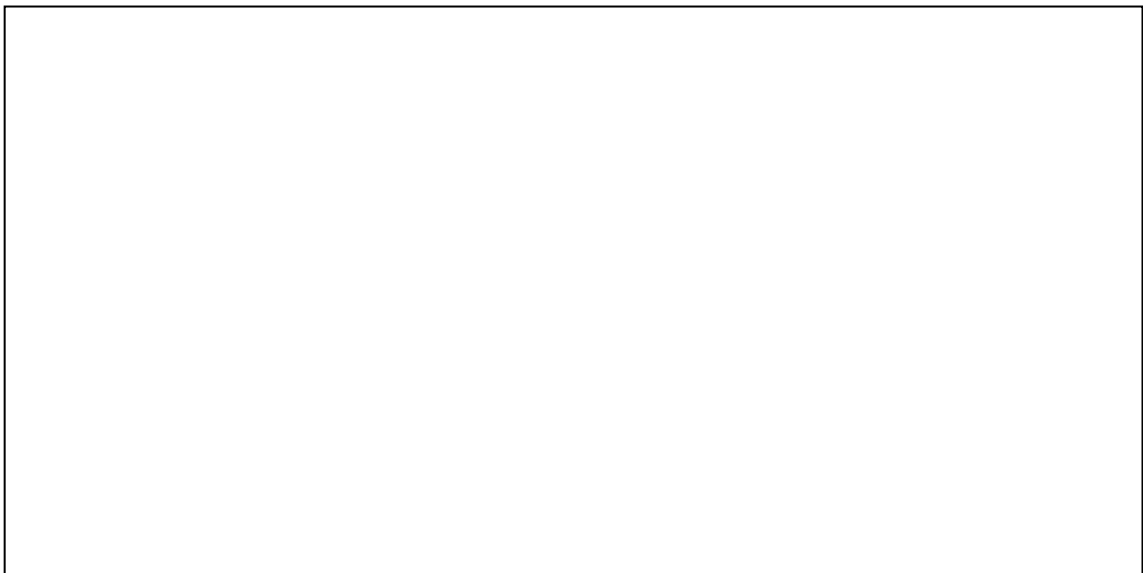


Figure 2.3 - Various proposed particulate toughening mechanisms. Figure and inset list from Pearson and Yee [12].

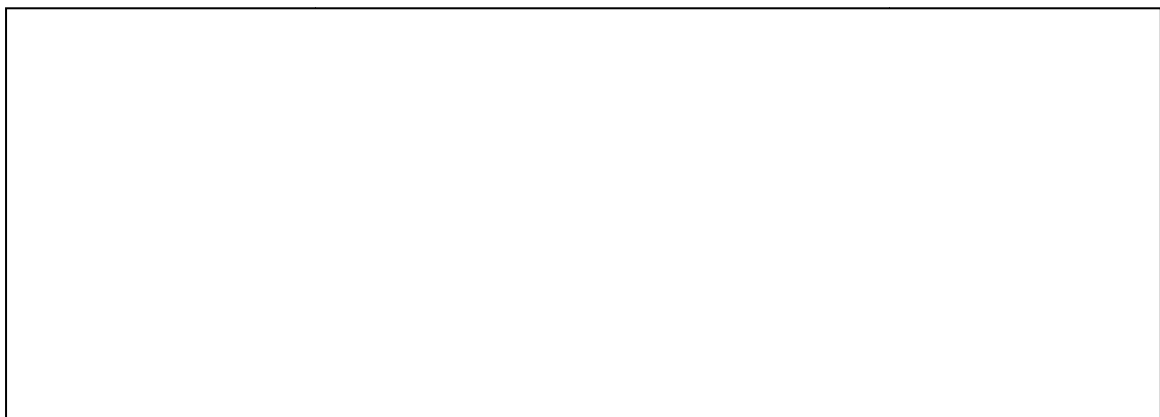
A notable omission from the literature is the lack of consideration of loading mode. It is intuitive that different mechanisms will have different contributions to performance in different loading modes.

Whilst liquid elastomer reinforcements significantly toughen epoxies, they result in reduced polymer stiffness [13] and poor composite hot-wet performance (performance at elevated temperature and high humidity; a critical condition for aerospace parts). Consequently, a large variety of different solid particles have been blended with epoxies in attempts to overcome liquid elastomer limitations. Much

work has been carried out on the addition of microscale thermoplastic particles [14, 15], highly structured microscale particles [16-19] and various nanoscale particles and structures [20-24] to improve toughness without significantly reducing stiffness (and sometimes increasing it) or reducing other desired mechanical and thermo-mechanical properties.

2.4.2 Nanoscale reinforcement and toughening

The addition of small amounts of nanoscale filler has frequently been identified as the future direction to improve a wide range of material properties [21]. Carbon nanostructures, such as carbon–nanotubes (CNTs), in either single or multiwalled form, ‘carbon black’ buckyballs and graphene (these three arrangements of carbon atoms are illustrated in figure 2.4) have tremendous stiffness and strength. Nanosilica and nanoclay (nanoscale silicate platelets) also have high strength properties and are similarly used. The principle of nanoscale toughening is that the surface area of the nanoscale toughening agent is exceptionally high compared to the same volume in a microscale structure. If well-bonded and well-distributed, a wide range of structural and other properties (such as heat and electrical conductivity) can be hugely improved.



a. Single walled carbon nanotube¹ b. Multi-walled carbon nanotube² c. Graphene³ d. Carbon black ‘buckyball’⁴

Figure 2.4 - Nanoscale carbon arrangements

¹ From Wikimedia commons:

http://upload.wikimedia.org/wikipedia/commons/9/9b/Carbon_nanotube.svg

² From Wikimedia Commons: http://en.wikipedia.org/wiki/File:Multi-walled_Carbon_Nanotube.png

³ From Wikimedia Commons: <http://upload.wikimedia.org/wikipedia/commons/9/9e/Graphen.jpg>

⁴ From Wikimedia Commons:

<http://upload.wikimedia.org/wikipedia/commons/0/0f/Buckminsterfullerene-perspective-3D-balls.png>

A number of studies have managed to demonstrate significant toughness improvements in nanoscale toughened epoxies. Studies by Ayatollahi et al. measured K_{Ic} , K_{IIc} [25] and mixed-mode failure K values [26] in multiwalled carbon nanotube (MWNT) toughened ML-506 epoxide with HA-11 polyamine hardener. Results were exceptionally high; the addition of 0.1% by volume MWNTs was found to increase K_{Ic} by 15% from an already surprisingly high 1.62 MPa \sqrt{m} to 1.86 MPa \sqrt{m} and K_{IIc} (measured by asymmetric 4PB, discussed in section 2.6.4.5) from 1.49 MPa \sqrt{m} increased by 22% to 1.82 MPa \sqrt{m} alongside strength and modulus increases, with further improvements with higher nanotube volume percentages.

However, there are drawbacks to this approach. The addition of unmodified nanoscale fillers to various materials frequently yields disappointing improvements (and sometimes reductions) in strength and toughness properties [27]. This is attributed mostly to poor or non-existent chemical bonding between the carbon lattice atoms and the polymer in nanoscale carbon structures and due to agglomeration (clumping of particles) in carbon and silica/silicate based structures. Improving chemical bonding by applying functional groups to the surfaces of carbon nanoscale fillers involves breaking the strong lattice structures, reducing the material properties of the strong carbon lattice structure and severely reducing the electrical conductivity properties [28]. This usually does result in improved epoxy mechanical properties including toughness, strength and stiffness, but little improvement in electrical conductivity is measured over unmodified epoxy [29].

The use of nanoscale fillers can reduce viscosity in the case of slippery, flexible single-walled nanotubes, but in other cases, can also result in very large increases in viscosity due to 'persistent molecular entanglement' [30]; epoxies containing CNTs have been described as being 'similar to a gel' [31, 32].

Consequently, making nanoscale composites is difficult and materials become costly to process, in addition to the obvious expense of nano-fillers. The introduction of structures that are liable to agglomerate has quality control implications. Furthermore, the nanoscale materials typically used have various health implications

due to their aspect-ratios and biopersistance, both of which are concerning similar to asbestos.

2.4.3 The addition of thermoplastic

The addition of solid particulate filler significantly increases resin viscosity and so the use of nanoscale and other bulk toughening solid filler particles has gained limited commercial popularity. Epoxy-thermoplastic mixture resins are used in typical current aerospace prepreg systems such as Cytec CYCOM 977-2, Hexcel HexPly 8552, and Toray T800H/3900-2 all of which are a significant percentage (20-30%) by weight thermoplastic. The thermoplastic forms a phase separated epoxy-thermoplastic morphology in the resin, and provides significant improvements in toughness. The effect on toughness, tensile and strength properties of increasing the percentage of poly(ether sulfone) thermoplastic (in copolymer form with reactive endgroups) is discussed in detail in Brooker *et al.* [33], which also shows the morphological differences as thermoplastic percentage is increased. The Toray T800H/3900-2 prepreg system also includes interlaminar toughening provided by polyamide thermoplastic particles of diameter around 30 μm [34, 35]. Interlaminar toughening is explored in sections 2.4.4 and 2.7.

2.4.4 Interlaminar toughening

A significant, relatively recent approach moves radically away from improving the toughness of the bulk matrix material and instead towards adapting the structure of the composite. Ordinarily in a composite, it has long been seen as an advantage to have as high a fibre volume fraction as possible; the stiffness of the epoxy matrix is ~ 3 GPa whilst the stiffness of an intermediate modulus carbon fibre is ~ 300 GPa. Maximising the fibre volume fraction results in minimal gap between plies (figure 2.5a). Generally, creating a gap of resin between plies significantly increases the unconstrained area in which yielding can occur around a crack tip and so both mode I toughness and also mode II toughness are increased. It was found in the 1970s that adding a fine 'veil' of tough thermoplastic, such as Mylar[®] BoPET (biaxially-orientated polyethylene terephthalate) between plies created a tough interlaminar

region and increased interlaminar toughness and damage tolerance considerably [36]. However, unlike co-continuous thermoset-thermoplastic blends such as those described in section 2.4.3, a complete region of thermoplastic can typically leave the composite susceptible to reduced solvent resistance (depending on the thermoplastic employed). Furthermore, since they are solid at room temperature, thermoplastic veils significantly degrade drape and tack⁵ performance in composites in their prepreg form.

Microscale particles [14], short fibre interleaves [37] and thin, non-woven interleaf layers or 'veils' formed from nanoscale fibres [38-40] have all been identified as successful interlaminar toughening agents in composite systems to improve mode I and II toughness. Microscale interleaf toughening with tight size control has the added benefit of controlling the interlaminar spacing [5], improving consistency. Without Interlaminar Toughening Particles (ILTP), neat resin interlaminar gaps vary in thickness hugely. The aforementioned study found a nominally 41 μm gap ranged from 4 μm up to 120 μm periodically, with a standard deviation of 21 μm .

The mechanisms surrounding toughness are only partly understood. Studies by Stevanovic *et al.* [41-43] showed G_{IC} to be a function of interlayer thickness and also ILTP concentration. In mode II the behaviour is more complicated; experimental data presented in this thesis (chapter 7) show variation in composite G_{IIC} of almost 300% for interlaminar toughened systems with equivalent particle concentrations and the equivalent interlaminar thicknesses. These data show that interlaminar shear toughness is not simply a function of particle size and distribution but is also heavily dependent upon the micromechanical behaviour of the particulates. The interlaminar regions used in the aforementioned Stevanovic *et al.* studies were very large compared with today's cutting-edge interlaminar toughened systems. The interlayer thicknesses used were from 150 μm up to 500 μm , resulting in unconstrained, bulk toughened-polymer behaviour occurring in the interlayer. Typical interlayers in current and 'under-development' commercial aerospace carbon-epoxy

⁵ Drape is the ability of a prepreg to conform to the shape of a mould whilst tack refers to the stickiness of an uncured sheet of prepreg. Ideally there should be enough adhesion to hold layers of prepreg to each other, but be low enough that air bubbles can be squeezed out.

systems are generally an order of magnitude thinner to minimise compromising strength and stiffness with respect to weight [4, 34, 35]. The ABS ILTP in the study can be seen to have irregular shape and a large size distribution.

A study closer to the materials used in this thesis was carried out by Groleau *et al.* [5] who performed mode II tests on CFRP composites with nylon ILTP. This study claimed Nylon-12 particles were picked for convenience only, yet interestingly, Torayca 3900-2, one of the more successful interlaminar-toughened epoxy systems available, also uses Nylon-12 particles. Clearly commercial interlaminar toughening is still in its infancy, with much improvement possible with the correct understanding of the science. Toughening mechanisms in the Groleau study were found to be unclear but matrix microcracking around the particles was observed and particles were observed bridging these cracks, pinning the damage behind the main crack front. This is consistent with the observed behaviour in bulk thermoplastic-toughened resins under mode I loading (typically improving toughness by 10-50%) so the large increases in G_{IIC} remain not fully explained.



a. Damage in a non-interlayer toughened CFRP composite (T800H/3631, from [34])

b. Damage in an interlayer toughened CFRP composite (T800H/3900-2, from [34])

Figure 2.5 - Micrographs of damaged composites. Note the visible interlaminar gap in b. *cf.* the much thinner gap in a. All micrographs from Takeda *et al.* [34].

There is some evidence that toughness values are strongly related to the ability of the material to keep the crack in the interlaminar region, rather than the weaker intralaminar/interfacial⁶ region. A study by Kageyama *et al.* [35] showed a number of micrographs of interlaminar fracture. Figure 2.6, reproduced from this study, shows a typical example of mode II crack growth in an interlaminar toughened composite. It shows a crack kink from the sharp square-notch of the starter crack film toward the interface between interlaminar layer and the fibre bed. The propagated crack shows evidence of crack bifurcation and growth at 45° angles. In a second micrograph, presented here alongside a corresponding K curve in figure 2.7 the progression of crack growth in pure mode I loading from interlaminar fracture to intralaminar fracture can be seen, directly alongside a corresponding drop in toughness. Both of these specimens (and personal communication with other experts [4]) suggest that keeping the crack in the interlaminar region for as long as possible is paramount to maximise interlaminar fracture performance.



Figure 2.6 - “Edge view of mode II crack growth in T800H/3900-2”, from [35], scale bar is approximate⁷.

⁶ The intralaminar is within the fibre layer, interlaminar is in the resin between the fibre layers, the interfacial region is the area of the interface between fibre layer and resin-rich layer. Further descriptions can be found in section 2.2 and figure 2.1.

⁷ The source did not supply a scale, however the interlaminar region is described as being 30µm in thickness.



Figure 2.7 - Decrease in (mode I) toughness in T800H/3900-2 interlaminar toughened composite with delamination growth measured by DCB specimen, alongside a specimen fracture surface. Black fracture surface indicates intralaminar growth whilst white indicates interlaminar crack growth. Note the scales are (intentionally) aligned. From [35].

The method of applying the ILTP used in T800H/3900-2 is to mix particles into the bulk resin and allow the fibres to sieve the particles into the interlaminar region [35]. The particles increase the viscosity of the resin. However, in this case, the added difficulties in processing are accepted for improved performance. If microscale particles can be deposited on the resin prepreg surface directly, or interleaf layers applied without ruining drape or other prepreg behaviour, the resin viscosity remains virtually unaffected, making the approach more desirable and industrially workable than bulk toughening methods using fillers such as nanoparticles [4].

No studies were found in the literature that compare the performance of different interlaminar particles. Due to the strong effects specimen type, lay-up and starter-crack method have on ' G_{IIC} ' measurements, it is sadly impossible to compare the performance of different particles in different studies.

It has been established that there is a strong relationship between increased composite G_{IIC} and increased composite compressive strength after impact (CAI) [8], reduced delamination from impact and other improvements in other damage-tolerance related properties in regular [44] and interlaminar toughened composites [35, 45]. Consequently, the G_{IIC} improvements offered by interlaminar toughening are of great interest in the development of aerospace composites.

2.4.5 Relationships between resin and composite fracture performance

Resin properties do not always transfer well to composites and it is well established that improving a property at a resin level is no guarantee of improved composite properties. However, mode I toughness in composites has been shown by a number of studies to generally be improved by increased mode I toughness of the matrix resin [8]. Data from a variety of researchers for a wide variety of different toughening methods were compiled by Kim *et al.* [46] and a figure from this study is reproduced in figure 2.8. Another compilation of mode I resin and composite toughness values, showing the same trend, can be found in Anderson [9].

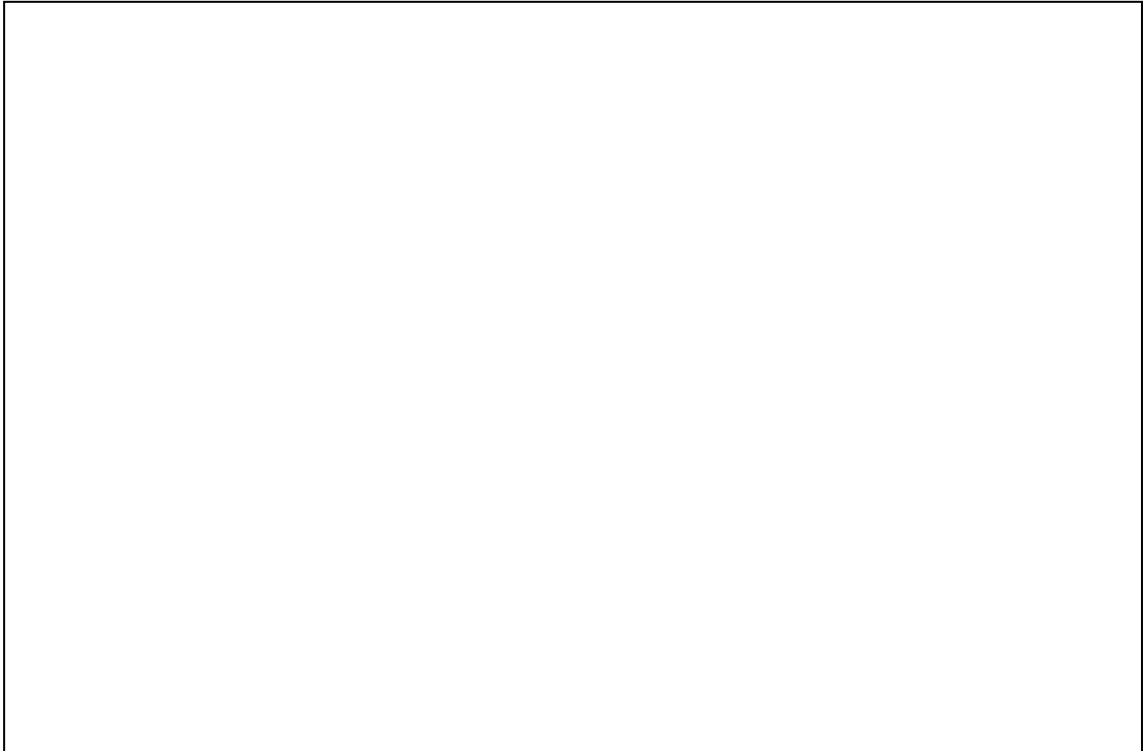


Figure 2.8 - The relationship between resin mode I toughness and composite mode I toughness in epoxy-carbon composites, taken from Kim et al. [46]. Stiff, strong epoxies with good hot-wet performance suitable for aerospace applications are generally toward the bottom of the curve, with typical resin G_{Ic} values of $< 1 \text{ kJ/m}^2$.

2.5 Crack paths and directional stability; the T -stress

Equation (2.1) shows the first three terms of the mode I Williams crack tip stress solutions in a Cartesian stress form. The second term of the Williams crack tip stress solution, the non-singular T -stress, is a fracture parameter of some significance and will be discussed further in later chapters. Figure 2.9 shows the Cartesian and polar coordinate notation that will be used to describe the stress distribution around a crack tip.

$$\begin{aligned}
\sigma_{xx} &= \frac{K_I}{\sqrt{2\pi r}} \cos \frac{\theta}{2} \left(1 - \sin \frac{\theta}{2} \sin \frac{3\theta}{2}\right) + T + A\sqrt{r} \cos \frac{\theta}{2} \left(1 + \sin^2 \frac{\theta}{2}\right) + O(r) \\
\sigma_{yy} &= \frac{K_I}{\sqrt{2\pi r}} \cos \frac{\theta}{2} \left(1 - \sin \frac{\theta}{2} \sin \frac{3\theta}{2}\right) + A\sqrt{r} \cos \frac{\theta}{2} \left(1 - \sin^2 \frac{\theta}{2}\right) + O(r^{3/2}) \\
\tau_{xy} &= \frac{K_I}{\sqrt{2\pi r}} \cos \frac{\theta}{2} \sin \frac{\theta}{2} \cos \frac{3\theta}{2} - A\sqrt{r} \sin \frac{\theta}{2} \cos^2 \frac{\theta}{2} + O(r)
\end{aligned} \tag{2.1}$$

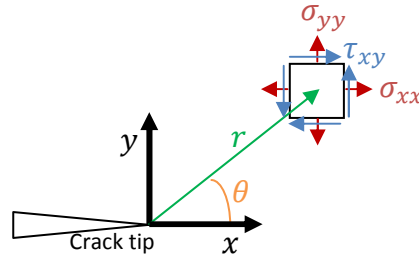


Figure 2.9 - Illustrating the crack tip notation

Physically, the T -stress is a finite stress parallel to the crack. Cotterell [47] first identified the T -stress as controlling the directional stability of the crack tip. It is difficult to condense this study more succinctly than the abstract thus:

“The stress distribution at the tip of a crack can be expanded as a power series. The first term, usually called the stress intensity factor, determines the initiation of fracture in a brittle material. In this paper it is shown that the second, third and fourth terms have the following effects:

- (a) *The second term [the **T-stress**] controls the stability of the crack’s direction,*
- (b) *The third term controls the stability of the crack’s propagation,*
- (c) *The fourth term determines whether the maximum shear stress on the prolongation of the crack increases or decreases with distance from the crack tip.”*

Cotterell – Notes on the paths and stability of cracks (1966) [47].

Cotterell defined two types of crack propagation, class 1 and class 2, depending on the stability of the path. Class 1 cracks kink or curve back on themselves whilst class

2 cracks diverge away from their original path. Cotterell's illustration is reproduced in figure 2.10. The sign of the T -stress was shown to directly affect this kink direction; positive T -stresses result in unstable crack kinking (figure 2.10-a), whilst negative T -stresses result in stable crack kinking (figure 2.10-b).



- a. Positive T -stress: Unstable crack path b. Negative T -stress: Stable crack path

Figure 2.10 - Crack path stability. From *Notes on the path and stability of cracks* [47].

Examination of the Williams crack tip stress solutions (equation 2.1) shows the T -stress to have a measurable effect on the form of the stress fields around a crack tip. The T -stress is well-known to influence the form of the fringe loops in photoelastic studies (and hence the stress field). A study by Christopher et al. [48] clearly illustrates the effect the T -stress has on the form of the elastic stress field shape. Illustrations from this study are reproduced in figure 2.11. Red triangles have been overlaid to more clearly show the crack position. Positive T -stress (figure 2.11-a) can be seen to cause the fringe loops to point backwards, whilst the opposite is true for a negative T -stress (figure 2.11-c).



- a. Positive T -stress b. Zero T -stress c. Negative T -stress
 $T = 1.5 \text{ MPa}$ $T = -1.5 \text{ MPa}$

Figure 2.11 - Theoretical photoelastic fringe patterns around a crack tip (cracks from left to right) for cracks subject to $K_I = 1 \text{ MPa}\sqrt{\text{m}}$ and varying T -stress values. Images from Christopher et al. [48]

Since cracks grow in the direction ahead of the crack that bisects the fringes [49], (i.e. the direction of minimum shear stress) one can see how the T -stress physically affects stability. The bisected angle between the fringes in the positive T -stress case, overlaid in figure 2.12-a, is obtuse, whereas in the negative T -stress case in figure 2.12-b is acute. This shows a visible difference in constraint around the crack tips. Cracks have been shown to grow in the direction of minimum shear stress [50]. The direction of minimum shear stress is tightly controlled in the negative T -stress case, whereas the direction of minimum shear stress in the positive T -stress case is much wider, giving the crack a higher amount of directional freedom. Angled crack growth will clearly not be pushed back toward the ‘ideal path’ illustrated in Cotterell’s diagrams of figure 2.10. Thus, the T -stress affects the ‘constraint’ in the direction of minimum shear stress and hence the direction of crack growth.

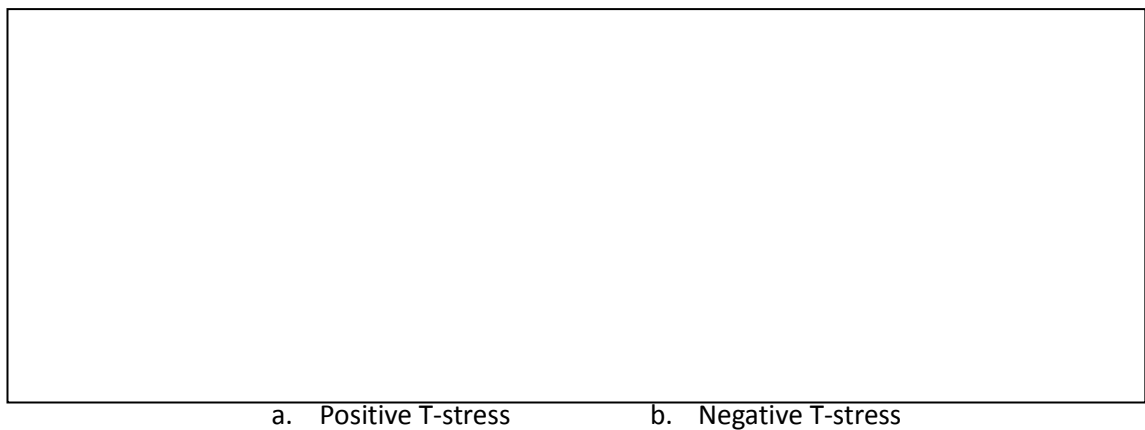


Figure 2.12 - Theoretical photoelastic fringe patterns around a crack tip from Christopher *et al.* [48], with overlaid fringe angles and crack growth

In addition to influencing the elastic stress field distribution, the T -stress is known to strongly affect the shape and size of the plastic zone at the crack tip [48, 51, 52]. Studies in the following years tabulated T -stresses for a variety of crack loading conditions [53].

Studies by Smith *et al.* [54, 55] showed the T -stress to strongly affect apparent toughness properties in brittle materials, especially under mode II loading. The difference between apparent and actual material properties in brittle materials subject to shear components is detailed further in section 7.4.1.

2.6 Fracture testing of polymeric materials: A concise review

2.6.1 Introduction

Since the predominant failure mode of most engineering components is mode I, studies of mode I (tensile) fracture are far more established than the less commonly encountered modes II or III. Simple and accurate tests and international standards exist to test mode I specimens in a wide variety of materials, including composites. However, other fracture modes are more problematic.

The interlaminar toughness of composites is extremely important; delamination is a common but difficult to detect damage mechanism in fibre composites. Much work has been carried out studying fracture of interfaces, such as adhesive joints or composite layers under shear loading. (Studies of specific interest to this project involving composites with particulate toughened matrices include [56-59]; countless more interlaminar studies exist). Limited work has been carried out on the mode II behaviour of bulk material with the aim of developing a more fundamental understanding of the materials' fracture behaviour, so that empirically-based toughening strategies can be developed.

2.6.2 Pure mode I tests

There are two primary test-specimens for loading bulk materials in pure mode I. These are the single edge-notched beam specimen (SENB) under three point bend (3PB) loading, figure 2.13a, and the compact tension (CT) specimen, figure 2.13b. Both of these specimen types are fully explained and described in the British and international standards [1] as well as the ASTM equivalent [60]. For the duration of this study, the British/International Standards have been used and will be referred to.

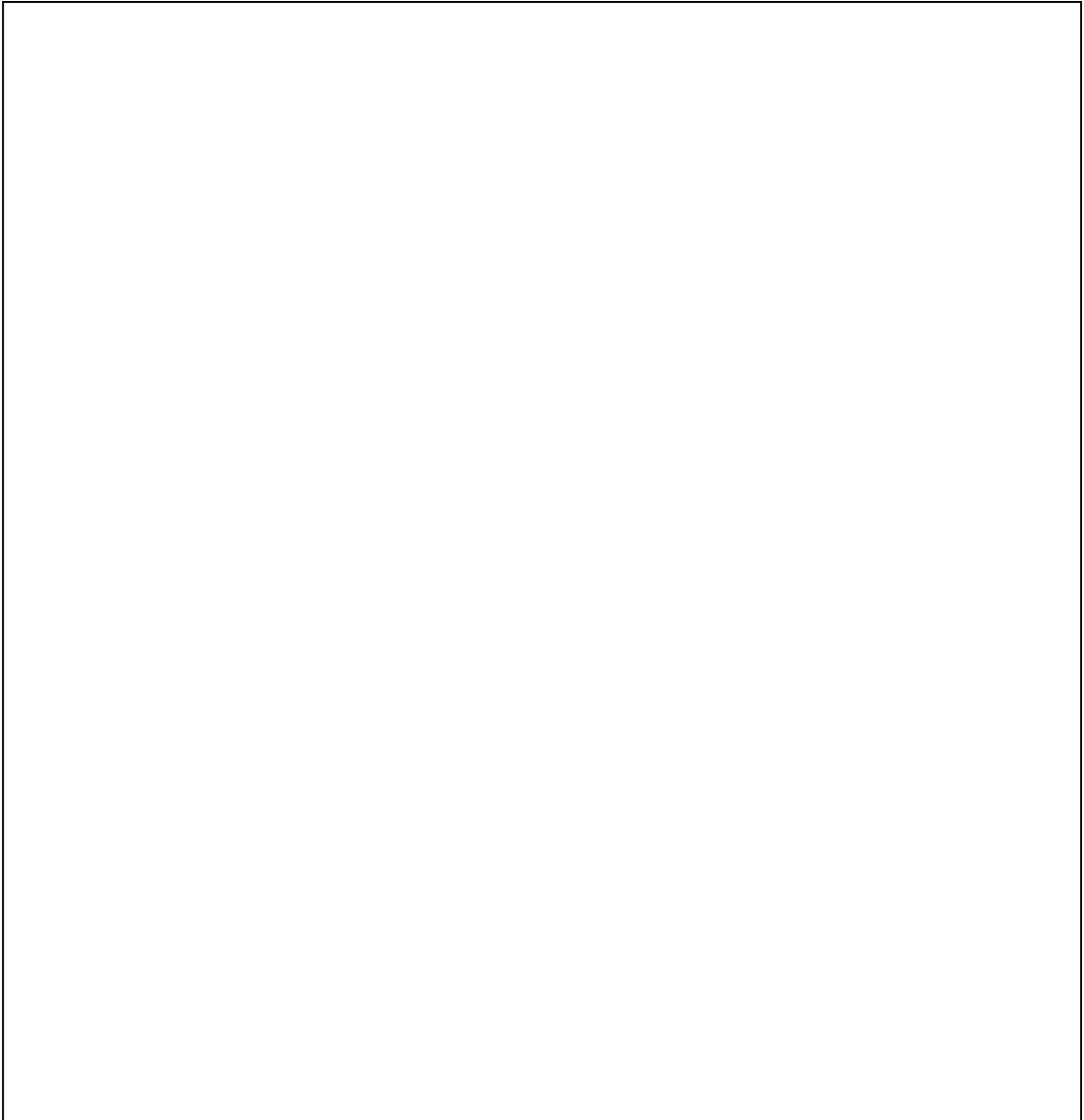


Figure 2.13 - The two standard specimen-types for determination of K_{Ic} , figures taken from BS ISO 13586:2000 (*Plastics: Determinations of fracture toughness (G_{Ic} and K_{Ic}). Linear elastic fracture mechanics (LEFM) approach*) [1]

CT specimens were selected for use over single edge-notch beam (SENB) specimens after some experimentation with both. It was quickly found that CT specimens undergo significantly lower levels of rigid body motion compared with beam-type specimens. The benefits of this are two-fold when measuring displacement fields using Digital Image Correlation (DIC) as in this body of work; a smaller field of view can be employed without the specimen region of interest moving out of shot, and the smaller levels of rigid body displacement results in lower strain field errors. The

DIC technique is explained in detail in section 3.3. DIC errors are explored in section 5.7.

In composite materials, specimens are typically subjected to mode I loading in either interlaminar or intralaminar orientations. Interlaminar tests typically involve forming a composite panel with a strip of release film in the centre plane to initiate a stress concentration. This forms the start of a crack, which is then made 'sharp' by the application of quasi-static tensile load to the sides, causing the starter crack to propagate and grow. Load is applied through either hinges or end-tabs (seen in figure 2.14).

Intralaminar testing is the testing of toughness in the fibre-rich areas instead. Creating a starter crack is difficult and the subject of much current research [61]. This study focuses on epoxy fracture in resin-rich interlaminar regions and so intralaminar testing will not be mentioned further.

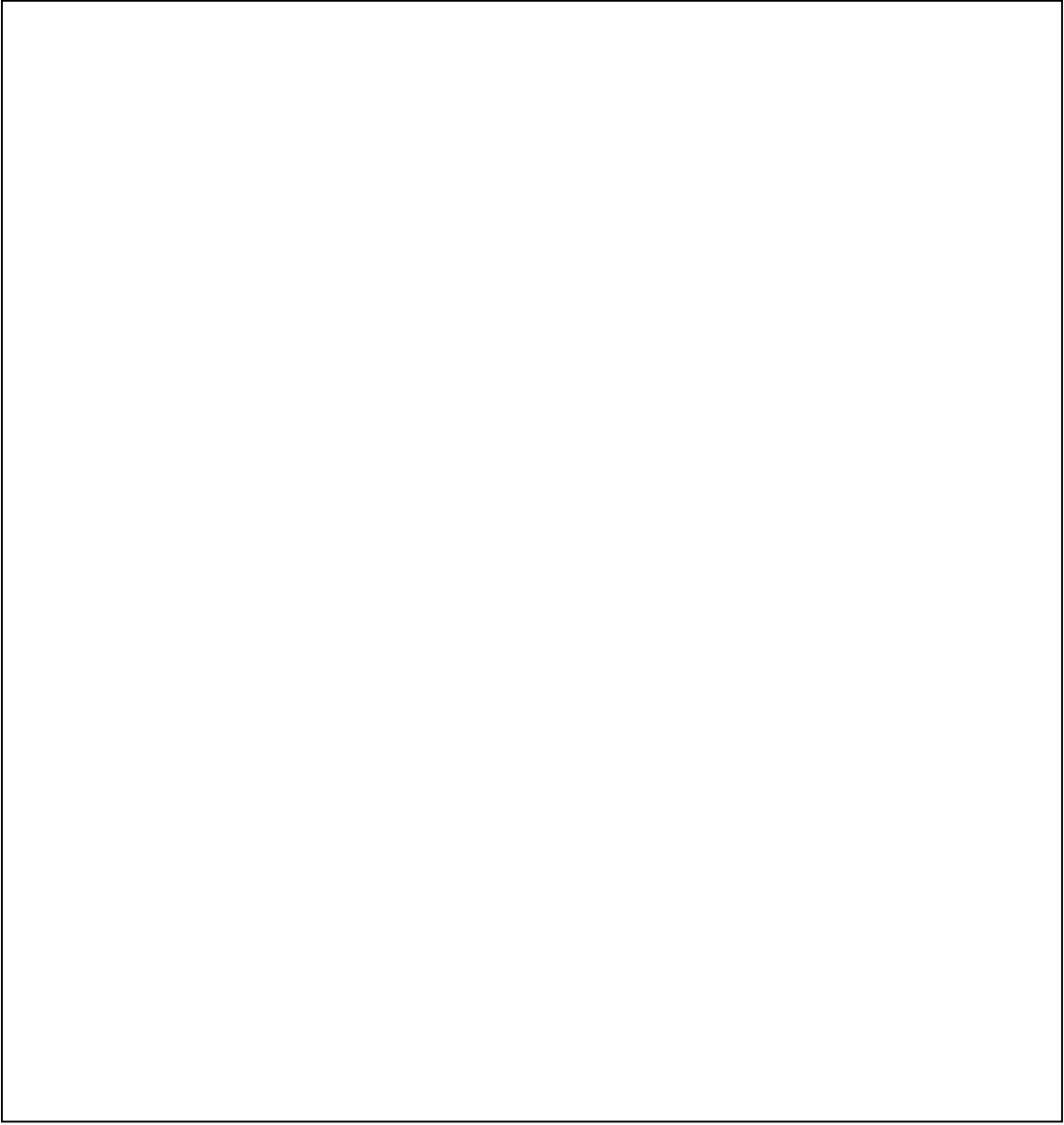


Figure 2.14 - The double cantilever beam specimen (from BS ISO 15024 [62])

2.6.3 Mode II test methods in composites

2.6.3.1 End-notched beam bending specimens

The general preferred method of mode fracture II testing in composites is the end notched flexure (ENF) test (figure 2.15) [63, 64]. This end-split, typically three-point loaded test specimen is analogous to the double cantilever beam (DCB) specimen (figure 2.14) used to measure K_{Ic} but instead loaded under three-point-bend (3PB) to produce a state of shear at the crack tip rather than tension. A pre-crack is created by placing a piece of release film in the centre-plane of the panel to act as a starter crack. Some applications of the ENF test involve the application of load to create a natural crack from this stress concentration before beginning measurement.



Figure 2.15 - The end-notched flexure specimen (from Carlsson *et al.* [63])

The specimen can be loaded in a number of ways including the most common three-point bend (3PB), four-point bend (4PB), and variations to improve crack growth stability. Alternatively, the specimen can be loaded at the cracked end with the other end held captive; the 'end-loaded split' (ELS) specimen [65]. The interlaminar shear specimen for composites is examined further in section 2.7.

2.6.4 Mode II and mixed-mode I/II loading of bulk materials

Whilst the geometry of laminar composites and adhesively bonded specimens constrains crack growth in the shear loading direction, it is more difficult to cause shear fracture in bulk specimens. Changing the method of producing shear across a crack tip to a more direct method increases the K_{II}/K_I ratio, thereby reducing the likelihood of mode I failure. A number of test specimens designed to directly load the specimen in shear exist, including the V-notched rail test [66], Iosipescu test [67],

Banks-Sills and Arcan shear specimen test [68], and the Richard compact shear specimen [69]. A number of these specimens are examined further below.

2.6.4.3 Compact shear type specimens

The compact shear specimen, described by Richard [69] loads an edge-cracked specimen of bulk (i.e. non-laminar) material in shear through pin connections. The specimen preparation is relatively simple compared to many other specimens, however, the specimen exerts a relatively low K_{II}/K_I on specimens. The study of the Richard specimen (figure 2.16) by Yuan *et al.* [70] calculates a values of K_{II}/K_I of around 8 for a/w (crack length over specimen width) values of 0.35.

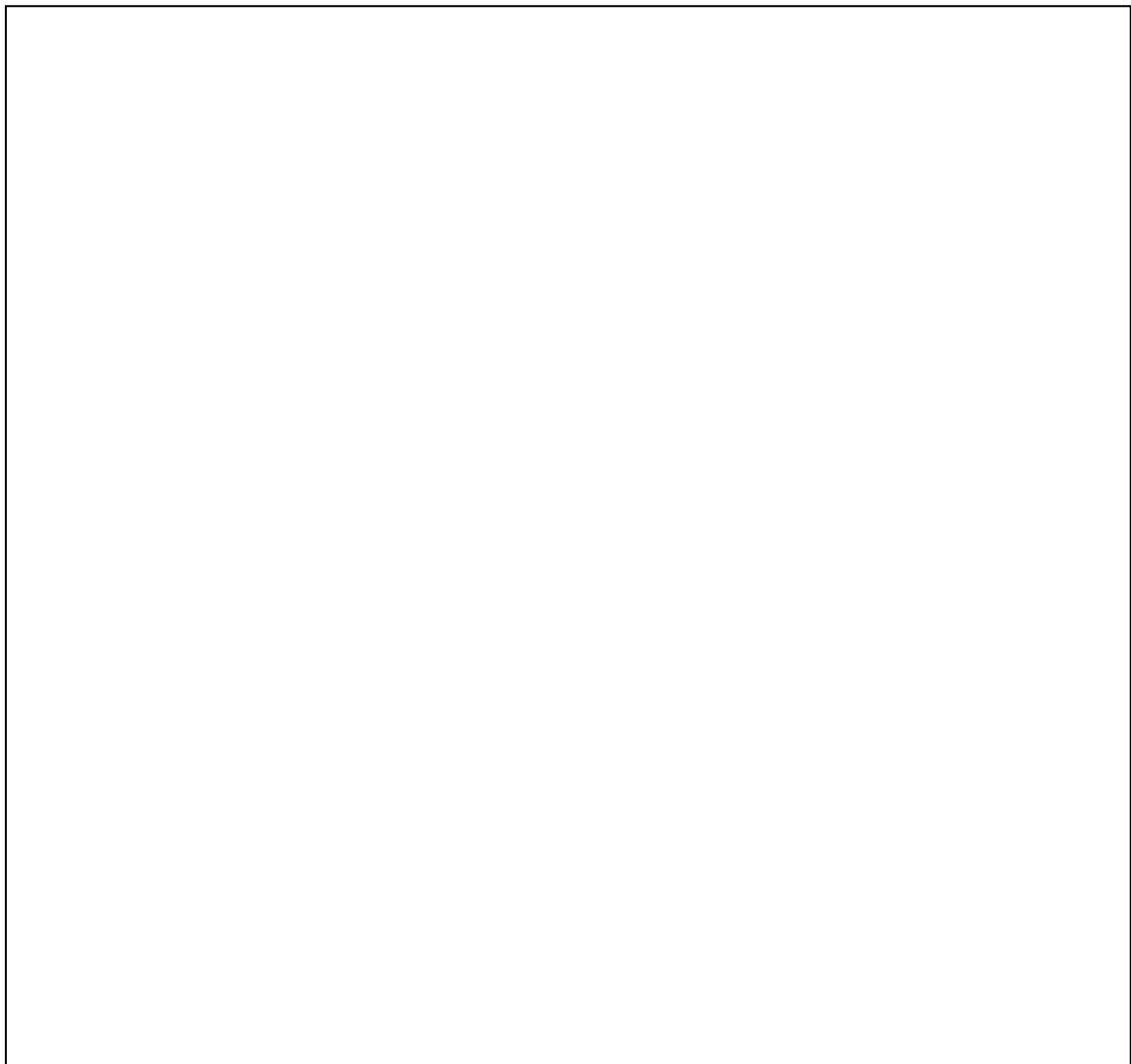


Figure 2.16 - Richard compact shear specimen (upper) and grips (lower) for measurement of K_{IIc} (from [69])

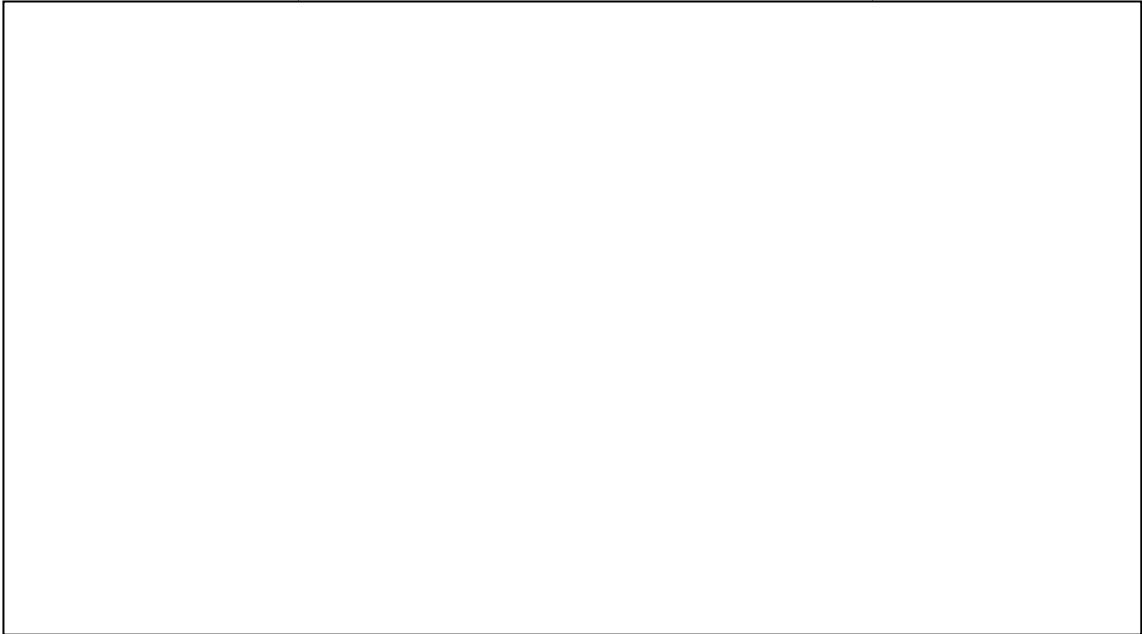
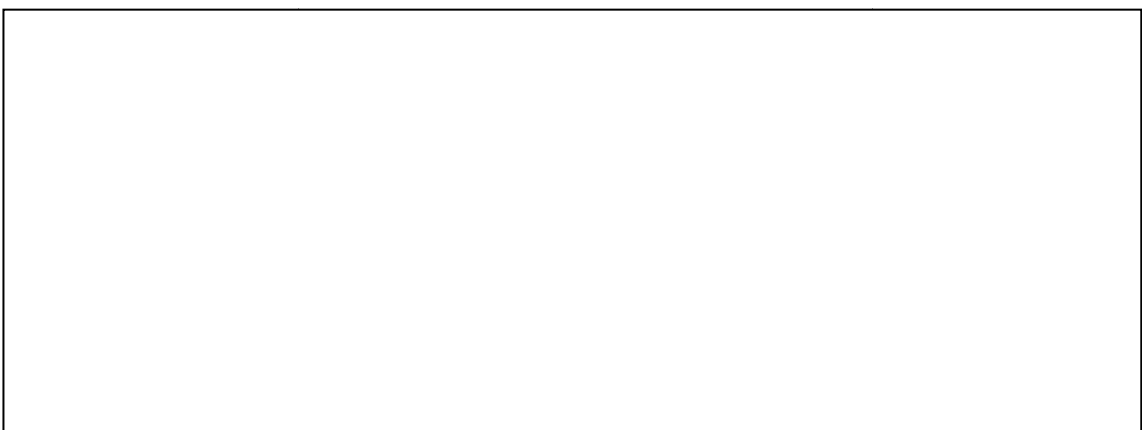


Figure 2.17 - Richard compact tension—shear specimen (a) for mixed-mode (I/II) loading and grips (b), detailed in [71], figure from [72].

2.6.4.4 Arcan-type specimens

The Arcan specimen was initially designed for determining K_{IIC} [68] and later developed into a mixed-mode specimen. Similar to the compact shear specimen, the angle of the crack and ligand (uncracked material across the width of the specimen) are chosen by varying which pins are to be used (figure 2.18 shows Arcan grips and specimen mounted at various orientations).



0° (pure mode I)

45° (mixed mode I/II)

90° (pure mode II)

Figure 2.18 - Arcan grips and specimen mounted at various angles, figure adapted from [73].

The Banks-Sills modification to the plain Arcan specimen is to attach, with adhesive, a frame to apply the load at a fixed angle. The Banks-Sills and Arcan specimen [68] in the original paper (figure 2.19) is cracked with a centre-crack cut with a diamond saw.



Figure 2.19 - Banks-Sills—Arcan modified Arcan specimen for measurement of K_{IIc} (from [68])

A finite-element study by Yuan *et al.* [70] evaluated the J -integrals, K_I and K_{II} values for a number of mode II specimens and found the Banks-Sills and Arcan specimen (figure 2.20) to have the highest K_{II}/K_I ratio, the most symmetric stress-fields and to have exhibited maximum stress ahead of the crack tip as desired of the specimen types they tested. As with many other Arcan-type specimens used by various authors, the specimen analysed by Yuan *et al.* however has an edge-crack instead of a centre-crack (figure 2.20). Whilst both methods put the crack tips in predominantly mode II loading, the use of an edge-crack enables the introduction of a naturally sharp crack by tapping a razor-blade into a notch root. Cutting a centre-slot with a diamond-saw creates a significantly blunter crack tip. Whilst a blunt crack tip is typical for sub-critical studies of stress-fields, for the determination of critical fracture parameters a crack as sharp as possible is required [1].

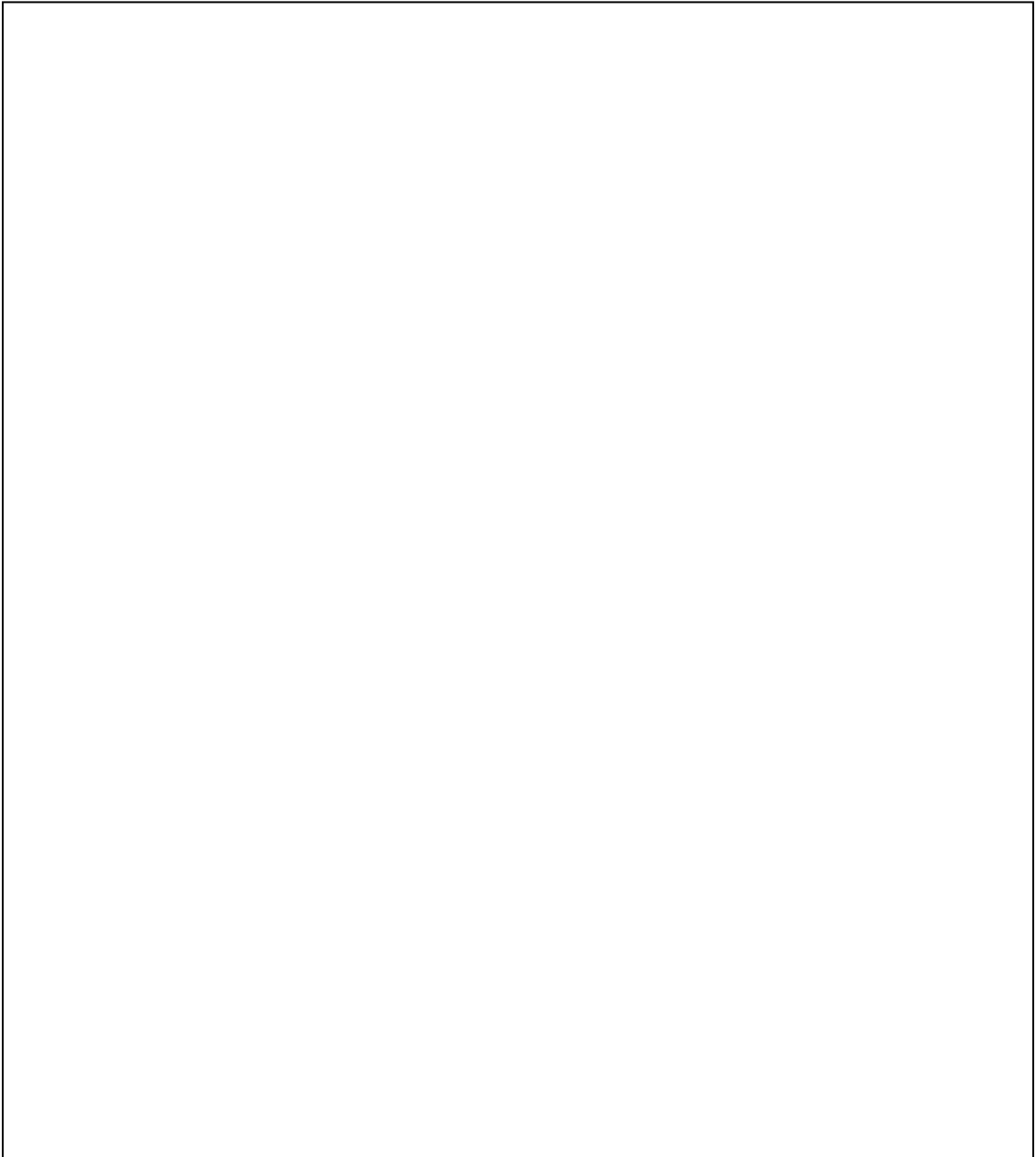


Figure 2.20 - Edge-cracked Banks-Sills – Arcan grips (a.) and specimen (b.) for mixed-mode loading (both taken from [73])

The mixed-mode arrangement of the Arcan specimen, in an edge-cracked form, can be found in a number of places in the literature [73, 74] and is shown in figure 2.20. The main difference between the Banks-Sills – Arcan style geometry and the Compact Shear geometry is the narrowing of the ligand (uncracked specimen width) in the Arcan-type specimens. It has been suggested that the effect of this is an increase in K_{II}/K_I value for pure mode II loading.

2.6.4.5 Four point bend mixed-mode and mode II specimens

Four-point bend tests can be performed to apply a mixed-mode loading to centre-cracked beam specimens.

The 4PB mixed-mode and mode II specimens will not experience the same excessive rigid-body motion as the mode I 3PB specimens already discounted for DIC analyses. A benefit of the 4PB loading system is that the effect of the loading pins on the specimen is clear and easily quantifiable, unlike six-pin Compact Shear-Tension (figure 2.17) and Arcan-type specimens (figure 2.20). Either the position of the loading pins can be varied (as illustrated in figure 2.22), and the crack kept central, or the crack location can be varied and loading pins moved. Specimen preparation is clearly very simple.

Ayatollahi et al. measured K_{Ic} and K_{IIc} toughness values in epoxies toughened with multi-walled carbon nanotubes [25] and mixed-mode toughness values [26] using 4PB specimens. Specimens in the pure mode II configuration (figure 2.21) were calculated to apply K_{II}/K_I values of 25 for $a/w = 0.5$ and considerably less as a/w is reduced; <5 for $a/w = 0.3$ (figure 2.23).

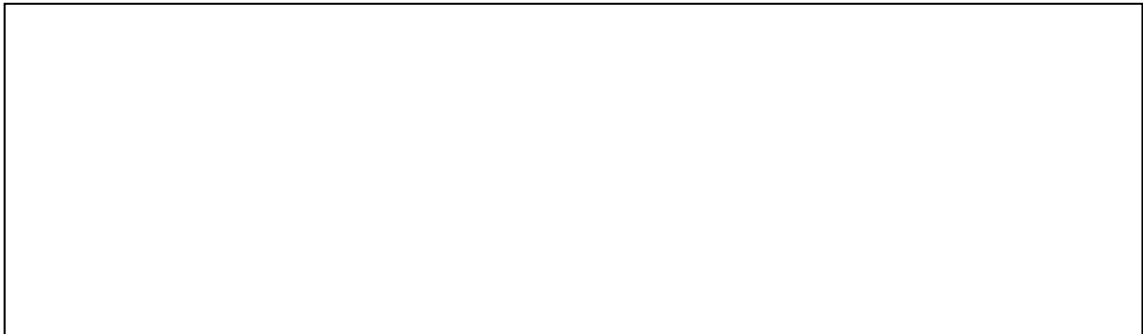


Figure 2.21 - Asymmetric four-point bend test for measuring K_{IIc} (from [25])

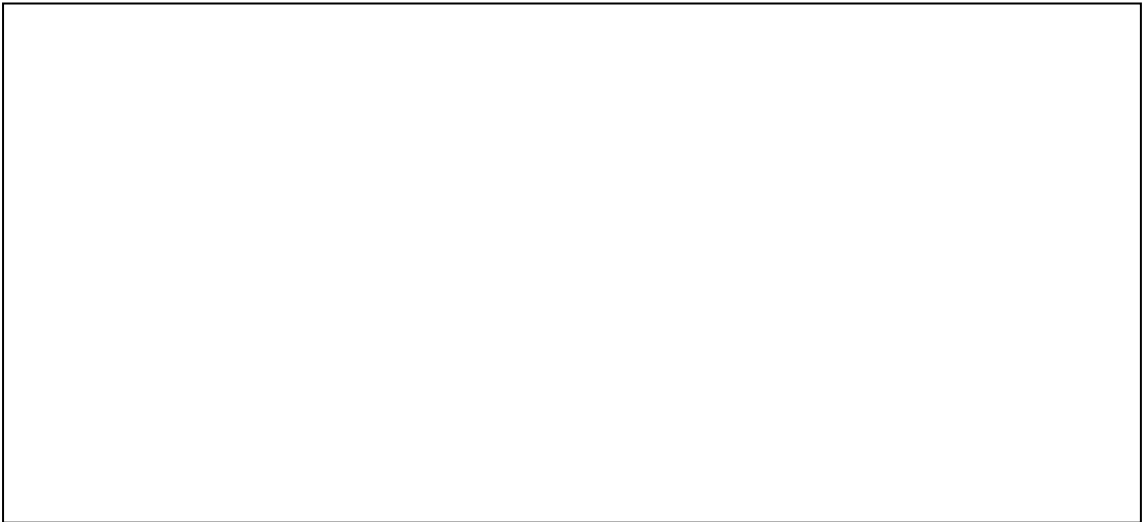


Figure 2.22 - Four-point bend specimen for mixed-mode (I/II) testing (from [26])

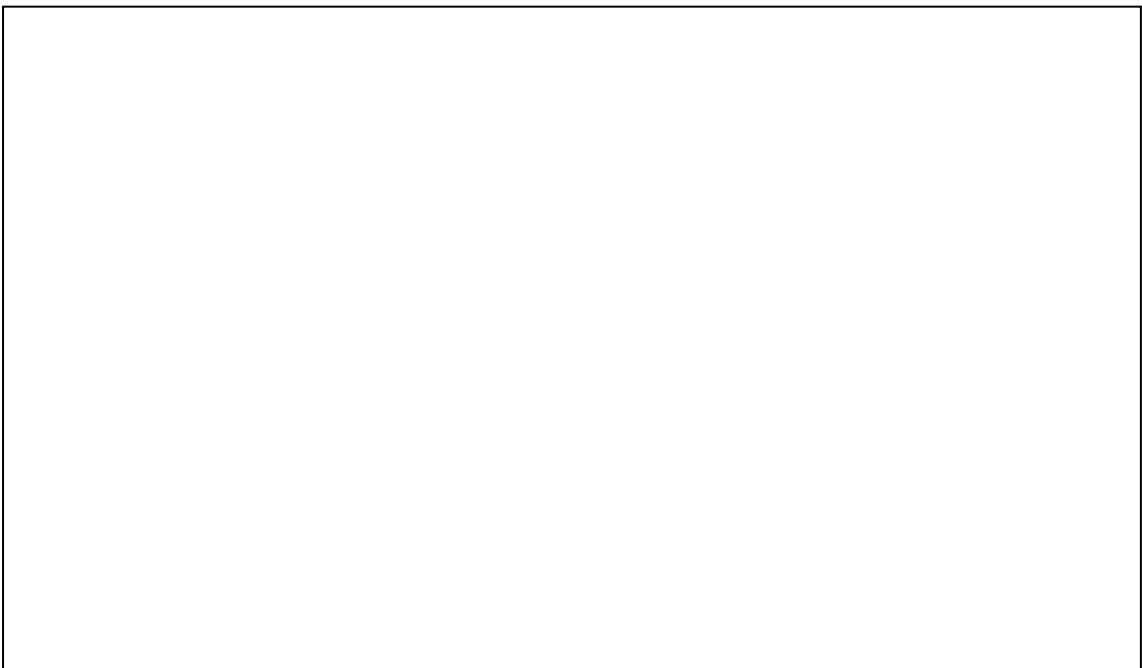


Figure 2.23 – The variation of K_{II}/K_I ratio versus the crack length ratio a/w for the asymmetrical 4PB mode II beam specimen from finite element simulation; data from [25].

2.6.4.6 Other mixed-mode specimens

Ayatollahi and Aliha [75] designed and tested a remarkably simple direct tension-based specimen, the diagonally loaded square plate (DLSP) specimen, capable of loading cracks in easily varied mode mixity from pure mode I to almost pure mode II requiring no special grips or alignment difficulties. An angled crack is cut into a square specimen loaded in tension across the two corners (illustrated in figure 2.24) with good results. However, the method of creating a crack in the material; namely through cutting a narrow slot with a thin fret-saw blade, does not create a natural or sharp crack. Various works [1, 76] (including the British Standards for fracture toughness) highlight the importance of a natural, sharp crack for measuring critical toughness values. In the toughened epoxies being studied in this thesis it is thought that the microscale morphology of a naturally 'sharp' crack could be significant in explaining differences in crack tip stability under mixed-mode loading between the formulations. Because of this, the Ayatollahi DLSP specimen was not considered. Instead, edge-crack methods that allow sharp cracks to be formed were pursued.

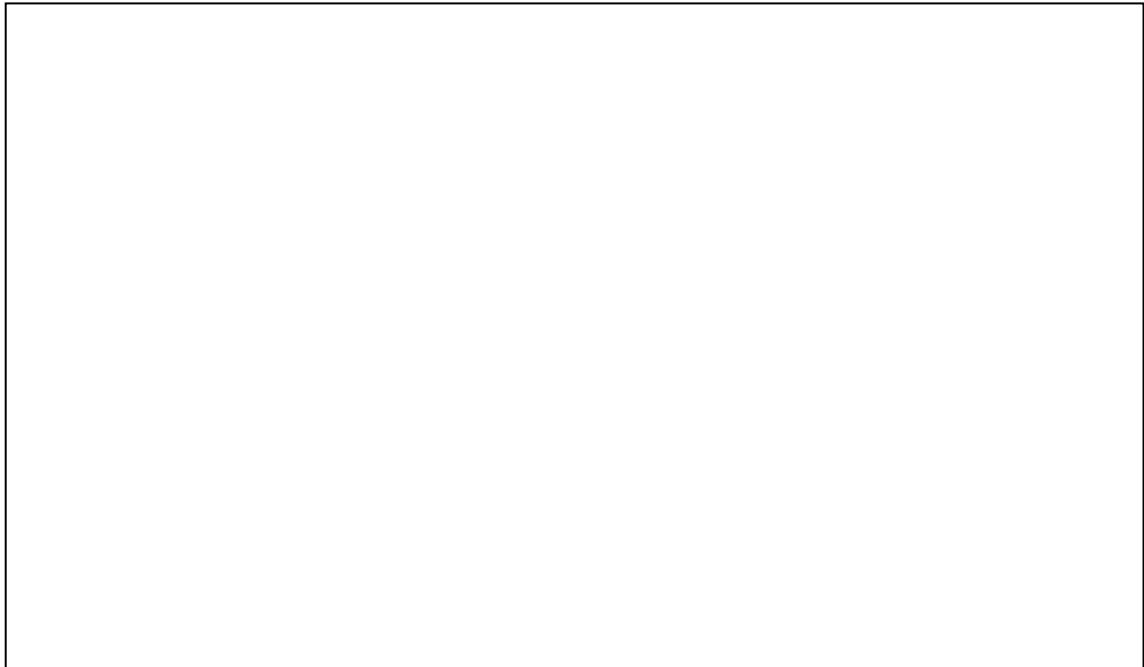


Figure 2.24 - Ayatollahi diagonally loaded square plate (DLSP) mixed mode specimen from [75]

2.6.4.7 Requirements and conclusions

Considering the previous work on the topic, a Banks-Sills – Arcan / Richards Compact Shear-style specimen/specimen grip will be produced with a simplified bolt-based grip system. The effect of bolted connections on the specimen will have to be analysed by observing strain fields, but this method will significantly speed up specimen testing over attaching specimens to grips with adhesive.

Whilst the asymmetric four-point bend (A-4PB) system looks the easiest system to employ, with benefit of simple specimen preparation and no pin-connections, it is subject to the same DIC-related limitations of the three-point-bend single-edge-notched-beam for mode I loading. There is a significant amount of rigid body motion anticipated in the A-4PB specimen for $K_I > K_{II}$. As mentioned previously, this causes issues when measuring displacement fields over small fields of view.

Also, the Arcan-type arrangement loads specimens in opening-shear, thereby causing minimal friction-based complications. The Williams stress-field solutions are defined as being valid only for situations where the crack flanks are traction-free. The reduced ligand length in Arcan-type specimens, compared with the compact tension shear specimen, results in a reduced required length of natural crack. Natural cracks propagated by razor-tapping in the materials under investigation could only successfully be applied between 1 and 5 mm in length (section 4.2.2 contains more information on the introduction of cracks). Cracks of the length required for compact shear specimens could only be produced by cutting a wider slot. Also, whilst Richard style compact shear specimens may be suitable for subcritical loading of specimens, it is fully intended to load each specimen to failure. Consequently, it was decided to use a narrowed ligand specimen, as per the Arcan design, with its higher maximum K_{II}/K_I .

Grip torque in Arcan-type specimens

A complication of loading Arcan specimens in partial or predominant shear is that their application results in a moment being exerted upon the test frame fixture and load cell, as shown in the free body diagram of figure 2.25. Side-loading to a load-cell can be damaging to the load cell and can result in incorrectly determined loads. If the

linkages are free to rotate, linkage rotation will occur and result in incorrect constraint. This was experienced in a first rough set of K_{IIc} tests performed by the author but not detailed or published here. A recent paper studied the constraint conditions of a commonly employed variation of the Arcan specimen [74]. Greer's FE studies and free-body analyses showed the actuator side load to vary with specimen angle⁸, and with loading member (beam AB in figure 2.25) and specimen flexural rigidity EI and length cubed l^3 (equation (2.2)). Greer's results are shown in figure 2.26; it can be seen that specimens under pure shear ($\theta = 90^\circ$) do not exert as much side load on the actuator as mixed-mode angled specimens.

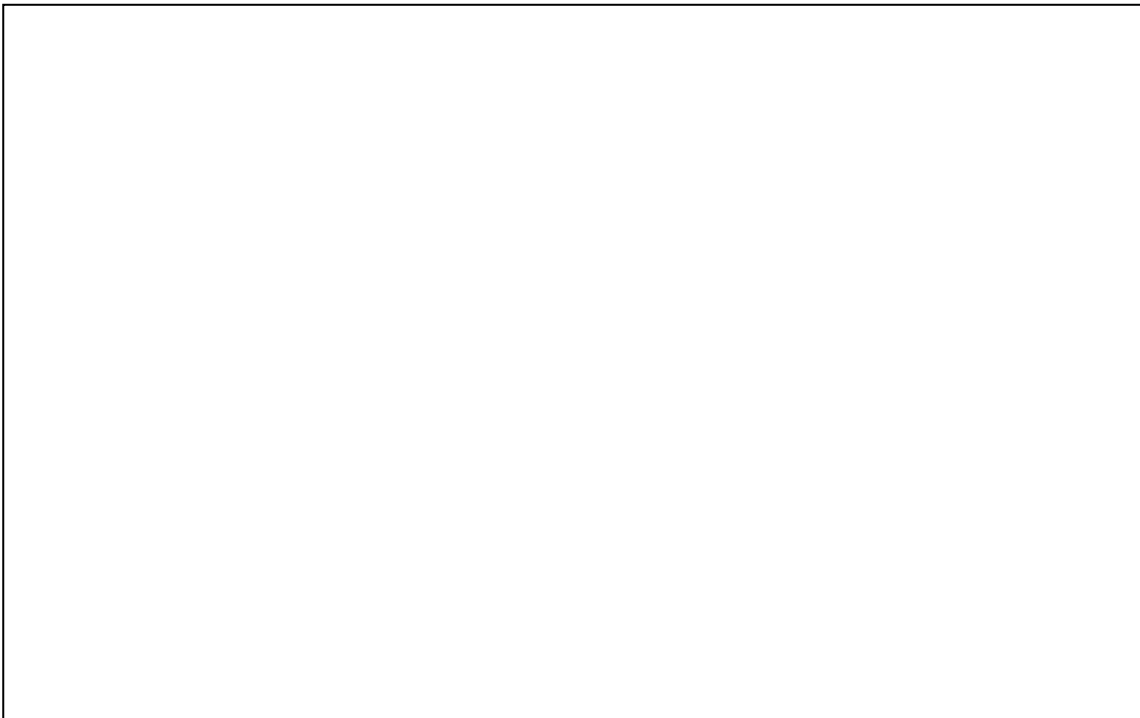


Figure 2.25 – Banks-Sills and Arcan free-body diagram. R is the reactionary sideways actuator/load cell load and M is the moment on the actuator/load cell. Taken from Greer *et al.* [74]

$$S = \frac{\left(\frac{El}{l^3}\right)_{AB}}{\left(\frac{El}{l^3}\right)_{CD}} \quad (2.2)$$

⁸ Loading angle is designated θ in Greer and figure 2.25. In the rest of this thesis specimen angle will be designated ϕ

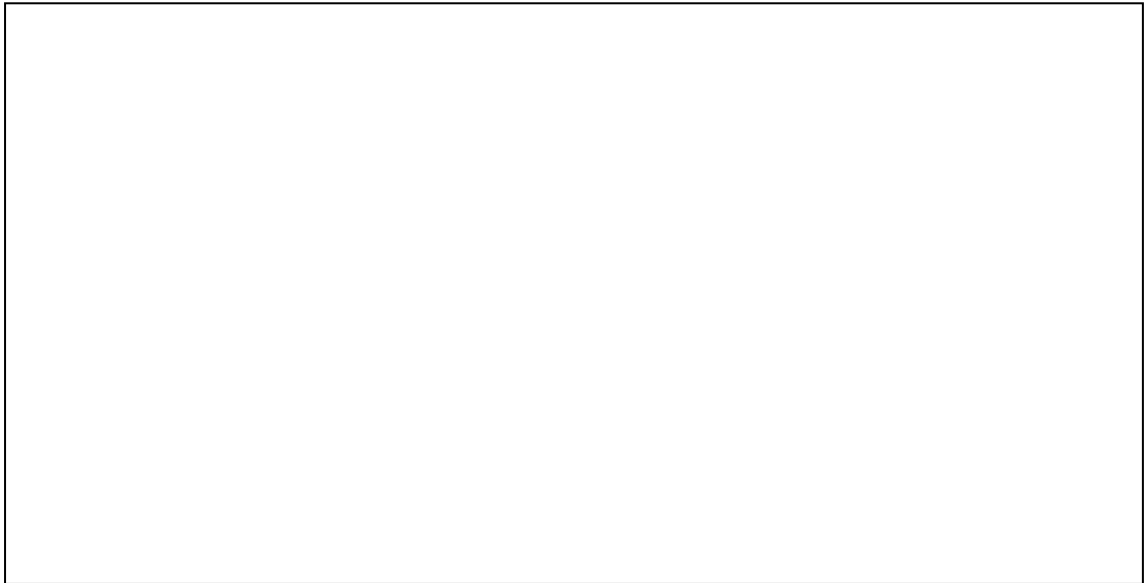


Figure 2.26 – Side loading of actuator in a typical Arcan-type specimen, from Greer *et al.* [74]

Grip and specimen rotation can be reduced by clamping grips rigidly at both ends rather than allowing them to rotate about a clevis pin fixture. Reducing the flexural rigidity of the loading beam *AB* relative to the specimen to relieve side load *R* will result in increased beam compliance, allowing a relaxation in specimen angle and deviation from pure shear loading.

The actuator side load is a necessary condition to keep the specimen as close to pure shear as possible for pure mode II tests.

Thus, a compromise must be made. The first option is to use high-capacity ‘pancake’ type load cell and a substantial test-frame, suited to maximum tensile load magnitudes higher than those expected (100 kN capacity *c.f.* 0.5 kN expected failure loads). This will result in considerably lower load-sensitivity but higher applied K_{II}/K_I .

The author’s experience in using fixed, fully-constrained compact tension grips found that grip and specimen alignment became a major challenge. It was considered that the three-hole design of the typical Arcan-type specimen would result in overconstraint with a rigid grip system. Overconstraint in compact tension specimens was found to result in markedly different *T*-stress values and cause difficulties in starting experiments from a free (or known) strain state, required for DIC analysis. In

the case of a three-hole, brittle mixed-mode specimen, it is believed that a state of over-constraint will result in considerable and unavoidable initial strain states. These would be difficult to measure which, compounded by the low load sensitivity of the equipment to be employed, will result in inaccurate data. To mitigate the effect of overconstraint, it is believed that specifying slightly undersized pins is an adequate solution.

If a lower-capacity load cell system is used with self-aligning, freely rotating clevis-pin attachments, the extra allowable rotation does not eliminate actuator side load, however there will be no over-constraint of the specimens. Pure mode II specimens will be subjected to lower theoretical K_{II}/K_I values, however these values are expected to be still significantly higher than many so-called 'mode II' tests.

It was decided that the convenience of a smaller test frame with more relaxed constraints were employed at the cost of reducing the applied K_{II}/K_I values. The use of DIC and fracture parameter extraction reduces the requirement of cracks to be subjected to exact levels of mode mixity since they can be directly measured.

2.7 Micromechanics of interlaminar shear cracks

2.7.1 G_{IIc} in composites

G_{IIc} is defined as the energy release rate, in J/m^2 , at the point of shear fracture in a material. Typically, shear fracture in composites involves a pre-existing crack between the plies being subjected to shear loading. Since composites are regularly produced in panel form, a state of shear loading is easily encountered when the part is subjected to bending, as shown by the loading arrangement of the ENF mode II fracture test (section 2.6.4.1).

Traditional mechanics assumes that since cracks are subjected to shear, and cracks grow between the plies, in the direction of shear, that shear failure occurs. In reality, it is widely agreed in academic circles that the concept of 'interlaminar shear fracture' is not realistic; at a material mechanistic level, failure can be seen to be tensile in nature [77]. Bonds are not seen to break by sliding mechanisms, but

instead shear hackles are seen on fracture surfaces (figure 2.27), the 45° shape of which denotes failure in the tensile direction. Thus, G_{IIc} as a measured material property in composites is a misnomer. Interlaminar shear tests such as ASTM D-5379 and ISO 14130:1997 include disclaimers specifically stating that they are not suitable for determining material properties for design parameters but are useful for qualitative material screening or quality control. This is because the materials tests do not measure true material properties, primarily as a consequence of the mechanistic differences between idealised pure mode II behaviour and real micromechanical behaviour. In bulk materials the T -stress has been identified as strongly affecting measured values of 'apparent' K_{IIc} [54, 55]. In the highly constrained interlaminar shear layer, the effect of T -stress and constraint on measured toughness values is clearly considerable.

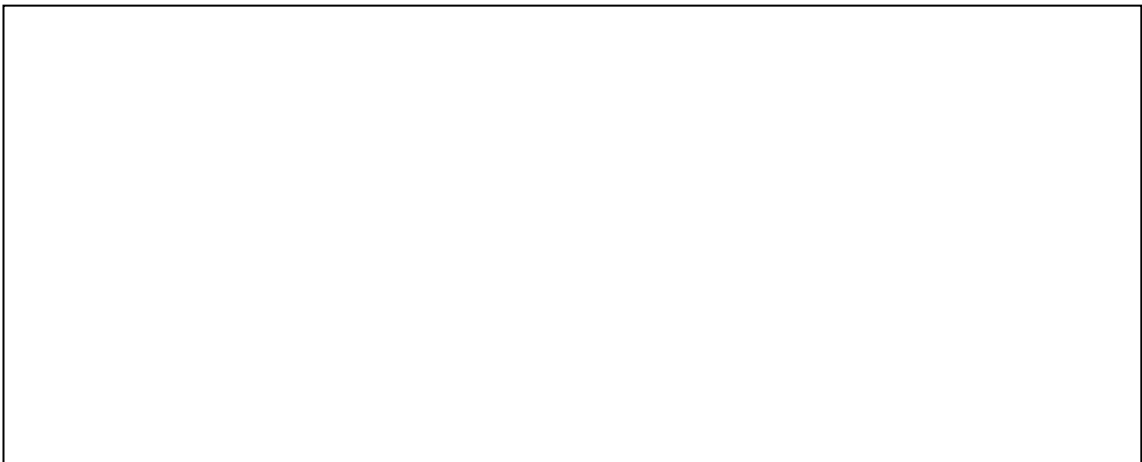


Figure 2.27 - Hackle formation in composites subject to shear load, from O'Brien et al. [77]

It is well-known that the mode II fracture toughness, K_{IIc} is generally higher than the mode I toughness, K_{Ic} in bulk (non-composite) materials [9]. This causes experimental difficulties when attempting to determine K_{IIc} in bulk material since crack kinking under pure or predominantly mode II loading is common. This deviation from a pure mode II failure path is usually ignored. However, it signifies that the energy release rate at the kink angle exceeds the strength-related material toughness G_c ; this is not the same as K_{II} exceeding K_{IIc} and failing at 0° kink angle as desired for the measurement of true critical material properties.

To measure true K_{IIc} or G_{IIc} , the failure mode of the specimen must be mode II which leads back to the requirement to constrain crack path by some method such as the addition of deep grooves. A study by Carpinteri et al. into the effect of aggregate size on G_{IIc} found no evidence for the existence of a mode II toughness parameter affecting the (kinked) fracture of their specimens [78]. A similar critique of G_{IIc} tests for composites was made by O'Brien [77] showing that the sliding shear mechanisms assumed by the fracture mechanics definitions of mode II failure do not occur. Instead tensile failures in the matrix occur under critical shear loading. This study also showed how the methods of testing mode II toughness in composites strongly affect the results; measured toughness is strongly related to the precrack conditions. Piggot *et al.* have published numerous studies examining (and criticising) the use of so-called shear fracture tests which consistently create tensile-dominated failure [79-81].

Despite such vocal criticism of mode II testing, the resistances of both laminar composite and bulk polymer to fracture under shear loading are physical characteristics of great significance to the composite material behaviour. Measured shear toughness values have been shown to be directly related to a number of important and quantifiable composite system parameters such as compressive strength after impact and delamination resistance. Ultimately, pre-cracked composite specimens loaded under shear fail in that direction and have a quantifiable resistance to this crack growth. It is important to understand and acknowledge the real physical meanings of measured ' G_{IIc} ' values and tests in order to understand and improve material behaviour.

In this study, the labels G_{IIc} and K_{IIc} will continue to be used to refer to the critical resistance to failure of natural cracks under shear loading. They will be regarded as material properties for comparative purposes, for a given test method rather than strictly critical, material properties relating to 'sliding' in-plane shear failure.

2.8 Conclusions

From a close study of the literature, a number of key points were identified. Firstly, it was decided that using specimen types with inherently sharp, natural cracks was necessary to ensure representative results.

No studies were found in the literature that attempt to characterise shear or mixed-mode composite fracture by observing or measuring parameters in the matrix material alone. This is surprising since tensile and mode I fracture properties are regularly measured in both academic and industrial environments in this way.

Thermoplastic particulate interlaminar toughening has been shown to be extremely effective in improving composite toughness, especially under shear loading. The effect is well researched but despite composites with particulate toughened interlaminar regions currently flying in commercial aircraft primary structures, the base mechanisms of why the toughening occurs are poorly understood.

The T -stress has become acknowledged as a useful second parameter to describe the stress state at crack tips. In many situations cracks cannot be described accurately by the singular (K) term alone without considering the non-singular (T -stress) term.

Interlaminar cracks loaded in shear show kinking crack paths that head toward the weaker interface between matrix and fibres as intralaminar cracking in composites. The crack kinking and high mode II component suggests that the T -stress could be a very interesting parameter to investigate.

The next chapter will explore methods of measuring fracture behaviour using an experimental mechanics approach.

Chapter 3.

Experimental mechanics techniques

3.1 Introduction

In this chapter, experimental techniques will be introduced in section 3.2, followed in section 3.3 by a more focused analysis of Digital Image Correlation (DIC) which, as will be explained shortly, was an obvious choice for this study. The DIC technique will be critically assessed and challenges discussed.

Section 3.4 of this chapter will examine the use of various experimental mechanics techniques to investigate fracture mechanics problems, with an emphasis on quantitative characterisation and parameter extraction.

The chapter will conclude with a plan of action for an experimental programme using experimental mechanics to investigate mixed-mode fracture in the toughened epoxies under study.

3.2 An introduction to full-field measurement techniques

3.2.1 Photoelasticity

The photoelastic effect is the change of the refractive index of a material, due to stress. This occurs in many amorphous, transparent materials.

The difference between the two refractive indices causes a phase retardation between the two components. The stress-optic law (equation (3.1)) gives the magnitude of the retardation for isotropic materials under plane stress, thus:

$$\Delta = \frac{2\pi t}{\lambda} C(\sigma_1 - \sigma_2) \quad (3.1)$$

where Δ is the relative retardation, λ is the wavelength of light, C is the stress-optic coefficient of the material and $(\sigma_1 - \sigma_2)$ is the difference in principal stresses.

Viewing a loaded body between polarising lenses shows interference fringes, caused by the stress state of the body. Isochromatic fringes show lines of constant principal stress difference, whilst isoclinic fringes show lines of principal stress direction. The fringe number N can be found by equation (3.2), thus the difference in principal stresses can be measured from the isochromatic fringes, and the direction of principal stresses can be identified from the isoclinic fringes.

$$N = \frac{\Delta}{2\pi} \quad (3.2)$$

The technique can be automated and used in three dimensions. More detailed explanations of photoelastic techniques can be found in the works by Dally & Riley [82] and Cloud [83].

Photoelasticity may at first seem like the ideal method of measuring crack tip stress fields in epoxies, allowing mixed-mode data to be extracted (there are numerous examples of this in the literature, however key studies with other relevance to this project are by Nurse and Patterson [84] and Zakeri *et al.* [85]). However, the toughened epoxies being studied are either completely opaque or dark brown and translucent. The translucent materials exhibit fluorescence caused by the significant percentage (~30%) of second-phase thermoplastic in the formulation, which complicates photoelastic measurements. Consequently, photoelasticity cannot be used for this study.

3.2.2 Electronic speckle pattern interferometry (ESPI)

ESPI measures displacement fields from interference of laser speckle patterns. Displacement fringe patterns are produced which then have to be converted into numerical field data. High cost, complex optical arrangement and stability requirements have limited the use of this technique which, whilst highly accurate, is tremendously less flexible than DIC.

3.2.3 Thermoelastic stress analysis

Thermoelastic stress analysis (TSA) is a full-field stress measuring tool that determines stress in specimens by the principle of thermoelasticity. As a load is applied to a material, a temperature change proportional to the change in the sum of the principal stresses occurs.

These temperature changes are very small (typically of the order of 0.001°C) [86].

$$\Delta T = -\frac{\alpha TV}{M c_E} \Delta(\sigma_1 + \sigma_2 + \sigma_3) \quad (3.3) \text{ from [86]}$$

where ΔT is change in temperature, α is the thermal expansion coefficient, M is mass, V is volume, c_E is the specific heat for constant deformation and $\Delta(\sigma_1 + \sigma_2 + \sigma_3)$ is the sum of the change in principal stresses. Thus, temperature change is proportional to change in the sum of the principal stresses.

These temperature changes occur only due to changes in principal stress and so this technique is almost exclusively used with cyclic loading rather than quasi-static loading conditions. TSA and DIC are currently by far the two most frequently used full-field stress/strain measurement techniques in the literature, in both materials/structure based literature and stress analysis and techniques-related literature. TSA is often seen as a complimentary technique to DIC, giving different information [87]. The requirement of cyclic loading gives rise to the technique often being used for cases of fatigue loading.

3.3 An introduction to digital image correlation

Digital image correlation (DIC) is a relatively recent experimental technique, developed in the 1990s at the University of South Carolina by a team led by Professor Mike Sutton [88]. DIC is used to calculate a displacement field by processing a series of digital images of a strained body.

In a 2D-DIC system, successive greyscale digital images of a specimen under loading are recorded using a digital camera system, usually alongside analogue data such as the signal from a load cell. Cross-correlation (or auto-correlation) algorithms are

performed on the images, relative to an initial state, thereby calculating full-field displacement fields across the specimen. Since successive digital images are inherently dimensionless, DIC can be performed over a variety of spatial and temporal dimensions, limited only by the limitations of image acquisition; DIC can be performed on nanoscale up to geological length scales and at ultra-high-speeds of hundreds of thousands of frames per second to a frame-per-year and beyond. However, complexity of image acquisition at the extreme ends of these spatial and temporal scales is not to be underestimated! High speed and high-magnification both typically involve low resolutions, difficulties in speckling, lighting, and triggering, and also severe reductions in accuracy.

In 2D-DIC, measurements are restricted to two dimensions (x and y). The introduction of more cameras and stereoscopic imaging techniques allows measurement of shape and displacement measurements in the out-of-plane (z) axis also. A typical laboratory experimental 2D-DIC arrangement is shown in figure 3.1.

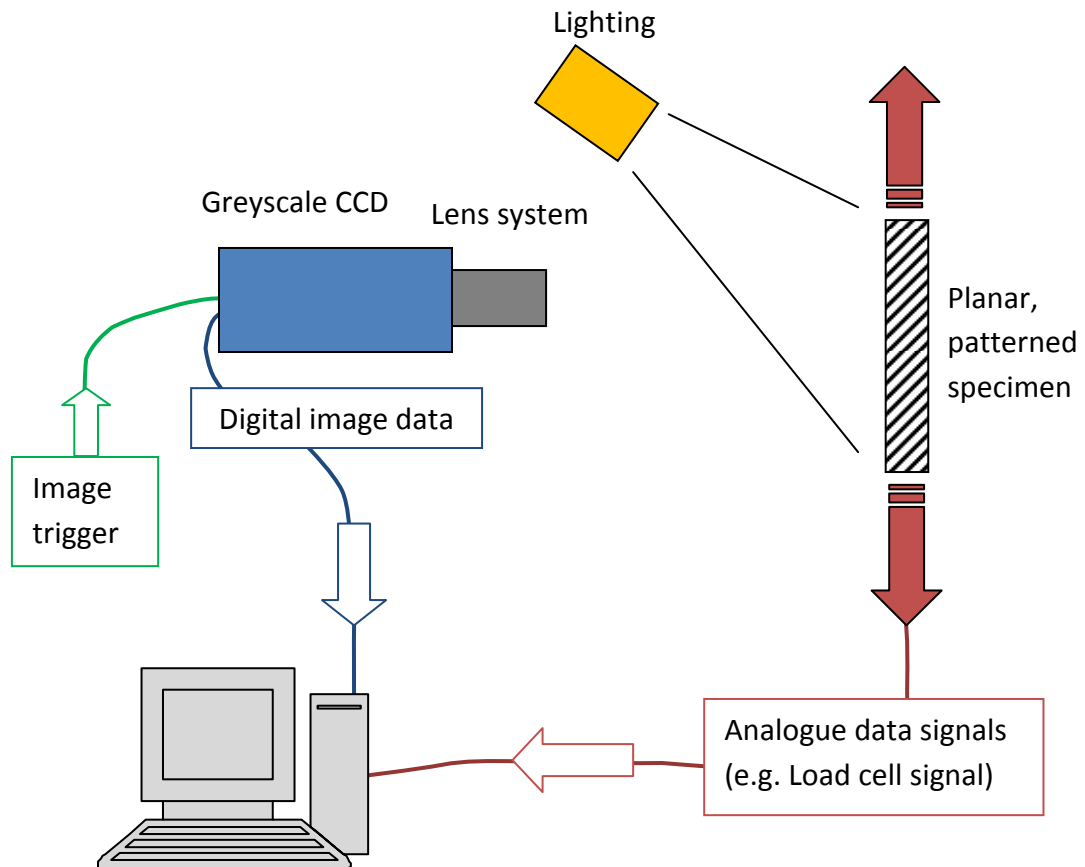


Figure 3.1 – Typical 2D-DIC schematic diagram

To identify displacement changes between successive images, the surfaces must have stochastic (random) high-contrast greyscale patterns, as in figure 3.2. These random patterns can either be natural, such as the microstructure of an alloy (figure 3.2a), titanium alloy microstructure, taken from Tschopp [89]), or the pattern must be put onto the surface of the specimen, typically applied either by light scratching (figure 3.2b), taken from López-Crespo [90]) or by applying a randomly speckled pattern with paint or particles (figure 3.2c).

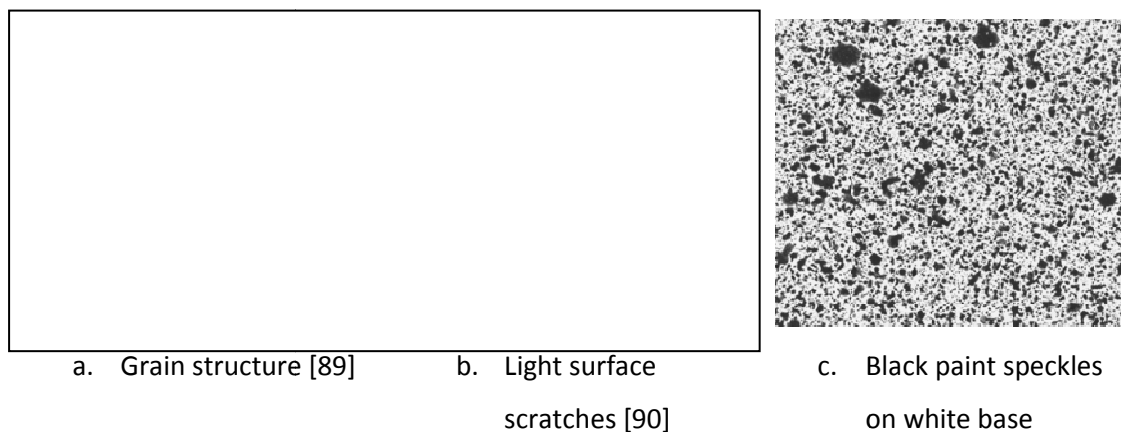


Figure 3.2 – Stochastic patterns formed by (a) grain structure (taken from [89]), (b) light surface scratches (taken from [90]), and (c) black paint speckles on a white paint base.

The series of digital greyscale images are processed by splitting the images into small square subsets (shown by the green squares in figure 3.3) and determining the displacement of the subset within the whole field of view. Whilst the term ‘tracking’ is commonly used, DIC algorithms do not track particles or patterns. Instead they use correlation functions to determine the translation of an entire greyscale subset.

A simple example of a correlation function is to sum the squared difference of the pixel intensity values across the subset for a range of possible displacements u and v in the x and y directions respectively. At the correct translated position, a peak occurs in the correlation function, giving the required displacement vector, as shown in figure 3.3.

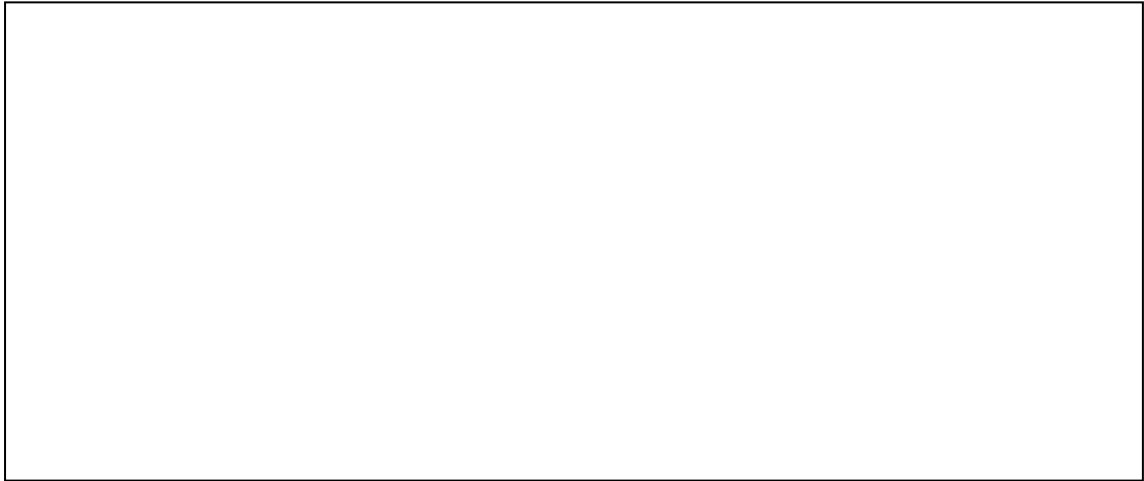


Figure 3.3 - Illustrating the cross-correlation function. Taken from LaVision Strainmaster brochure [91]

Commercial DIC algorithms are more complex in order to improve speed, accuracy, error handling and deal with large deformations. Algorithms typically include steps to smooth displacement field data, steps to guess the likely position of the next vector based on previous calculations and iterative refinement of the correlation in an effort to produce clean, smooth strain fields with minimal computational time. A comprehensive explanation of the mathematics and other practical issues of DIC can be found in the excellent book by Sutton *et al.* [92]. It is worth mentioning at this point that there are significant differences between the different ways some commercially available algorithms perform the cross-correlation. Direct, discrete cross-correlation is computationally enormous. There are two major directions to reduce computational times to reasonable levels; perform discrete cross-correlation algorithms with Fast-Fourier-Transform (FFT), or perform continuous cross-correlation algorithms by fitting bi-linear or cubic spline functions to the previously discrete pixel greyscale data and correlate these. Whilst most systems use the latter method, LaVision DaVis Strainmaster 7.1, used in this work, uses the former method. The major consequence of this difference is that LaVision subset sizes are typically much larger than with other commercial systems (64x64 subset sizes are common in Strainmaster, whilst 10-30 pixels square is more common in other packages). A consequence of the FFT function is that FFT requires square windows of length 2^n pixels, whereas no such restrictions apply for spline-based, continuous function cross-correlation.

From the illustration in figure 3.4 it is clear that the quality of the random pattern is extremely important in allowing displacements to be calculated. Simplistically, if the pattern is too fine for the image resolution, then pattern recognition will be impossible. If the pattern is too coarse, then accuracy will be reduced. Also, if the pattern is too regular, then unique correlation solutions cannot be found. The pattern must be isotropic, aperiodic and non-repetitive, and a high contrast. Speckle patterns produced by black paint spatter on a white background fulfil this requirement and their ease, low-cost and flexibility have resulted in paint speckles being the most commonly used speckle pattern.



Figure 3.4 – Illustration of the DIC technique showing successive images of a strained body. Reproduced from Correlated Solutions website [93]

An important requirement for obtaining good images is appropriate lighting and optical arrangement. Making full use of the intensity range of the camera system employed, with a wide range of greyscale values from the darkest levels all the way to white is necessary for good correlation and high quality results. Lighting is an important factor in obtaining good results [92, 94, 95]; light must be consistent, flat and bright enough that the greyscale images make wide use of the camera intensity range. Specular reflections from shiny surfaces are important to avoid since they severely hamper correlation. Diffuse lighting can be used to minimise specular reflection. Lighting and greyscale information are discussed further in section 3.3.1.

DIC can be used to measure a huge range in local strains, algorithms capable of measuring strains from $50 \mu\epsilon$ (0.005 %) up to 2000 % and beyond [91, 96]. Measured strain resolution is limited by image quality, which in turn is dependent upon optical

quality and arrangement, lighting, and speckle pattern suitability. Strain fields on three-dimensional surfaces can be measured by using multiple cameras, allowing out-of-plane displacements also to be measured, as shown in the stereoscopic camera arrangement in figure 3.5.



Figure 3.5 – Stereoscopic 3D digital image correlation (courtesy of Panos Eftymiadis)

True three-dimensional digital volume correlation (triaxial) strain-field measurements have been measured using x-ray tomography and correlation algorithms [92, 97, 98], however the quantity of data produced for such applications is tremendous (100 volumetric images consisting of $1024 \times 1024 \times 1024$ 8-bit voxels⁹ will have the size 100 GB) and the requirement of a through-thickness pattern requires significantly more thought than simply spray-painting a surface. Since the materials of interest in the current research will be in sheet-form, are solid and non-metallic (unlike the metal foams studied by Roux [97, 98] using this technique), and the fracture properties of interest can be studied with plane-strain specimens, this voxel-based technique will be ignored and wherever 3D-DIC is mentioned subsequently in chapters 4-7, it refers to stereoscopic surface DIC.

The accuracy of the DIC technique is strongly dependent upon the specific experimental arrangement, including choice of optics, quality of alignment, quality of

⁹ a voxel is the volumetric equivalent of a pixel

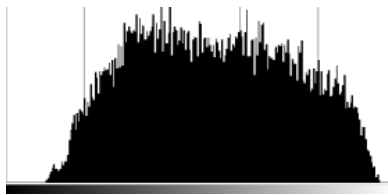
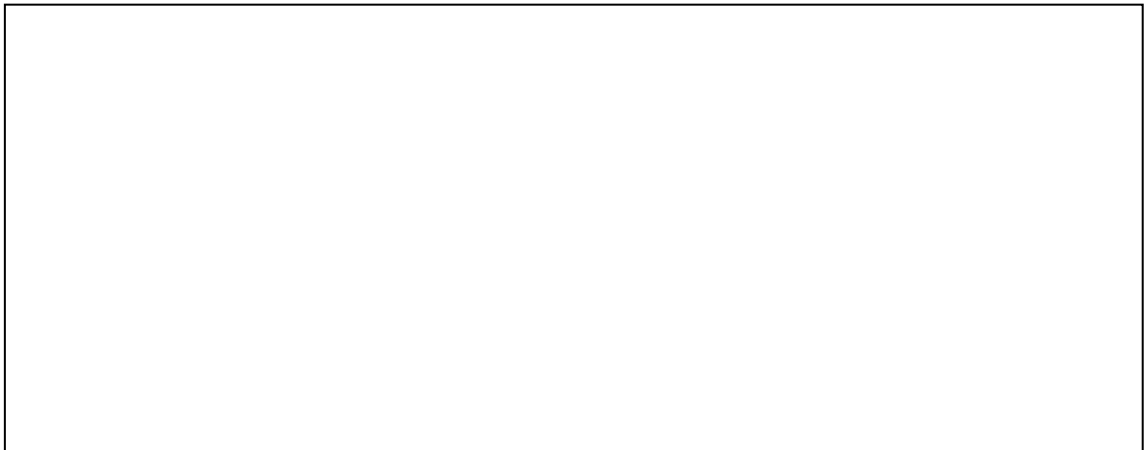
speckle pattern, and choice of algorithm parameters. A simple and effective way of assessing the quality of an experimental arrangement is to translate an unstrained, speckled specimen and performing the correlation algorithms on the images. Strain fields should clearly be zero, and the \pm strain levels present in the translated specimen are a good indication of the accuracy limit of the complete arrangement.

Whilst the DIC technique is mature, DIC measurements can be validated by a number of methods if desired, including by strain gauge or by alternative experimental mechanics techniques such as TSA, the grid method [99], ESPI or photoelasticity.

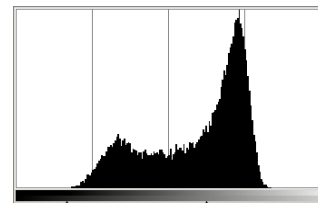
3.3.1 Speckle pattern analysis

Work by Sutton *et al.* [92], the creators of the Correlated Solutions DIC packages Vic2D and Vic3D, found 'ideal' speckle patterns to consist of a high-contrast, stochastic greyscale pattern of feature-size 3.25 pixels with overall speckle size of 10.5 pixels. Despite utilising different algorithms derived from particle image velocimetry (PIV) software, LaVision StrainMaster documentation [100] identifies the same 3 pixel ideal feature size.

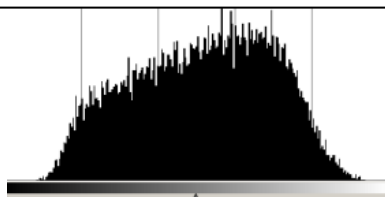
There is some debate in the literature whether a Gaussian, flat or bi-modal image intensity distribution offers best correlation. In the experience of the author and colleagues, provided the pattern is of appropriate resolution and contrast, the image intensity distribution makes an insignificant difference. Furthermore, attempting to control the intensity distribution with a simple black-on-white spray-can or airbrush paint speckle is unrealistic. Figure 3.6 shows four example speckle patterns, all completely appropriate, alongside their intensity distribution. Each of these four examples were taken from a Correlated Solutions speckle-pattern guide [95] as examples of appropriate speckle patterns.



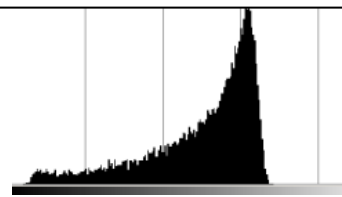
a. Fairly flat distribution



b. Bimodal distribution



c. Roughly Gaussian distribution



d. Distribution showing a strong peak

Figure 3.6 - Example speckle patterns and their intensity distributions (speckle patterns from Correlated Solutions [95])

Good lighting and paint speckles of a sufficient size with focused optics were generally found to give fairly flat intensity distributions. ‘Sufficient size’ was found to be higher than the oft-quoted “3 pixels”; speckles of size 5-8 pixels were found to be at the lower-limit of robust correlation with the system used. Also, interrogation windows with the manufacturer-recommended “minimum of 3 speckles” were found

to be grossly inadequate, with subsets requiring many more speckles to successfully correlate.

Patterns with too little black paint typically showed strong peaks at the upper end of the spectrum. Speckles that were too large resulted in a more bi-modal distribution, as is intuitive since a larger proportion of pixels will be either black or white relative to the pixels resolved on the boundary of the paint speckles. Strong Gaussian distributions were only experienced with poorly focused optics. Patterns with highly reflective parts resulted in 'hot-spots' in which a distinctive peak occurs at the top of the spectrum, such as in figure 3.7. Hot spots such as this are well known to damage correlation [92, 100] and were avoided. Common causes of hot-spots are damage to the speckle pattern or the effect of dust particles sticking to the wet paint surface, highlighting the importance of protecting the speckle pattern between painting and testing.

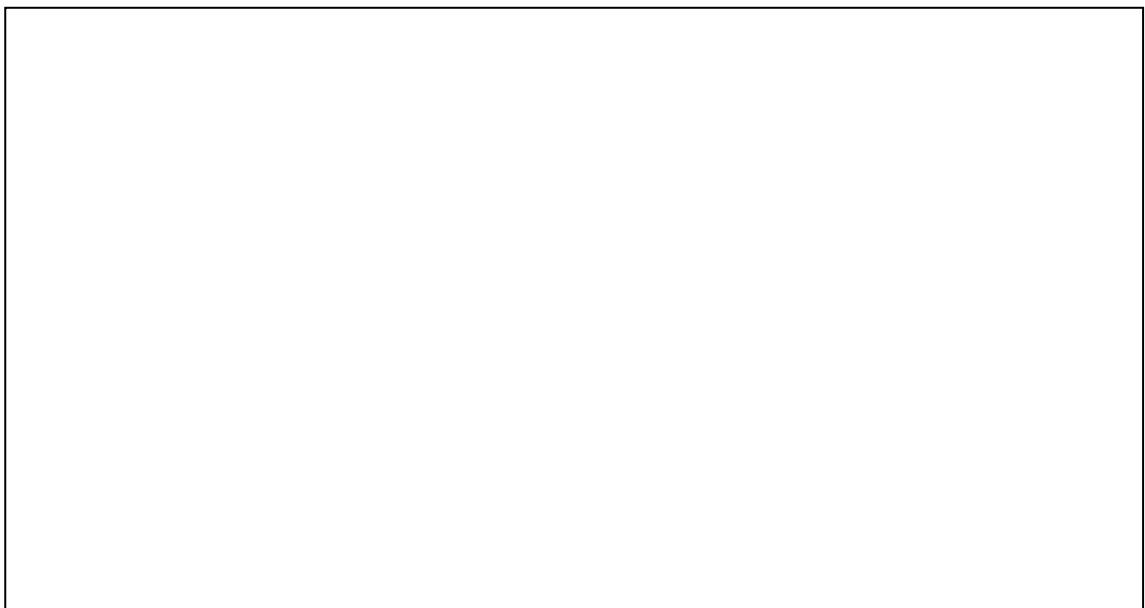


Figure 3.7 - Poorly speckled/imaged specimen with reflective white paint and associated intensity distribution (from LaVision Strainmaster manual [94])

In this project, intensity distribution measurements have been used to check for saturation of the CCD sensor from specular reflection; it was found that the shape of the intensity distribution alone was a poor indicator of speckle pattern quality.

Paint has long been regarded as the most reliable method of preventing unwanted surface reflections (causing bright saturated spots on digital images, damaging

correlation) and producing consistent, scalable (some skill needed), and to some extent, quantifiable patterns [92].

At such a small scale, an important consideration for both paint-speckle and surface scratch patterns was found to be reflection from three-dimensional effects such as hemispherical paint blobs or scratch leading edges. As specimens translate, deform, or rotate, these out-of-plane features were found to reflect light differently; this prevents the recorded speckle image being fixed to the surface, especially if illumination is not axial. It is for this reason that black speckles on a white background have been preferred over white on black in this project; a study by Crammond *et al.* [101] similarly found black speckles on white background to produce lower errors than white-on-black. Care still has to be taken since blobs of supposedly matt black paint can still cause some specular reflection.

Approaches to measure speckle pattern quality have been proposed [101-103]. Experience has shown that provided a specimen has a random pattern that can be seen to shift a small amount each recorded step then appropriate choice of algorithm and integration window size (and overlap) will result in correlation and an accurate displacement field. However, structured and quantitative assessment of speckle patterns such as in the recent studies by Crammond *et al.* [101] and Pan [104] would have been useful at the beginning of this work. The study by Crammond *et al.* is one of few to also address the problem by linking easily measurable physical characteristics (such as speckle size, density and number-per-subset) with resulting errors in DIC. The approaches in the other listed works are typically less practical, as they involve performing image-processing algorithms and attempting to find minima/maxima for a number of criteria; making the improvement of a speckle pattern a far more abstract proposition. It is noted that the experience of the author, colleagues and other DIC users is similarly frustrating in that the mathematically 'optimum' speckle and subset sizes are not correct in practice. There is a trade-off between strain resolution and strain accuracy and it is ultimately down to the user to select appropriate algorithms for a task. The speckle patterns and subset-sizes used in this project have been applied qualitatively, using the software package suggestions as a starter.

3.4 Mixed mode fracture testing: Parameter extraction and DIC studies

Experimental mechanics techniques allow the researcher to quantify fracture behaviour and characterise materials by measuring fracture parameters. Single parameters do not accurately describe the nature of crack tip stress fields or of fracture behaviour in many cases, especially where plasticity is significant [52]. Experimental mechanics techniques now allow multiple parameters such as K (stress intensity factor), T (T -stress), CTOA (crack tip opening angle), CTOD (crack tip opening displacement) and J (the energy contour integral), to be measured with reasonable accuracy (these parameters are all explained further in Anderson [9]). Whilst the materials being studied in this project are relatively brittle and well-described by elastic stress solutions [9], the ability to extract multiple parameters and measure crack tip stress fields is desirable over load and analytical equation based methods. The brittle, low-plasticity nature of the materials tested, and the interest in behaviour of cracks in epoxy under mode II loading naturally leads stress intensity factors K_I and K_{II} and the T -stress to be parameters of primary interest.

Digital image correlation provides a convenient tool for determining displacement fields around crack tips. From the displacement fields, fracture parameters can then be extracted. Much work has been carried out on the extraction of mixed-mode stress intensity factors from DIC displacement data [105-108]. This extraction typically involves fitting displacement field data into either the Williams' stress field solution [105], reproduced in equations (3.4-3.5), or through the Muskhelishvili approach [84, 109]. A number of alternative approaches have been used, including the use of the Westergaard crack tip stress field solutions for predominantly mode I loaded cracks only [49, 110], but these have been found less accurate and more limited than the two aforementioned approaches.

Extraction using the Williams approach involves fitting stress, strain or displacement fields to an appropriate form of the Williams stress solutions; an infinite series reproduced in equations (3.4-3.5), typically by either least-squares or Newton-Raphson iterative methods.

Mode I:

$$\begin{aligned}
\sigma_{xx} &= \sum_{n=1}^{\infty} \frac{n}{2} r^{\frac{n}{2}-1} a_n \left\{ \left[2 + \frac{n}{2} + (-1)^n \right] \cos \left[\left(\frac{n}{2} - 1 \right) \theta \right] - \left(\frac{n}{2} - 1 \right) \cos \left[\left(\frac{n}{2} - 3 \right) \theta \right] \right\} \\
\sigma_{yy} &= \sum_{n=1}^{\infty} \frac{n}{2} r^{\frac{n}{2}-1} a_n \left\{ \left[2 - \frac{n}{2} - (-1)^n \right] \cos \left[\left(\frac{n}{2} - 1 \right) \theta \right] + \left(\frac{n}{2} - 1 \right) \cos \left[\left(\frac{n}{2} - 3 \right) \theta \right] \right\} \\
\tau_{xy} &= \sum_{n=1}^{\infty} \frac{n}{2} r^{\frac{n}{2}-1} a_n \left\{ \left(\frac{n}{2} - 1 \right) \sin \left[\left(\frac{n}{2} - 3 \right) \theta \right] - \left[\frac{n}{2} + (-1)^n \right] \sin \left[\left(\frac{n}{2} - 1 \right) \theta \right] \right\}
\end{aligned} \quad (3.4)$$

Mode II:

$$\begin{aligned}
\sigma_{xx} &= - \sum_{n=1}^{\infty} \frac{n}{2} r^{\frac{n}{2}-1} b_n \left\{ \left[2 + \frac{n}{2} - (-1)^n \right] \sin \left[\left(\frac{n}{2} - 1 \right) \theta \right] - \left(\frac{n}{2} - 1 \right) \sin \left[\left(\frac{n}{2} - 3 \right) \theta \right] \right\} \\
\sigma_{yy} &= - \sum_{n=1}^{\infty} \frac{n}{2} r^{\frac{n}{2}-1} b_n \left\{ \left[2 - \frac{n}{2} + (-1)^n \right] \sin \left[\left(\frac{n}{2} - 1 \right) \theta \right] + \left(\frac{n}{2} - 1 \right) \sin \left[\left(\frac{n}{2} - 3 \right) \theta \right] \right\} \\
\tau_{xy} &= \sum_{n=1}^{\infty} \frac{n}{2} r^{\frac{n}{2}-1} b_n \left\{ \left(\frac{n}{2} - 1 \right) \cos \left[\left(\frac{n}{2} - 3 \right) \theta \right] - \left[\frac{n}{2} + (-1)^n \right] \cos \left[\left(\frac{n}{2} - 1 \right) \theta \right] \right\}
\end{aligned} \quad (3.5)$$

The Muskhelishvili approach (originally detailed in [111]) involves expressing the stress field around a crack tip in the form of two complex analytical functions. The expression is formed as a complex Fourier series and boundary conditions applied, thereby defining the crack. These expressions are then solved, determining K_I and K_{II} .

A comprehensive review of these methods, and of the design and testing of the fracture parameter extraction tools used in this project can be found in [112].

As a complimentary technique much more suited to materials studied in fatigue, thermoelastic stress analysis (TSA) has also been employed to determine stress fields and fracture parameters, using both the Williams method and the Muskhelishvili approach [112, 113].

Prior to DIC being widely used, Nurse and Patterson successfully extracted predominantly mode I stress intensity factors from photoelastic fringe patterns around thin notch ‘cracks’ in photoelastic of turbine blade firtree¹⁰ models under

¹⁰ A ‘firtree’ is the multiple dove-tail notched, fir tree shaped turbine blade root which fits into a correspondingly shaped fitting on the turbine rotor disc.

compression [49] using the Westergaard stress equations. Their later study [84] extracted mixed-mode stress intensity factors of cracks under 4PB shear loading using the Muskhelishvili approach.

The Williams approach, taking the non-singular T -stress term into account, was first applied to extract stress intensity factors from photoelastic fringe patterns in the 1970s by Sanford and Dally [114]. They used only two terms of the Taylor series of the Williams solution; consequently they describe their errors as within around $\pm 10\%$ for K_I and $\pm 13\%$ for K_{II} , 68% of the time, i.e. one standard deviation.

A commonly experienced issue of extracting fracture parameters using the Williams stress solution is that more than the first two terms of the series must be used to obtain accurate results. Zanganeh found that using three terms of the Williams stress solution measured K_I and K_{II} values to $\pm 13\%$ accuracy. Convergence occurred with the use of 15 or more terms, at an accuracy of $\pm 7\%$ [112]. Using current computer hardware, computing stress intensity factor solutions with the Williams approach using 20-50 series terms takes 0.5-2 seconds using Zanganeh's algorithms. Whilst obtaining full convergence is necessary for accurate results, it is not computationally invasive.

A benefit of the Williams approach over the Muskhelishvili approach is the ability to extract the T -stress from displacement data. A complication of this was shown by Zanganeh *et al.* [105], namely that the method requires an accurate crack tip location. An ill-defined crack tip, just a few pixels from the real location, whilst accurate enough for good K_I and K_{II} values using either the Williams or Muskhelishvili approach can give noticeably inaccurate T -stress values. A comprehensive assessment of crack tip location sensitivity will be presented in section 5.3.2. Ideally, a robust algorithm to locate the crack tip from displacement data (such as the algorithm presented in the discussed paper) is required. The T -stress is well-established as an important fracture parameter governing crack path stability [115, 116] and an important consideration in mode II tests [117]. The T -stress has been explained in more detail in section 2.5.

López-Crespo *et al.* successfully measured mixed mode (I/II) stress intensity factors (SIF) in fatigue cracked metallic specimens using the Muskhelishvili approach [109]. Specimens were 'speckled' by lightly scratching the surface and crack tip displacement fields determined using DIC. Crack tips were located using the Sobel edge-finding routine and were found to be adequately accurate for K value extraction. More recent work [105] from the same research group advises using more sophisticated crack tip finding algorithms, determining the crack tip from displacement fields to give a crack tip location accuracy sufficient for T -stress extraction.

The study by Du *et al.* [108] used DIC to extract mixed-mode fracture parameters from an aircraft panel specimen. Muskhelishvili's approach was used, following López-Crespo's method [109]. The study showed the applicability of the Muskhelishvili method, combined with the Sobel edge-finding algorithm, to fracture problems with tough materials and large displacements.

Numerous studies in fracture parameter extraction have been carried out by Hild and Roux [98, 106, 118, 119]. The pair have developed their own modular DIC system, CORRELI^{Q4}, the key purpose of which was to create a DIC system to integrate with finite-element analysis in order to reduce noise and allow easier processing of displacement field data. This allows the integration of geometry, displacement field form and any other *a priori* knowledge of the specimen behaviour to be integrated into the algorithms. Among other benefits, this offers efficiency improvements over running displacement field calculation in one package, then applying crack tip locating algorithms and finally running fracture parameter extraction algorithms. This system is not commercially available.

A recent review of DIC applied to fracture problems carried out by Yates *et al.* [120] reviewed methods applied to a number of more complex problems including plasticity and anisotropy. Significantly, they found some differences between finite element T -stress values and T -stress values extracted using the Williams method with Zanganeh's 'DICITAC' software [121]. The differences were attributed to FE limitations with real features such as "*non-planar crack, crack front curvature,*

surface residual stresses... material anisotropy and crack closure"; all affecting T -stress values in real specimens.

3.5 Concluding remarks

Whilst 3D-DIC is the method of choice for many DIC studies, the added complications in the calibration stages especially reduce the appeal of the stereoscopic approach. The added experimental speed, convenience and availability of equipment makes 2D DIC a more desirable system provided out-of-plane related errors are within acceptable levels. These will be carefully measured and assessed. However, it is expected that using the 2D approach is an acceptable trade-off that will allow more experimental data of an acceptable quality to be recorded in an equivalent time-frame.

For future work, a more robust validation of the DIC results could be performed either by using further experimental mechanics techniques in parallel to support the measurements, or through the use of additional traditional measurement devices. Thermoelastic stress analysis, Moiré techniques, the Grid method, and photoelasticity (for the NEAT resin) could all be used to confirm the validity and accuracy of the measured data. Strain gauges and CTOD clip-gauges are good examples of more traditional measurement tools which could also give confidence in the measurement system.

Whilst the T -stress was identified in chapter 2 as a fracture parameter of interest, it has been identified that it is a relatively challenging parameter to measure. The second-order nature of the term makes it significantly more difficult to measure than stress intensity factors. The applicability and sensitivity of the DIC method to measure T -stress in relatively brittle materials such as epoxy is unknown; T -stresses have previously only been measured by DIC in much tougher materials with larger displacements.

In the next chapter, a series of experiments will be described, which will use the DIC fracture parameter extraction technique on standard, well established and well understood specimen types to assess the applicability and limitations of the method.

Chapter 4

Meso-scale mode I fracture studies

4.1 Introduction

The aim of the experiments described in this chapter was to perform standard, well-understood fracture tests on a set of materials of interest. The use of standard mode I specimens allows results from traditional load-based methods to be compared to values determined using an experimental mechanics approach. This will allow a comprehensive quantitative assessment of the accuracy and limitations of the experimental mechanics technique. Fracture parameter extraction, using DIC, has been carried out using experimental mechanics in many studies in metallic materials; some of these have been discussed in section 3.4. Few studies have tested materials to destruction or explored the use of parameter extraction tools to measure critical material properties. Accuracy of stress intensity factors determined using DIC and parameter extraction tools are regularly reported as being within 10%, however, comprehensive error analyses and parametric sensitivity studies were not found in the literature. The materials tested in this study are thought to be ideal candidates for parameter extraction using DIC; epoxy behaves in a much more linear elastic way than the metal alloys the technique is typically tested with. Process zones are comparatively small, and failure is typically sudden.

Compact tension (CT) specimens were made and tested to destruction under pure mode I loading in order to obtain K_I values through the classical, load-based linear elastic fracture mechanics (LEFM) energy method. This method is documented in the British Standard “*Plastics – Determination of fracture toughness (G_{IC} and K_{IC}) – Linear elastic fracture mechanics (LEFM) approach*” (BS ISO 13586 [1]). As previously mentioned in section 2.6.2, CT specimens were selected over single edge-notch beam specimens (SENB) due to the significantly lower levels of crack tip rigid body

motion in testing and hence increased accuracy in digital image correlation (DIC) measurement.

To complement the classical approach, the DIC method was employed to determine the full-field displacement fields using a long-field microscope covering an area 6.0 mm × 4.5 mm around the crack tip. This allowed the same K_I values to be determined through extraction from Williams' crack tip stress field solutions, alongside the T -stress, a further fracture parameter discussed in section 2.5.

This chapter covers the experimental work carried out to obtain the data, as well as subsequent data processing. The results are presented and discussed in chapter 5.

4.1.1 Materials

Initially two epoxy blends were supplied by Cytec Engineered Materials, one high-toughness aerospace grade resin, to be treated as a control, and one experimentally toughened formulation. The experimental formulation was the control resin with a thermoplastic particulate filler. The thermoplastic particles formed approximately 10% by weight of the final material. Toughening particles had a mean diameter of 35 μm .

The details of the toughening particles are industrially sensitive and were not disclosed. Toughened material was supplied, referred to as 'formulation SHEFF-F2'; for this reason the two materials will be referred to henceforth as **NEAT** for the unmodified control resin and **F2** for the SHEFF-F2 thermoplastic toughened resin. 'NEAT' has sometimes been abbreviated to simply '**N**'. Later, a further three particulate toughened formulations were supplied; SHEFF-F3, SHEFF-F4 and SHEFF-F5. These formulations will be referred to as **F3**, **F4** and **F5** respectively. These are again the same unmodified control resin with around ten percent by weight different spherical thermoplastic toughening particles, ranging from 25 μm to 35 μm in diameter. The material F4 was slightly different to the others; the F4 toughening particles were bonded to the matrix with a diffuse interphase.

Material was supplied in cast plaques 150 mm × 100 mm, typically 4.0-5.5 mm thick. Cast plaques have a meniscus and textured base and especially in the case of the

particulate toughened formulations, a resin-rich top layer. A 0.2 mm layer was removed from the top and bottom faces of each plaque to remove the non-homogenous outer layers; this was especially important when observing surface displacement fields. This is detailed in section 4.2.1.

Plaques were autoclave cured to the same cure schedule (i.e. temperatures, pressures, ramp-rates and dwell times) as the composite cure schedules for the resins and so residual stresses related to resin shrinkage during cure should be comparable to those in a fibre composite. This does, however, ignore the considerable effect on resin residual stresses that the difference in coefficients of thermal expansion between epoxy and carbon fibre has.

Some of the supplied plaques were slightly curved, and all had an unrepresentative top surface as a consequence of the vacuum oven degassing process. The NEAT plaques of resin were passed between the polarisers of a polariscope to (qualitatively) assess levels of stresses due to the machining process. Stresses were present, but acceptably low compared with the (also low level) inherent thermally induced residual stresses from the cure process.

4.2 Meso-scale compact tension tests

Compact tension (CT) specimens were created to the specifications of the International Standard BS EN ISO 13586:2000 (*Plastics, Determinations of fracture toughness (K_{Ic} and G_{Ic}), Linear elastic fracture mechanics approach*) [1].

Specimen dimensions are shown in Figure 4.1. Specimens manufactured from formulations F3, F4 and F5 were machined with grooved slots instead of square slots (figure 4.2). Specimen thickness was limited to the thickness limits of casting epoxy; because the curing process is highly exothermic, thickness is limited to around 5.5 mm. As a result a compromise had to be made between using very small, thick specimens and larger, non-standard thinner specimens. It is unusual to use CT specimens as thick as this standard advises; the thickness advised is to ensure plane-strain conditions in virtually every material that may be studied. It is left to the user

to check the validity of the assumptions. This validity check can be found in section 5.2.1.

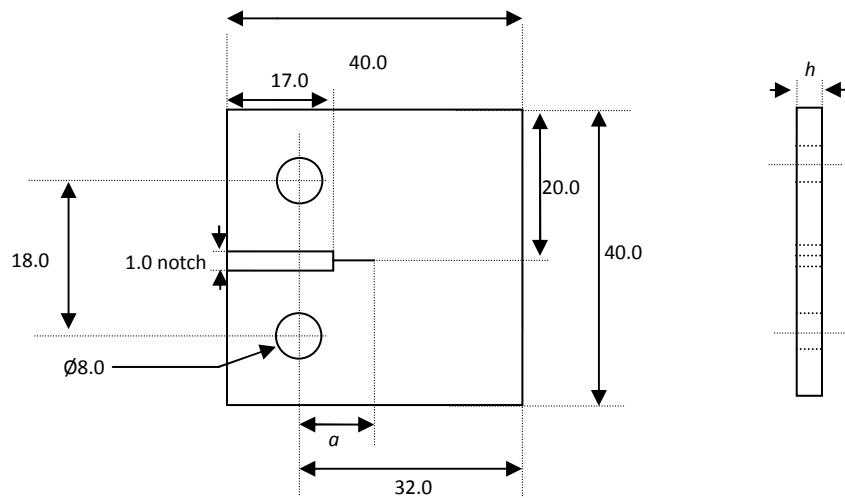
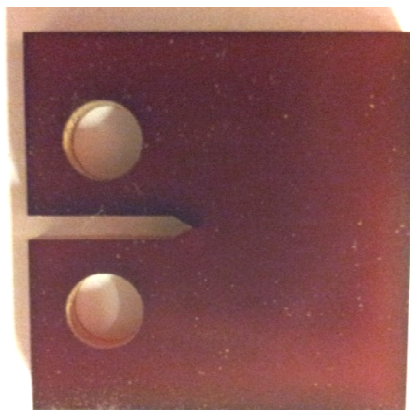


Figure 4.1 – Compact tension specimen dimensions (dimensions in mm)



a. Grooved notch specimen



b. Square slot specimen

Figure 4.2 – Variations in specimen dimensions

Whilst the standards aim to measure the plane strain fracture toughness, the surfaces of the specimen are in a state of plane stress. A sufficiently thick specimen, i.e. where thickness $h \gg \bar{r}$ where \bar{r} is the process zone radius, can be assumed to be in a state of plane strain, whilst the contrary is true for a very thin specimen. The expected plastic zone radius for brittle polymers such as the epoxies studied is below 1 mm. Consequently it was expected that the specimens would fall well within the boundaries for the 'plane strain' assumption required by the standard to be

acceptable. The specimens can later be seen to fulfil the plane-strain conditions required by the assumptions for the K_{Ic} calculations in section 5.2.1.

Whilst the specimen being in a state of (predominately) plane strain is acceptable, this does not change the fact that DIC measurements are taken at the surface, which is in a plane stress condition. However, provided the crack-length through the thickness of the specimen is consistent, the stress intensity factor can be assumed to be consistent through the thickness [1].

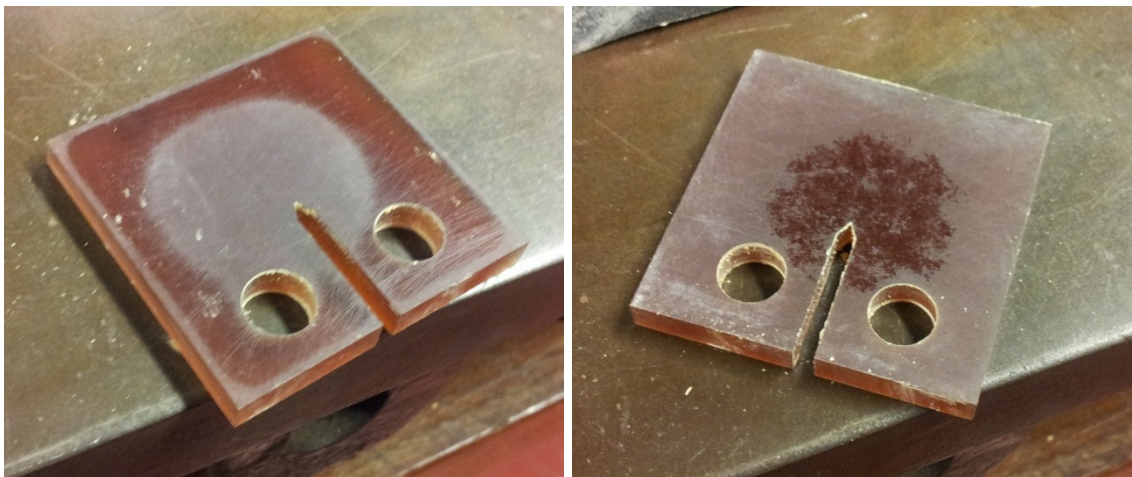
These specimens were designed to be made from square pieces in accordance with the suggestion of BS ISO 13586 [1]. This allowed orientation to be selected after cutting, prior to drilling and notch-cutting, on a specimen-by-specimen basis to avoid any small impurities and to select the orientation with the most consistent ligand thickness. The surface material on the top and bottom faces was then removed in the method described in the next section. Specimens were numbered using a permanent marker in the form MAT-CT-XX where MAT is the material (i.e. NEAT/F2 etc., CT referring to 'compact tension', and XX being specimen number; e.g. F2-CT-08). A number of rough test specimens were made and numbered (including studies using natural texture and scratches as a speckle pattern) and so the results presented here do not all start from '01'.

4.2.1 Specimen thickness preparation

Two methods were used to achieve remove the top and bottom faces to remove the unrepresentative top and bottom surfaces caused by the casting and degassing process. Firstly, the top faces were milled before specimens were machined. Slight plaque curvature (caused by residual stresses during the cure process) meant that the resulting specimens were too thin, significantly wedge-shaped, and due to clamping constraints, the plaques could not be milled to the edges. Residual stresses were not relieved in this process, simply material was removed until the specimens were flat.

A simpler method was found to be to machine specimens first and then remove the top and bottom surfaces using progressively finer wet abrasive paper on a flat steel work-surface. Polishing down to a P240 finish left a good, flat surface finish relatively

quickly, without removing too much material. It was observed that the dust from the removed material distinctively changed colour from orange to white once the resin-rich depth had been completely removed. The use of wet abrasive paper prevented airborne epoxy and thermoplastic dust. Plaque curvature can be seen in the specimen in figure 4.3a-b which has been sanded on either side removing some, but not all, of the unrepresentative surface, clearly showing a convex (a.) and concave (b.) shape.



a. Front (convex)

b. Reverse (concave)

Figure 4.3 - A compact tension specimen part way through the face preparation. The darker colour is the un-sanded shiny resin surface whilst the white is the polished area.

4.2.2 Introducing a starter crack

Sharp cracks were initiated in the specimens by tapping a fresh single-edged razor-blade into the notch root using a small steel block. The 1 mm wide notch was found to hold the blade snugly, parallel to the crack so very few specimens were lost to over-tapping and most tapped cracks were central and mostly straight.

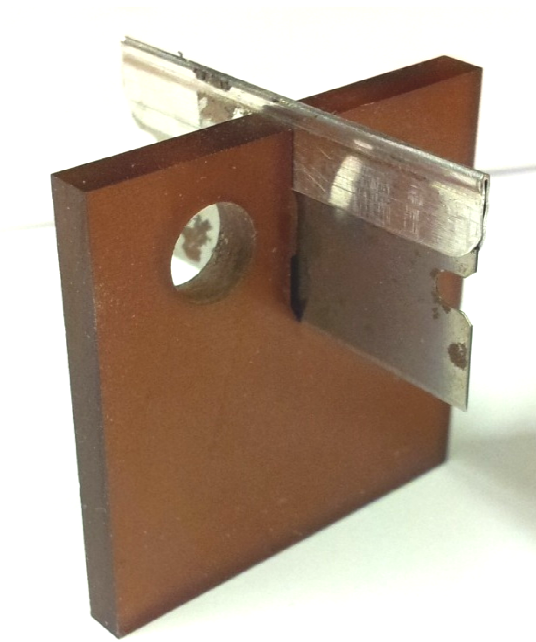


Figure 4.4 - Tapping a natural crack with a razor blade into a grooved notch. Note the crack propagated ahead of the razor blade

Initial crack lengths and ligand lengths were measured on both sides using a travelling microscope (figure 4.5) and specimen dimensions and thickness measured using Vernier callipers and micrometer screwgauge respectively. Later specimens were prepared with a sharp groove instead of a flat notch (figure 4.2). This had the result of generally straighter cracks which required more energy to initiate. This is thought to be a consequence of higher machining stresses in the bed of the sharp notches than at the front of the flat groove.

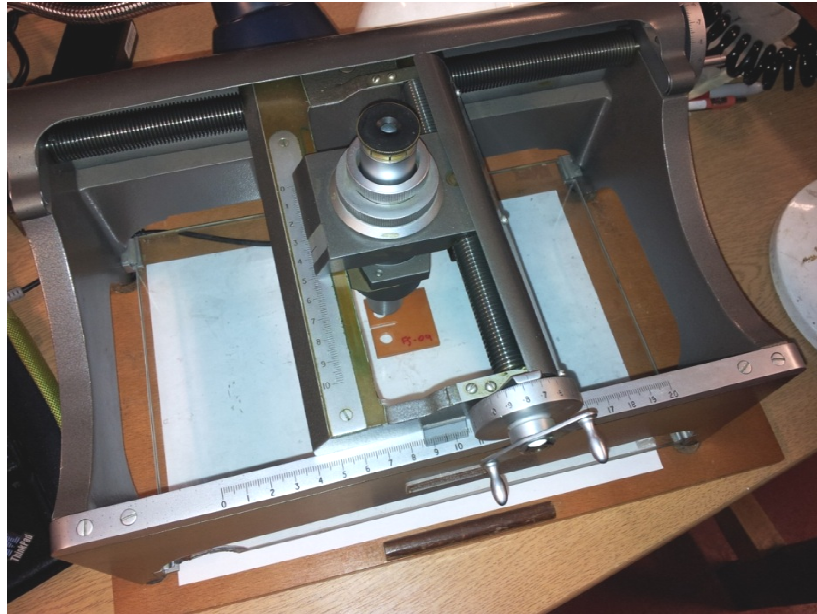


Figure 4.5 – Measuring crack length using an x-y Vernier travelling microscope

4.2.3 DIC speckle pattern

For digital image correlation (DIC) to be carried out, a speckle pattern was applied by painting with a fine airbrush (Central Pneumatic ‘Deluxe airbrush kit’ 95810 using an AS AB-AS18 Mini Piston type “On-demand” airbrush compressor). Initially, some rough-cut specimens were made and tested without applying a speckle pattern to see if applying a paint layer could be avoided. Light scratches were applied to the surface with P1000 abrasive paper however it was quickly found that achieving a suitable pattern in the materials to be tested was difficult. Too many scratches gave little contrast. What appeared to be an appropriate amount of scratches resulted in artefacts in the strain fields; calculated strains could be seen to closely follow the scratch pattern on the specimen. Consequently the well-established paint-speckle technique was used instead.

Black (‘Black (Indian) 028’) and white (‘White 011’) Daler-Rowney FW Artists’ Acrylic Inks were each separately thinned with water and isopropanol thinner in the ratio approximately 4:1:1 (paint : water : isopropanol), giving a paint mix with a similar viscosity to skimmed milk, as suggested by the airbrush instructions. As a future reference, it was found that these high-quality acrylic inks gave a relatively shiny finish which had implications in the lighting methods used for DIC and for a thermoelastic stress analysis study carried out within the research group concurrent

with this project. It was found that replacing the portion of water with additional isopropanol gave a faster-drying, less shiny finish. Pots of considerably thicker modelling acrylic paint (such as Tamiya acrylic paints) were found to give the least shiny finish but were more difficult to thin appropriately and consistently.

A 10 mm wide strip down the specimen ligand was masked with masking tape and first a thin layer of white acrylic paint applied using an airbrush (figure 4.6 shows this stage of the process). Once dried, black acrylic paint speckles were applied by carefully feathering the nozzle button. Speckle size was controlled by adjusting the nozzle, pressure and dual-action (air/ink) trigger and much practice on scrap material. A pressure of around 2 bar (30 psi) was found to be effective for this airbrush. This was viewed in an optical microscope to analyse speckle size, shape and density. Speckles applied to the specimens were consistent across the painted area, were randomly distributed and exhibited no visible bias towards any direction.

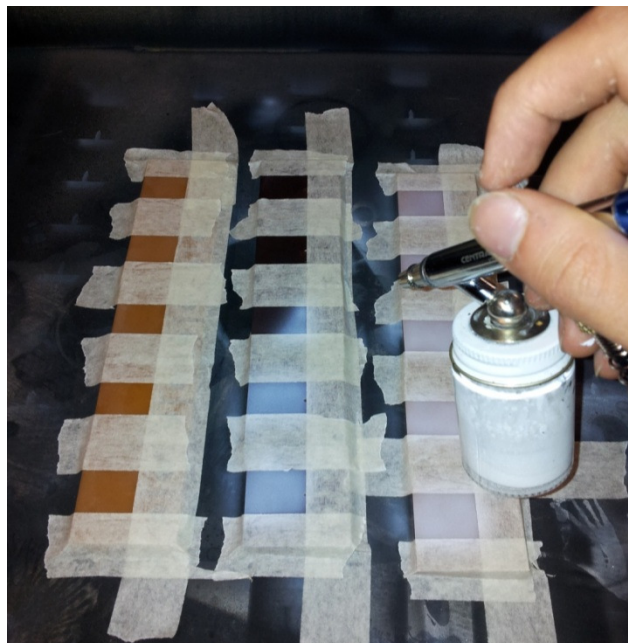


Figure 4.6 – Applying a thin white acrylic base by airbrush

A sample specimen speckle pattern is shown in figure 4.7. This image has been taken from the raw DIC image data and are presented uncompressed so visible pixels are seen as analysed by DIC. As can be seen from the scale and from the pixel size of figure 4.7, the speckles applied are around 5-15 pixels in feature size. As discussed later, it is advised for future works for more care to be taken in achieving a range of

speckle sizes when producing airbrush speckle patterns. A new airbrush system with a range of nozzle sizes has since been purchased.

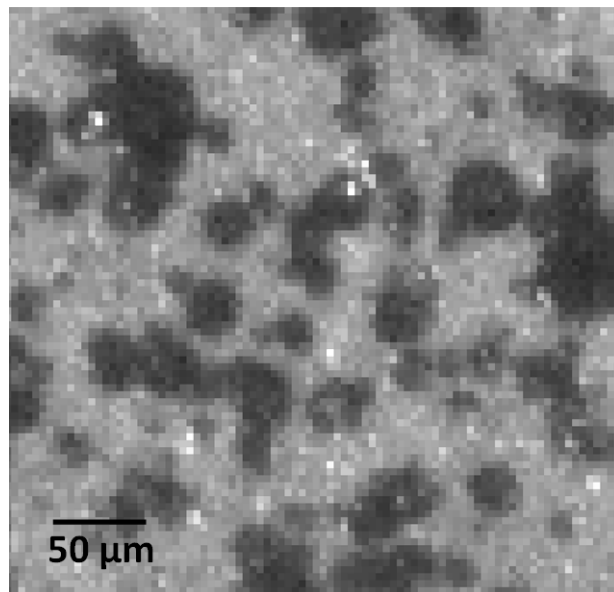


Figure 4.7 - CT specimen speckle pattern at pixel-level

4.2.4 Mechanical arrangement

Specimens were loaded in a JJ-Lloyd electrically actuated test-frame (type T22K) (figure 4.9a). Simple compact tension grips were designed to offer a clear view of the specimen region of interest. The design of these grips is shown in figure 4.8. The grips were designed in a modular arrangement so that parts could be replaced if specimen thickness or size was changed. The central grip piece was made from mild steel whilst the front and rear faces were made from 4.0 mm thick 2024-T6 aluminium sheet. The clevis pin attachment allows free rotation of the grips so that torsionally loading the specimens is avoided. The face of the grips was painted black to reduce the effect of reflection on the polished alloy surface. At such low critical loads the self-weight of the small grips used had to be calibrated out of the results so as not to affect load accuracy.

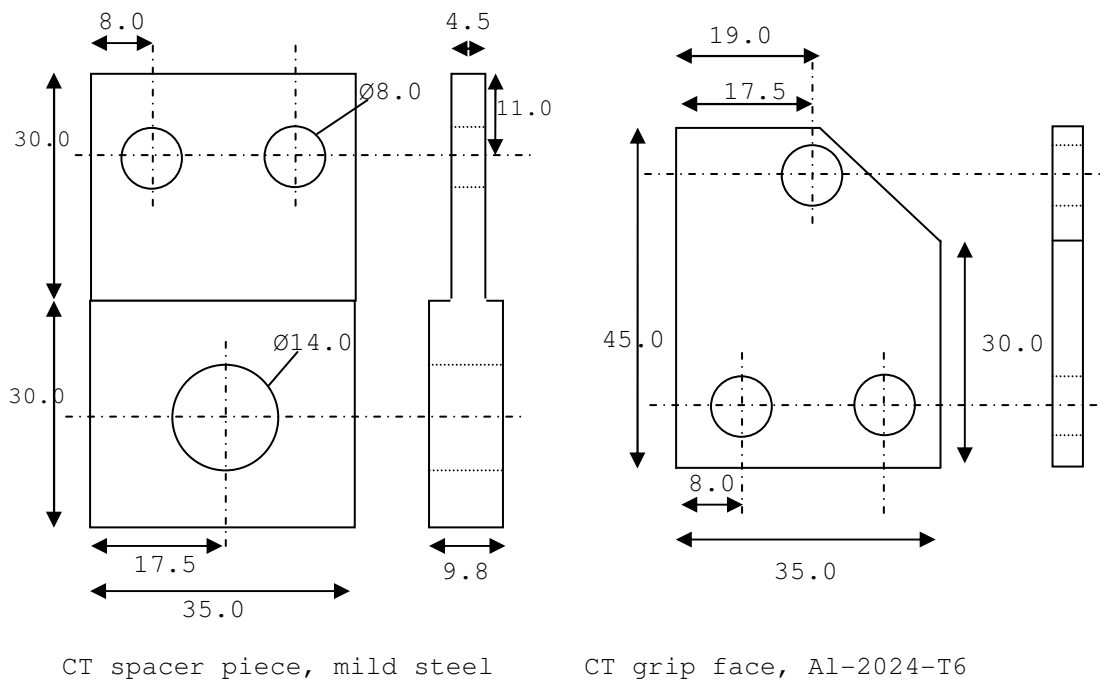


Figure 4.8 – Compact tension grip designs (dimensions in mm)

In accordance with the relevant standard [1], specimens were loaded in tension at a nominal speed of 1.0 mm / min. A 500 N canister-type load cell was calibrated prior to testing and used for the duration of the tests.

Due to unfortunate equipment failure, tests on F3, F4 and F5 materials were performed on a benchtop Lloyd Instruments TA500 (figure 4.9b). The TA500 is a single-column, low-capacity system, equipped with a 500 N load cell, designed primarily for the testing of medical devices, food, textiles, gels and other low-strength materials. As such, it has much lower compliance than a traditional mechanical test frame and was found to be insufficiently rigid for DIC measurements. Specimens displayed significant out-of-plane motion which made taking accurate optical measurements impossible. Consequently, tests on materials F3/4/5 were repeated on a vastly more rigid electromechanical Mayes system (figure 4.9c). The load data from the TA500 results was considered unaffected by the system rigidity. The load data from the Mayes is however is of some uncertainty; the Mayes has a 100 kN load cell and the typical failure loads of the specimens are magnitudes lower at around 100-200 N. The amplification of such a small signal,

combined with the subsequent conversion by the workstation DAQ (data acquisition card) resulted in a low signal-to-noise ratio.

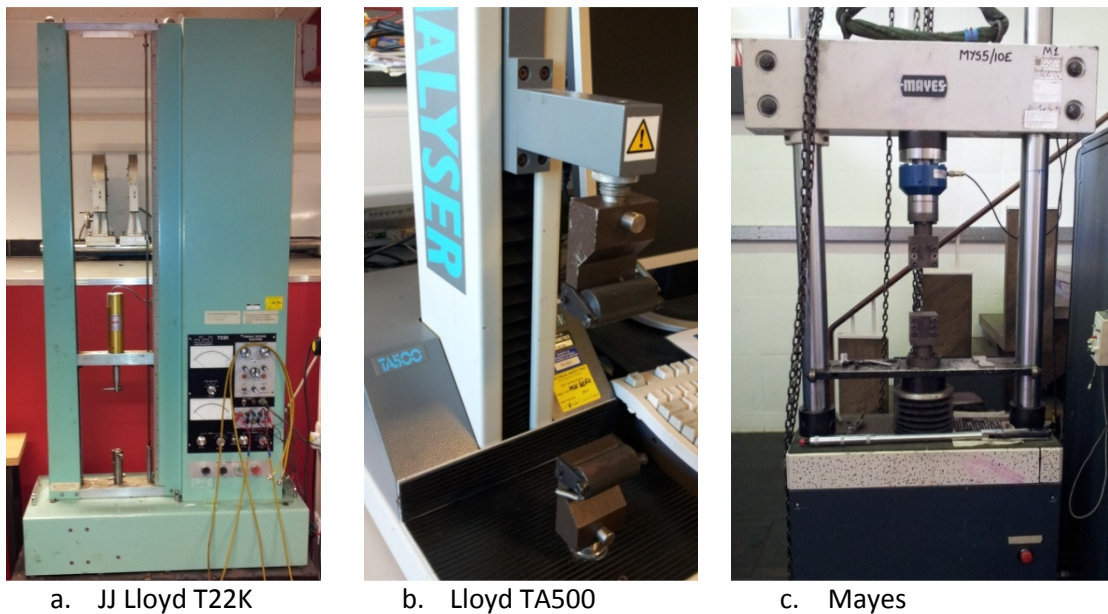


Figure 4.9 – Test frames used

4.3 Optical arrangement

The region of interest for epoxy fracture strain measurements is the radius 2-3 mm around the crack tip. This area was observed by pointing a long-field microscope lens and digital camera at the specimen and recording images alongside load data by using a data-acquisition card. A c-mount Navitar PreciseEye far-field microscopic lens was chosen giving a field of view of 6.0×4.5 mm. The lens was attached to a LaVision ProVision X2.0 digital camera giving 14 bit greyscale 2.0 megapixel images (1600×1200 pixels) at a frame rate of up to 30 Hz (tests showed the camera→DAQ→PC arrangement to have sufficient bandwidth to record frames comfortably at up to 7 Hz at the full resolution of the camera). The camera system was attached to a Manfrotto tripod via a custom two-axis micrometer stage; allowing fine adjustment of the camera position. The optical arrangement is shown in Figure 4.10.

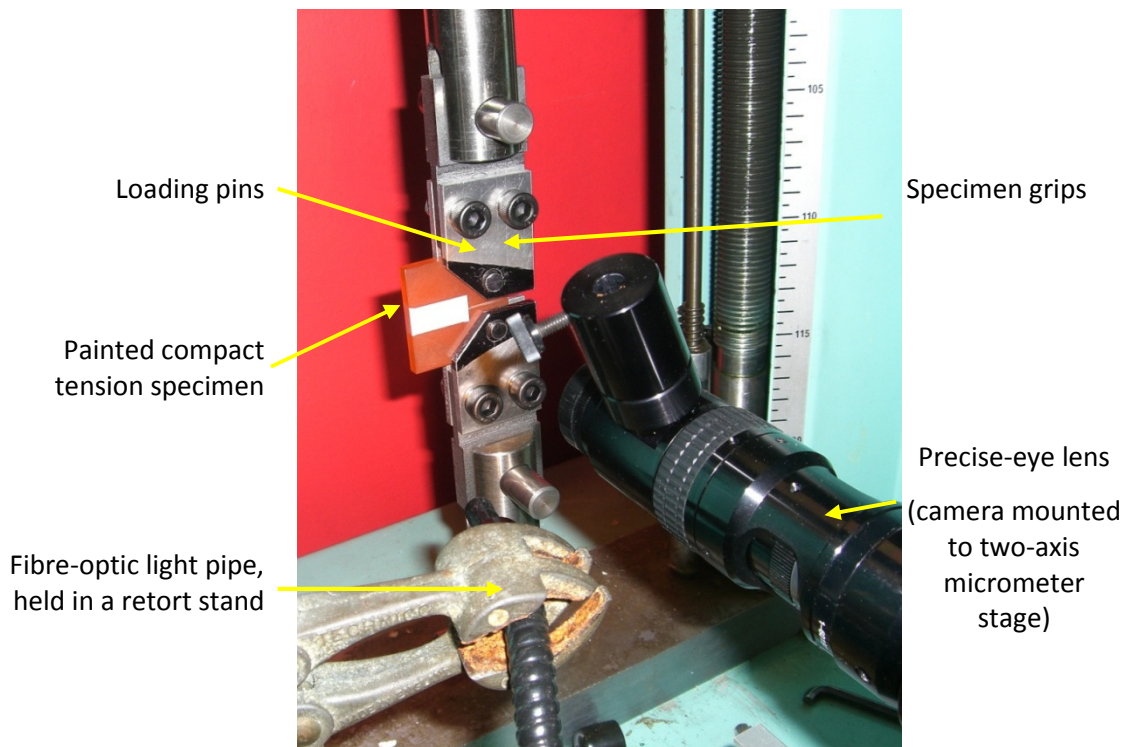


Figure 4.10 – CT specimen experimental arrangement

Specimens were illuminated with a fibre-optic light pipe, offering bright, consistent white illumination at a low temperature. Heating the surrounding air causes atmospheric refraction resulting in significant errors in DIC measurements [92] and so is best avoided. Initially, coaxial illumination was used, however the black and white acrylic paint was found to be similarly reflective under direct illumination. Instead the light was angled obliquely at the specimen, this diffuse lighting offering the high contrast required. Speckle pattern requirements have been discussed in section 3.3.1.

The DIC system was calibrated by placing a steel rule in the plane of the surface specimen, taking a still image, and measuring point-to-point across the rule. This measurement was checked by measuring the steel rule at various angles and positions (in the plane of the specimen). This simple calibration showed the low radial distortion of the PreciseEye lens and the accuracy of the camera alignment to be high with measurements to be accurate to within 0.14% [122]. A more complete explanation and discussion of the DIC method and calibration can be found in section 4.3.1.

A limitation of the PreciseEye lens was that the lens has an exceptional short depth of field of within 0.2 mm. Slackness in the specimen grips resulted in small out-of-plane rigid body displacements when the specimens were loaded, whereby the specimens would no longer be in focus. Irrespective of focal issues, out of plane displacements of this magnitude are associated with significant errors apparent in measured ε_{xx} and ε_{yy} (for more information see the error analysis in section 5.6). To overcome this issue, small preloads of typically 15-25 N were applied to the specimens before the lens was focused. As an unintended consequence, the 'unloaded' strain state of the specimens in the DIC measurements was taken at a considerable 10-25% of the critical load measured and so this had to be taken into consideration in the DIC results. The issue and the solution to the problem is discussed in section 5.3.4. The CT tests for F3, F4 and F5 formulations and all mixed-mode tests were carried out later and this problem eliminated by pre-loading the specimens to align everything, focusing the optics, then unloading the specimens to a stress/strain-free state. Whilst the PreciseEye lens has a fine-adjustment wheel to adjust the focal length of the lens by 3 mm, the lens was strictly focused using the micrometer stage; thus the focal distance was kept constant. This ensured that the distance between camera and lens was maintained to within the 0.2 mm depth of field of the lens and so slight variations in specimen position in the z direction (i.e. perpendicular to the plane of the specimen) would not affect the quality of the calibration.

4.3.1 DIC calibration

For 2D DIC, calibration in its simplest form defines a length measurement per pixel. The easiest way of doing this is by taking an image of a steel rule at the same focal distance as a specimen and defining a distance between two points on the image. A photograph of the optical arrangement is shown in figure 4.11 and a screenshot of the process is shown in figure 4.12. As a simple check, the steel rule is translated and rotated and measurements made in the x-direction, y-direction and diagonally. Figure 4.11 shows calibration being performed on a mixed-mode specimen used in chapters 6-7.

This form of calibration requires the pixel length to be consistent across the whole field of view. In some situations this is not the case. Optical elements, especially those with large zooming capabilities, can exhibit a degree of ‘barrel’, ‘pincushion’ or a combination of the two forms of radial distortion. These distortions can be mathematically corrected for in the calibration processes. The fixed focal-length Navitar PreciseEye lens system used for this project was chosen in part for its exceptionally low level of distortion, so this calibration stage was not carried out. Checking the length measurements across the field of view, as mentioned previously, gave confidence in the lens specifications.



Figure 4.11 – Steel rule in the plane of a specimen for 2D calibration (note; the specimens were pushed flush with the grip fronts for testing so the focal + calibration planes were kept consistent.)

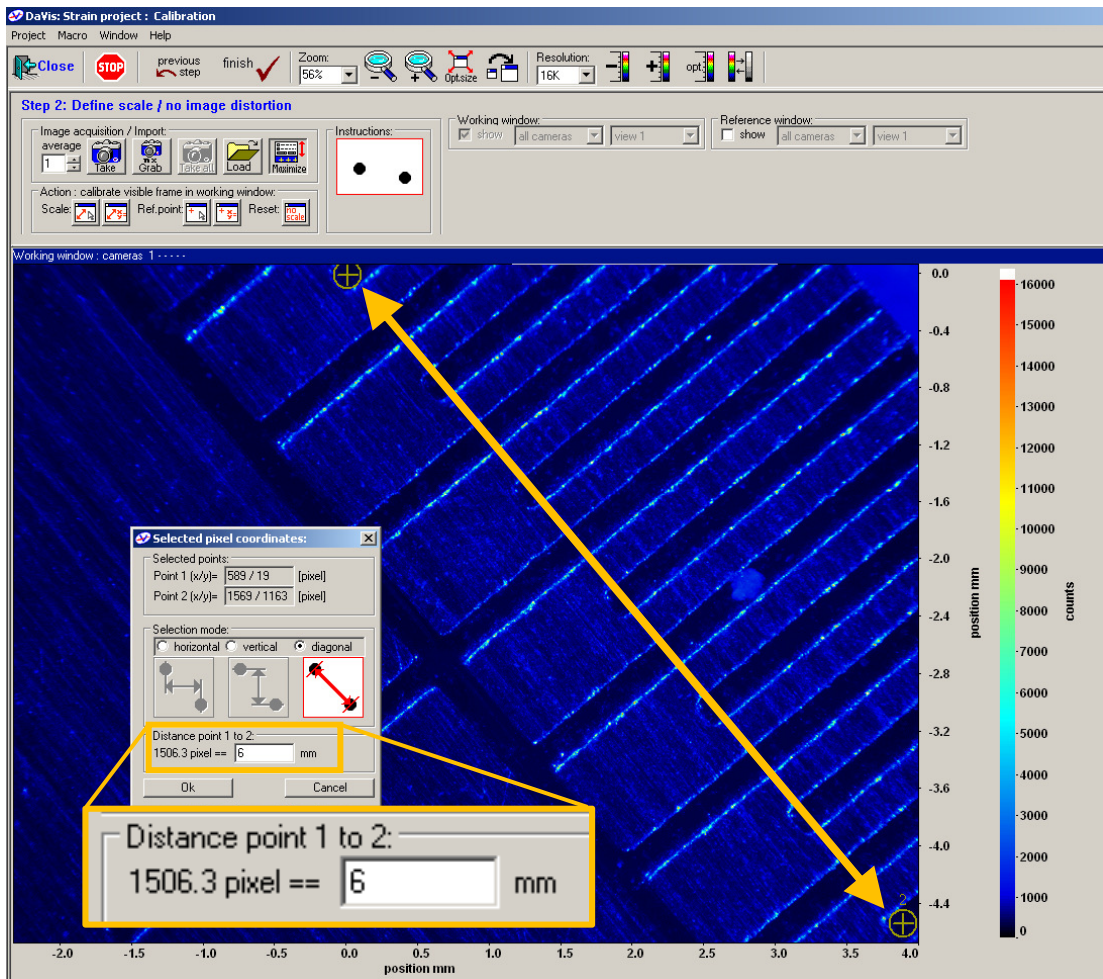


Figure 4.12 – Screen-shot of the 2D calibration process showing a 6.0 mm span selected on an image of a steel rule (orange dimensioning is overlaid for clarity).

4.4 Data acquisition and loading details

Images were acquired at a nominal 1 Hz using a CAMLINK image data-acquisition card. Load data were recorded alongside the acquired images using a National Instruments DAQ, all coordinated by LaVision image/data acquisition functions in DaVis StrainMaster 7.1. Subsequent checks on the time signatures of the image data showed images to be consistently recorded to within ± 0.01 seconds of the nominal 1.0 Hz.

As mentioned previously, loads were applied to the specimens by displacement control at a nominal 1.0 mm / min, in accordance with BS ISO 13586 [1].

4.5 DIC algorithms

Choosing a subset size and overlap is one of the fundamental decisions that affect the quality of results. Displacements are determined across the entire subset and so the smaller the subset selected, the higher the displacement field resolution. The higher the size of the subset, the more greyscale information the algorithms have from which to determine displacement, so the more accurate the displacement. Subset size selection must be based on the amount of displacements in the specimen, how continuous the displacements are, and the nature of the speckle pattern. Ultimately, since the time taken to perform correlations is now much lower than in previous years, and in the order of minutes rather than hours (indeed at the time of writing some real-time calculations can be performed on the newest hardware with the latest software), it is typical for users to try a number of different subset sizes and algorithm options until satisfied.

ϵ_{yy} strain fields were determined using different subset sizes to check the results for subset-size sensitivity. In the LaVision 7.1 DIC software, strain fields are calculated from the displacement fields in a separate step from the correlation step. Whilst less efficient than other algorithm choices, calculating strain fields directly from the displacement fields allows us to more easily judge the best algorithm parameters for a given set-up. The results of this are shown in figures 4.13. In each case the crack is in the field of view, pointing from left to right. The figures clearly show that the spatial resolution cost for increasing window size is huge. Additionally, these figures show the effect of discontinuities on strain-field measurement. Strain fields have been scaled between 0.1% and 1.5%; the white/grey areas show strains higher than 1.5%. An area of false strain is visible around the crack flank due to the sudden discontinuity in the displacement fields. This is an artefact of the strain field algorithms which proliferate a false strain around the area of the discontinuity.

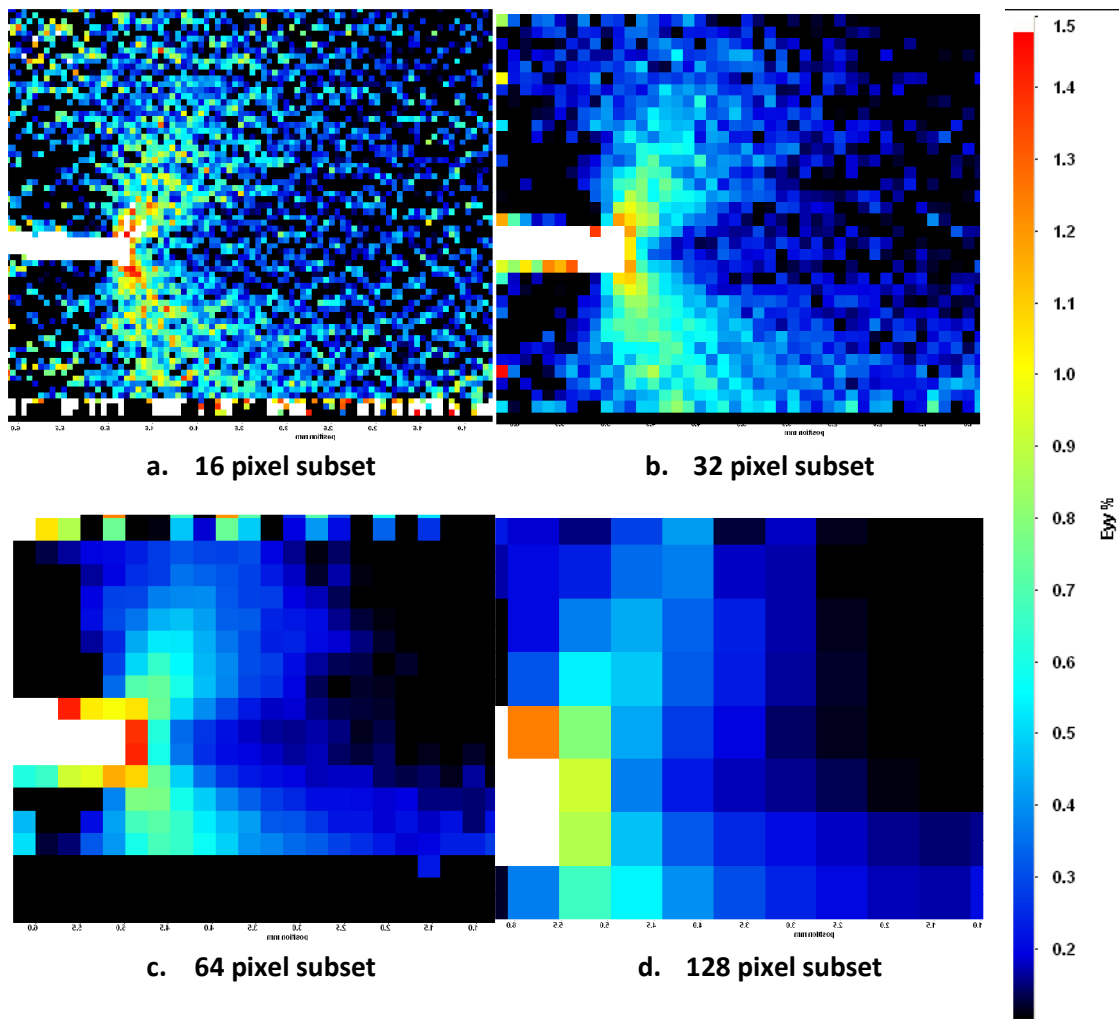


Figure 4.13 - ϵ_{yy} (unsmoothed) strain fields around a crack tip in a CT specimen determined using differing subset sizes.

It is possible to interpolate strain fields from the values determined at each centre-point, to produce much smoother results. The ϵ_{yy} raw, unsmoothed strain fields in figures 4.14a-d have been calculated for a number of different window sizes. Note that interpolation is not the same as smoothing; smoothing involves simply adding extra values between calculated strain values, usually at an average of the two, whereas interpolation involves determining strains at full pixel resolution by fitting continuous functions between the measured displacement values (see the difference between figure 4.13d and figure 4.14d, both from the same displacement field data at 128x128 pixel window size).

The interpolated strain fields of 4.14 closely follow the expected shape for strain fields around a crack tip, whereas the interpolated strain fields of 4.14a (16 pixel

subsets) are clearly noisy, and the interpolated strain fields of 4.14d (128 pixel subsets) are spatially insufficient. Interpolation clearly shows how the accuracy of the pointwise strain measurements is strongly affected by the window size. Interpolation of strain fields is computationally very expensive and for this reason, this step has been performed only on individual frames.

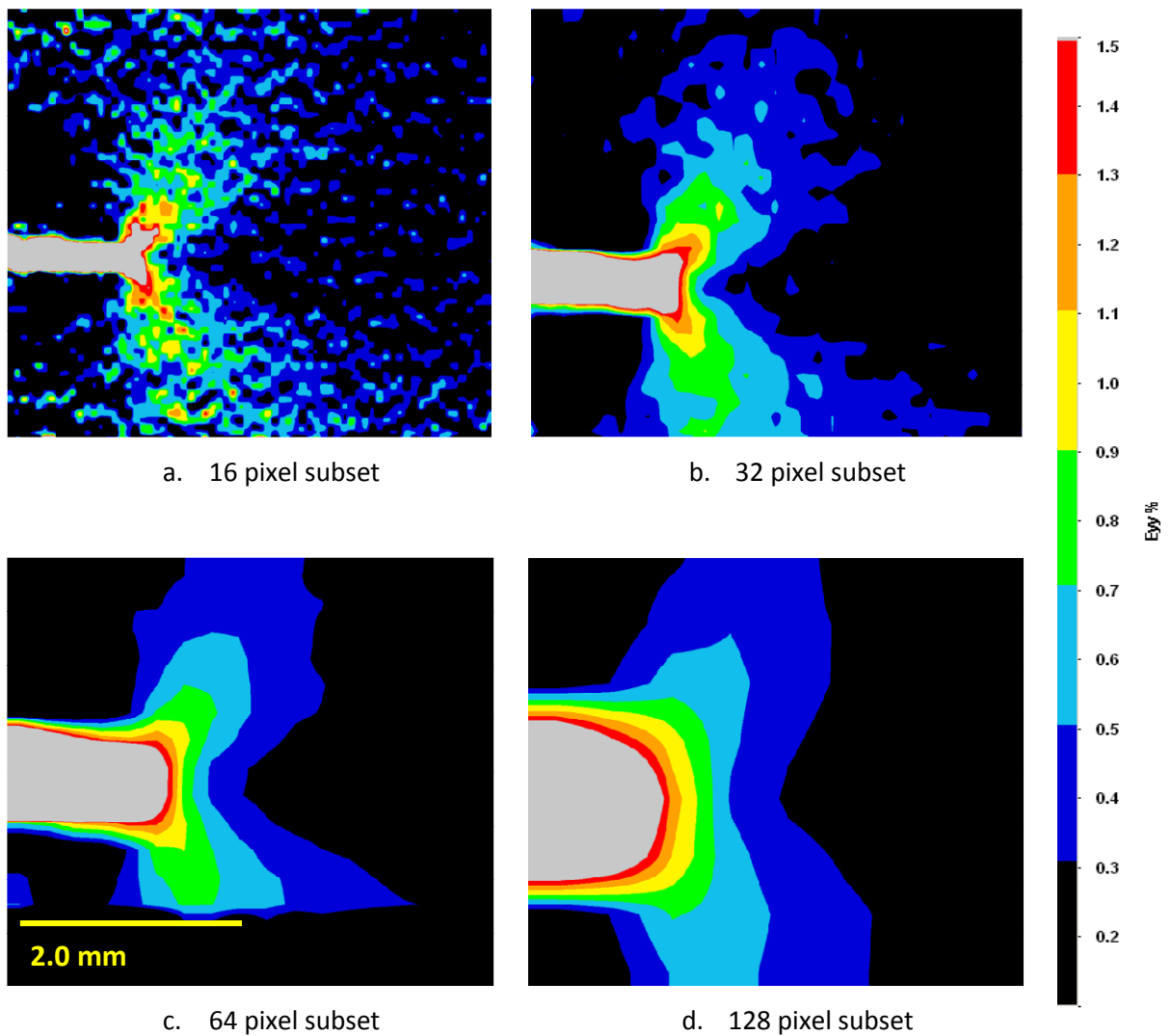


Figure 4.14 – ϵ_{yy} (interpolated) strain fields around a crack tip in a CT specimen determined using differing subset sizes

Increasing the overlap (or in some packages, referred to as reducing the step size) reduces the problem of reduced spatial resolution. Figure 4.15 shows the (unsmoothed) strain fields from analyses performed with large integration windows with overlap. It can be seen that the spatial resolution is significantly improved, and the strain field quality appears smoother and closer to the expected shape.

Reassuringly, both the unsmoothed and interpolated strain fields from 4.15 b,d and 4.14 b,c all look similar and so any of these options can be used with confidence that the strain fields are not especially sensitive between these options.

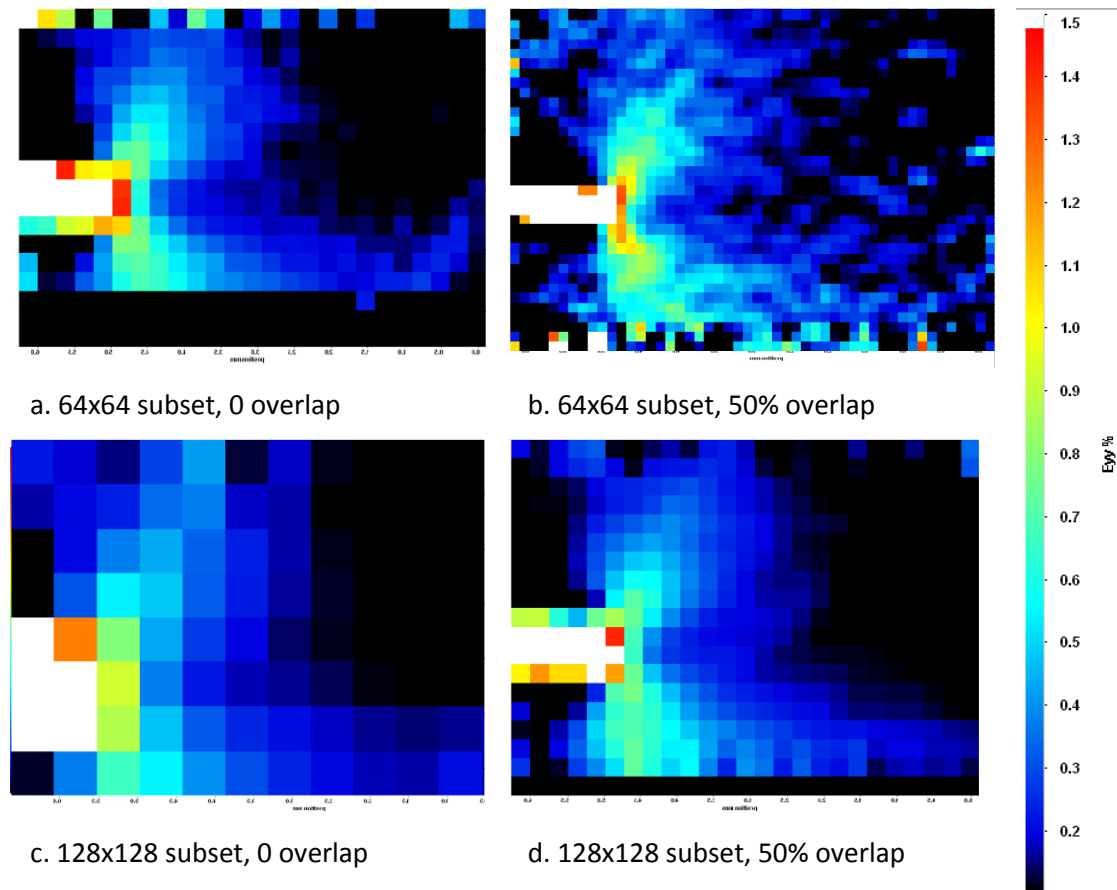


Figure 4.15 – ϵ_{yy} (unsmoothed) strain fields around a crack tip in a CT specimen for two window sizes, each determined both with zero, and with 50% overlaps

After experimentation, it was decided that a multipass algorithm with 64 pixel smallest subset, overlapped 50 % (i.e. 32 pixels) produced the best compromise between accuracy and resolution. An ϵ_{yy} strain field determined using this subset size is shown in figure 4.16.

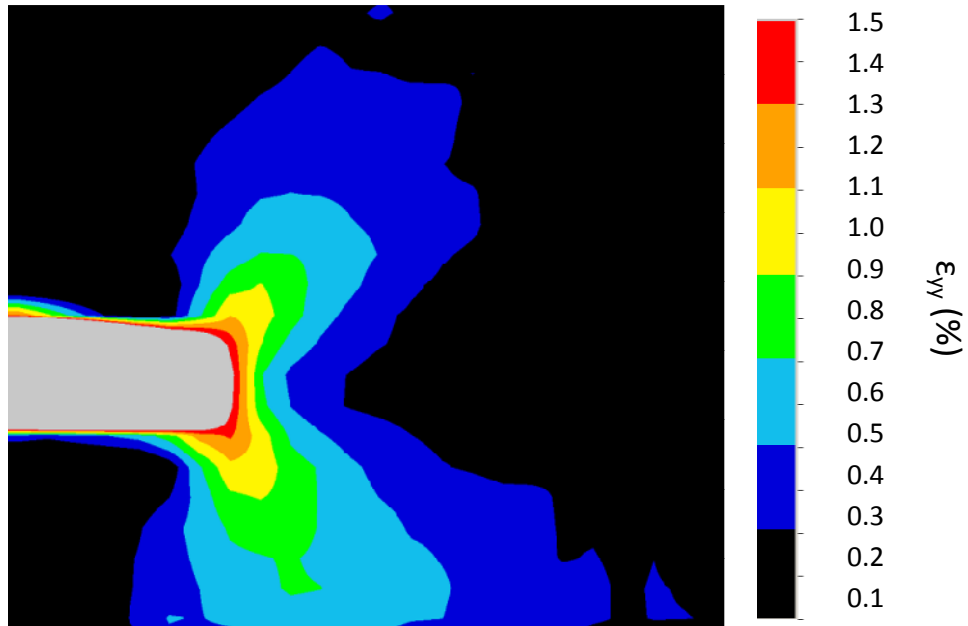


Figure 4.16 - ϵ_{yy} (interpolated) strain fields around a crack tip in a CT specimen determined using multi-pass 64x64 pixel subset size with a 25% overlap (with a 128x128 pixel first evaluation).

For completeness and for reference, the following algorithms, algorithm options and variables were chosen:

Table 4.1 - Selected DIC algorithms

Correlation mode	Relative to initial frame
Integration window	Square
Primary subset size	128 pixels, 2 pass, 50% overlap
Secondary subset size	64 pixels, 2 pass, 50% overlap
Postprocessing	Default LaVision multipass smoothing algorithms

Chapter 5

Mode I: Results, analysis and discussion

5.1 Introduction

The results from the experiments described in chapter 4 are presented here. Fracture parameters have been extracted from DIC displacement fields and compared with values from the standard load-based method. The sources of error associated with the experiment are assessed and levels of confidence in the test procedure are discussed.

5.1.1 Determining critical load values

As per the relevant standard followed (BS ISO 13586 [1]), critical loads were taken as the maximum load during loading. Under the 1.0 mm/min displacement control loading, in most cases the materials followed a linear increase in load, up to sudden failure. The load curves showed crack growth and failure to be fast, sudden and brittle. Observation of the acquired image data showed that noticeable (unstable) crack growth did occur in specimens of NEAT and F4 materials. ‘Pop-in’ (i.e. a load peak dropping to a lower value as crack initiation occurs and crack tip stress is relaxed) was observed in the load measurements of individual specimens. In these cases, the pop-in fracture initiation value was recorded as maximal. Specimens of materials F2, F3 and F5 tended to exhibit some slow, steady subcritical crack growth (of the order of up to 0.5 mm) prior to sudden unstable failure. The slow crack growth typically occurred only in the last ten frames. The effect of slow crack growth on the load values was visible only as a slight plateau in load values. Subcritical crack growth is discussed further in section 5.3.6.

The unstable fast crack growth present in NEAT and F4 materials was not present in the other toughened formulations, which tended to grow at critical loading by more sudden slip-stick mechanisms. The slip-stick phenomena observed in F2, F3 and F5 materials did not occur over distances relevant to the measurement of K_{IC} ; fast crack growth tended to occur 5-10 mm at a time (i.e. well out of the field of view of the camera) before subsequent arrest.

The compact tension tests have been performed at different times with different equipment. All NEAT and F2 specimens were tested on a JJ-Lloyd T22K universal test frame with a 500 N load cell. Tests were performed on specimen numbers 01-04 for materials F3, F4 and F5 on a benchtop single-column Lloyd Instruments TA500 Texture Analyser with a 500 N load cell. Whilst the load accuracy of these tests was high, due to the nature of the test frame, the DIC measurements performed at the same time were inadequate and so a further set of F3/4/5 tests was performed using a substantially stiffer dual column 100kN capacity Mayes electric test frame. As mentioned in section 4.2.4, the Mayes set-up gave a low load signal-to-noise ratio measurement. To minimise the effect of this noise, a least-squares smoothing process has been applied to the Mayes load data; the effect of this is shown in figure 5.1.

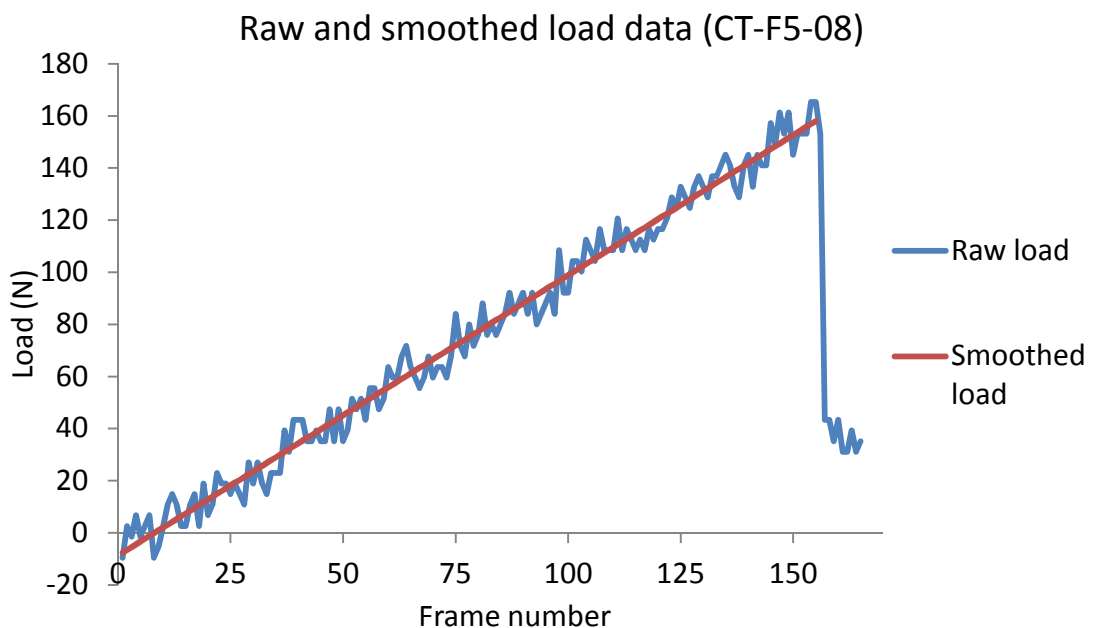


Figure 5.1 - Raw and smoothed load data for noisy Mayes load cell data

5.2 Classical load cell results

Using the classical linear elastic fracture mechanics (LEFM) approach documented in the British Standard BS ISO 13586 “*Plastics – Determination of fracture toughness...*” [1], K values were calculated at applied failure load $F = Q$. Failure load Q was identified as the highest load value before unstable fracture occurred. For the stress intensity factors at failure, K_Q to be admissible as plane strain fracture toughnesses, K_{Ic} , a number of criteria have to be met. These are noted in section 5.2.1.

The term $f(a/w)$ in equation (5.1) represents the geometrical or ‘shape’ function; a function of a (crack length), w (specimen width) and of the specimen geometry. Tabulated shape functions for a/w ratios exist, however for accuracy this value was calculated for each specimen from the equations in the British Standard BS ISO 13586. Using the classic LEFM expression (5.1) where K is the stress intensity factor, F is applied load, h is specimen thickness and other parameters are as previously defined, a provisional toughness value K_Q was produced. The results of this process are tabulated in table 5.1.

$$K = f(a/w) \frac{F}{h\sqrt{w}} \quad (5.1)$$

Table 5.1 – Load cell LEFM results

Material	Specimen	Crack length a (mm)	Thickness h (mm)	Failure load Q (N)	K_Q (MPa.\sqrt{m})
NEAT	NEAT-CT-02	11.57	3.90	97.8	0.93
	NEAT-CT-03	11.53	3.95	104.0	0.97
	NEAT-CT-04	11.65	3.98	100.0	0.93
	NEAT-CT-06	10.96	4.18	116.0	0.98
F2	F2-CT-06	11.22	4.73	150.3	1.14
	F2-CT-07	11.56	4.77	157.8	1.22
	F2-CT-08	11.83	4.52	145.5	1.21
	F2-CT-09	12.40	4.32	129.5	1.18
F3	F3-CT-01	11.40	3.95	134.0	1.26
	F3-CT-02	11.31	3.95	153.3	1.40
	F3-CT-03	14.02	3.55	101.0	1.29
	F3-CT-04	11.01	4.03	157.4	1.38
	F3-CT-06	11.19	4.33	159.4	1.39
	F3-CT-07	12.13	3.60	139.8	1.45
F4	F4-CT-01	11.14	3.43	92.5	0.97
	F4-CT-02	12.53	3.56	105.3	1.18
	F4-CT-03	10.31	3.73	106.1	0.95
	F4-CT-04	11.02	4.40	126.1	1.09
	F4-CT-05	11.31	3.85	121.2	1.08
	F4-CT-07	11.50	4.07	128.5	1.12
	F4-CT-08	11.82	4.37	133.17	1.11
F5	F5-CT-01	10.99	4.00	136.0	1.20
	F5-CT-02	11.01	3.93	144.9	1.30
	F5-CT-03	11.50	4.13	140.3	1.25
	F5-CT-04	10.62	4.24	152.8	1.23
	F5-CT-06	11.62	3.96	151.1	1.34
	F5-CT-07	10.92	3.56	130.5	1.28
	F5-CT-08	11.64	4.22	158.0	1.35

5.2.1 Checking the validity of the LEFM assumptions

An important part of testing for plane strain fracture toughness is a validation step to ensure that the specimens tested were predominantly plane strain. This is especially true for materials such as the aerospace epoxies tested which are limited in thickness by the nature of the material; the high-cure temperature epoxies tested cannot easily be made in thicker sections without incurring a thermal-runaway¹¹.

For the plane strain conditions to be met, the size of the process zone (the area in which plasticity or similar energy absorption mechanisms such as shear yielding occurs) is required to be suitably small compared to the ligand length and specimen thickness.

Tensile testing of the material showed the (0.2% strain) yield stress to be approximately 50 MPa for each formulation. The characteristic process zone radius can be estimated by the characteristic length \bar{r} by equation (5.2).

$$\bar{r} = \frac{(K_Q)^2}{(\sigma_Y)^2} \quad (5.2)$$

Assuming LEFM behaviour, the process-zone radius for the F3 formulation (the largest process-zone material tested) can be shown to be:

$$\bar{r} = \frac{(1.33 \times 10^6)^2}{(50 \times 10^6)^2} = 0.708 \text{ mm} \quad (5.3)$$

This distance is sufficiently small for the thickness, crack length and ligament widths to all be significantly greater than $2.5 \times \bar{r}$, as required to be considered appropriately plane-strain by BS ISO 13586 [1], ensuring K_Q can be regarded as K_{Ic} . Average K_{Ic} values alongside standard deviations and standard errors (standard error being the standard deviation of a population over the square root of the population size) are

¹¹ Thermal runaway or ‘exotherm’ are the terms used to describe a rapid, uncontrollable and potentially dangerous increase in temperature caused when the inherently exothermic cure process forms a positive feedback loop; the increased temperature of the material causes an increase in rate of reaction, almost certainly resulting in thermally degraded (ruined) material and potential damage to equipment

presented in table 5.2. The K_{Ic} values calculated from the LEFM load cell data can be seen to be consistent; standard deviations and errors are acceptably low for brittle materials of this type.

Table 5.2 – Averaged K_{Ic} values from load cell based LEFM method

Formulation	K_{Ic} (MPa.\sqrt{m})	Standard deviation (MPa.\sqrt{m})	Standard error (MPa.\sqrt{m})
NEAT	0.952	0.031	± 0.015
F2	1.188	0.023	± 0.011
F3	1.362	0.066	± 0.027
F4	1.072	0.077	± 0.029
F5	1.279	0.052	± 0.020

5.3 Extraction of fracture parameters from DIC displacement fields

DICITAC (Digital Image Correlation Intensity factor and T-stress Analyser Code) [121], a Matlab-based program created by Dr. Mohammad Zanganeh at the University of Sheffield as part of his PhD thesis [112] was used to extract fracture parameters from individual displacement field ‘frames’ produced by the DIC calculations. The software gives a number of options to the user, including K_I and K_{II} extraction, using either the Muskhilishvili [111] or the Williams [123] crack tip stress solution approaches. Use of the Williams method allows extraction of the T -stress. The DICITAC software solves the Williams stress solution equations, in a Cartesian, displacement form (equations 5.4-5.5) to find the unknown constants for the displacement fields (using input elastic properties) using a Moore-Penrose pseudoinverse least squares method [112].

$$\text{Mode I} \begin{cases} u_I = \sum_{n=1}^{\infty} \frac{r^{\frac{n}{2}}}{2\mu} a_n \left\{ \left[\kappa + \frac{n}{2} + (-1)^n \right] \cos \frac{n\theta}{2} - \frac{n}{2} \cos \frac{(n-4)\theta}{2} \right\} \\ v_I = \sum_{n=1}^{\infty} \frac{r^{\frac{n}{2}}}{2\mu} a_n \left\{ \left[\kappa - \frac{n}{2} - (-1)^n \right] \sin \frac{n\theta}{2} + \frac{n}{2} \sin \frac{(n-4)\theta}{2} \right\} \end{cases} \quad (5.4)$$

$$\text{Mode II} \begin{cases} u_{II} = - \sum_{n=1}^{\infty} \frac{r^{\frac{n}{2}}}{2\mu} b_n \left\{ \left[\kappa + \frac{n}{2} - (-1)^n \right] \sin \frac{n\theta}{2} - \frac{n}{2} \cos \frac{(n-4)\theta}{2} \right\} \\ v_{II} = \sum_{n=1}^{\infty} \frac{r^{\frac{n}{2}}}{2\mu} b_n \left\{ \left[\kappa - \frac{n}{2} - (-1)^n \right] \cos \frac{n\theta}{2} + \frac{n}{2} \sin \frac{(n-4)\theta}{2} \right\} \end{cases} \quad (5.5)$$

$\kappa = (3 - \nu)/(1 + \nu)$ for plane stress conditions,

$\kappa = 3 - 4\nu$ for plane strain conditions

μ is the shear modulus; $\mu = E/2(1 + \nu)$

a and b are constants to be found, ν is Poisson's ratio

Equations (5.4) and (5.5), the Williams solutions in a Cartesian displacement field form, are taken directly from the thesis of Zanganeh [112]. By expanding the equations, it can be shown that $K_I = a_1/\sqrt{2\pi}$, $K_{II} = -b_1/\sqrt{2\pi}$, and $T = 4a_2$, thus by solving for a_1 , b_1 and a_2 , the desired fracture parameters can be determined.

As discussed in section 3.4, multiple terms of the Williams stress solution expansion must be used to obtain accurate results. In this study it was found that solving for the first fifteen terms was required for converging results. The computational time penalty for increasing this value was minimal and so 20 terms of the Williams solutions were used.

Stress intensity factors measured in this way will be described as being measured using the **DICITAC/Williams** method. Stress intensity factors determined from load cell measurements using the method outlined in the British Standard BS ISO 13586 [1] will be referred to as having been measured with the **British Standard/load cell** method.

5.3.1 Region of data collection

Few studies investigate the effect the region of data collection has on extracted fracture parameters. The effect of the location of the data collection window was assessed by extracting fracture parameters from a wide range of regions. Sensitivity to the inclusion/exclusion of displacement vectors behind and/or in the immediate vicinity of the crack tip was tested for a pure mode I specimen, 00-F5-06. This was not a compact tension specimen; so that a theoretical value of T -stress can more easily be obtained, a CT specimen was not used (some issues with the CT experiments are discussed in section 5.5). 00-F5-06 is an Arcan-type specimen, described later in section 6.2, which transfers a close-to-uniform uniaxial tensile stress across the crack ligand.

The matrix of figure 5.2 shows the ranges tested. In order to display displacement vectors as arranged in their specimen location, displacement vectors are presented in a grid of their x and y locations, separated into u and v (displacements in x and y directions respectively). The magnitude of the vector component is represented by the z -dimension; in this case colour. Scale bars have not been included in these figures for clarity. Areas with displacement vectors identify the areas defined as a data collection window. Crack tip location is indicated with a cross (cracks are from left-to-right). Subsequent stress intensity and T -stress results are presented in table 5.3.

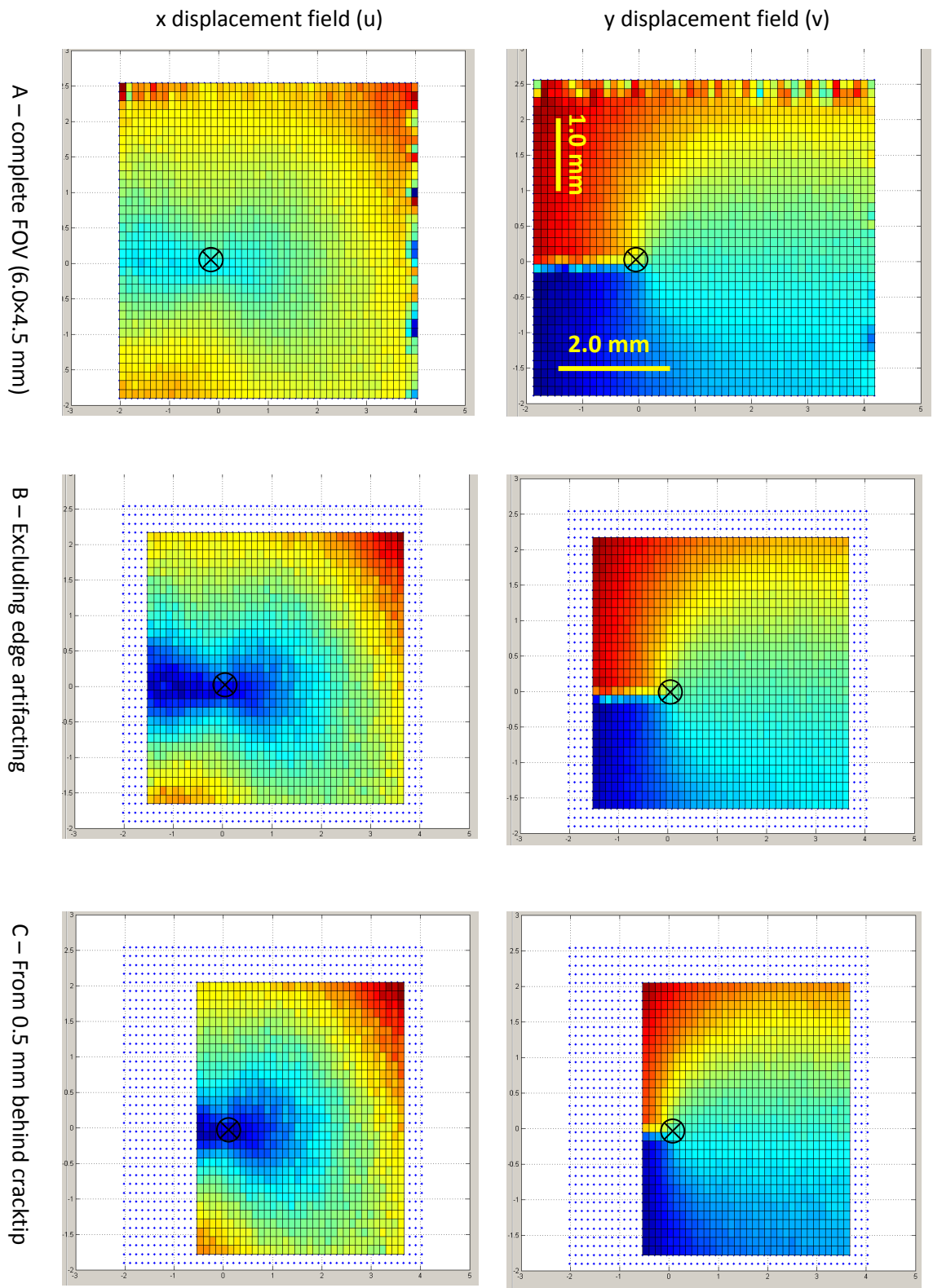


Figure 5.2 continued...

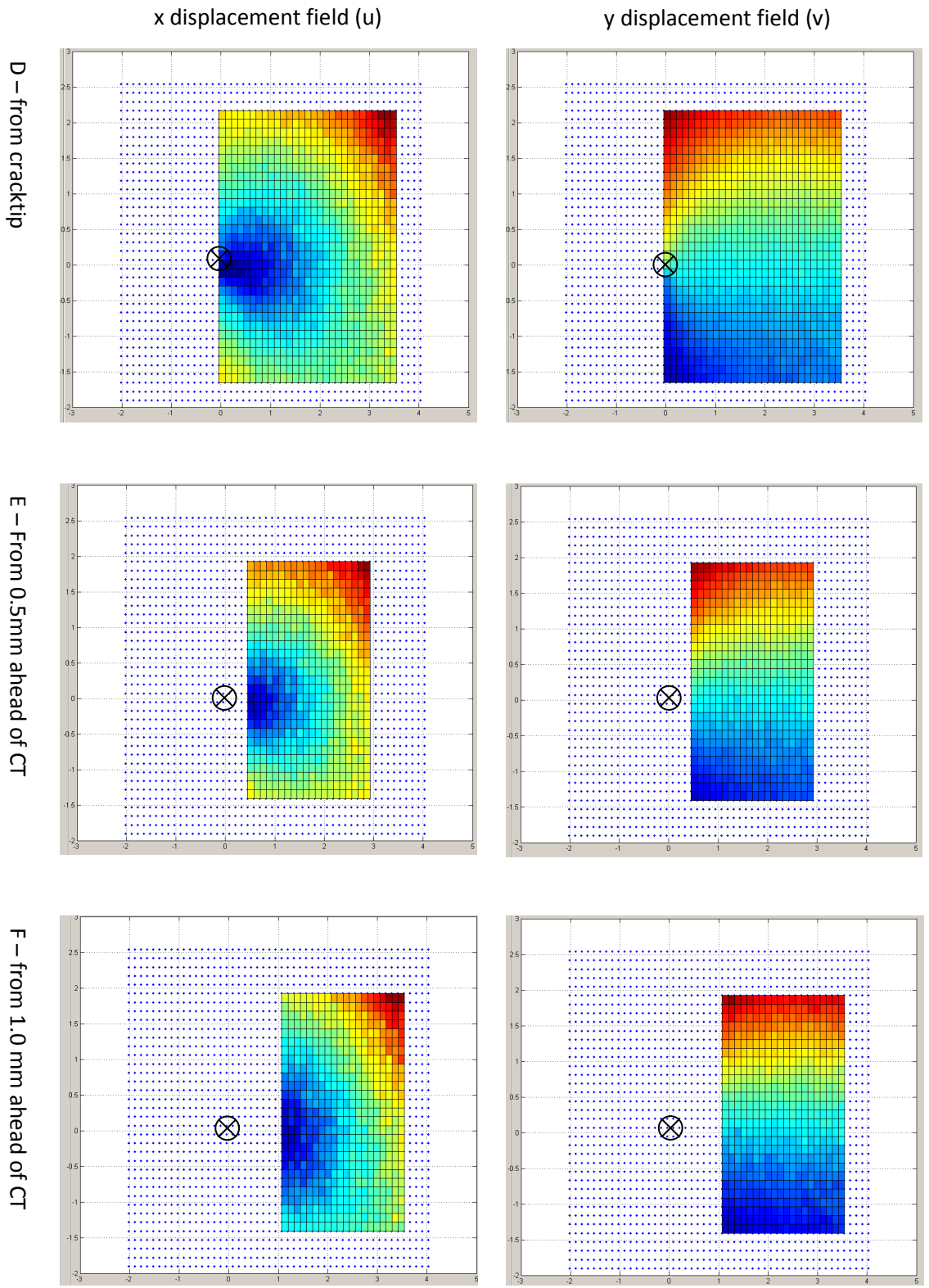


Figure 5.2 continued...

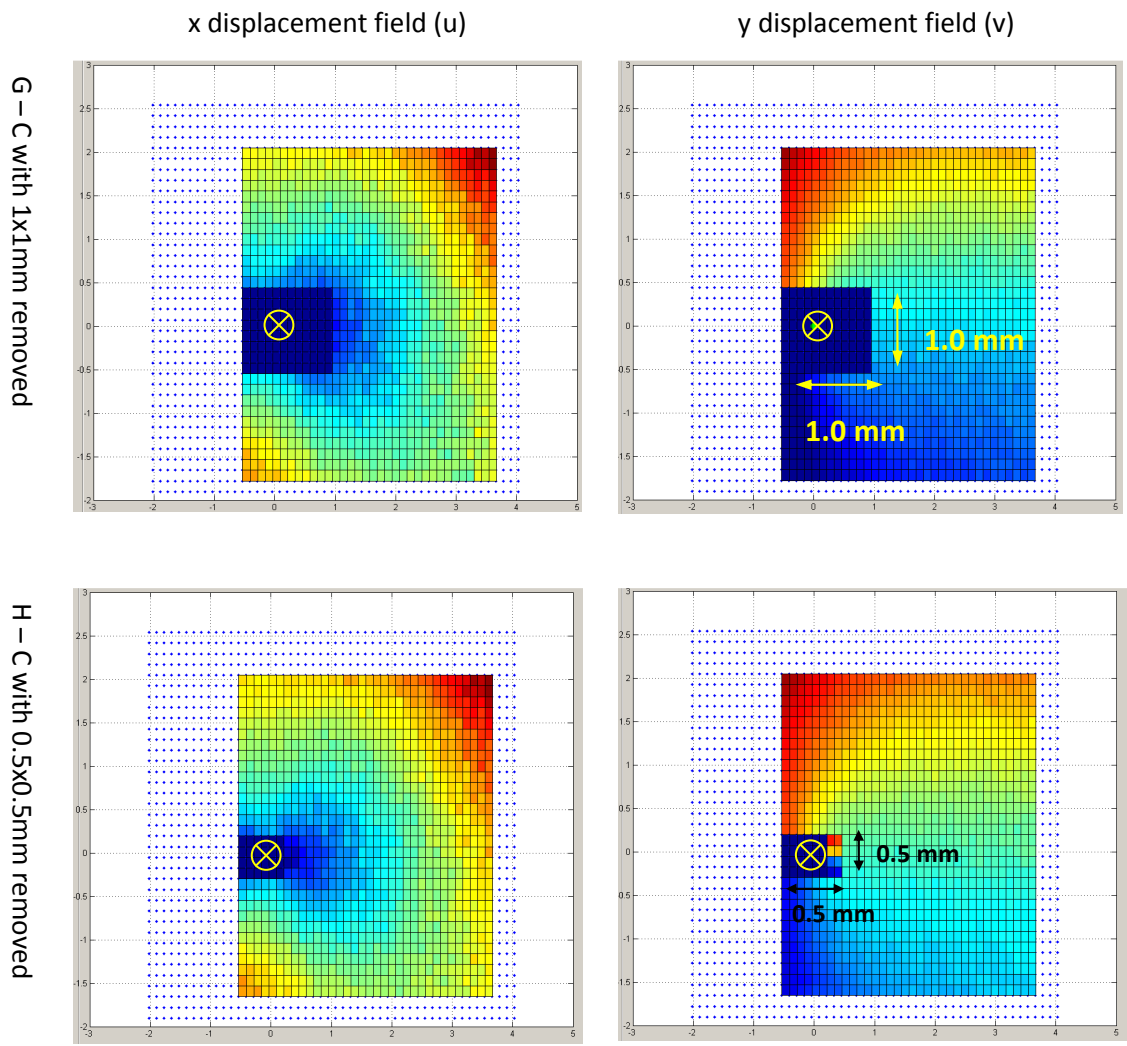


Figure 5.2 – Matrix showing data point regions in a pure mode I specimen. Crack tips are indicated with crosses.

Theoretical values for K_I and T -stress are **1.12 MPa \sqrt{m}** and **-3.83 MPa** respectively. K_{II} should be zero. Section 11.1 in the appendix explains the derivation of the theoretical values. Theoretical T -stress values are also discussed later in section 5.5. As a point of reference, the K_I values determined by DICITAC can be assumed to have an accuracy limit of ± 0.02 MPa \sqrt{m} and as a rough comparison, T -stress values can be assumed to have an accuracy limit of a magnitude higher, of around ± 0.2 MPa, based on the displacement field accuracy associated with variation. A full error analysis can be found in section 5.6

Table 5.3 - Stress intensity factors and T-stress values measured by DICITAC for various displacement vector windows

Window	K_I (MPa \sqrt{m})	K_{II} (MPa \sqrt{m})	T (MPa)	Field of view description
A	1.103	-0.055	-4.852	Complete. Includes edge-induced artefacts and 2.0 mm behind crack tip
B	1.125	-0.060	-5.306	Excludes edge artefacts. Includes 2.0 mm behind crack tip
C	1.131	-0.008	-5.649	Includes 0.5 mm behind crack tip
D	1.173	0.110	-4.223	Field of view from in line with crack tip
E	1.171	0.437	-0.075	Excludes all data behind crack tip; range is 0.5 mm ahead of crack tip
F	1.338	1.115	1.854	Excludes all data behind crack tip; range is 1.0 mm ahead of crack tip
G	1.147	-0.060	-1.797	As for C, excluding 1.0 mm \times 1.0mm square ahead of CT and all behind
H	1.140	-0.013	-5.005	As for C, excluding 0.5 mm \times 0.5 mm square ahead of CT and all behind

Table 5.3 shows that as the window moves ahead of the crack tip, the accuracy of the results is compromised. K_I appears to be less sensitive to window location than either K_{II} or the T -stress. A false, non-zero, value of K_{II} appear to be caused by lack of data in the most extreme cases of windows E and F, whilst the measured values of K_I are within 20% of the correct value. A measured T -stress of -5 MPa is both within the natural deviation from theoretical values and within the accuracy of the

technique experienced in other studies [105, 112]. Studies found in the literature that make an effort to methodically select a data-window cover the extraction of stress intensity factors; no studies were found that discuss or measure the effect of altering the data window when extracting T -stress data, other than a comment on computed displacement field accuracy by Zanganeh [112]. The study of data-collection windows for Williams stress solution extraction by Nurse and Patterson [84] is concerned with extraction from photoelastic data, which typically use narrow notches over natural cracks. Since the crack tips measured in this project are naturally sharp, the Nurse and Patterson sharpness considerations (i.e. one must not use data within a radius of 5ρ from the 'notch' tip, where ρ is the notch tip radius) can be safely ignored.

The T -stress measurement can be seen to be extremely sensitive to the location of the data-points used; it seems that taking data behind the crack tip is essential. The Williams method appears to be insensitive to the effect of errant vectors near to the crack tip or across the crack flanks in this case. It is suspected that due to the relative brittleness of the materials studied, and hence the low levels of plasticity, that data can be taken very close to the crack tip. Indeed window G (figure 5.3 and table 5.3) suggests that for measuring T -stress, data close to the crack tip is required for accurate measurements whereas it is not required for stress intensity measurement. Removing data close to the crack tip (window F) did not appreciably improve data but range G shows that the consequence of removing too many is poor T -stress results.

Residual error plots from the fitting of the Williams stress solutions to the displacement fields support the inclusion of near-crack tip vectors; they typically show a single line of vectors as appreciably higher error in fitting than the rest of the data. The quality of fit between measured data and Williams displacement fields is not compromised by their inclusion and stability of solution appears to be unaffected.

From the results of this analysis, data collection windows of the range of B or C have been employed in the subsequent measurement of fracture parameters in this project.

5.3.2 Crack tip location

It was found that using displacement fields with more vectors, calculated by running DIC algorithms with a high overlap, caused significant time penalties without improving accuracy.

Processing time was dominated by the crack tip search algorithm. Running DICITACs “pattern-search” crack tip search algorithm (documented in [105]) for a 64×64 pixel, 75% overlap integration window (60×60 vectors for the region studied) took over nine minutes (580 seconds) whereas the same size integration window with a 50% overlap (30×30 vectors) took around twenty seconds (calculations run on a Windows XP Pro (32 bit) workstation using an Intel Core 2 Duo E8500 at 3.16 GHz and 3.2 GB RAM).

The accuracy of the defined crack tip location was found to hugely affect the determined T -stress values. Crack tip locations inaccurate by a number of pixels gave fairly consistent K_I values alongside strongly variable T -stress values. In one pure mode I specimen, the defined crack tip was translated incrementally from the pattern-search location (supported by the recorded image data) and DICITAC K_I and T -stress measurements recorded. Matrices containing the values are shown in tables 5.4 and 5.5. These matrices have been visualised in figures 5.3 a-b.

Table 5.4 - T -stress values (in MPa) determined for a matrix of displacements (in mm) from true crack tip location in x and y directions (Δx and Δy respectively).

$\Delta y \backslash \Delta x$	-0.4	-0.2	0	0.2	0.4
-0.4	-12.08	-9.742	-7.938	-6.493	-5.268
-0.2	-11.85	-9.109	-7.001	-5.352	-4.023
0	-9.764	-7.269	-5.300	-3.708	-2.393
0.2	-11.10	-8.142	-6.142	-4.513	-3.179
0.4	-11.39	-8.736	-6.562	-5.025	-3.683

Table 5.5 – K_I values (in MPa \sqrt{m}) determined for a matrix of displacements (in mm) from true crack tip location (Δx and Δy respectively).

Δx	-0.4	-0.2	0	0.2	0.4
------------	------	------	---	-----	-----

Δy					
-0.4	1.271	1.169	1.073	0.9782	0.8935
-0.2	1.317	1.205	1.100	1.002	0.9089
0	1.372	1.254	1.142	1.035	0.9336
0.2	1.289	1.179	1.078	0.9818	0.8915
0.4	1.237	1.139	1.045	0.9561	0.8719

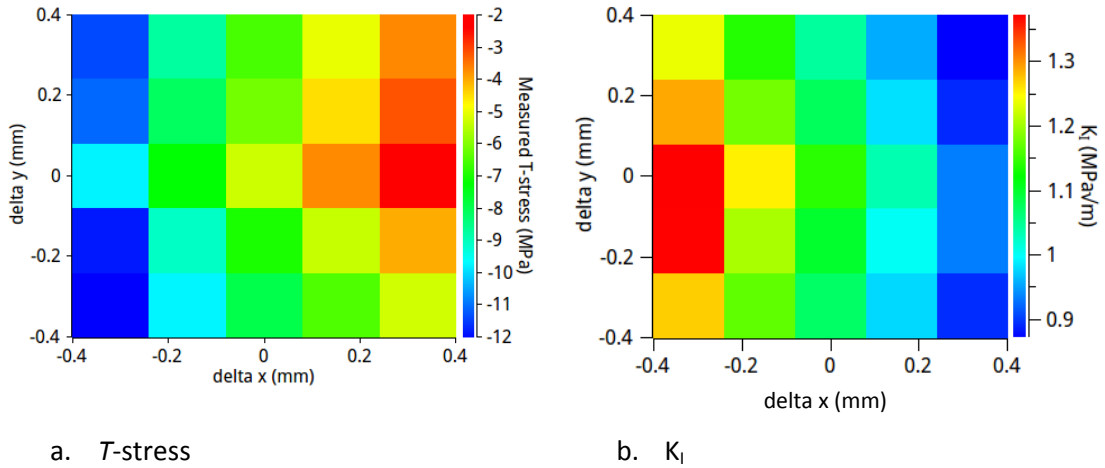
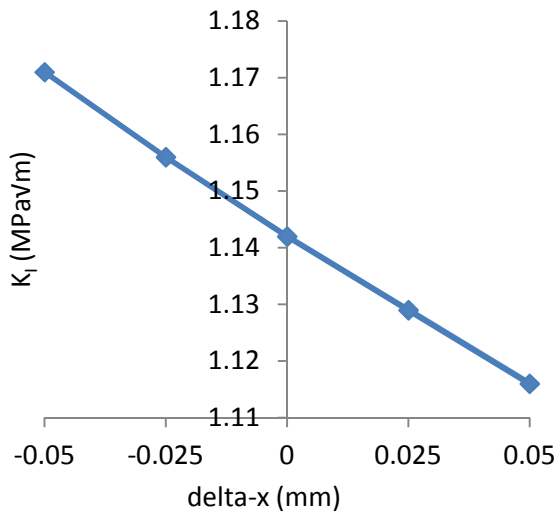
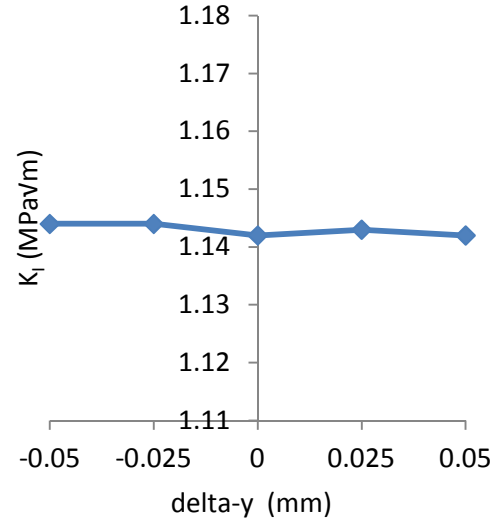


Figure 5.3 - DICITAC-measured values of T -stress and K_I in a mode I specimen with differently defined crack tip locations.

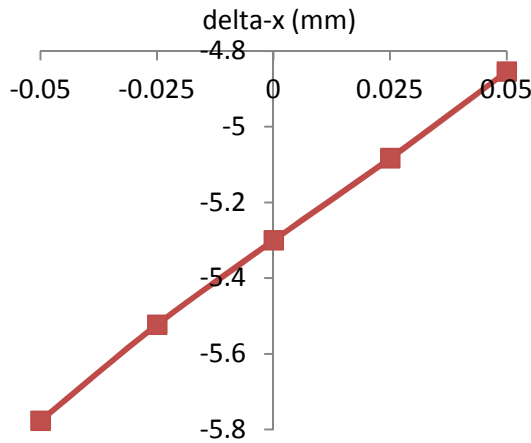
The data from table 5.4 and figure 5.3-a shows how the measured T -stress values are up to 72% erroneous (-9.11 MPa *c.f.* 5.30 MPa at the correct location) when the defined crack tip is wrong by ± 0.2 mm in both x and y directions. The maximum error at the same locus for K_I is 14% (0.982 MPa√m *c.f.* 1.142 MPa√m determined by DICITAC at the correct location and the theoretical value of 1.12 MPa√m determined from load data). It is noted that 0.2 mm is a large error in location; in the optical arrangement applied in this study it is equivalent to 43 pixels. Figures 5.4a-d show the T -stress and K_I measurements as crack tips are mislocated by ± 25 μm and ± 50 μm , equivalent to a more realistic ± 5.3 and ± 10.6 pixels respectively.



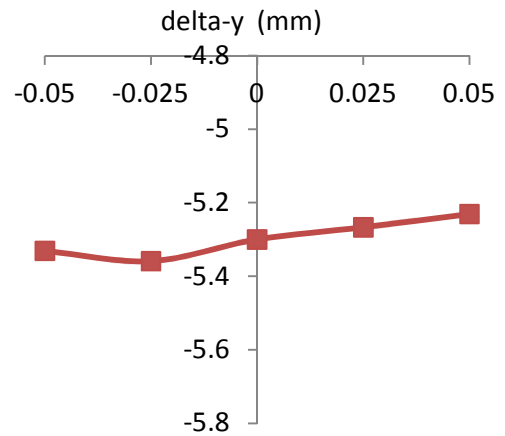
a. K_I , varying location with x



b. K_I , varying location with y



c. T , varying location with x



d. T , varying location with y

Figures 5.4 – DICITAC measured values of K_I and T in a mode I specimen with differently defined crack tip locations. Crack tip locations are limited to varying x and y directions separately.

Figures 5.4a-d show that both the stress intensity factor and the T -stress measurements are considerably more sensitive to crack tip definition in the x -direction than the y -direction for this pure mode I case. If the x -location of the crack tip is ill-defined by 6 pixels (0.025 mm), the resultant error in K_I is ± 0.014 MPa√m, equivalent to $\pm 1.2\%$. For the same location offset, the resultant T -stress error is ± 0.22 MPa, equivalent to $\pm 4.2\%$. As discussed in section 5.6.3, the crack tip locating algorithm used in this study determined crack tips with approximately a ± 6 pixel variation. This result goes some way to explain the observation by Zanganeh [112]

that measured T -stress is highly dependent on the accurate definition of the crack tip location, whereas stress intensity factors were less dependent.

5.3.3 Young's modulus correction

Two elastic moduli are required in order to calculate stress intensity factors from displacement fields using the Williams stress solutions. Young's modulus and the Poisson's ratio are used in DICITACs implementation. Values obtained from Cytac Engineered Materials were initially used for the parameter extraction. These values are listed in table 5.6.

Table 5.6 – Young's moduli, courtesy of CEM.

Material	Young's modulus E (GPa)	Poisson's ratio ν
NEAT	3.49	0.39
Particulate toughened	3.12	0.39

The tensile response of epoxy is not completely linear. The British Standard tensile test method for plastics, BS EN ISO 572-1 (*"Plastics. Determination of tensile properties"*) [124] defines the Young's modulus of thermoset and thermoplastics as stress over strain between $5 \mu\epsilon$ and $25 \mu\epsilon$. Using modulus values determined in accordance with the British Standard resulted in systematic inaccuracies between DICITAC-extracted K_I values and values from the load cell method. Figure 5.5 shows clear divergence between the DICITAC-determined values (red points) and the load cell theoretical values (blue line). Note, the DICITAC data here has been corrected as described shortly in section 5.3.4.

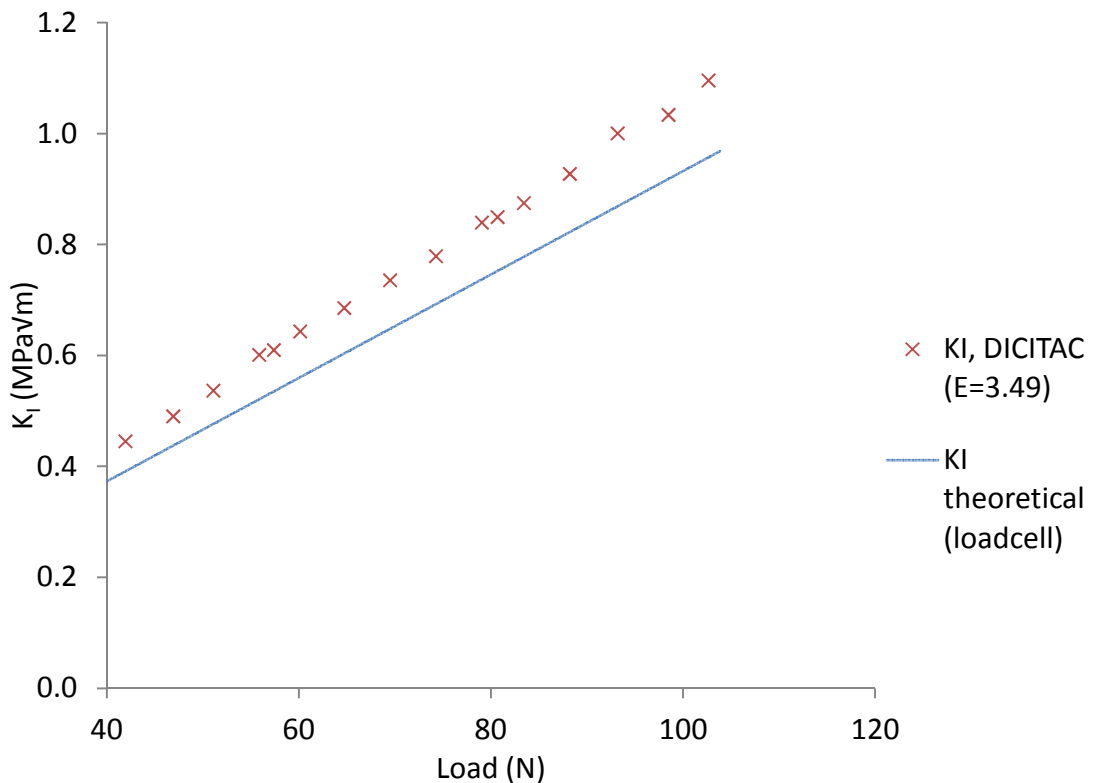
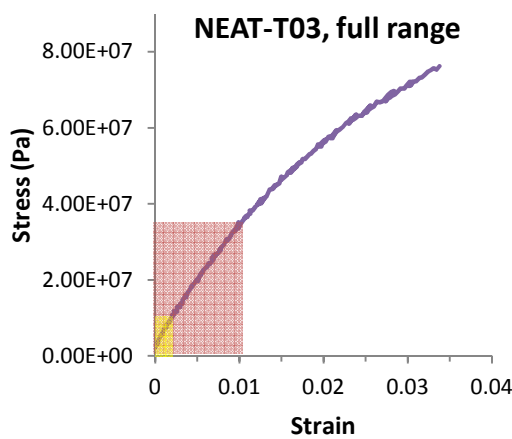


Figure 5.5 - Comparing load cell K_I values with DICITAC K_I values using BS EN ISO 572 method modulus in DICITAC method

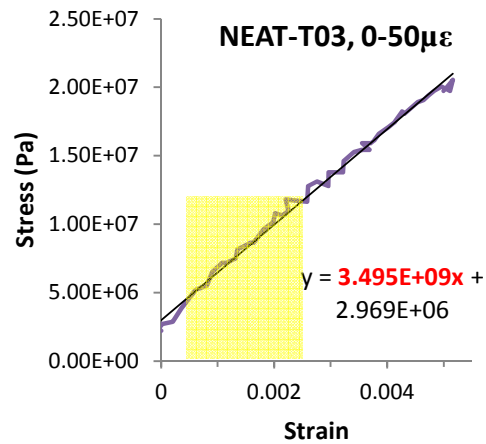
Tensile tests were performed on the resins and Young’s Modulus values were determined for a higher strain range, typical of that experienced in the fracture specimens. More details of the methods used are presented in the appendix (section 11.2 in the appendix) for the sake of brevity and focus. One stress-strain plot can be found in figure 5.6 to illustrate the non-linear behaviour of the materials. Figure 5.6a shows the complete tensile test, to failure, of a NEAT resin specimen. The range of the BS EN ISO 572 method is highlighted and reproduced in figure 5.6b.

A strain-range representative of the strains measured in the fracture experiments was initially chosen as the strain-range visible in DIC measurements at a nominal crack tip stress concentration of 1.0 MPa√m. Since the crack tip is a singularity, and given, furthermore, the limitations of DIC in measuring strains across discontinuities such as cracks, visibility must be defined. It has been arbitrarily defined here to be the strain measured from 0.5 mm from the crack tip. This coincides in the region between both the size of one subset (0.30 mm) and the radius of the estimated

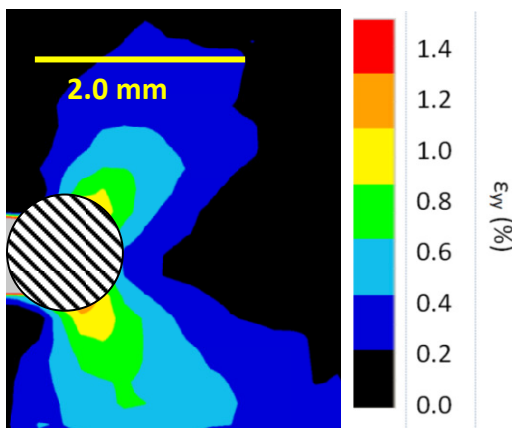
plastic zone (0.71 mm; see section 5.2.1) and so has been considered an informed initial guess at a modulus modifying function. Figure 5.6c shows the ϵ_{yy} strain field around a crack tip under pure mode I loading of 1.0 MPa \sqrt{m} . The masked range indicates a circle of radius 0.5 mm. As can be seen, this range is equivalent to a strain range of around 0-1% strain and it is this range which will be used to define as the elastic range to determine a modulus for the purposes of parameter extraction.



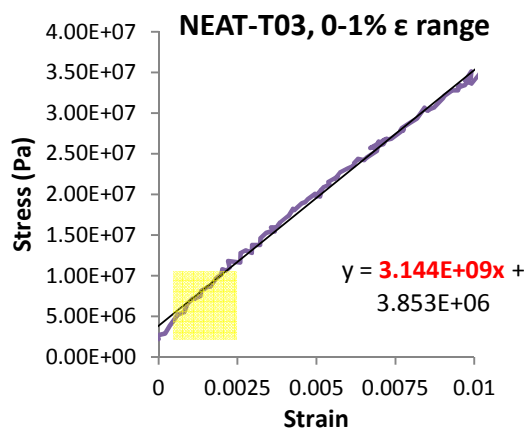
a. Full stress-strain plot (BS range indicated in yellow)



b. Low strain range (BS range indicated in yellow)



c. Strain (ϵ_{yy}) plot around crack tip, excluding a circle with a diameter of 1.0 mm



d. Appropriate strain range for DICITAC

Figure 5.6 – The effect of strain range on measured Young’s modulus values

Table 5.7 shows the measured stiffness values in the range 0-1% strain. These results will be used as modulus properties for all following DICITAC results.

Table 5.7 – Young’s moduli used for DICITAC method. Values marked * courtesy of CEM.

Material	Youngs modulus E for 0-1% strain range. (GPa)
NEAT	3.15
F2	3.06
F3	3.18*
F4	3.11*
F5	2.91*

As will be seen later, load cell and Williams’ solution derived results using the modified modulus values are in close agreement throughout loading.

5.3.4 Strain-offset correction

DIC displacement fields are measured relative to the unstrained state of the first, unloaded image in the series. As mentioned in section 4.3, due to the optical arrangement, the specimens were preloaded to a small but significant load before focusing the camera. Consequently the specimens were under a significant strain at the ‘unstrained’ initial image frame, frame zero. The ‘preloads’ involved were of the order of 15-25 N; this equates to 10-20% of the critical load.

Figure 5.7 shows the effect of this non-zero initial strain state. The stress intensity values measured using DICITAC are offset from those measured using the British Standard method.

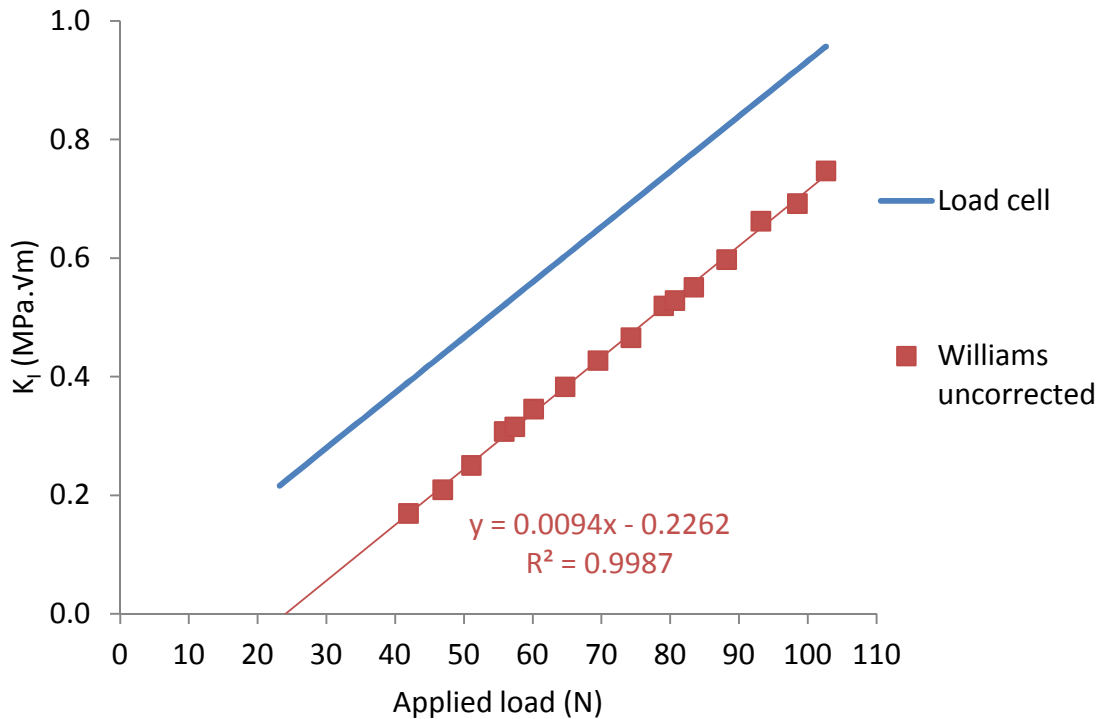


Figure 5.7 - Uncorrected, incorrect Williams/DICITAC K_I values alongside values measured using the standard (BS ISO 13586) method for specimen NEAT-CT-03

Using the principle of superposition, assuming linear elastic behaviour (which is already assumed by using the Williams method), a method of adding a finite value to extracted parameters was carried out to remove this offset. For the K_I values this was a simple matter of adding the K_I obtained through the Williams method $K_{I_{raw}}$ to the K_I value calculated using the load and geometry approach of BS EN ISO 13586 [1] at frame zero. This, however, is not a complete solution to the problem since one of the primary benefits of using experimental mechanics parameter extraction is to not require load-data, shape functions etc. thereby allowing stress intensity factors to be measured in situations where these are not available or tabulated values are unreliable.

As can be seen in Figure 5.8 , the addition of the appropriate load cell derived $K_{I_{frame=0}}$ (for the case of the pictured NEAT-03, this is 0.2162 MPa.v̄m) results in a very close match between K_I values obtained by the established load and geometry LEFM approach and the K_I values extracted from DIC data using the Williams approach. The y-intercept of a regression line through the uncorrected Williams-derived K_I values is also shown in Figure 5.7. This value (-0.2262 MPa.v̄m) is within

5% of the load cell value. These results show that the linear regression y-intercept of the DICITAC values can be used to correct for non-zero initial strain, provided load measurements have been recorded.

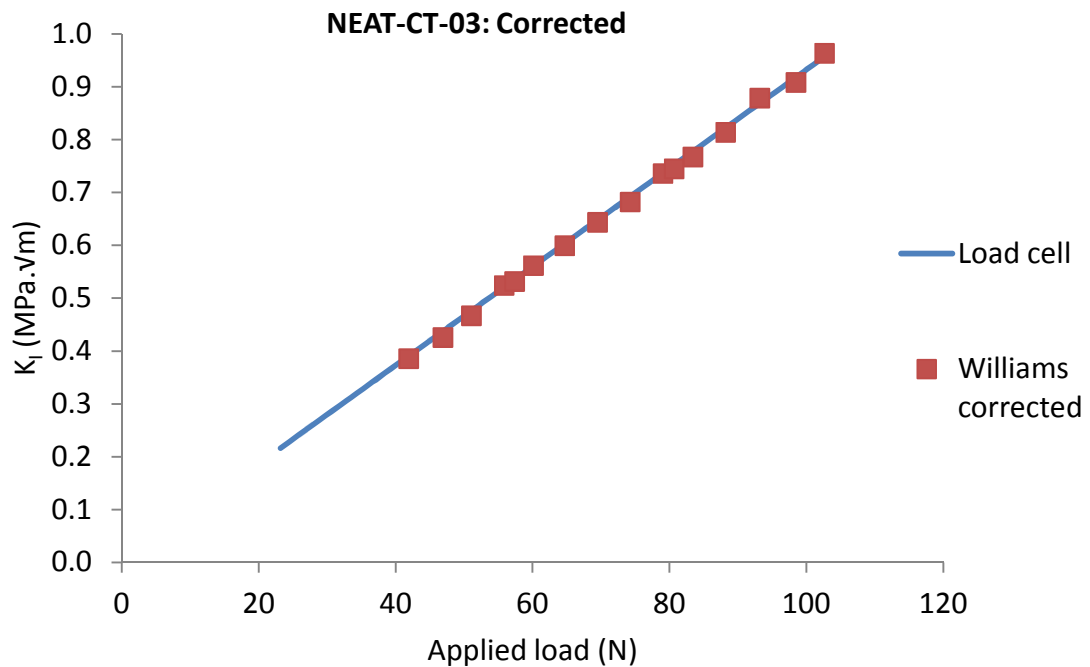
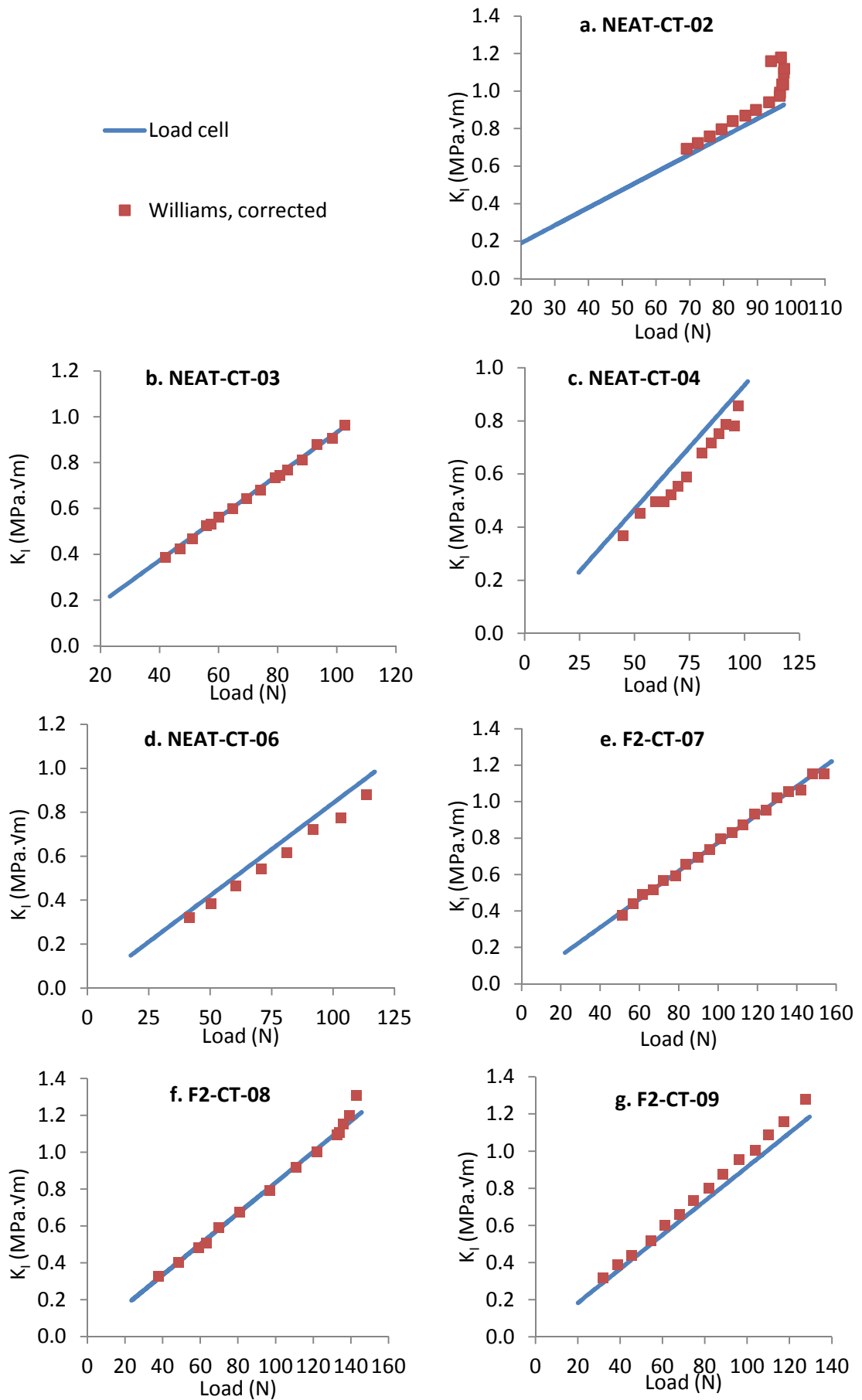
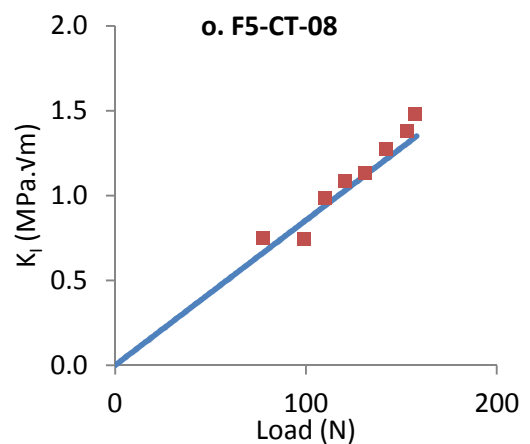
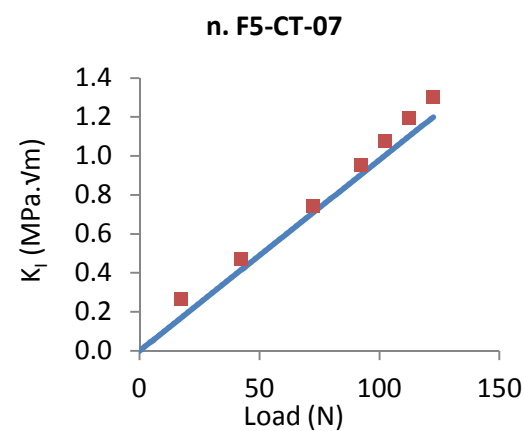
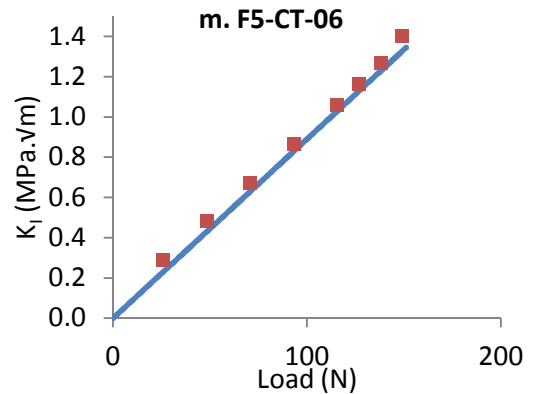
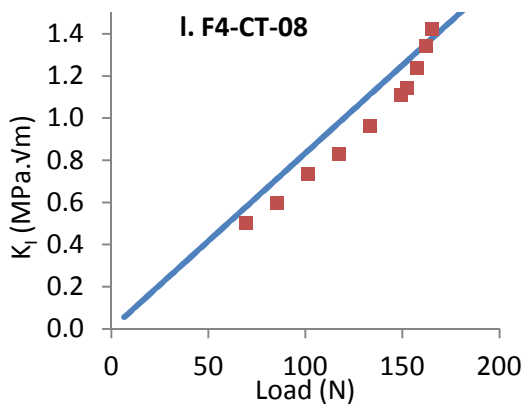
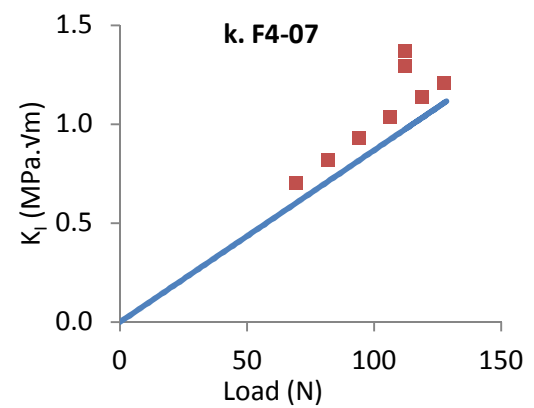
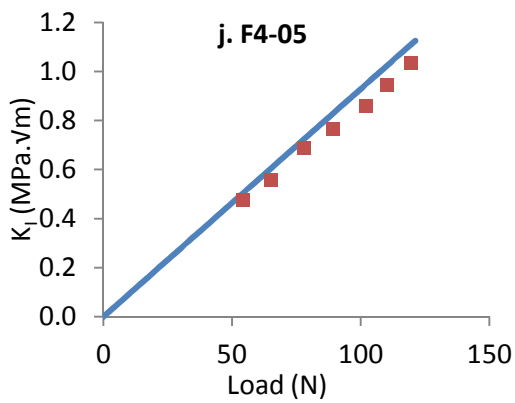
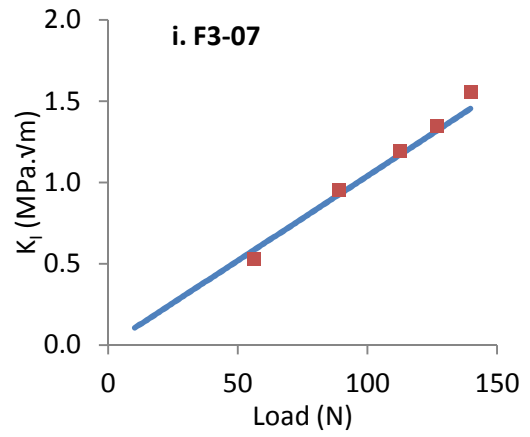
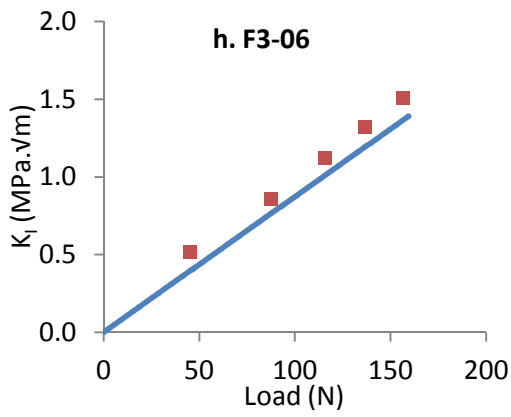


Figure 5.8 – Corrected Williams/DICITAC K_I values and British Standard load cell derived K_I values for specimen NEAT-CT-03

5.3.5 Stress intensity factor results

Stress intensity curves produced with the British Standard method, alongside corrected DICITAC-measured stress intensity values for fifteen specimens are shown in figures 5.9a-o.





Figures 5.9 – Stress intensity factors extracted using DICITAC alongside values determined with the standard method

As can be seen in figures 5.9a-o, the corrected DICITAC K_I values are generally very consistent throughout the duration of loading. In many of the specimens (figure 5.9c,d,h,j,k, and l) a small offset is apparent between DICITAC values and load cell values. This does not appear to be systematic; the DICITAC values are offset both above and below the load cell-derived values. It is possible that these offsets have been caused by inaccuracies in the load cell-derived method and could be caused by imperfect geometry. In the case of the F3, F4 and F5 specimens, the inaccuracy at small loads of the 100 kN Mayes load cell used could have a considerable effect on the accuracy of the standard method K_I values.

The reasons for some spurious DICITAC values toward the point of failure become more apparent when standard load method and DICITAC stress intensity values are plotted against frame number. For example, figure 5.9k shows disparity near the point of fracture in specimen CT-F4-07, which can be explained by the “pop-in” phenomenon that occurred in the specimen, clearly visible when the stress intensity values can be directly compared for each frame they were calculated for, shown in figure 5.10. Crack growth occurred after the pop-in point but the load cell stress intensity values have been calculated for original crack length.

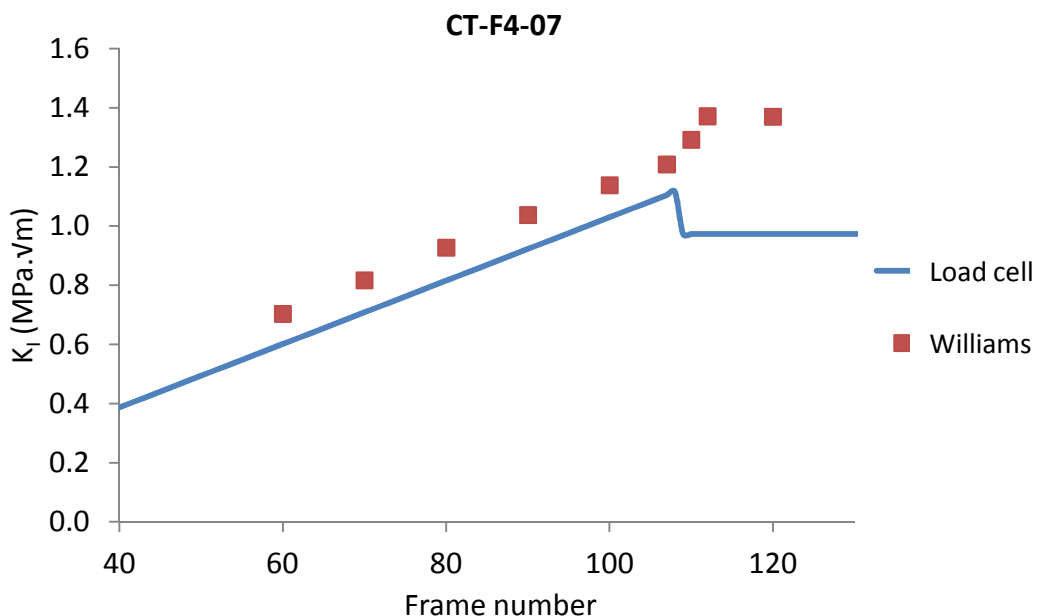


Figure 5.10 - Stress intensity factors plotted against frame number for specimen CT-F4-07 using both the Williams DICITAC method and the standard method, showing the discontinuity as crack growth occurs

Toward critical loads, specimens with crack growth result in disparity between load cell values and DICITAC values, especially apparent when both are plotted against load. An example of this disparity can be clearly seen in specimen NEAT-CT-02 (figure 5.11).

5.3.6 Crack growth in specimens

In all specimens cracks remained stationary until close to critical loading. Significant near-critical crack growth was seen in a number of pure mode I specimens of the NEAT resin and F4 formulations. In the F2, F3 and F5 formulations some damage progression was observed in some specimens.

Figure 5.11 shows the K_I values from the standard load method alongside the DICITAC determined K_I values for specimen NEAT-CT-02, in which significant crack growth was observed. For true comparative purposes, these data are presented relative to acquired frame number. This is equivalent to loading time in seconds (since the images were acquired at 1 Hz) and proportional to cross-head displacement.

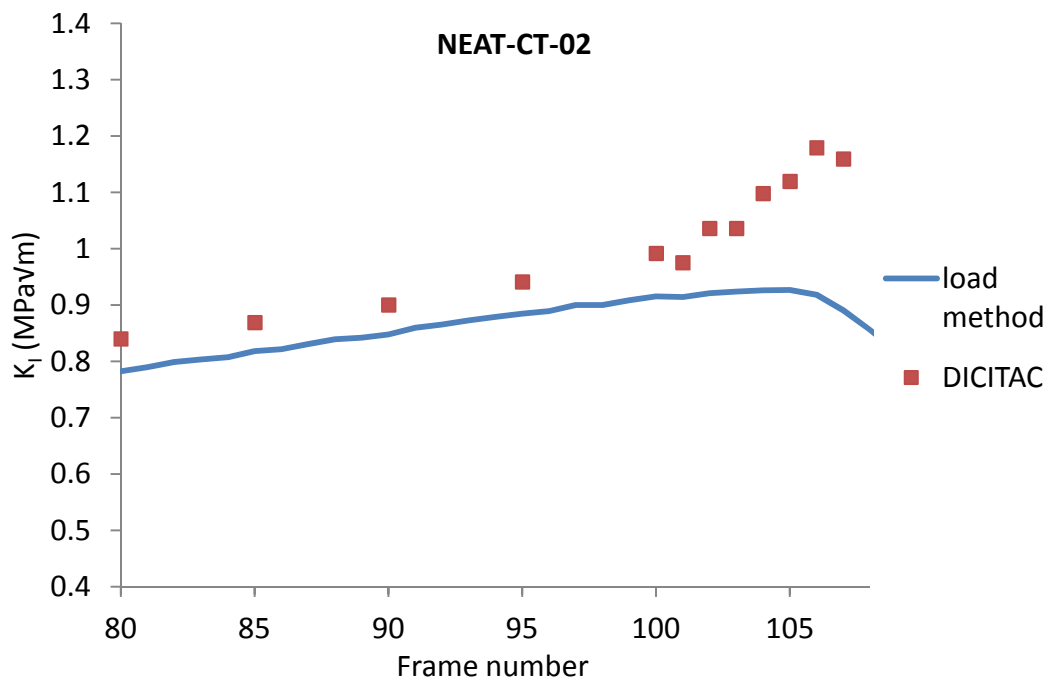


Figure 5.11 - K_I measured by load cell and DICITAC methods, plotted for individual frames; illustrating the effect of unstable crack-growth (crack begins to propagate unstably at frame 102)

There is a clear divergence between load cell K_I values and DICITAC K_I values after the onset of fast crack growth (at frame 102). The load cell values have been calculated for initial crack length only. The same is visible in the results for a number of other specimens including F2-CT-08 (fig 5.9f), F4-CT-07 (fig 5.9k) and F4-CT-08 (fig 5.9l), all of which also exhibited 'subcritical' crack growth. In figure 5.12, values of load cell K_I have been corrected for the increase in crack length, measured directly from the acquired digital images.

It can be seen that the specimen continues to support an increasing load after the fast crack propagation has begun (at frame 102), in which time the crack length was measured to increase by ~ 2.0 mm.

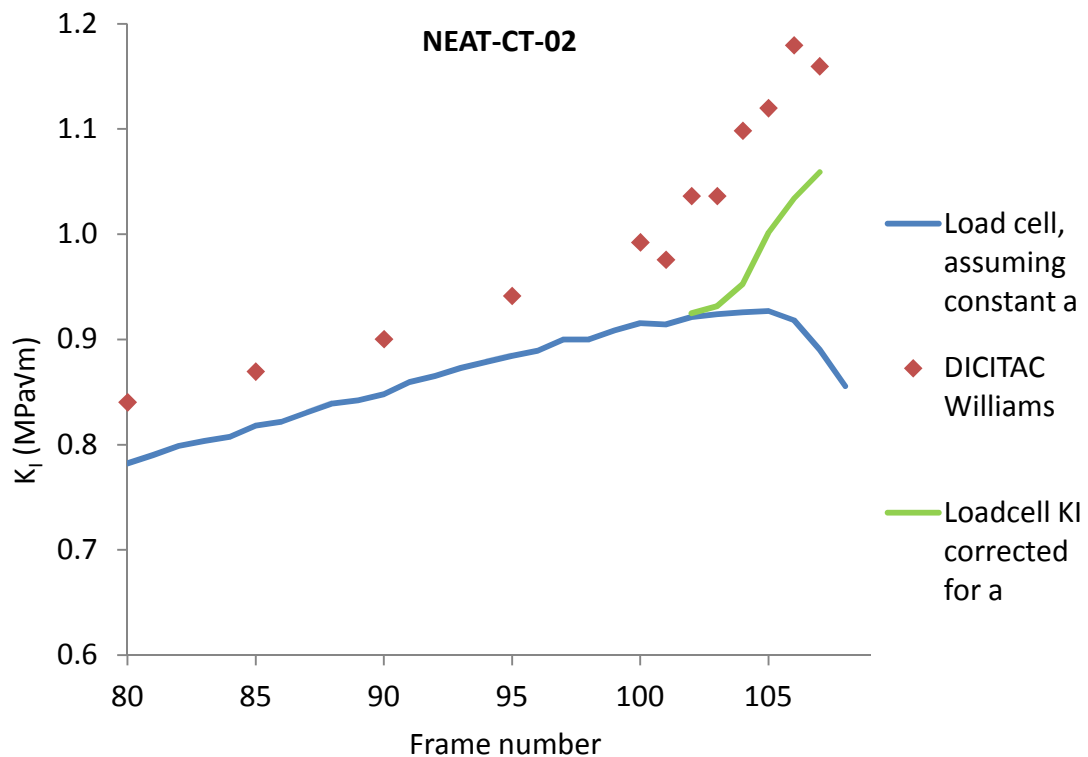


Figure 5.12 - K_I in NEAT-CT-02 measured by load cell and DICITAC methods, plotted for individual frames around a crack-growth event. A curve of load cell determined values, recalculated using measured instantaneous crack lengths has been added (lime green).

When the load cell data around the critical region is corrected for the increasing crack length, there is a close match between load cell and DICITAC determined

values for the duration of loading. However, these observations show a limitation of using the Williams or similar methods to measure critical toughness values in materials that exhibit unstable crack propagation prior to failure. Using a load-based measurement technique, without correcting for propagating crack length, gives a maximum K_I value at what is typically regarded as the material plane strain fracture toughness, K_{Ic} . Using the Williams technique gives no such obvious failure point, and it is clear that extracting a single stress intensity factor immediately prior to failure will not necessarily give a critical, static, stress intensity factor but instead a dynamic stress intensity factor.

It is clear that in the case of growing cracks, care must be taken to ensure appropriate stress intensity factors are measured and recorded as ‘critical’.

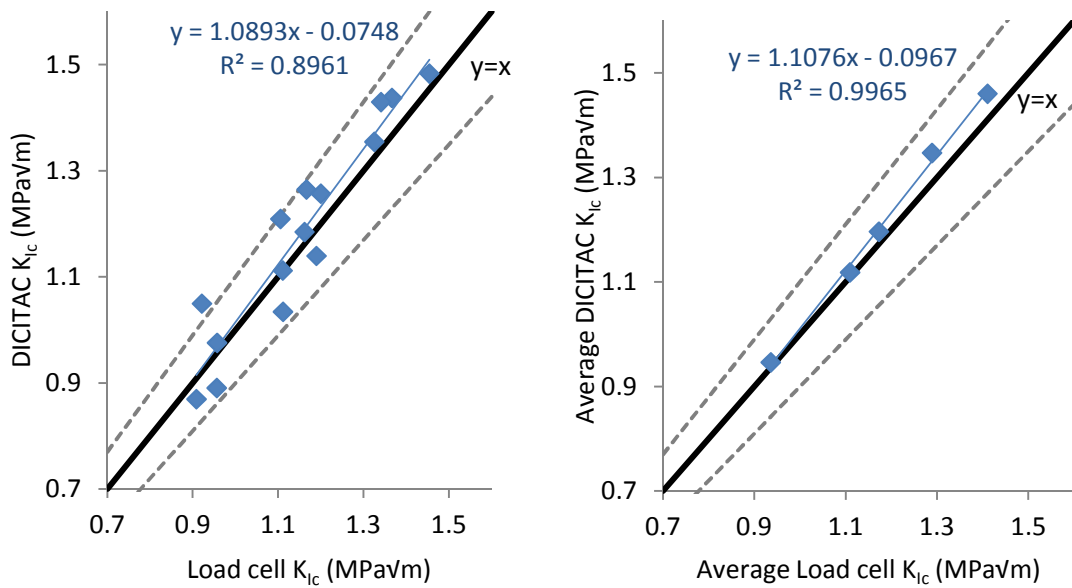
5.3.7 Measuring K_{Ic} with DICITAC

Values of K_{Ic} immediately prior to failure (where failure includes the onset of unstable crack propagation) have been isolated from the K_I values extracted from the displacement fields for the specimens tested using DICITAC, and subsequently corrected for the initial strain condition. These values, the average for each material, and the standard deviations and standard errors are presented in table 5.8.

Table 5.8 – Material average K_{Ic} values determined using DICITAC

Material	DICITAC K_{Ic} (MPa√m)	Standard deviation (MPa√m)	Standard error (MPa√m)
NEAT	0.946	0.052	±0.030
F2	1.196	0.072	±0.036
F3	1.460	0.023	±0.016
F4	1.118	0.072	±0.041
F5	1.347	0.071	±0.041

Figure 5.13 shows a comparison between the DICITAC-measured values of K_{Ic} and the load cell measured values. A line showing $y = x$ with an error boundary of ±10% has been added to the graph.



a. All specimens

b. Average for each material

Figure 5.13 – Comparing DICITAC and Load cell measured values of K_{Ic} . Solid black line marks $y = x$, dotted lines are $\pm 10\%$. Linear regression lines are shown.

The data in figures 5.13a-b show the individual critical values measured by DICITAC to be mostly within $\pm 10\%$ of the load cell values. The load cell values measured here are being considered as perfect values; however, these are subject to their own significant errors in measurement arising from load cell inaccuracy and inaccuracy in measuring the specimen width, thickness and crack-length. Average values can be seen to be equivalent to load cell measured values. This result gives confidence in using this method in more challenging situations such as mixed-mode loading, where the ‘standard’ load-based methods of measuring fracture parameters are less reliable.

5.4 T -stress

T -stress values were extracted from the DIC displacement fields using DICITAC at the same time as stress intensity factor extraction. The first set of CT specimens tested (NEAT and F2) were subject to the same non-zero initial strain state problem as the compact tension specimens. This was corrected for. A comprehensive comparison with theoretical values and the effect of constraint was performed and is presented in section 5.5.

5.4.1 *T*-stress correction

A correction for the zero-strain offset was carried out on the *T*-stress data. However, instead of adding an offset based on the analytic T/σ value at the preload, the *T*-stress at the initial frame was determined entirely from the uncorrected *T* values measured at a number of points throughout loading.

From the principle of superposition of elastic strains (as used for the *K* value correction), and the knowledge that T/σ is constant throughout the course of loading of a specific geometry [53, 125], the *T*-stress can be corrected for non-zero initial strain. The uncorrected *T*-stress values were plotted against load cell load. The values can be seen in figure 5.14 to form a straight line, proportional to applied load with a *y*-intercept offset. Since T/σ can be considered constant, a correct *T*-stress against load curve for a compact tension specimen can be expected to extend linearly towards the origin.

Manipulating the *T*-stress data so that it follows this involves taking the *y*-intercept *T*-stress value from the linear regression curve and subtracting it from the raw *T*-stress values. The intercept of the linear regression curves has been calculated using Microsoft Excel's `=intercept()` function. This process is illustrated in figure 5.14 and figure 5.15.

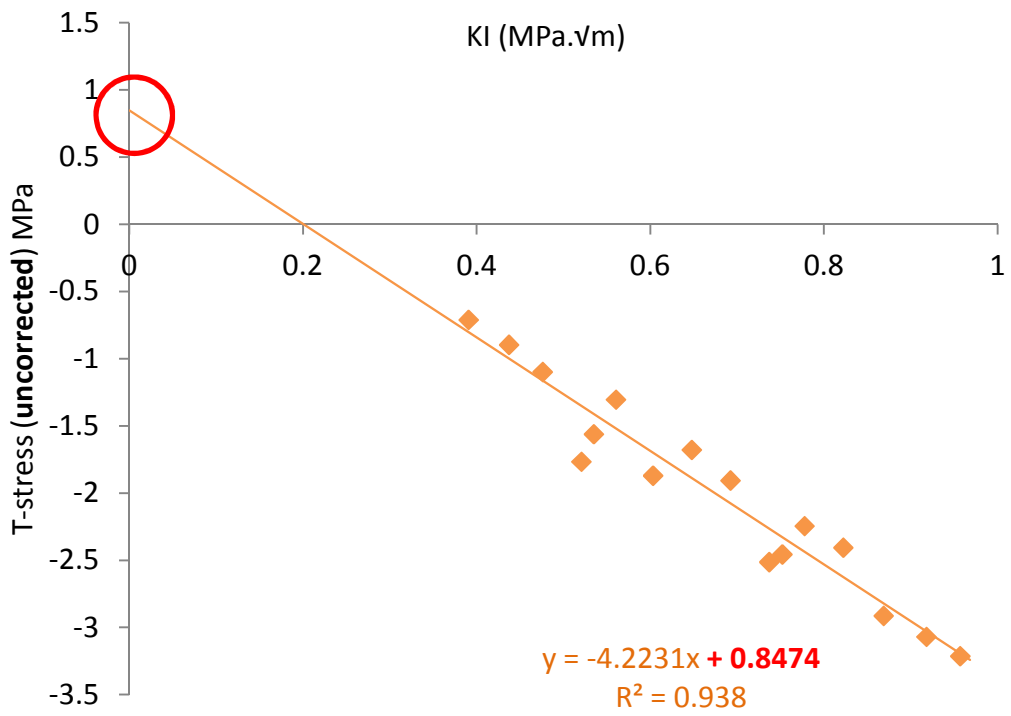


Figure 5.14 – Uncorrected T -stress values for specimen NEAT-CT-03

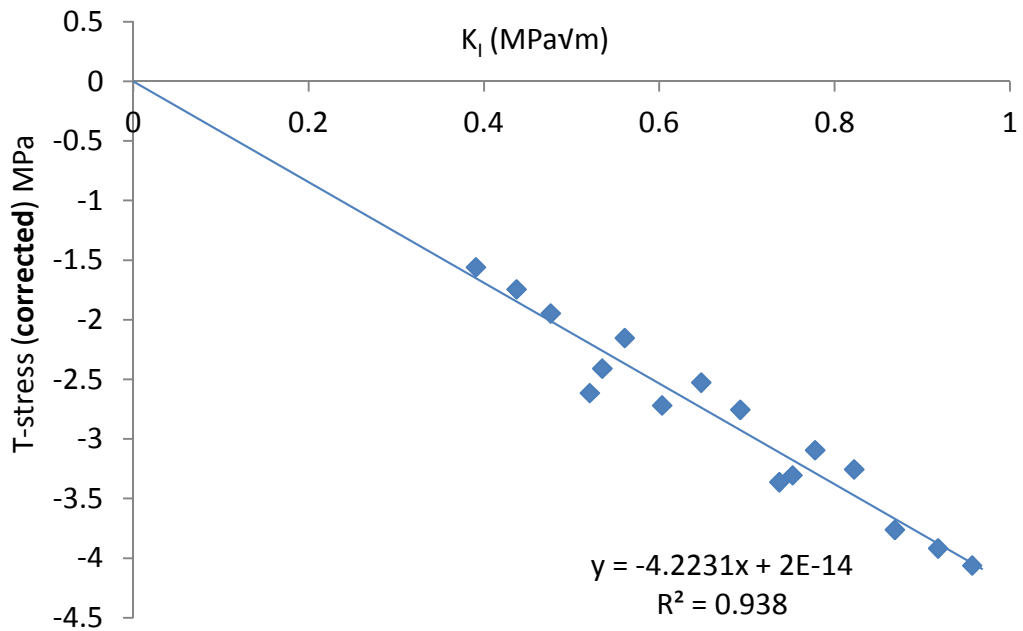
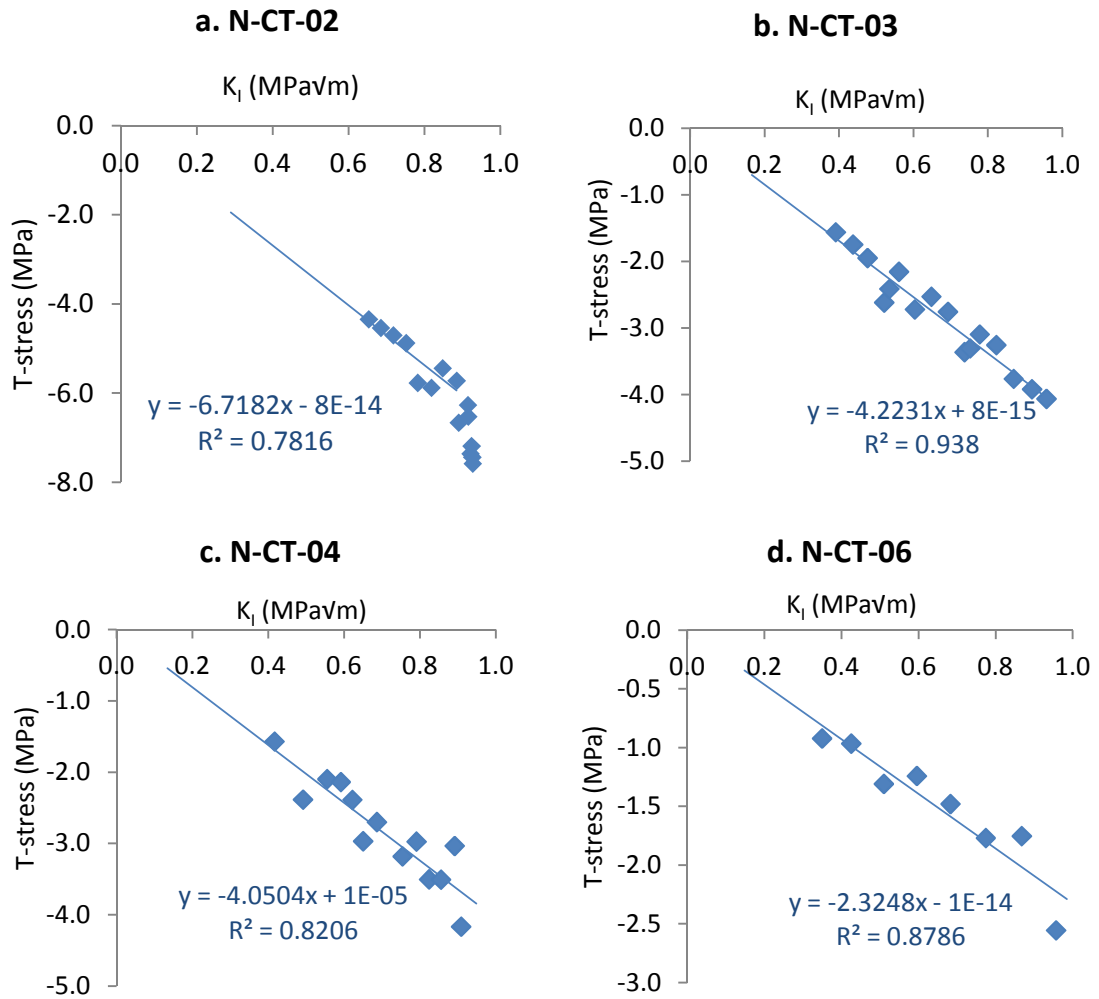


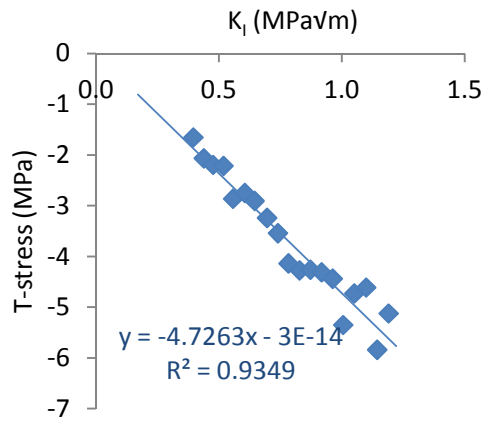
Figure 5.15 – Corrected T -stress values for specimen NEAT-CT-03

5.4.2 Corrected T -stress values

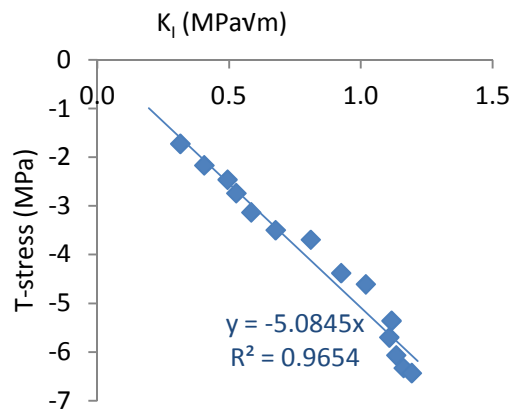
The following figures 5.16a-o show the corrected T -stress values determined throughout loading for the specimens tested. In the instance of crack growth (such as in specimen N-CT-02), the region of crack growth has been excluded from the linear regression used for T -stress correction.



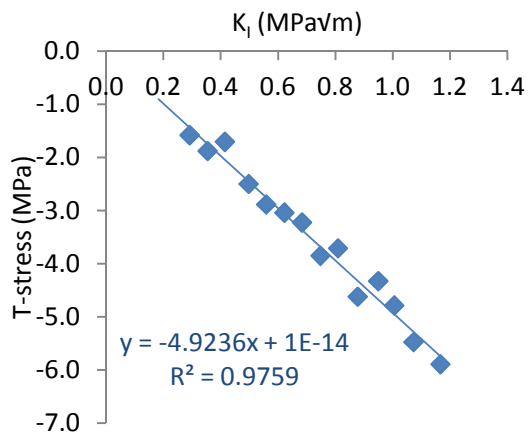
e. F2-CT-07



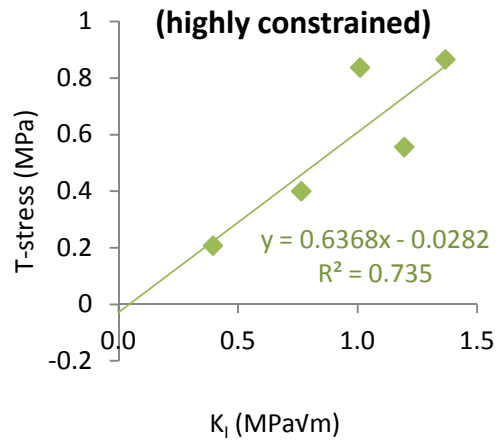
f. F2-CT-08



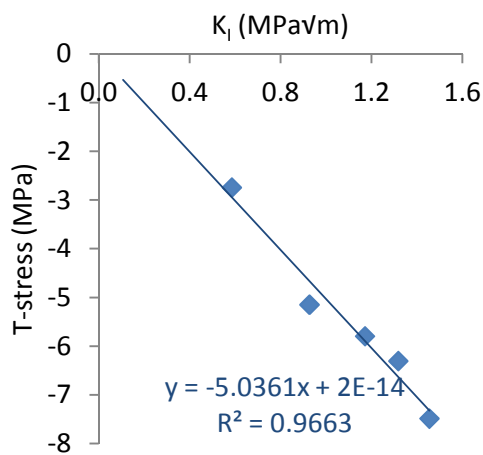
g. F2-CT-09



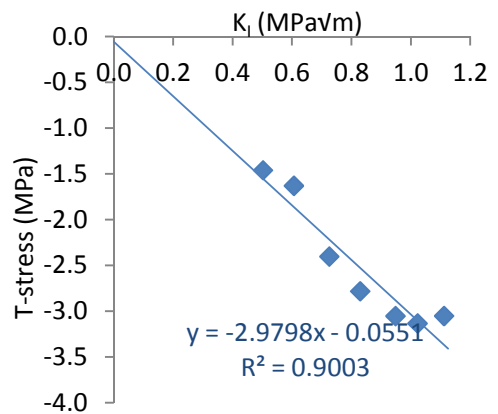
h. F3-CT-06



i. F3-CT-07



j. F4-CT-05



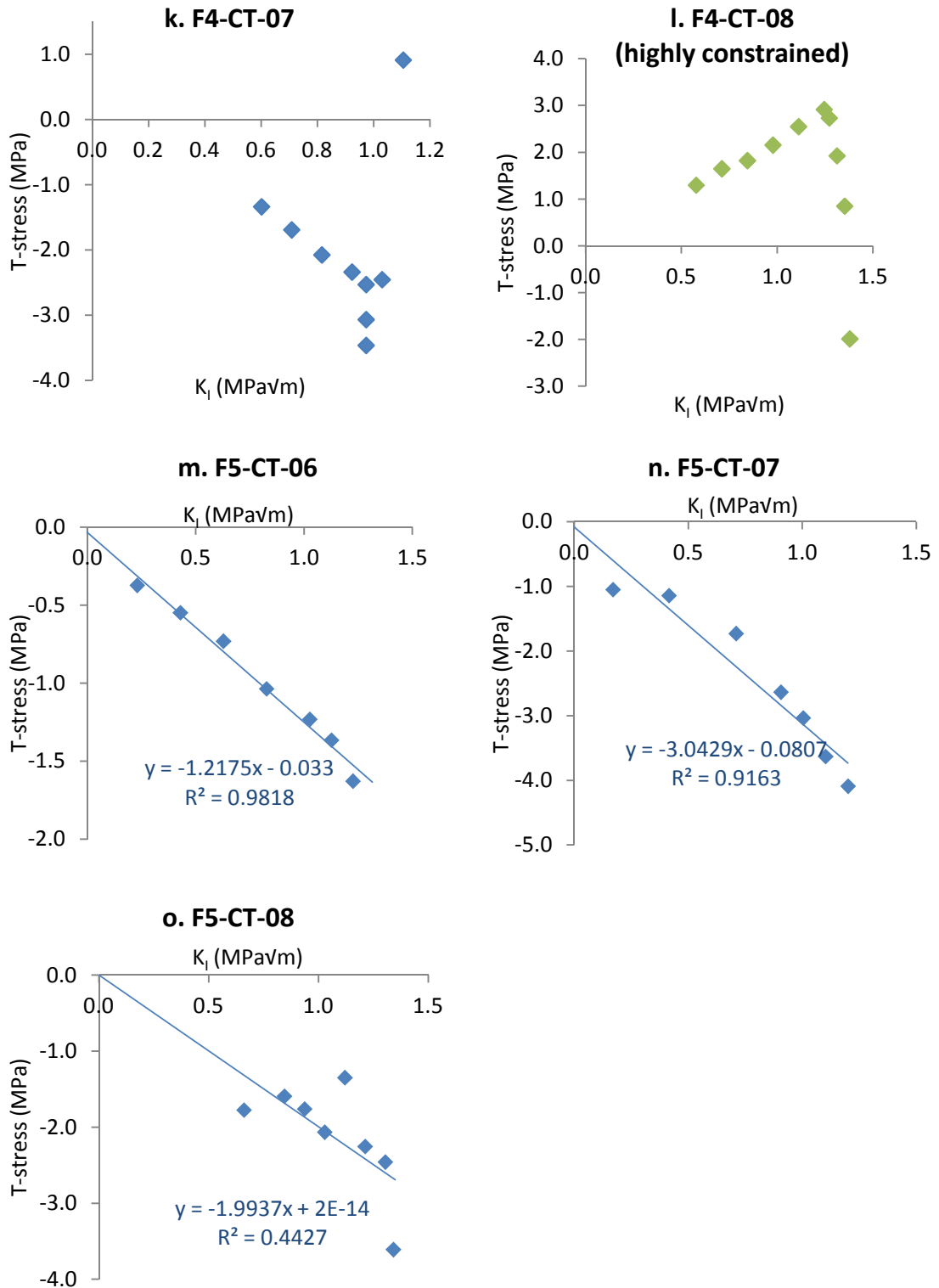


Figure 5.16 – Corrected T-stress values for all specimens

Generally, it can be seen that T -stresses increase (in magnitude) linearly as applied load is increased. There are however, a number of specimens in which sudden

discontinuity is observed around critical loading. Crack growth appears to considerably change the measured value of T -stress.

Almost all of the T -stress values presented here are negative. The tabulated data for T -stresses in compact tension specimens all define positive values of T -stress. This issue is examined in close detail in section 5.5.

5.4.3 Determining T/σ_0

T/σ is a function of a/w and so direct comparison only makes sense for specimens of equivalent crack length.

Applied stress σ_0 can be defined using equation 5.6. T/σ has been determined by multiplying the least-square linear regression of T -stress values against (load cell derived) K_I by $\sqrt{\pi a}$, in equation 5.7.

$$\sigma_0 = \frac{K_I}{\sqrt{\pi a}} = \frac{f(a/w)P}{t\sqrt{w\pi a}} \quad (5.6)$$

where all variables have their normal meanings; $f(a/w)$ is the shape function as defined in BS ISO 13586, P is load, t is specimen thickness, w is specimen width (as defined in figure 2.13b) and a is crack length.

$$T/\sigma = \frac{\Delta T}{\Delta K_I} \sqrt{\pi a} \quad (5.7)$$

Values of T/σ for all specimens are presented in table 5.9. Note the two positive values of T/σ (marked with an asterisk) that coincide with high loading constraint. The validity of these values is discussed in the next section.

Table 5.9 – T/σ (averaged throughout loading) for all specimens. Specimens with high constraint are marked *

Specimen	T/σ	Standard deviation
N-CT-02	-2.50	0.22
N-CT-03	-0.803	0.061
N-CT-04	-0.775	0.081
N-CT-06	-0.434	0.047
F2-CT-07	-0.898	0.067
F2-CT-08	-0.985	0.064
F2-CT-09	-0.975	0.070
F3-CT-06*	0.030	0.007
F3-CT-07	-0.888	0.051
F4-CT-05	-0.573	0.051
F4-CT-07	-0.510	0.086
F4-CT-08*	0.436	0.014
F5-CT-06	-0.254	0.033
F5-CT-07	-0.557	0.063
F5-CT-08	-0.388	0.062

5.5 Comments on the validity and accuracy of the T -stress results

The T -stress values measured in this study for CT specimens do not agree with those in the literature. Tabulated results by Sherry et al. [53] and by Fett [126] using various methods both show T/σ values in compact tension specimens to be roughly proportional to a/w , and more significantly, are positive.

Whilst Sherry's study presents these values with little comment on their derivation, the more recent work by Fett identifies and comments on differences in analytic values obtained using different boundary conditions, especially for small values of a/w .

Both works agree that T/σ for semi-infinite edge-cracked plates under uniform, uniaxial tensile stress is around -0.6. Sherry *et al.* lists values for finite width plates and presents work from a number of studies, all of which agree T/σ is around -0.6 for square specimens with values of a/w between 0.2 and 0.5. The consideration

which appears to cause the debate in T -stress values in CT specimens is the bending moment caused by the loading pins.

In this study, two different pin/grip arrangements were used which resulted in positive and negative measured T -stress values. The British Standard requires that specimen loading pins are free to rotate (*“the loading pins and holes shall be smooth and a loose fit to minimize friction”*) and grips to be ideally self-aligning to ensure that specimens can align themselves to a direction of pure tension [1]. Specimens with this arrangement were found to fail with stable crack paths (figure 5.17a) and T -stresses were measured as negative. Specimens F3-CT-06 and F4-CT-08 were tested with more rigid grips and tested with tighter fit loading pins. These were found to fail with unstable crack paths (figure 5.17b) and T -stresses were measured as positive.

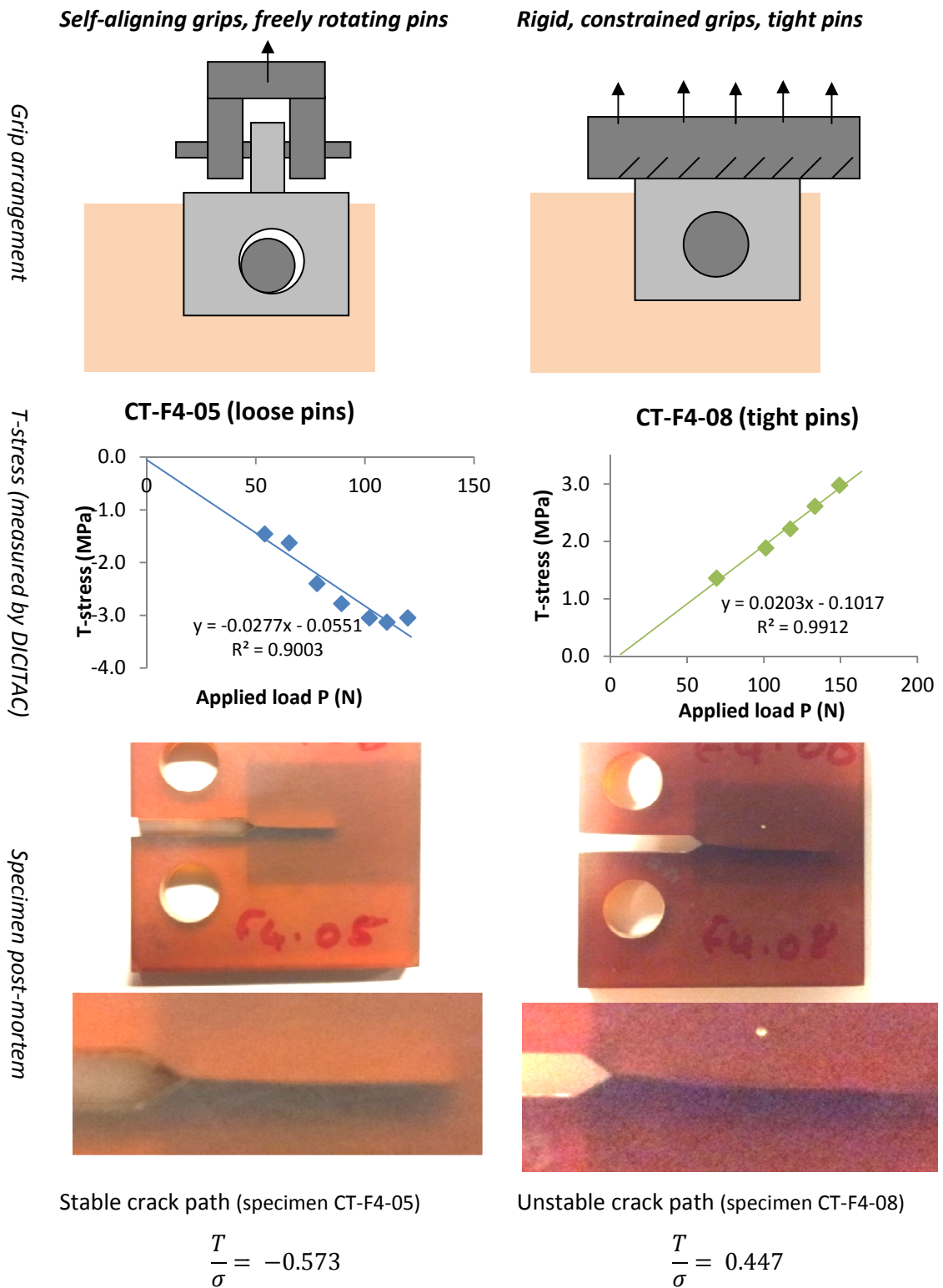


Figure 5.17 - Crack path stability variation with specimen grip arrangement

The T/σ value for the loose pinned, low-constraint specimen CT-F4-05 is -0.573 . This value is typical of the similarly constrained specimens tested and is extremely close to the theoretical values [53, 125, 126] for an equivalently sized edge-crack in a finite width plate subject to uniform uniaxial tensile load.

Theoretical values were calculated from the tabulated data presented in the recent compendium of T -stress values by Fett [125] which presents data from Kfourir, Cotterell and Leever & Radon as well as his own. Data is tabulated in terms of $\beta_T(1 - \alpha)^{1/2}$ where β_T is the biaxiality ratio and α is the ratio a/w :

$$\beta_T = \frac{T\sqrt{\pi a}}{K_I} = \frac{T}{\sigma} \quad (5.8)$$

The data itself is reproduced in figure 5.18.



Figure 5.18 – Taken directly from Fett’s compendium of T -stress results [125].

The T/σ value for the tight-pinned, highly-constrained specimen CT-F4-08, determined using DICITAC, is $+0.447$. Reading values from Fett’s compendium gives $\beta(1 - \alpha)^{1/2}$ values of 0.35 and 0.28 for the results Fett compiled from the literature and from Fett’s method respectively. At a measured α value of 0.352 , this $\beta = T/\sigma$ is 0.434 and 0.347 for the respective methods.

The DICITAC T -stress of 0.447 compares closely to the tabulated theoretical values of T/σ for compact tensions specimens of 0.434 or 0.347 depending the source of the tabulated data.

Interestingly, an earlier compendium from Sherry *et al.* lists significantly higher T/σ values of between 2.0 and 3.0 for equivalent values of α (reproduced as figure 5.19).



Figure 5.19 – T -stress results from Sherry *et al.* [53].

Fett's compendium describes T -stress values as being calculated "*for a standard CT specimen loaded by point forces*". It also states "*it has to be noted that the results in Fig. C16.2a [reproduced here as figure 5.18a] were not derived for the standard CT specimen with large holes... the T -stress was determined by applying of shear tractions along the loading line and by application of point forces in the centres of fictitious holes. In Fig C16.2b [reproduced here as figure 5.18b] the test specimen...was modelled with point forces to be active at the contact points*".

A noticeable difference between the two loading scenarios used is the crack path, shown in figure 5.17. The nature of the crack paths fits with the findings of Cotterell [47] for the measured values of T -stress for each scenario.

It seems clear from the multitude of physical phenomena that support the measured values of both positive and negative T -stress that there is considerable difference between levels of constraint in the boundary conditions applied to measure T -stress values and between levels of constraint that can occur in a laboratory setting. Performing a comprehensive parametric study of the effect of loading pin size and

variation in typical specimen constraint in test specimens is beyond the scope of this project.

Once the issue was identified and confirmed by testing with tighter-fitting pins, the remaining (CT) tests were performed using the original, loose-fitting pins for consistency. The measured K_{Ic} values appeared unaffected by the differing constraint. This is supported by the analytical work of Smith *et al.* [54] in which they found that measured K_{Ic} was fairly insensitive to applied T -stress, whereas K_{IIc} was found to be strongly affected.

It is reiterated that the pins used were thought to be chosen in compliance with the British and International Standard for determination of fracture toughness in plastics (BS ISO 13586 [1]). This defines hole size only and requires holes and pins to be “smooth and a loose fit”, which the undersized 7.2 mm diameter pins certainly were in the specimens 8.0 mm diameter holes.

The equivalent standard for metals (BS 7448-1:1991 *Fracture mechanics toughness tests, K_{Ic} determination in metals* [127]) defines dimensions more explicitly. Specimen holes are to be $0.25w$, pin diameters $0.24w$, and the clevis hole at least $0.26w$ (where w is the specimen width).

The complete lack of agreement with tabulated T -stress values is of some concern. However, the physical behaviour of the specimens including: the shape of the strain fields from DIC; stress fields from brief photoelastic analysis; post-mortem analysis of the crack paths and experimentation with differently constrained systems; all imply that the measured negative values are valid and correct.

The accuracy of the measured values is difficult to assess. Measured T -stress values have been previously shown to be not in close agreement with theoretical values [120]. Reasons typically attributed to this are twofold; firstly, the T -stress, being a second order, ‘small’ term is relatively more difficult than singular stress intensity factors to measure accurately. Secondly, small deviations in real geometry from the idealised case (such as crack angle, consistency through a specimen, sharpness and accuracy of loading direction and load-paths) are thought to have a significant effect

on the actual T -stress value [120], and so a true comparison between theoretical and measured values is inherently difficult. However, T -stress measurements have been extracted using the Williams solutions using thermoelastic stress analysis measurements to within $\pm 2\%$ theoretical values [113] and so it is suspected that it is unfair to blame the accuracy of the DIC method on inherent specimen imperfections.

The huge differences in T -stress caused by varying the pin size shows how sensitive the T -stress is to loading conditions; however, when constraint was kept the same, results appear to be comparable. The documented [112] accuracies found in real specimens tested using DICITAC with standard metallic specimens quoted accuracies of $\pm 15\text{-}35\%$ for T -stress determination for individual frames. It is thought that this represents a conservative assessment of the accuracies. Averaging T -stress results across a number of points through loading is hoped to minimise scatter and improve the accuracy of the method.

A complication of the non-zero initial strain condition in the CT tests is that in order to correct the T -stress values by the linear regression offset method, significant extrapolation back to zero-load is necessary and so this correction can cause a significant systematic measurement error. However, since the value of T/σ has been measured using the slope of the T -stress against K_I least squares regression line, the absolute accuracy of the T -stress values is not required for T/σ measurements.

Ultimately, it appears clear that the T -stress has not often been measured experimentally and theoretically derived values are extremely sensitive to boundary conditions. Any direct measurements of the T -stress add to the body of knowledge on this topic. The results of this chapter show that it is easy to inadvertently load specimens with different levels of constraint, despite supposedly following standards. Lessons learned regarding the constraint of specimens will be applied to the mixed-mode tests described in chapter 6.

5.6 Error analysis

5.6.1 Out of plane displacement: Poisson contraction

A simple Finite Element Analysis (FEA) was performed using ANSYS to assess the effect of out-of-plane displacement due to the contraction in the specimen. A simplified compact tension specimen geometry was created (the deformed specimen can be seen in figure 5.20), with a sharp notch replacing the crack. This was meshed using 8-node blocks. A thickness of 4.5 mm was chosen. The mesh was refined around the crack tip. Linear elasticity was assumed, with a Young's modulus of 3.1 GPa. The lower pin was constrained and a 150 N load was applied, split between nodes on the upper pin-hole. The out-of-plane strains ϵ_{zz} (where the z-axis is in the positive direction, facing out of the page) were calculated; results are shown in figure 5.20.

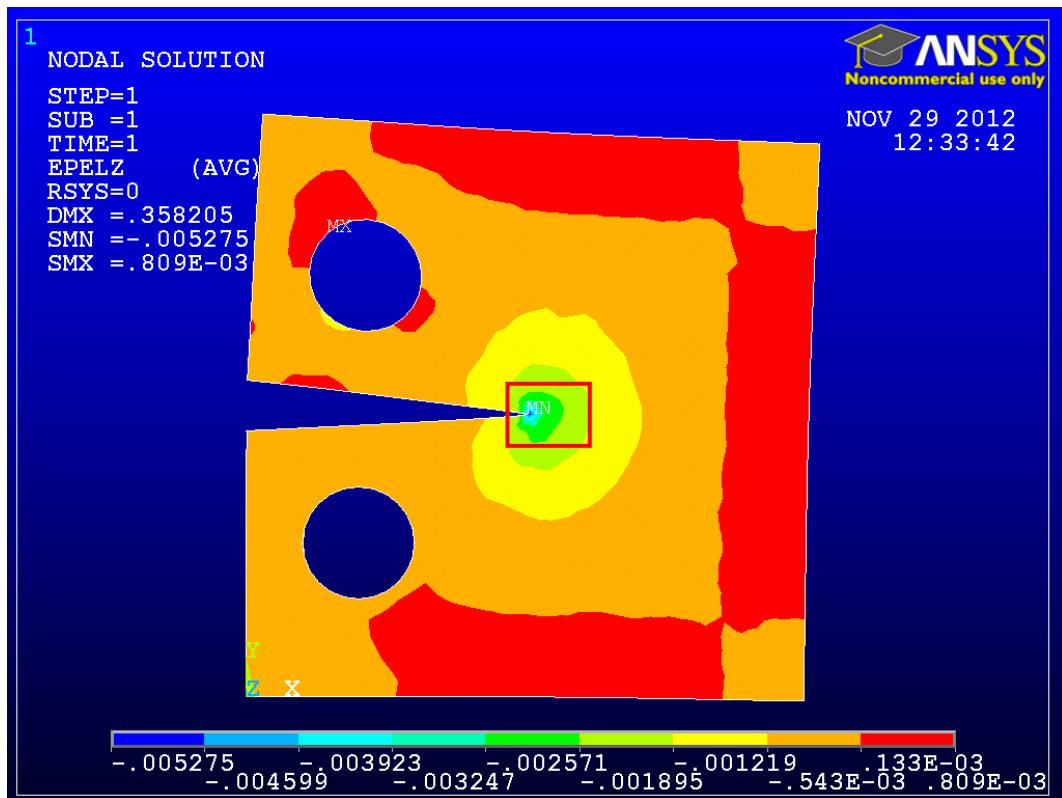


Figure 5.20 – ϵ_{zz} in a compact tension specimen (subjected to 150 N) determined using finite element analysis. The DIC field of view is overlaid with a red rectangle.

The maximum out-of-plane strain, ε_{zz} of a 4.5 mm thick compact tension specimen under typical failure load (150 N) is shown in figure 5.20. The out of plane strains over the 6.0 x 4.5 mm field of view range almost entirely between -0.0019 and -0.0030, considering a thickness of 4.5 mm, this corresponds to an out of plane contraction of between 8.55 μm and 22.1 μm .

Using equations 5.9, which will be introduced properly in the following section, this corresponds to an expected strain error of between 93 $\mu\varepsilon$ (0.009%) and 240 $\mu\varepsilon$ (0.024%).

After the test programme had been completed, one 3D-DIC test was performed on a F5 CT specimen (F5-CT-3D01) with Rob Wood from GOM as a site demonstration with the view to purchasing a system. The measured out-of-plane displacement field is reproduced in the appendix as figure 11.2. Measured displacements can be seen to be in close agreement with those analytically predicted.

5.6.2 Out of plane displacement: Rigid body motion

The most significant variation in z-displacement experienced would be due to rigid body out-of-plane motion which could feasibly be an order of magnitude higher than caused by ε_{zz} discussed in section 5.6.1.

The very narrow depth of field of the diffraction-limited, f/4.5 Navitar PreciseEye lens system used is quoted in the manufacturers brochure as 0.10 mm [122]. Focusing the lens, connected to the LaVision ProX camera, onto a speckled surface, and varying the z position of the camera using a micrometer stage showed focus to be noticeably affected at this distance. A translation of 0.5 mm resulted in grossly inadequate, blurred images. Assessing the focus of the start and end frames of the tests shows the rigid body displacement in the z-direction can be estimated as being within 0.1 mm.

Sutton et al. [128] showed strain error from out of plane displacement to be approximately equal to the out of plane displacement ΔZ divided by the object distance (i.e. the distance between object and lens), as shown in equation 5.9. For

positive ΔZ , i.e. out of plane motion away from the camera, negative strains are experienced. The working distance of the lens (i.e. distance between the front of the lens system and the focal plane) was measured as 92 mm. This is a worst-case measurement for Z since the centre-plane of the lens is approximately 10 mm behind this and so the true value of Z is likely to be ~ 100 mm.

$$\varepsilon_{ij_{false}} \approx -\frac{\Delta Z}{Z} \quad (5.9)$$

The Williams stress solutions show stress intensity factors to be directly proportional to strain, indeed this was exploited in the zero-strain correction presented in section 5.3.4. The strains in specimens at $1.0 \text{ MPa}\sqrt{\text{m}}$ from a distance of 0.6 mm from the crack tip ‘singularity’ have been measured as ranging from around -0.2% to 0.4% for ε_{xx} and 0.05% to 1.2% for ε_{yy} for a number of compact tension specimens in pure mode I. Considering the higher strains of the y -axis, the addition (or subtraction) of the $\pm \varepsilon_{false}$ out-of-plane error therefore can be assumed to be approximately $K_{error} \approx \frac{\Delta Z}{92} \times \frac{1.0 \text{ MPa}\sqrt{\text{m}}}{0.012}$. Values of estimated K_{error} at $K_{I_{true}} = 1.0 \text{ MPa}\sqrt{\text{m}}$ have been tabulated below for various out-of-plane displacements in table 5.10.

Table 5.10 – Errors due to out-of-plane displacement

Out of plane displacement ΔZ (mm)	ε_{yy} error	DICITAC stress intensity error ($\pm \text{MPa}\sqrt{\text{m}}/\text{MPa}\sqrt{\text{m}}$)	Optical notes
0.011	1.19e-4	0.010	No noticeable effect on image
0.025	2.72e-4	0.023	
0.05	5.43e-4	0.045	
0.1	1.09e-3	0.091	Noticable reduction in focus
0.2	2.17e-3	0.181	Significant loss of focus
0.5	5.43e-3	0.453	Severe loss of focus

The very short depth of field of the optics gives confidence that out of plane motion was under a conservative 0.2 mm.

5.6.3 Errors induced by DIC algorithms

Error caused by inaccuracy in correlation is difficult to measure since it is dependent upon a number of factors, not least the quality of the speckle pattern itself. Consequently it is difficult to quantify the accuracy of the algorithms with any certainty.

As a rough indicator of the level of accuracy of the effect of the algorithms used, a (compact tension) specimen was loaded to $K_I = 0.77 \text{ MPa}\sqrt{\text{m}}$ (84% of the fracture toughness of the base resin) and unloaded, and strain fields determined in the unloaded position. The loading curve is shown in figure 5.21. In an unloaded state in an elastic material, clearly a zero-strain state should exist, however this test was also performed to identify levels of subcritical plasticity. This was repeated at a non-zero strain state by measuring the strain difference between two loaded positions. The green markings on figure 5.21 show the frames used to measure unloaded strains, and the red markings show the frames used to measure relative strains between two loaded strain states.

For the unloaded case, the displacement fields u and v , (displacement in x and y directions respectively), measured by DIC are shown in figure 5.22 and the measured strains, separated into ε_{xx} and ε_{yy} are shown in figure 5.23. Measuring residual strains at zero load with finite displacement is a typical method of analysing a particular DIC arrangement commonly found in the literature, including being a favoured method of Sutton *et al.* [92].

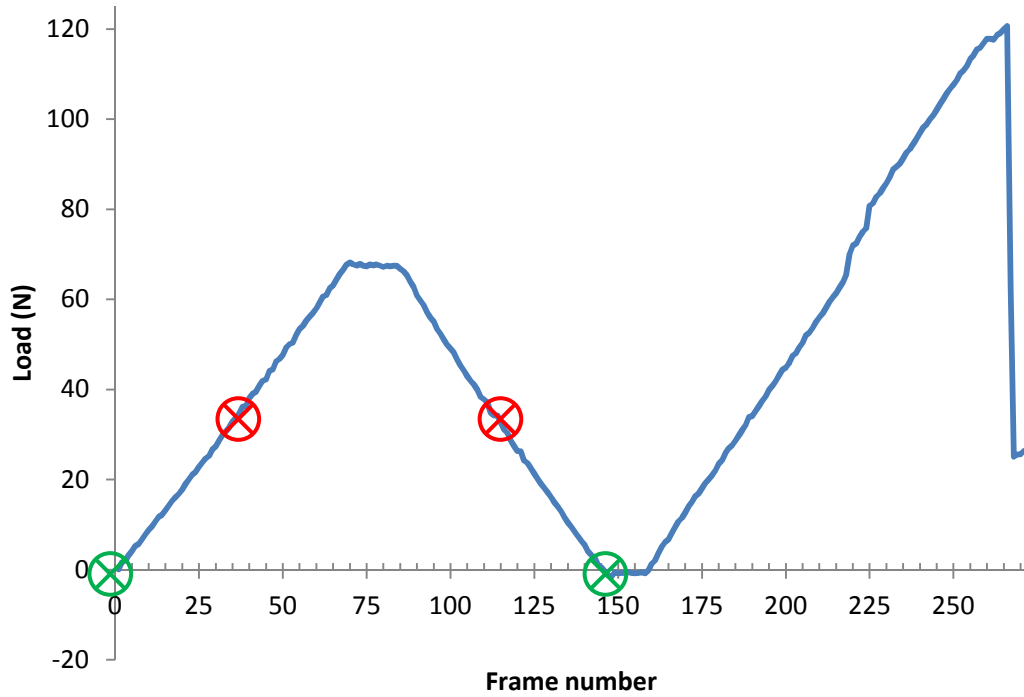
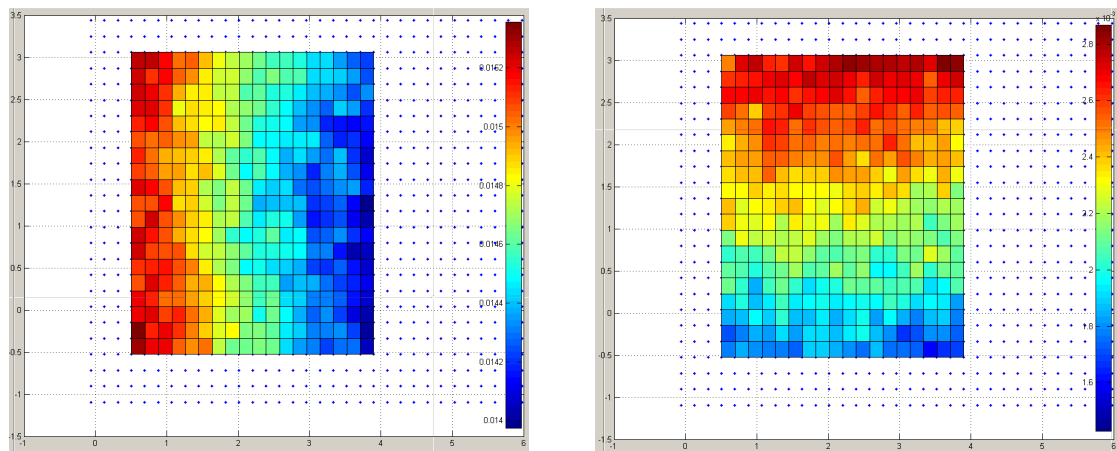


Figure 5.21 – Specimen F2-CT-08 loading curve. Loading positions used for the strain error analysis are highlighted.



u [Scale bar: 14.0 to 15.3 μm]

v [Scale bar: 1.6 to 2.8 μm]

Figure 5.22 - displacement fields from an unloaded frame after subcritical loading and subsequent unloading. Fields of view are equivalent to those used for parameter extraction (section 5.3.1)

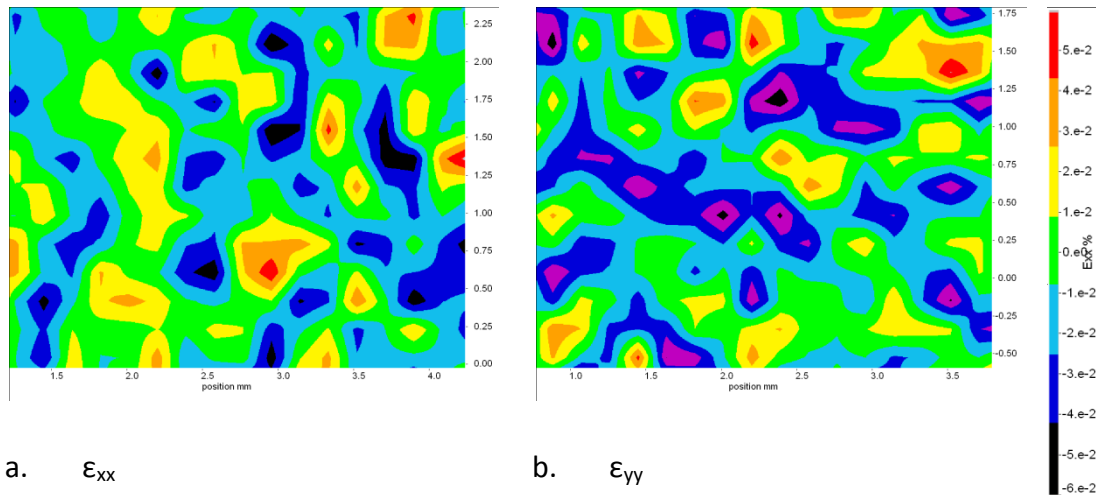
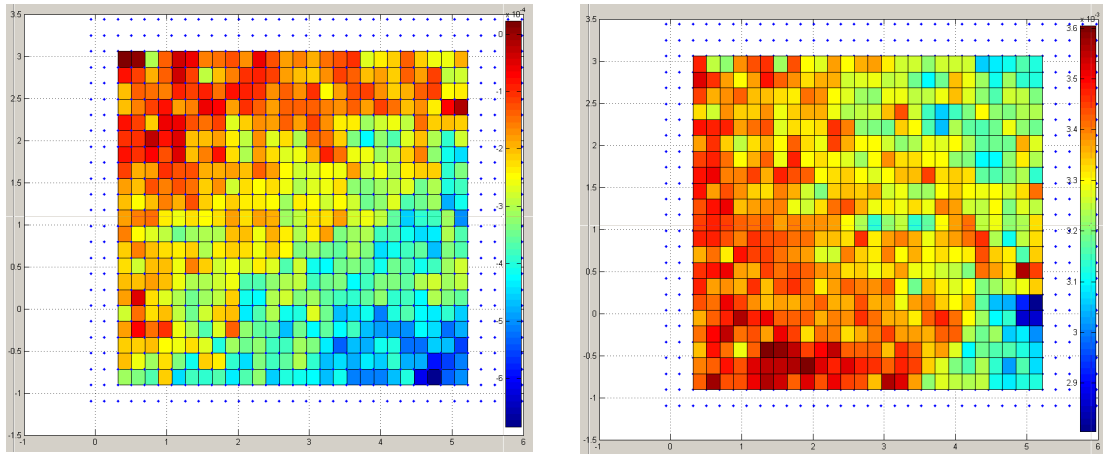


Figure 5.23 - Strain difference between two unloaded frames, separated by subcritical loading and unloading, in a.) x and b.) y directions. Scale bar $\pm 0.06\%$.

Displacement field data are shown in figures 5.22. The displacement field data shows a clear bias. It is suspected that, as the specimen became strain-free, it was able to move out-of-plane, thus exhibiting a systematic strain error. It is worth pointing out that the overall displacement discrepancy between the minimum and maximum values is under 0.3 pixel lengths in this case (one pixel length is $4.7 \mu\text{m}$). This is higher than the oft-quoted accuracy of the DIC technique of 0.02 pixels; however, these tests have been performed with a non-telephoto lens from a short distance, and so optics-induced errors will be inherently higher and so this error level is not unexpected.

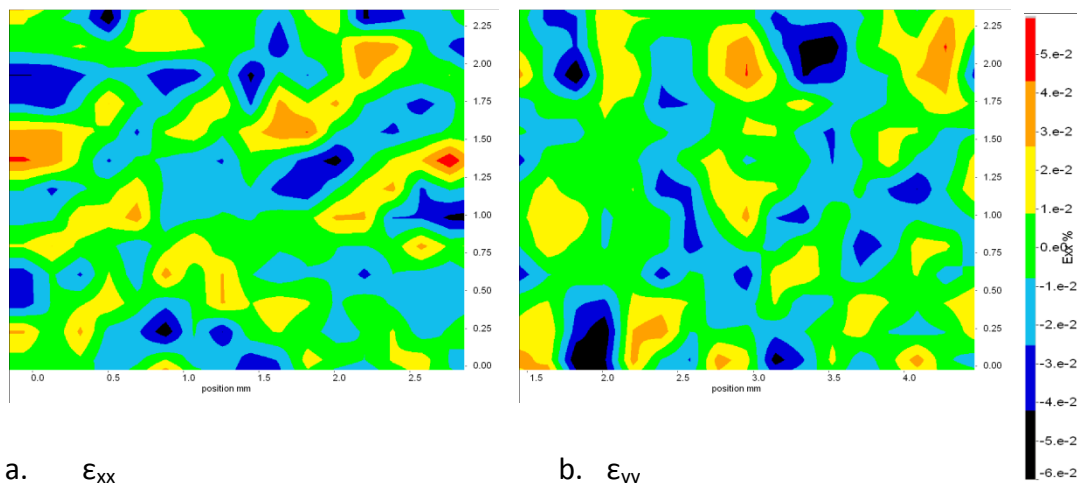
Taking two frames at almost equivalent load, one part way through the loading phase (34.7 N) and one part way through the unloading phase (34.8 N), (the red crosses on the loading curve in figure 5.21,) showed much less displacement field bias and significantly lower displacement field variation, $0.6 \mu\text{m}$ for u and $0.7 \mu\text{m}$ for v . These can be seen in figures 5.24. This is equivalent to 0.15 pixel lengths.



a. u [scale bar: 0.0 to $-0.6 \mu\text{m}$]

b. v [scale bar: 2.9 to $3.6 \mu\text{m}$]

Figure 5.24 – Displacement fields from correlating two frames under equivalent load, one before and the second after further subcritical loading



a. ϵ_{xx}

b. ϵ_{yy}

Figure 5.25 – Strain difference between two frames under equivalent load before and after further subcritical loading in a.) x and b.) y directions. Scale bar $\pm 0.06\%$.

The strain measurements in the unloaded specimen, figure 5.23, can be seen to be consistently within $\pm 0.05\% \epsilon$. In the loaded specimen, figures 5.25, strain difference between the equivalent loads is around half that, at around $\pm 0.025\% \epsilon$. This level of error is well within an acceptable level and in line with the expected accuracy of the technique.

These errors correspond to the expected variation in stress intensity factors determined using DICITAC; reading from table 5.10, if strain fields are consistent

between frames with background noise of $\pm 0.025\% \varepsilon$, a variation in K_I of approximately $\pm 0.023 \text{ MPa}\sqrt{\text{m}}$ could be expected. Figure 5.26 shows load cell K_I values alongside DICITAC K_I values, with K_I error bars of $\pm 0.023 \text{ MPa}\sqrt{\text{m}}$. Whilst the load cell derived data is being treated as correct, it is subject to some \pm uncertainty itself due to load cell scatter and inaccuracy, and \pm errors in crack length measurement.

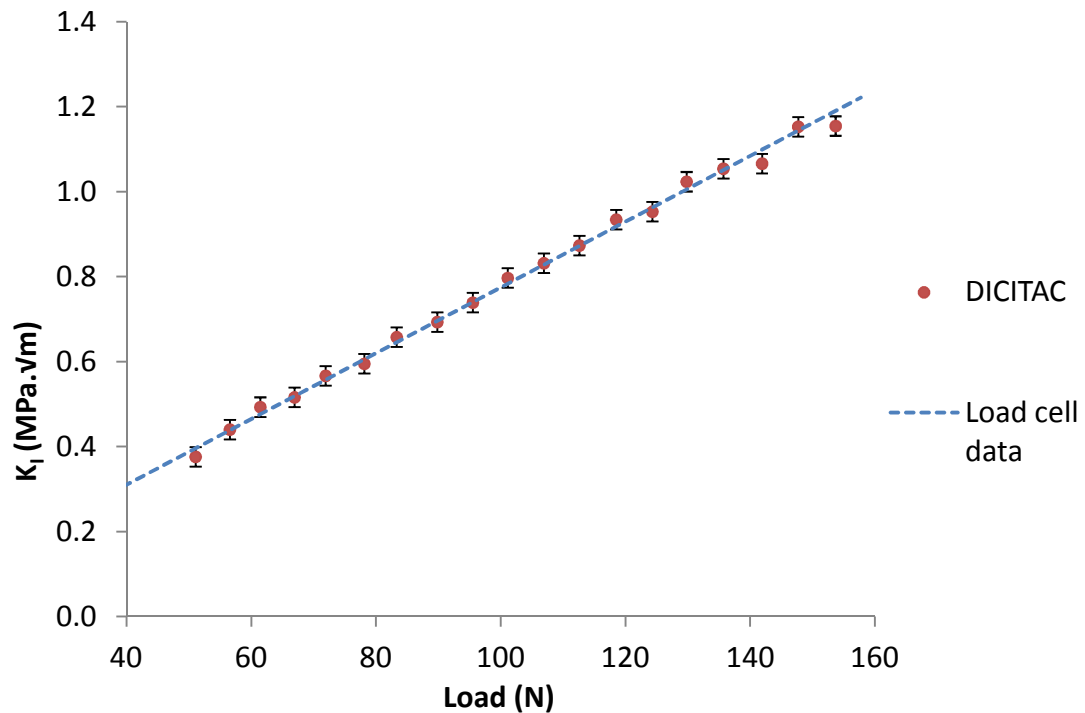


Figure 5.26 – Compact tension DIC extracted K_I values alongside load-based K_I values with error bars from DIC strain field analysis. DICITAC data have error bars of $\pm 0.023 \text{ MPa}\sqrt{\text{m}}$; the error associated with expected out-of-plane motions.

5.7 DICITAC-induced inaccuracies

The DICITAC pattern-search algorithm used to locate the crack tip was applied as part of the fracture parameter extraction process. As determined in section 5.3.2, discrepancies in crack tip location of 6 pixels related to $\pm 1.2\%$ errors in K_I measurement and $\pm 4.2\%$ in T -stress measurement. An estimation of the accuracy and consistency of the crack tip locating algorithm was performed by recording the crack tip locations determined with the algorithm for one specimen, CT-F2-09. The x

and y locations for either specimen are shown in figures 5.27a-b. Locations are measured in their position, in mm, on the field of view. The origin, and hence the absolute x and y values of the crack tip location, is/are of no significance. The origin was assigned by the LaVision StrainMaster DIC software during the calibration as the first point in the calibration measurement and was not reassigned to a more physically meaningful location.

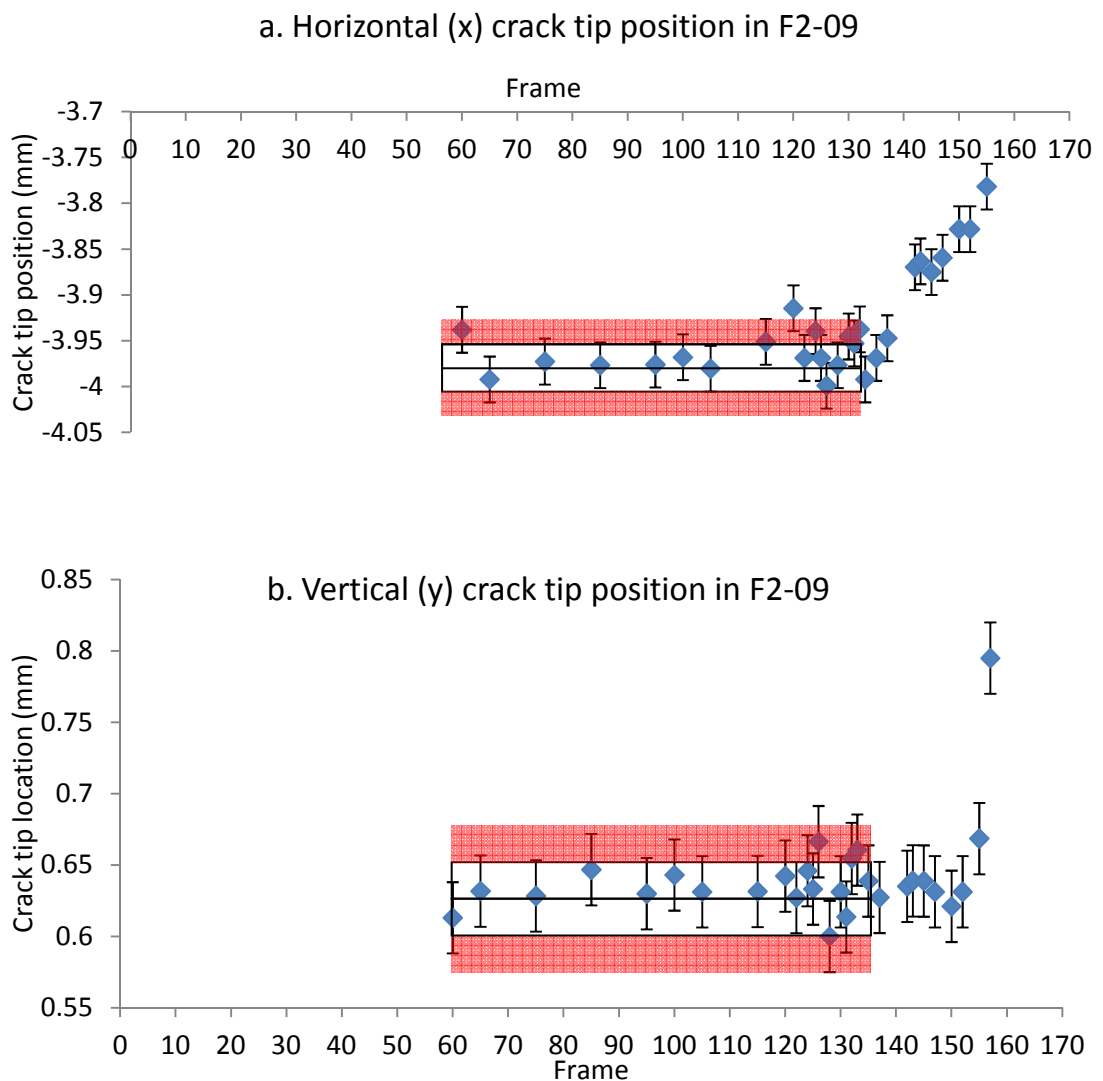


Figure 5.27 – Horizontal (a) and vertical (b) crack tip positions, as located using the DICITAC pattern-search crack tip locating algorithm

Figures 5.27a-b show some variation in the location of the crack tip using the pattern-search algorithm. At frame 135 some stable crack growth was observed in the specimens, and this can be seen in a change in crack tip location in the x-

direction. The error bars in these figures are set at ± 0.025 mm; equivalent to a ± 5.7 pixel error, the consequence of which was examined in section 5.6. Focusing on frames 60 to 135, throughout which the crack tip was stationary, the measured locations are, with a small number of exceptions, within ± 0.025 mm of an average value (this boundary is marked on the figures). These exceptions could explain the noticeable spurious T -stress measurements that can be seen when alongside many other values.

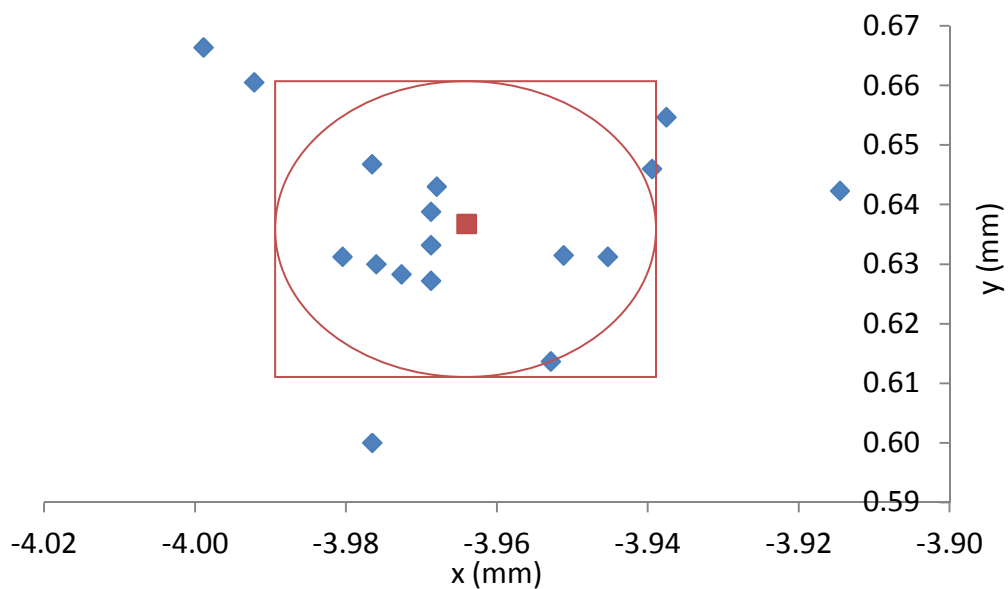


Figure 5.28 – DICITAC-determined crack tip locations for specimen F2-CT-09 in the stationary crack loading region. Mean value is indicated by a red point.

Figure 5.28 shows a scatter-plot with the crack tip locations between frames 75 and 135. The red point is the mean x and y location values. Overlain are a circle of radius 0.025 mm and a square of sides 0.05 mm in length. There is an approximately 2:1 ratio of values inside to outside of the square and an approximately 3:2 ratio of values inside to outside the circle. Values do appear to vary with a random, Gaussian nature and so the errors from poor crack tip location should be removed by taking measurements for various frames and averaging.

5.8 Initial fractographic analysis

This section is included for completeness only; a proper fractographic study of the specimens has not been performed and only two micrographs are presented here. Figure 5.29 is a low-magnification image of a NEAT resin specimen. The starter crack has been applied from the left and the area with river markings is the fracture surface from the CT test. Note the very distinct starter crack-front.

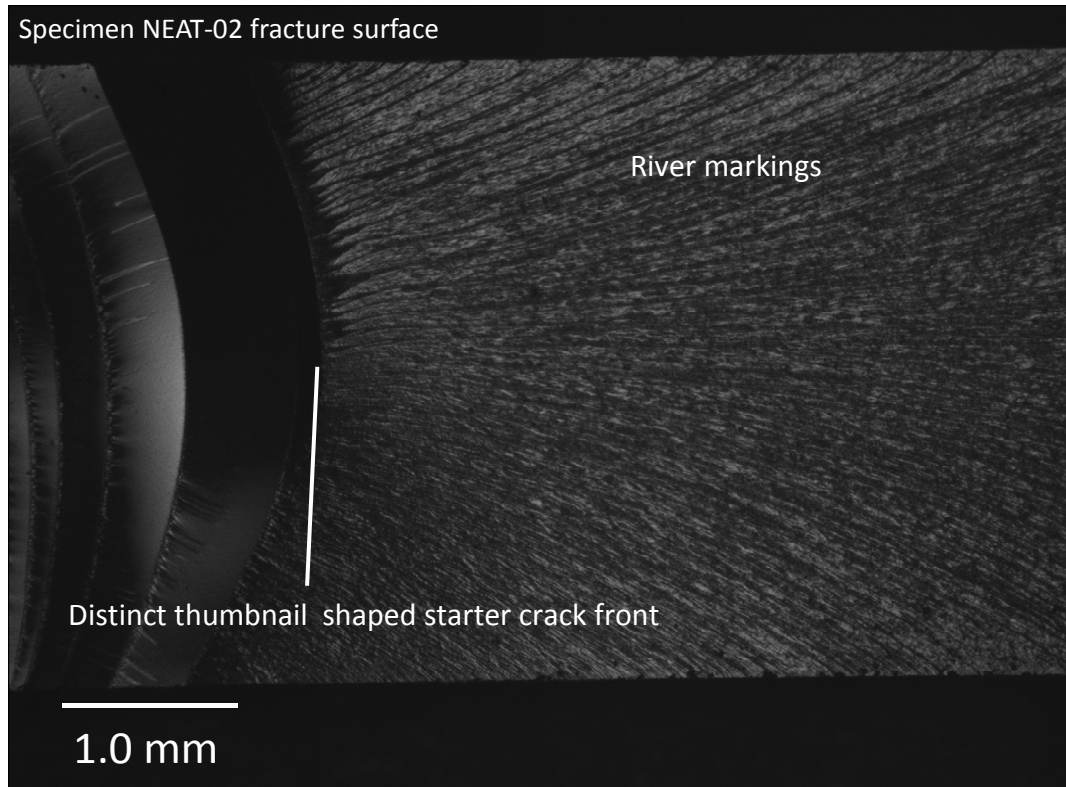


Figure 5.29 – NEAT-02 fracture surface

Figure 5.30 shows the same field of view of an F2 specimen; the surface is very rough; cracks have propagated in the resin around the particles, strongly suggesting crack-pinning and crack path deflection-based toughening mechanisms. There is only a faint suggestion of the location of the much rougher starter crack. A closer view of the specimen roughness is shown in figure 5.31.

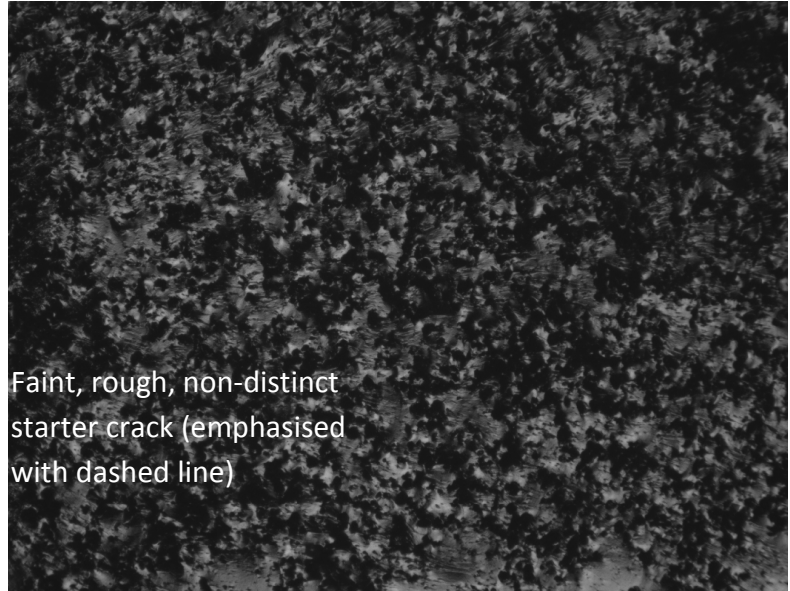


Figure 5.30 – F2-09 specimen fracture surface

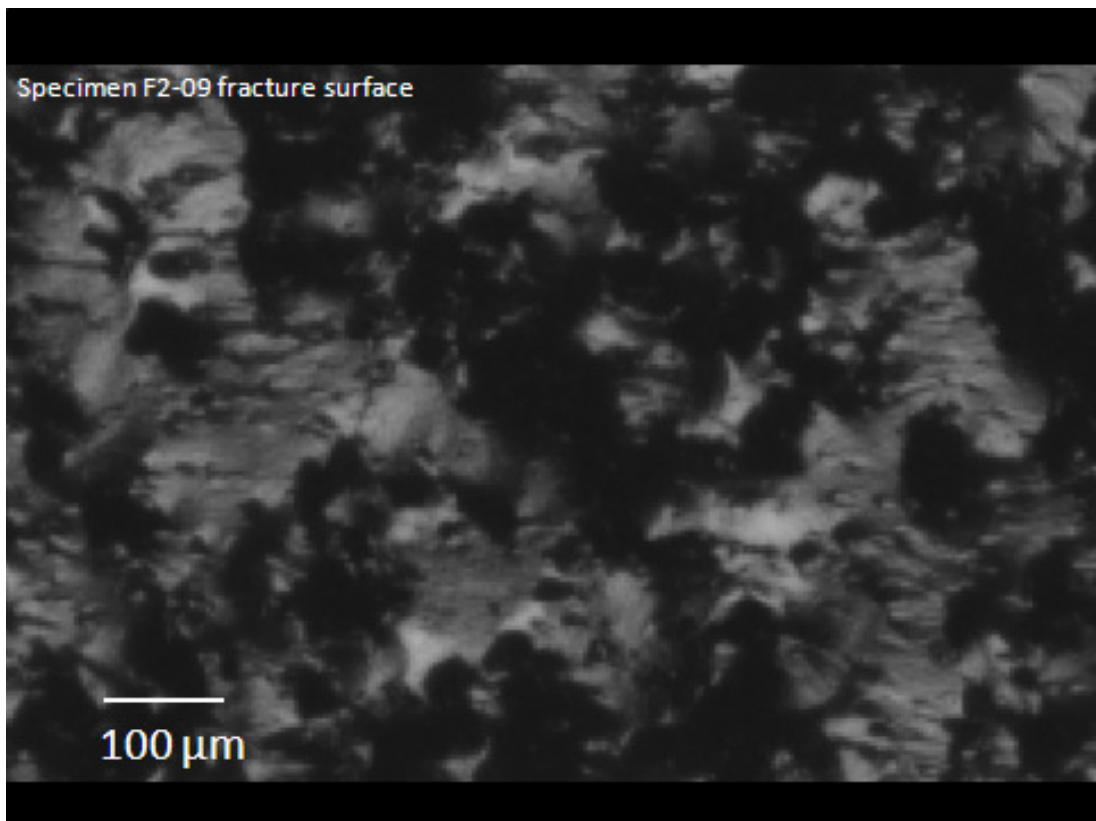


Figure 5.31 – F2-09 fracture surface (enlarged)

All fracture surfaces of the F2, F3 and F5 resins are all extremely rough, indicative of substantial crack redirecting mechanisms. Evidence of widespread crack-pinning is apparent. NEAT and F4 resin fracture surfaces are smoother, showing some river markings, unlike typical untoughened pure epoxy systems which usually exhibit mirror-like featureless surfaces [129]. F4 specimens' fracture surfaces show the crack-front to have travelled through the toughening particles.

5.9 Concluding remarks

It is well known that 2D-DIC is not only incapable of measuring out-of-plane deformations and rigid body motion, but also that the accuracy of measurements is severely compromised by the presence of any variation in the z (out of plane) axis [92, 128]. The current widespread use of commercial 3D-DIC systems in experimental mechanics leads to the obvious question “why didn't you use 3D-DIC for this study?” In answer to this question, it was deemed not necessary for this project. These tests have been performed on flat, brittle specimens that exhibit low ε_{zz} at the typical stresses σ_{xx} and σ_{yy} around the crack tip and the error figures presented in table 5.10 support this. It was felt that the superior available optics, equipment availability and increase in the number of tests possible would be more beneficial to data quality over the added amount of time required to set up and test using 3D-DIC.

Important considerations regarding the use of digital image correlation techniques in testing specimens subject to small preload conditions were identified. These were successfully accounted for and direct comparison between stress intensity factors determined using DIC and DICITAC were found to be in close agreement with theoretical values. The validity and accuracy of T -stress results were assessed and it was concluded that they were generally acceptable and were measured at around the accuracies expected for the technique. The comparison with theoretical values was promising; values were either in agreement with theory, and where differences between databook and measured values existed, values were in agreement with appropriate theoretical values. It is felt that the techniques can be transferred to

mixed-mode specimens with confidence. Care will be taken to eliminate or mitigate the sources of problems identified, such as inconsistency in loading constraint and the non-zero initial strain state in DIC measurements. It will be seen in chapter 7 that crack growth does not typically occur in the mixed-mode specimens and so extracting critical values from displacement field data was less problematic.

From the experiments discussed in this chapter, a strategy for investigating fracture with a shear component was formed. Key points are listed below:

- Applied speckles were found to work acceptably well although speckles were somewhat higher than 'ideal' and required subset sizes for robust correlation were large, and so efforts will be made to reduce the speckle size. Whilst large subset sizes are not an intrinsically bad thing, having a choice of sizes is better than being forced into using the most stable solution.
- Crack tips could only be located in CT tests by using the visible notch root. It is anticipated that locating the crack tip in mixed-mode tests, in which the camera will be repositioned between each loading angle, that markings on the specimen will be helpful.
- Specimens with low crack-tip rigid body translation are required at the fields of view of interest to this topic, and sharp natural crack tips are important in toughness measurement and so an edge-cracked, compact tension-style mixed mode test is preferred.
- The crack-tip locating algorithm was found to be reliable and consistent in the pure mode I case. It is intended to use the algorithm in the mixed-mode case where it is expected to aid calculations especially in situations where the crack tip may not immediately appear from the raw image data in cases of limited mode I crack opening.
- To avoid the strain offset problems caused by preloading specimens, and to avoid the accuracy issues of poorly focused optics, an alternative preload/focus strategy must be used. It was planned that specimens would be loaded up to a preload of ~ 30 N, the load held and optics focused, and then the specimens unloaded and the crosshead stopped at

the point of zero load. The plan was then to check the focus and begin the test, checking the acquired images 'live' for any signs of poor focus caused by out of plane displacement.

- *T*-stress data was found to show large amounts of scatter. As specimens approached failure, some specimens showed strong discontinuities in *T*-stress. This was especially true for cracks with kinking. It is hoped that measuring this parameter in materials whose morphology is thought to affect kink stability will be of interest, but statistical significance may be low.

Chapter 6

Mixed-mode (I/II) experiments

6.1 Introduction

A review of the literature, presented in chapter 2, showed relatively brittle polymeric materials such as epoxy, loaded in mode II in-plane shear fail through crack-kinking tensile mechanisms. This behaviour can also be seen at the microscale in carbon-epoxy composites (section 2.7). Rather than investigate pure mode II behaviour alone, it has been decided to investigate the range of mode mixities from pure mode I to pure mode II. It is thought that due to the kinking, mechanistically tensile failure mode of cracks in epoxies subjected to shear, investigating mixed-mode behaviour will allow better understanding of the effect of fracture under shear loading.

In this investigation the failure in different materials has been analysed in terms of the stability of crack paths and resistance to fracture by extracting T -stress and K_I and K_{II} values. Parameters have been extracted from DIC displacement data measured in mixed-mode Arcan-type specimens. The work of the previous two chapters, comparing standard results with experimental mechanics measurements, has given confidence in the parameter extraction method employed here.

The work of this chapter follows directly from chapters 4 and 5 and develops the investigation into mixed-mode (I/II) and mode II shear behaviour. This chapter contains details of the experiments performed whilst the chapter 7 presents the results and a discussion of their implications. Where the experimental arrangement is unchanged from the pure mode I tests described in chapter 4, the reader will be referred back to the relevant sections.

As discussed in section 4.1.1, the resins tested in this project are structurally very similar, yet exhibit significant differences in toughness behaviour in their bulk form, and even more so when part of a composite interlayer. Of the toughened resin

formulations F2-5, each is made up of 90% unmodified resin (the NEAT formulation) and 10% thermoplastic spherical particulate. The spherical particulates are all of similar size and are distributed similarly throughout the material. The minimal differences in size and distribution do not account for the widely varying mode I and II composite toughness of the resin systems.

Whilst the materials seem very similar, they have widely differing fracture performance in composite structures. Figure 6.1 shows G_{IIc} values for carbon-epoxy composites of the tested epoxy formulations. Since the NEAT resin does not have any particles to create and control an interlaminar gap, the value for NEAT resin is not necessarily directly comparable with the other resins. The four particulate toughened formulations were tested using consistent lay-up and testing procedures. Data were supplied by Cytec Engineered Materials.

By considering the simple rule-of-mixtures effect on material stiffness, it can be safely assumed that the effective stiffness of the particles and their interfaces is mostly very similar. Whilst size and distribution of particles are widely acknowledged to strongly affect toughness performance, if these are kept constant (or very similar) then there must be further factors that cause these differences. Factors that are difficult to predict or measure include the strength of the interface and interphase between particle and matrix and the triaxial residual stress state around and between particles caused by thermally intensive cure process. Residual stresses are well known to strongly affect fracture behaviour of materials [9]. The approach taken in this study is to observe and measure the effect of the particles on resin fracture behaviour at a bulk scale, instead of attempting to measure the three-dimensional interaction between crack, matrix and particle at a microscale.

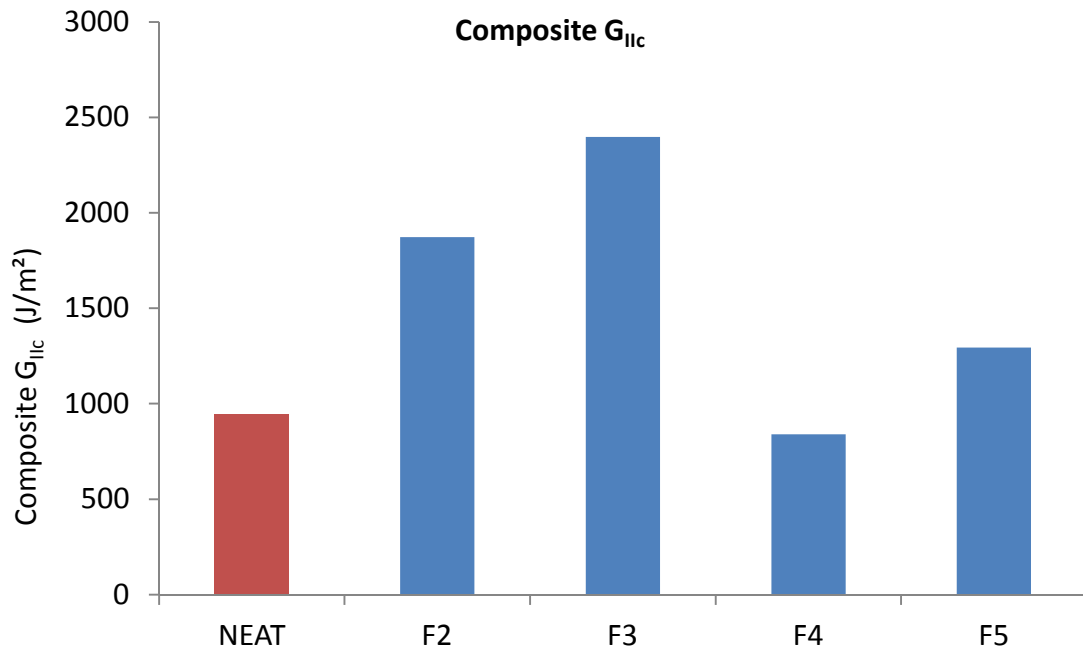


Figure 6.1 - Composite G_{IIc} (shear fracture) performance of thermoplastic particulate interlayer-toughened carbon fibre-epoxy systems alongside the unmodified 'NEAT' resin. Data courtesy of Cytec Engineered Materials.

6.2 Specimens and grip design

A study of mixed-mode tests was carried out (presented in section 2.6) and a mixed-mode Arcan/Banks-Sills type specimen was deemed to be most suitable for testing the bulk polymer specimens. Grip and specimen design can be found in figures 6.2 and 6.3 respectively. The Arcan-type mixed-mode specimen is loaded at numerous angles by changing loading pin positions (and hence specimen orientation). A separation between the loading angle positions of 15° is a natural choice for Arcan-type mixed-mode tests since it divides into 90° to give seven loading points from 0° (pure mode I) to 90° (pure mode II) with a reasonable spacing between holes in the grip faces. The loading orientations are illustrated in figure 6.4

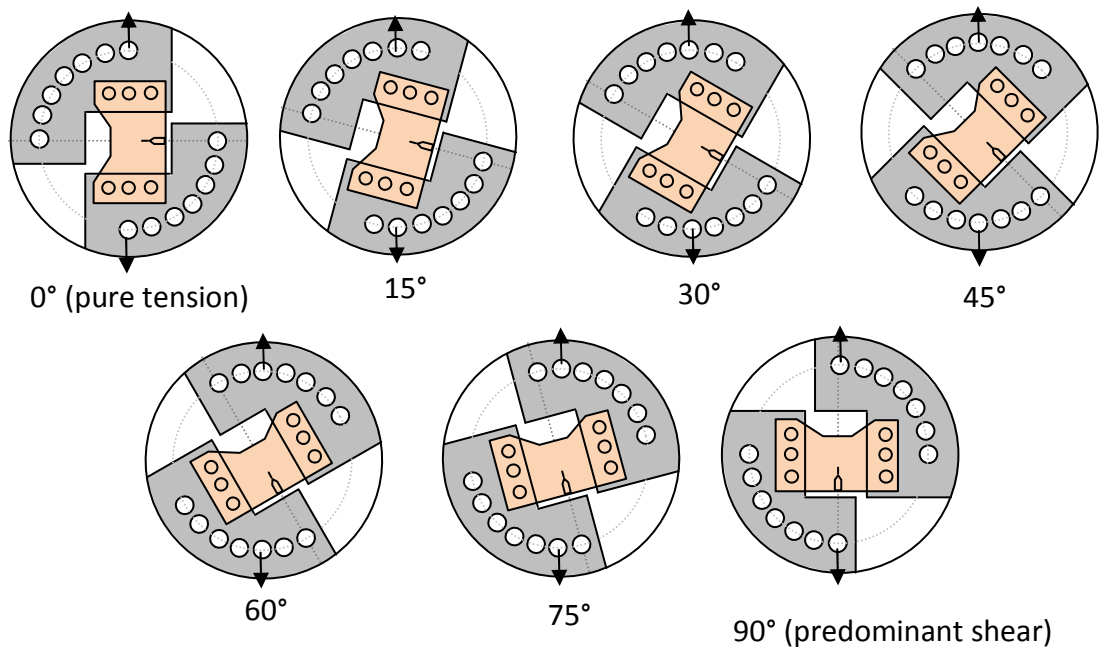


Figure 6.4 - Specimen loading orientations

Grip faces were machined from 4.0 2024-T6 aluminium sheet. Grip faces were connected to the clevis-pin loading points on the JJ-Lloyd T22K test frame through an intermediate milled mild steel spacer tab. The spacer tab part is shown in figure 6.5.

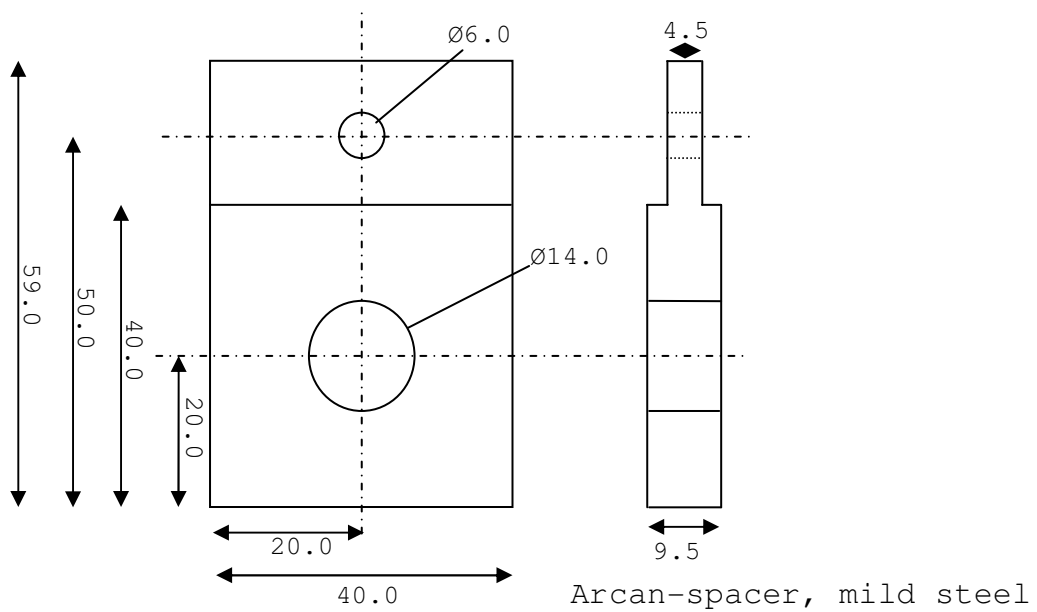


Figure 6.5 – CAD drawing of spacer part

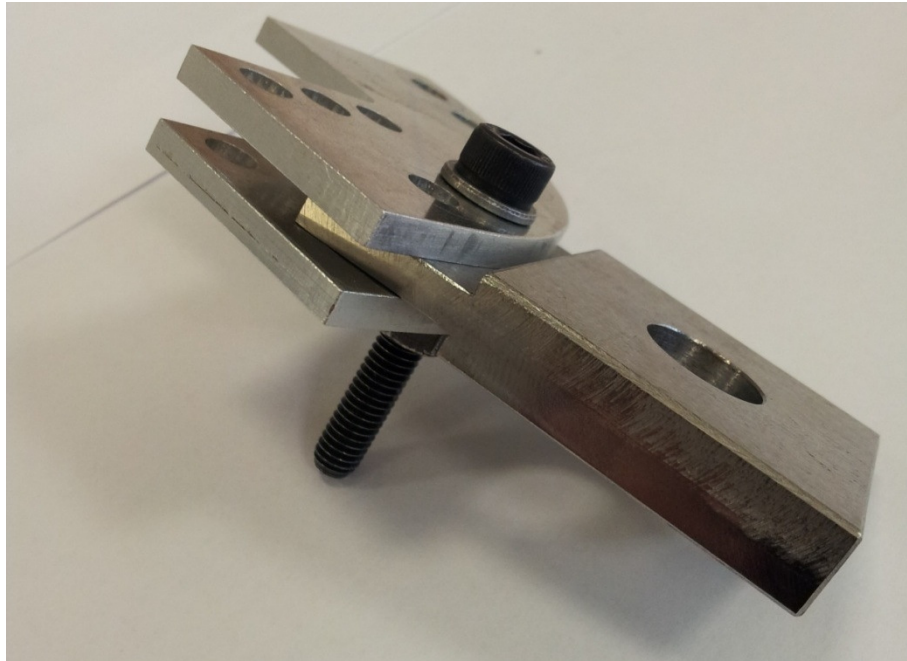


Figure 6.6 – Grip faces and spacer piece bolted together

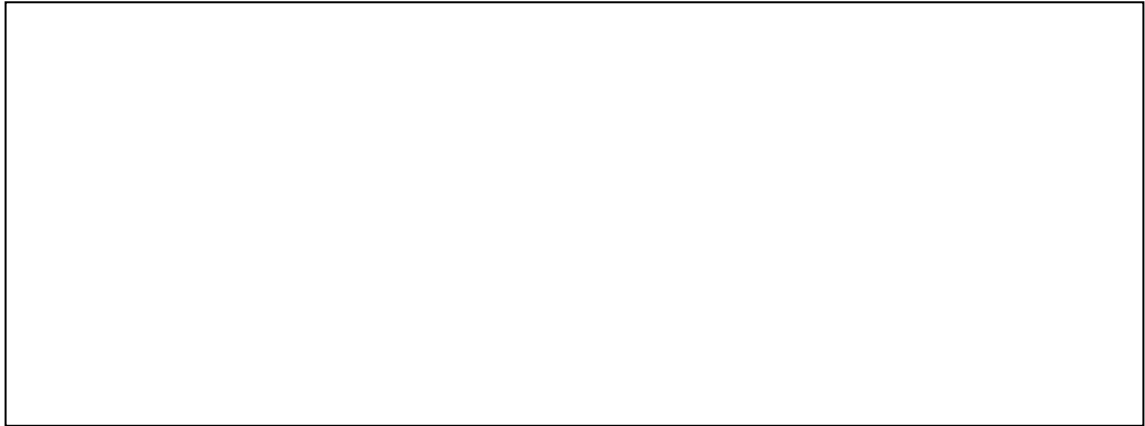
The two sets of grip faces were bolted together, each through one of the spacer tabs and two flat washers, at the required angle with a torque of 40 Nm through a single M6 cap-screw and matching nut. The relative low loads involved in the testing of the epoxies made this arrangement sufficient, effective and efficient. The strength of this grip arrangement will be insufficient for testing significantly tougher materials such as aerospace alloys but is sufficient for the epoxy tests performed here.

The 10 mm steel spacer tabs were slotted into clevis pin adapters which pin directly to the load cell and test frame. The small amount of allowable rotation was deemed necessary to minimise eccentric loading of the load cell to avoid damage. This was discussed in some detail previously in section 2.6.4.7. Figure 6.7 shows a photograph of the grip arrangement.



Figure 6.7 – A painted mixed-mode specimen in the assembled grips at a 45° loading angle.

Specimens were connected to the grips using machine screws, shown in figure 6.7. Specimens were loaded through the shanks of three M6 machine screws of measured diameter 5.95 mm each side. The hole diameters, measured as 6.00 mm, prevented over-constraining the specimens and ensured a stress-free state before loading. Connecting specimens to the grips using six net-sized silver steel loading rods would create significant strains in the specimen due to overconstraint and was deemed an unnecessary and detrimental complication. There are two methods of overcoming this overconstraint; one is to reduce the size of the loading pins by a distance larger than the tolerance of the specimen manufacture, the second is to elongate the three loading holes in different directions, as shown in figure 6.8. The undersized pin solution was selected for ease of machining and specimen fitting and should have the same effect in preventing over-constraint. With hindsight, the more elegant elongated hole solution may be less sensitive to small variations in specimen dimensions and is recommended for future studies.



a. Taken from Zanganeh [112]

b. Taken from Richard [69]

Figure 6.8 - Elongated grip holes in the grip design specifications in two studies

6.3 Specimen preparation

Specimens were machined to the geometry shown in figure 6.3 from NEAT, SHEFF-F2, -F3, -F4 and -F5 resin plaques. A total of 18 specimen in each material were machined. As in the mode I tests, the top faces were removed to a depth of approximately 0.5 mm with progressively fine abrasive paper to remove the resin-rich top layer. A small amount of the bottom faces were removed so that the dust and airbubbles on the surface were removed. Sharp cracks were initiated through razor blade tapping and a paint speckle pattern applied using an airbrush. Through using a higher air pressure, speckle size was slightly smaller than in the CT tests, at approximately 15-30 μm (3-6 pixels). It was quickly determined that unlike in CT tests, the crack tips were too difficult to locate on the painted surfaces and so light markings at the crack tip were added to aid field-of-view selection. The crack tip locating markings were applied by measuring crack tip position roughly (with a steel rule) on the back face of the specimen, and applied to the front face with sharp nib marker (figure 6.9) and then a lighter, less intrusive method of 0.5 mm propelling pencil. These markings were used for ensuring correct field of view only and not used for defining the location of crack tip when using DICITAC to extract fracture parameters from the displacement fields.

The complete field of view and a pixel-scale enlargement are shown in figures 6.9 and 6.10 respectively. A completed specimen, with crack tip locating markings, is shown in figure 6.11.

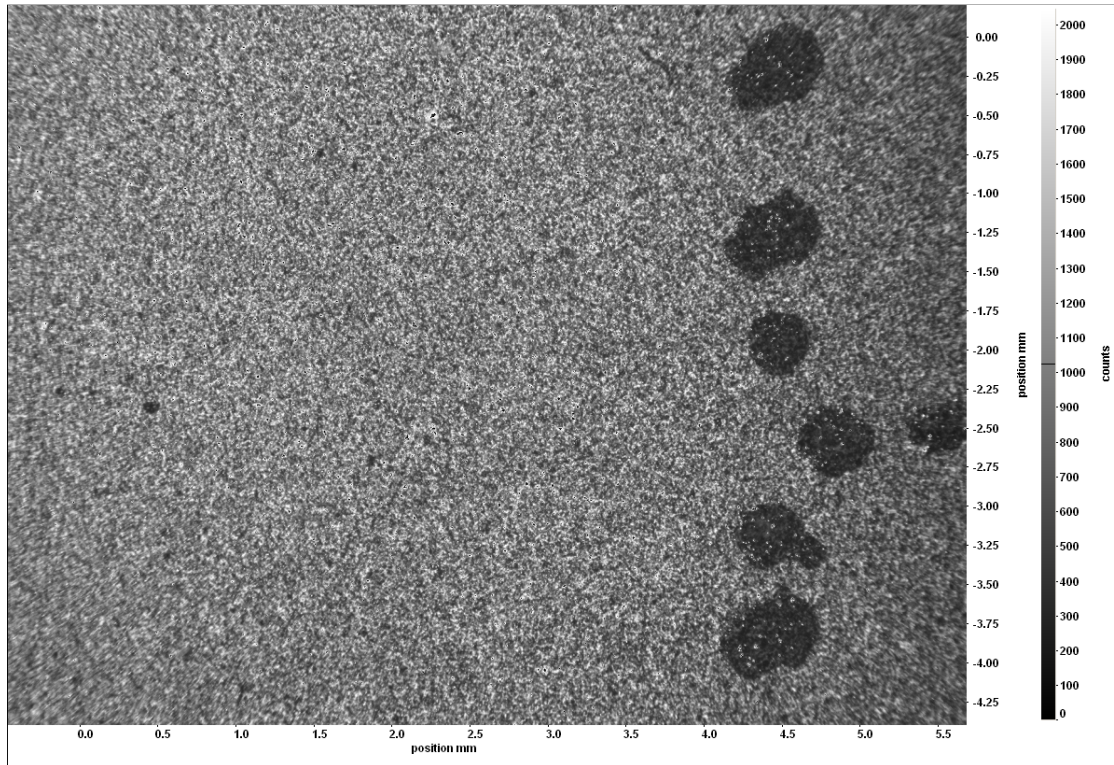


Figure 6.9 – Full field of view for a typical specimen (specifically 60-F2-08)

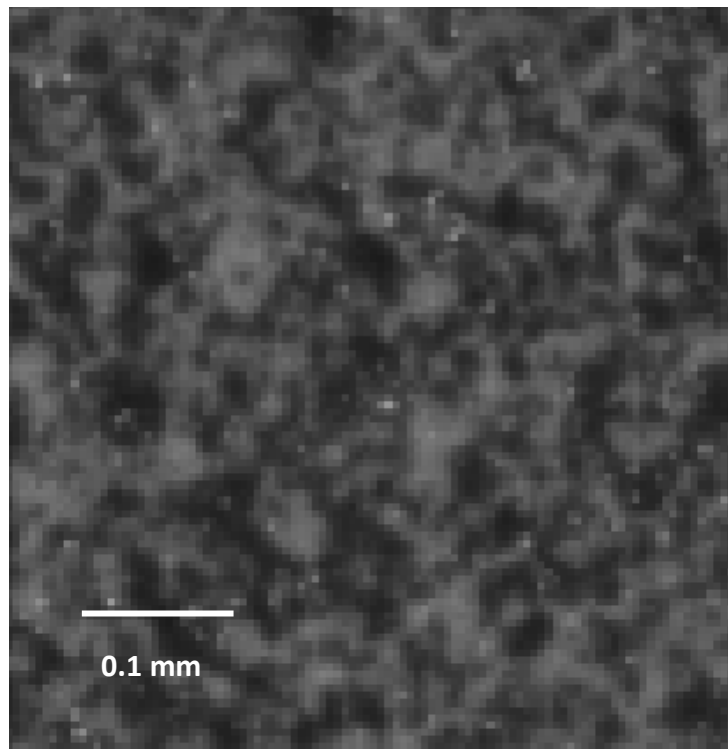


Figure 6.10 – Pixel-scale enlargement for a typical specimen

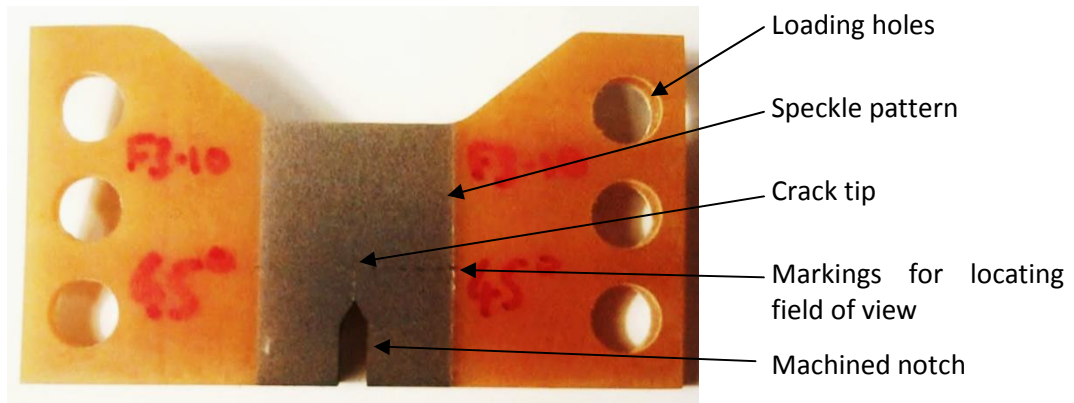


Figure 6.11 – Prepared specimen. Machined, sanded, crack-tapped, painted and marked with crack tip and specimen number and loading orientation.

Specimens were numbered in the form XX-MAT-YY where XX is the loading angle, MAT is the material type, and YY is a specimen number, e.g. 45-F3-10 is specimen 10 of formulation F3 and was loaded at 45°.

6.4 Experimental arrangement

As described previously in section 5.3 for the mode I tests, the digital image correlation (DIC) method was applied to allow the direct extraction of stress intensity factors. This methodology removes the reliance on either finite element analysis (FEA) or otherwise derived geometry/shape functions inherently required by exclusively load based methods.

In order to remove the need to rotate DIC displacement vector fields so that the crack is aligned parallel the x-axis, the camera was rotated, as seen in figures 6.12 and 6.13. Angular alignment was achieved using the graduated protractor markings on the tripod and checked against the acquired image. Bubble and digital spirit levels were also used to aid alignment.

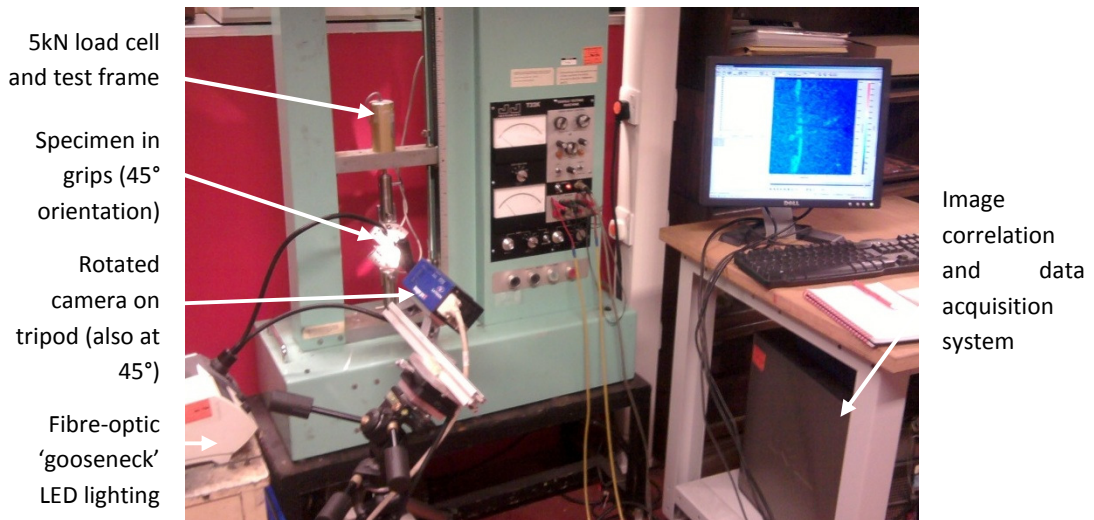


Figure 6.12 - Experimental arrangement, annotated

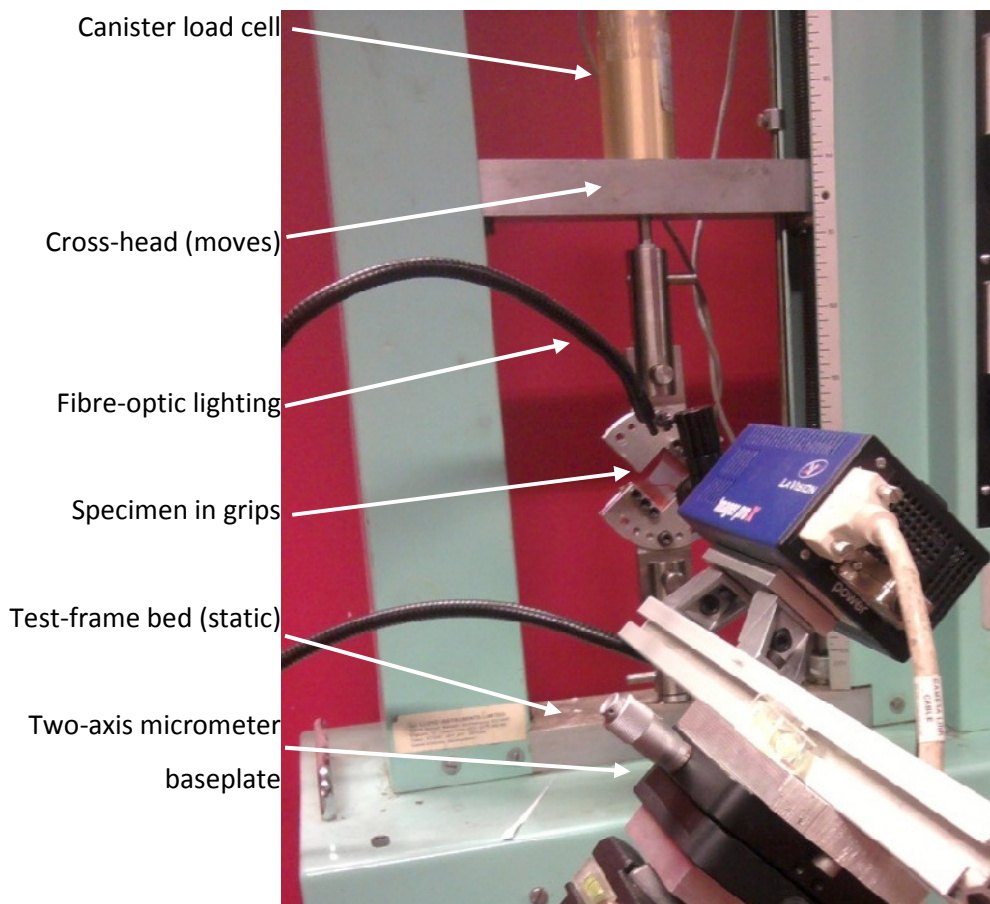


Figure 6.13 - Experimental arrangement, detail (lighting turned off for clarity)

Substantial pre-loads were applied to specimens (approximately 50 N; typical failure loads were 500-700 N) in order to align the specimens and grips and the camera focused on the taut specimen. Specimens were then unloaded just to the point of zero-strain state and loading/image recording begun. This removed the requirement

for any additional strains to be added numerically to correct for starting recording images from a preload, as was required in the previous experiments described in section 5.3.4.

Specimens were loaded to destruction at seven 15° load angle intervals (0°, 15°, 30°, 45°, 60°, 75°, and 90°), as indicated in figure 6.4, where 0° is pure tension and 90° is (ideally) pure shear. Specimens were loaded in displacement control at a nominal 1.0 mm/min.

The mixed-mode specimens were found to cause considerably higher loads and hence crack tip stresses for a given cross-head displacement, the Arcan-type specimens being inherently less compliant than the CT specimens. Consequently testing to failure took a smaller cross-head displacement and hence less time. Since 1.0 mm/min was the minimum cross-head displacement rate and could not be lowered further, the image acquisition rate was increased. Images were recorded at 2Hz (in the compact tension studies, images were recorded at 1Hz). Typical failure loads at higher levels of mode mixity were 500-700 N so a 5 kN load cell was used instead of the 500 N cell used in the compact tension tests.

Tests were performed on a single specimen per material in the pure mode I orientation first to ensure the measured failure stress intensity factor was the material toughness as established in the previous chapters. When it was established that the values were consistent with K_{IC} , tests in the range of mixed-mode angles were performed.

Two specimens of each material were loaded to destruction for each mixed-mode loading angle. Remaining specimens were tested mostly at 90°.

6.5 Digital image correlation

LaVision Strainmaster software was used to determine 2D displacement fields for the specimens. A reduced-size multipass algorithm, performing two iterations with 128x128 pixel subsets refined with a further two iterations at 64x64 pixels, with a

25% overlap was found to give stable and consistent correlation results for the speckle pattern used, as discussed in section 4.5.

6.6 Extraction of fracture parameters

K_I , K_{II} and T -stress values were extracted using DICITAC. This method has been described in detail in section 5.3 and so the details of the process will not be repeated. K_I , K_{II} and T -stress values were extracted at a number of points throughout the duration of loading. Critical values (i.e. at the point of failure) were determined for each specimen. As part of the DICITAC process, crack tip locations were determined using a pattern search (PS) algorithm. An analysis of this process was presented in section 5.8.

The extracted stress intensity factors are presented in chapter 7. Strain fields, failure criteria and crack kinking behaviour will also be presented and discussed.

The following three chapters contain the results and discussions thereof. Chapter 7 focuses on extracted stress intensity factors; chapter 8 presents crack kinking behaviour and comparison between kink measurements, measured stress intensity factors and theoretical failure criteria, supported by DIC strain map data; and chapter 9 presents and discusses measured T -stress values.

Chapter 7

Mixed-mode results and discussion: Stress intensity factors

7.1 Introduction

This chapter presents the results of the experiments described in chapter 6. Stress intensity factors at critical loading conditions are examined for each material and the behaviour of cracks in the materials subjected to shear components is explored. Methods of measuring K_{IIc} from the results are examined, and resin mode II toughnesses are compared with composite mode II fracture toughnesses.

7.2 Stress intensity factors

Section 5.3.5 showed that crack growth causes complications when using DICITAC to determine stress intensity factors at critical loading. The mixed-mode specimens tested here, with a few exceptions (discussed in section 9.2) failed instantaneously with no subcritical crack growth, negating the problem. DICITAC was applied as described in section 5.3 in the pure mode I tests. Critical mode I and II stress intensity factors were extracted, as were the non-singular T -stress, for all specimens.

7.2.1 Stress intensity values with increased loading

The results of the compact tension tests, presented in chapter 5, showed that whilst stress intensity factors and T -stress values determined using DICITAC increased linearly with load with little scatter. The magnitude of this scatter was consistent with the quantified errors caused by the crack tip locating algorithms. In some specimens the stress-intensity factors exhibited a constant offset from theoretical load cell values. Fracture parameter extraction using DICITAC is performed using a manual, frame-by-frame approach; consequently, it is desirable to be able to extract

a minimum number of frames. This is especially true if only critical values are required.

Instances of crack growth in the mode I specimens (section 5.3.5) were shown to prevent critical values from being determined directly from the frames immediately prior to failure. With few exceptions, crack growth was not observed in the mixed-mode specimens and so it was hoped that final frames could be used to determine critical stress intensity factors (and T -stress values). In order to test this, one specimen at each loading angle was picked at random, with a minimum of one specimen of each material. Fracture parameter extraction was performed on the selected specimens at around eight points throughout loading. In addition to these tests, some further specimens were selected (again, at random) and parameter extraction performed at four points throughout loading. These results are presented in figures 7.1. In each graph in figures 7.1, stress intensity factors K_I and K_{II} are both plotted on the same axis, in blue (diamonds) and red (squares) respectively.

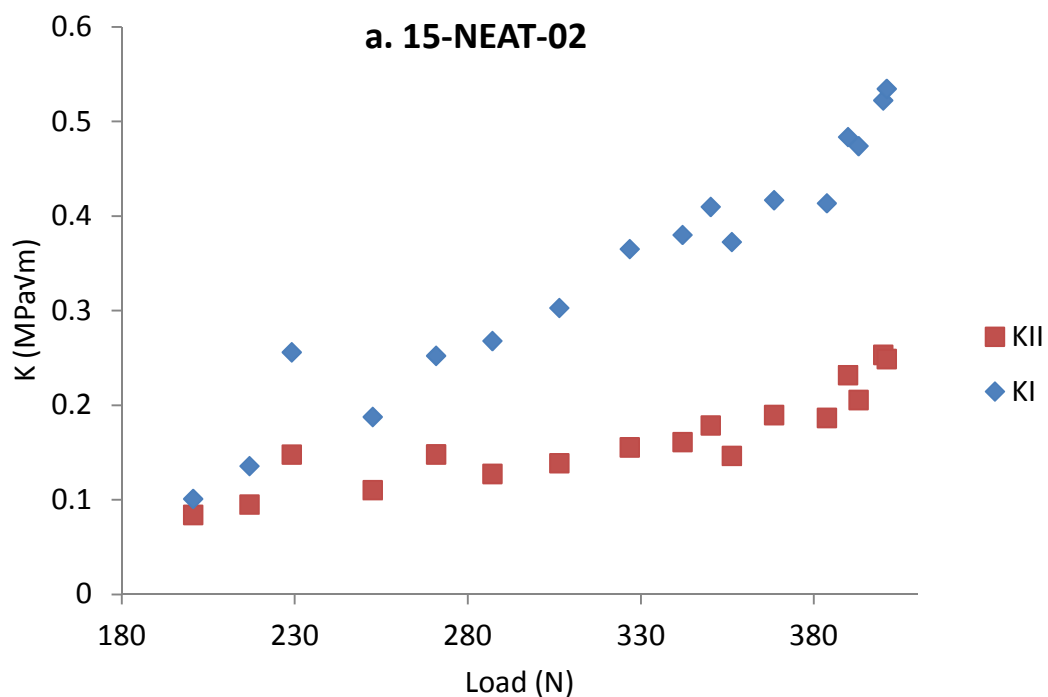


Figure 7.1 continued...

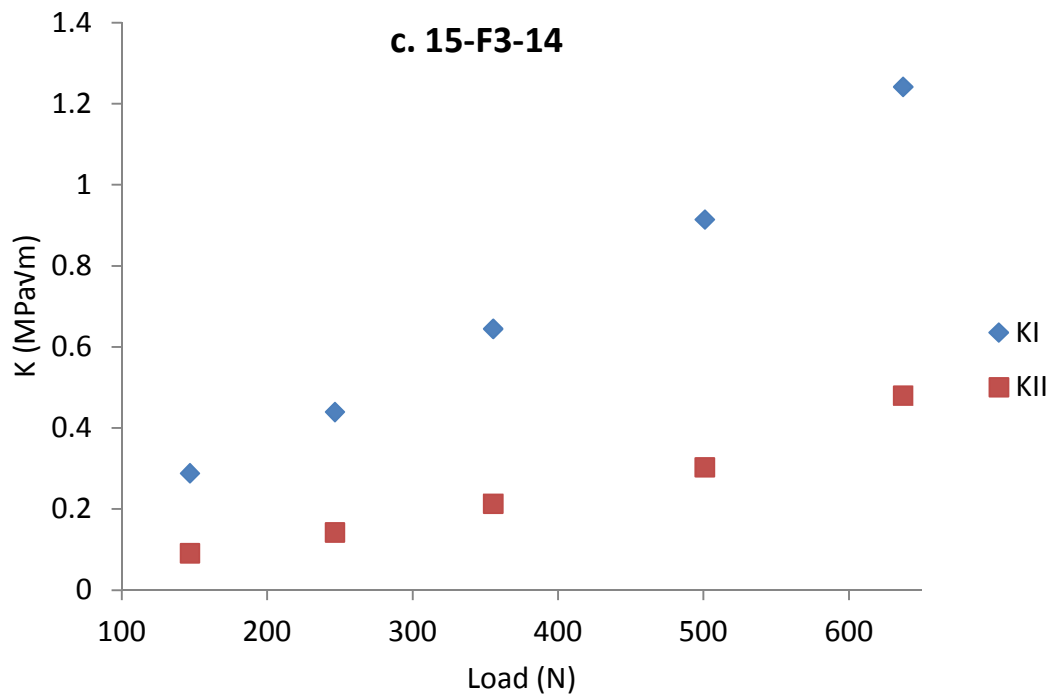
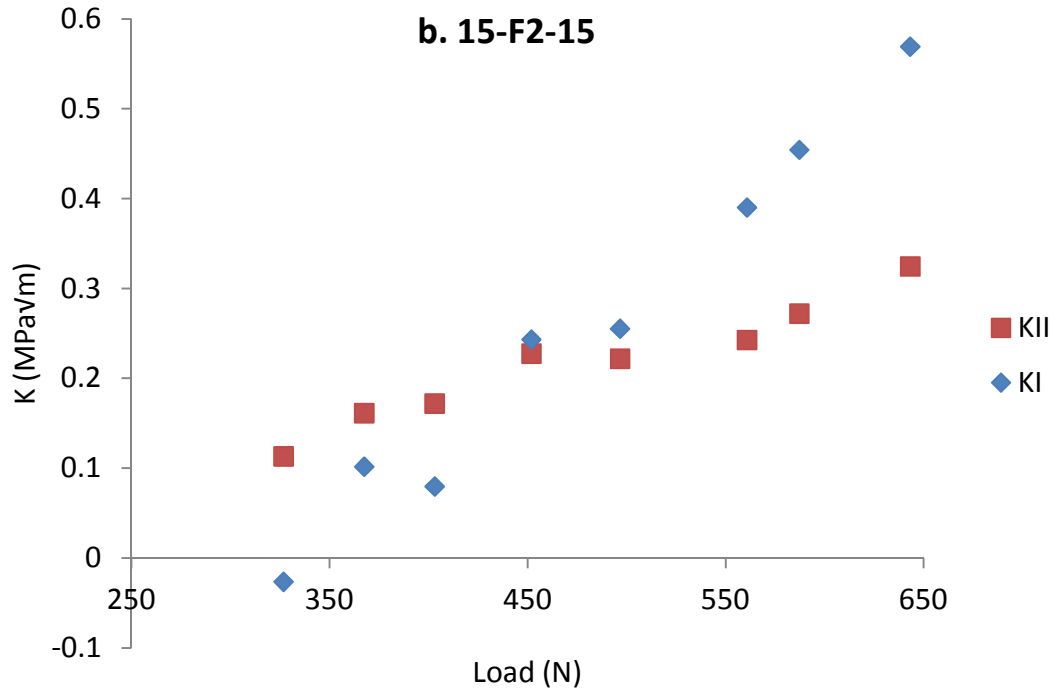


Figure 7.1 continued...

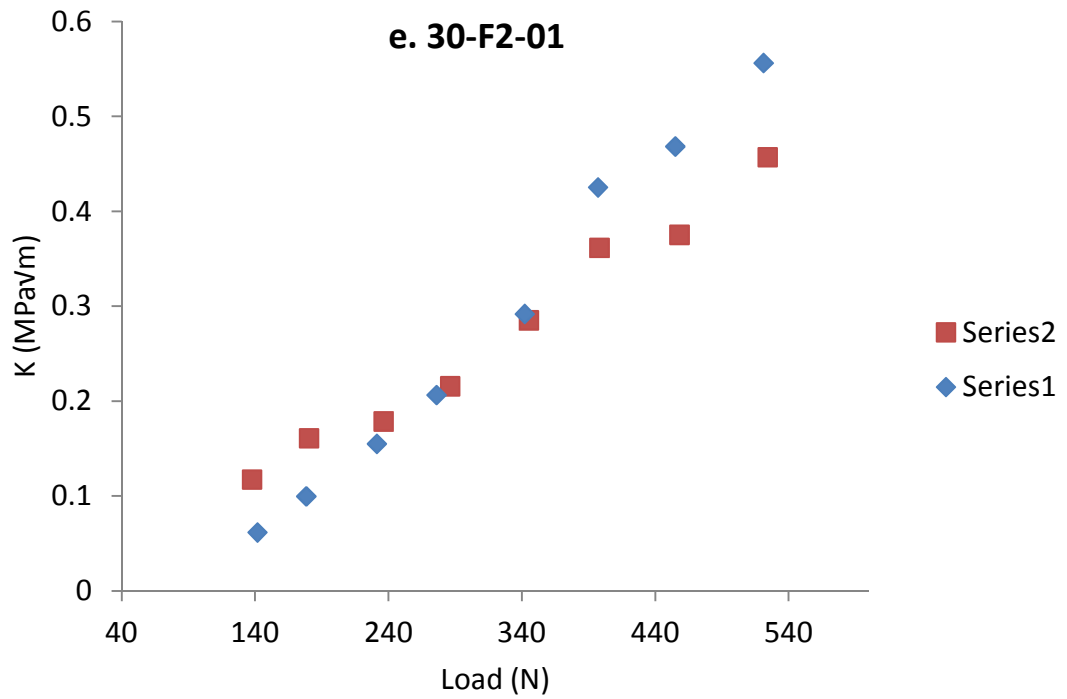
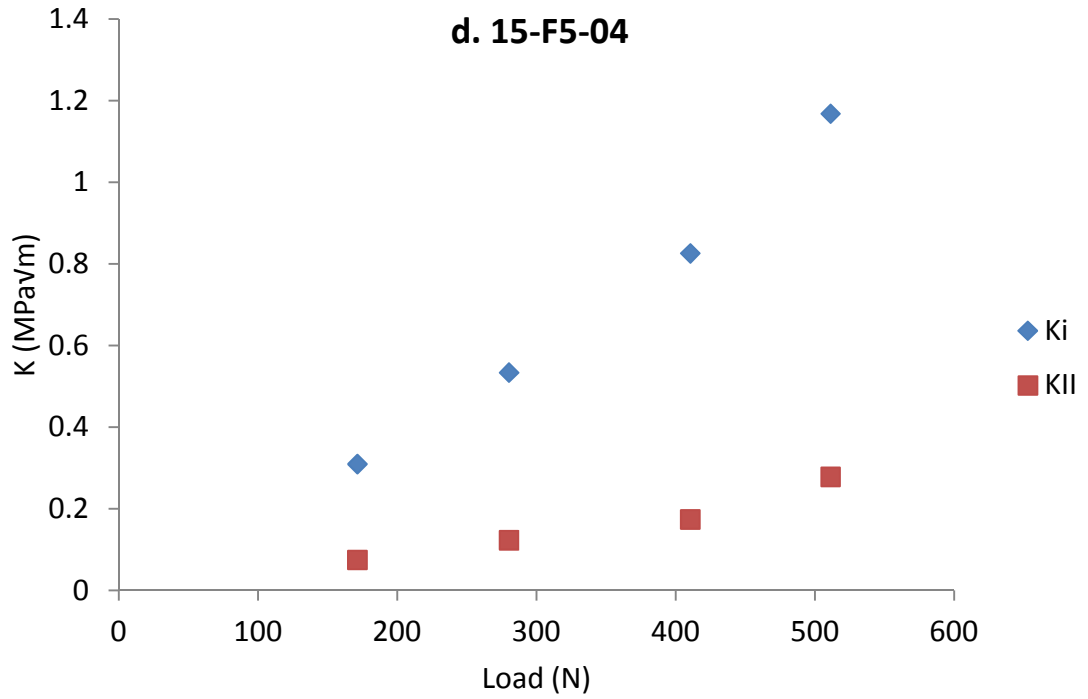


Figure 7.1 continued...

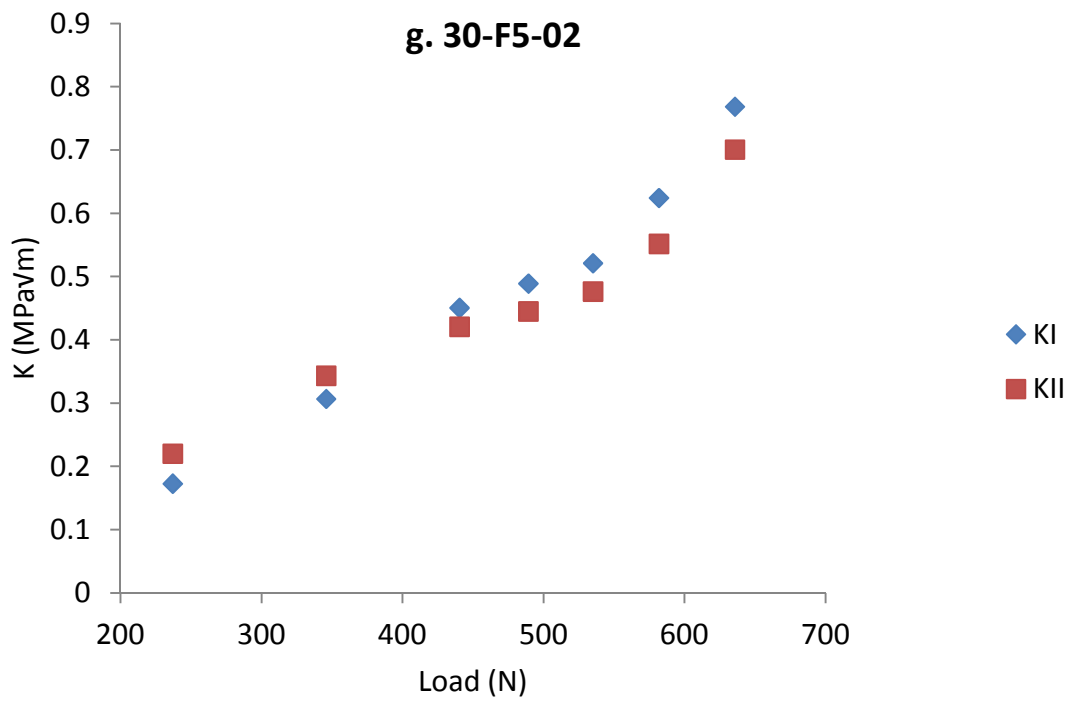
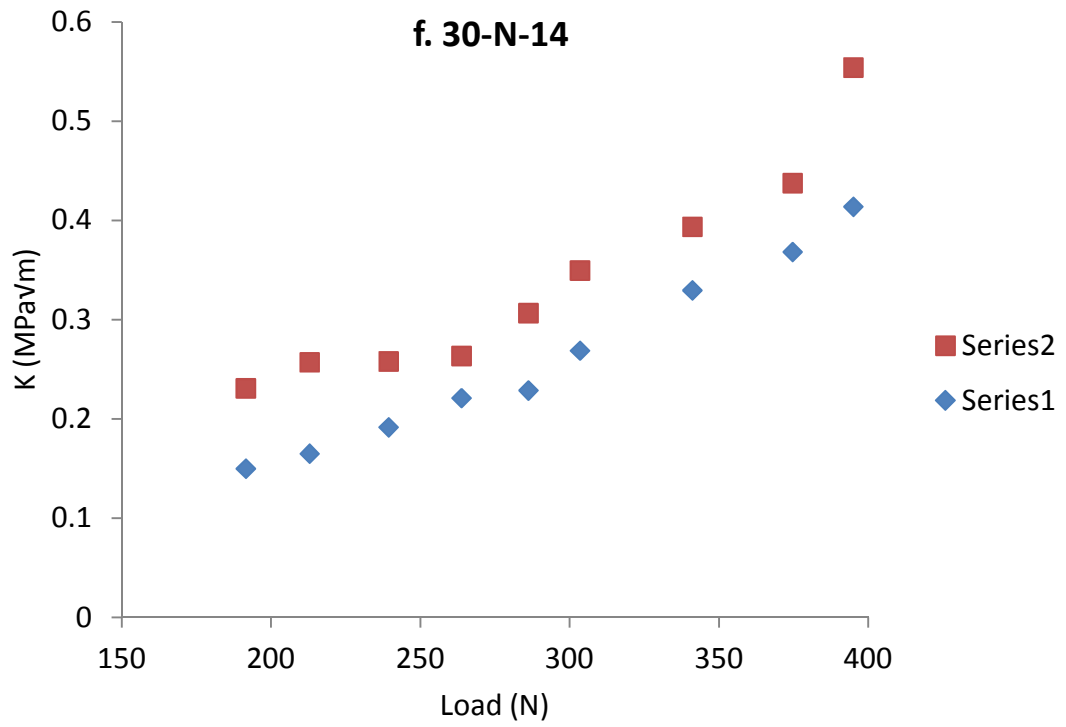


Figure 7.1 continued...

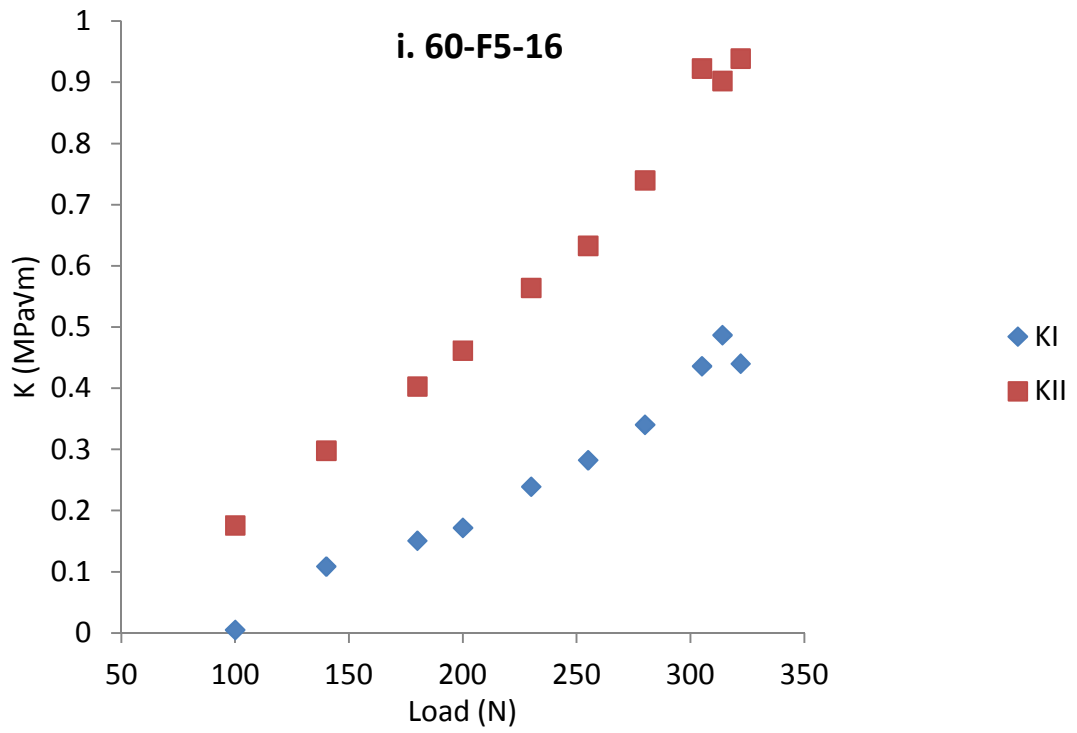
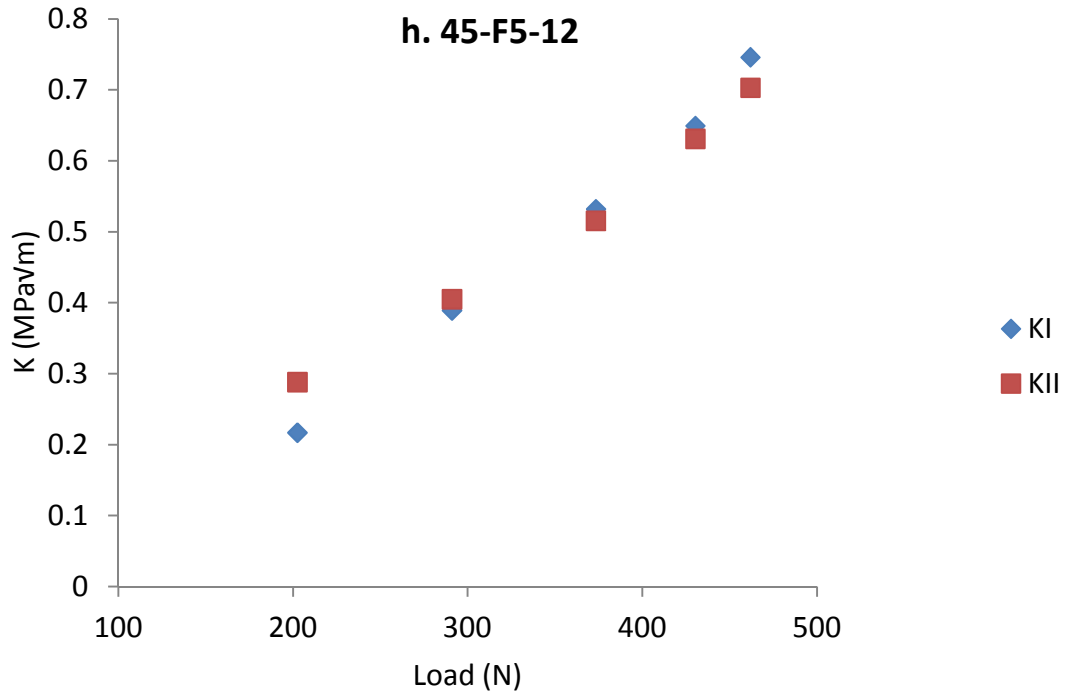


Figure 7.1 continued...

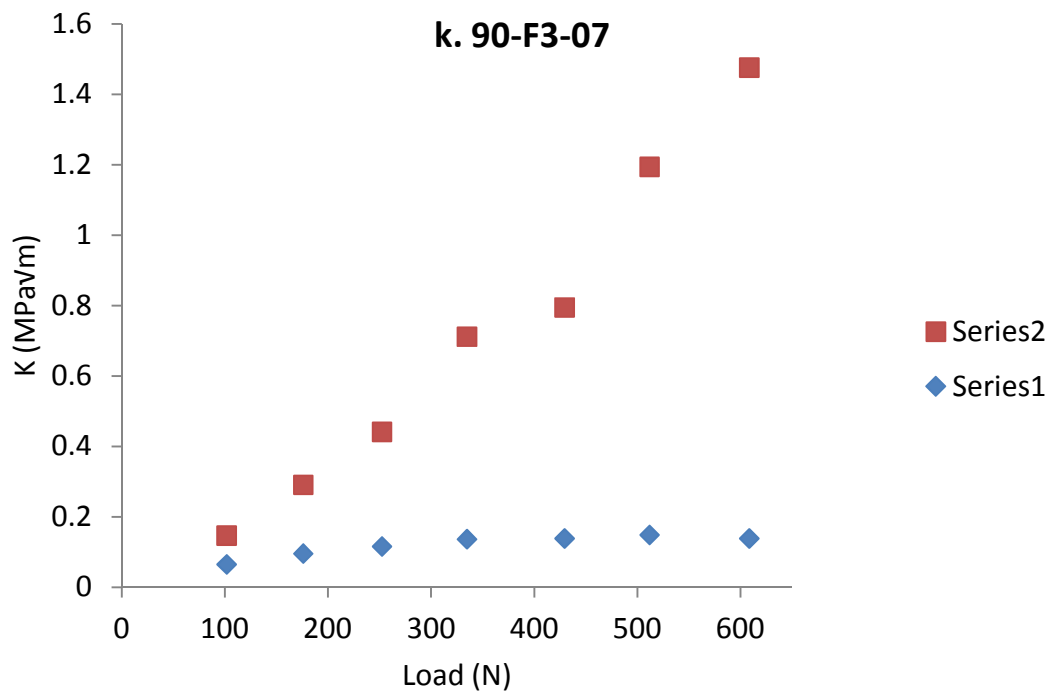
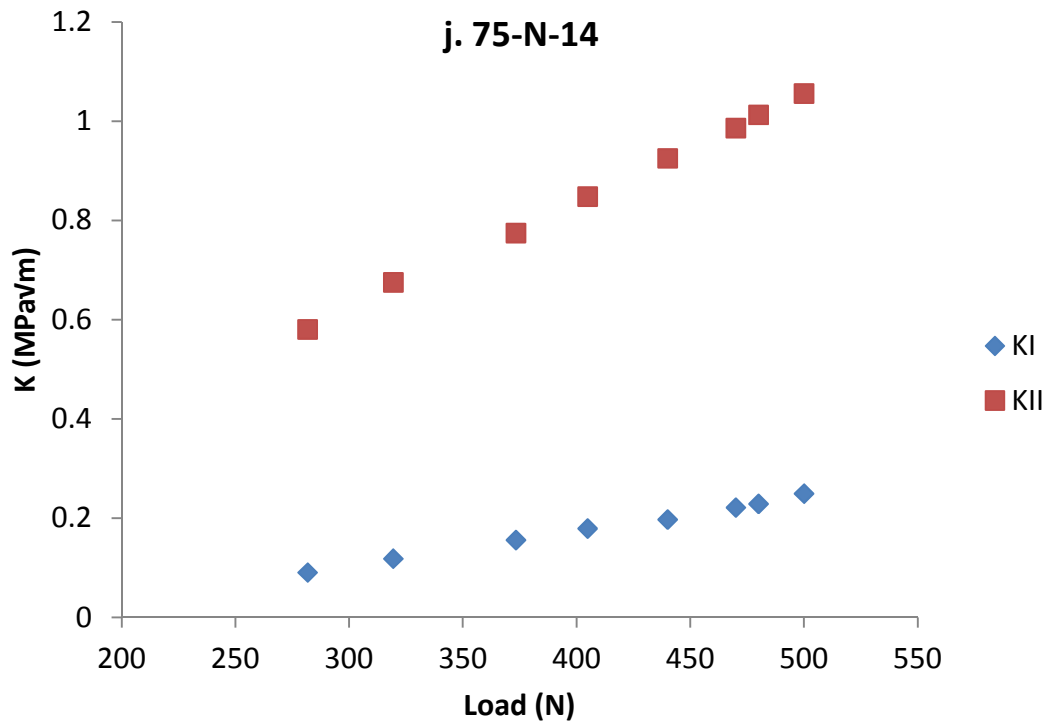


Figure 7.1 continued...

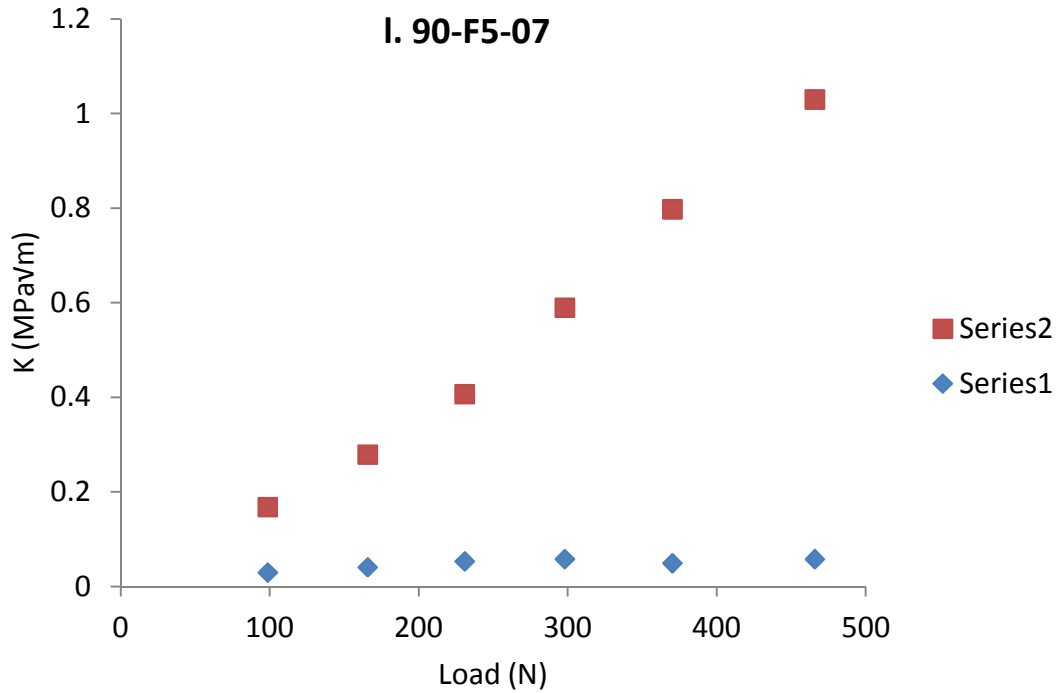


Figure 7.1 – Stress intensity factors extracted throughout loading for a number of specimens

Figure 7.1 shows that the near-critical nonlinearity in stress intensity factors, experienced in the mode I specimens (section 5.3.6), was mostly not observed in these specimens. However, it can be seen that the stress intensity factors did not linearly increase from zero; the mode mixity ratio can be seen to change throughout the course of loading. The cause of this is thought to be due to the inherent elasticity of the materials, which allows the crack-tip to change in angle. Analysis of the load data supports this assessment; whilst the load data obtained from pure mode I tests were linear throughout the duration of loading, the load curves for the Arcan specimens showed some nonlinearity. An example load curve is shown in figure 7.2. The JJ Lloyd T22K electric screw-driven test-frame employed for all the mixed-mode tests is operating at its lowest displacement rate, at around 5% of its maximum load rating (of 20kN) and is known to reliably and consistently load at a constant rate of displacement.

45-f5-14

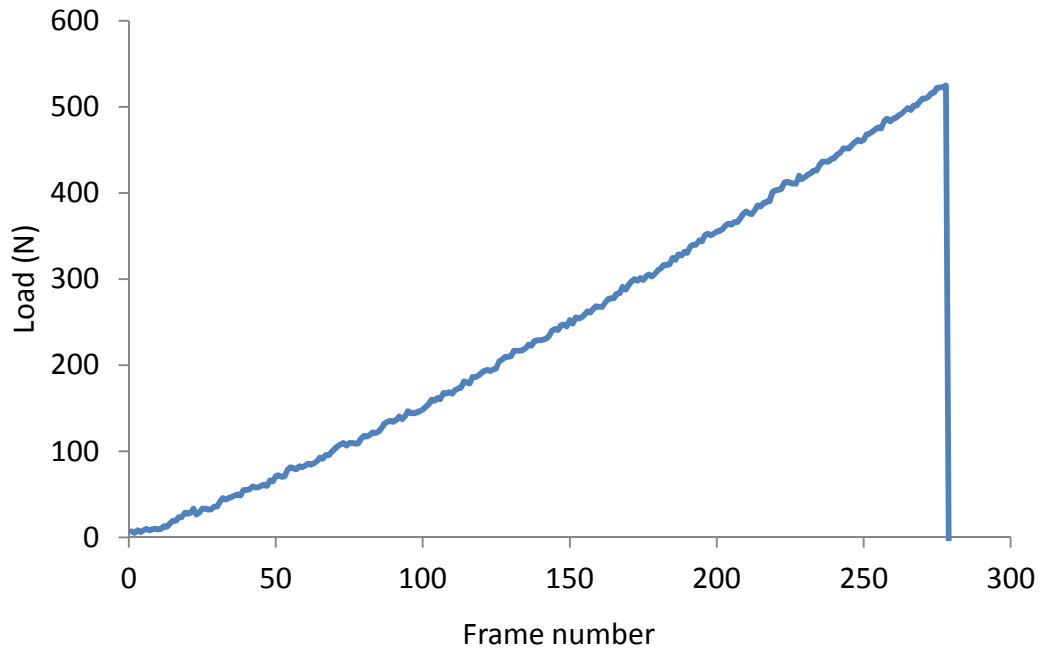


Figure 7.2 – Load curve against frame number (directly proportional to crosshead displacement) for specimen 45-F5-14

7.2.2 Critical values

The compact tension specimens tested in chapter 4 and discussed in chapter 5, exhibited subcritical crack growth. All the mixed-mode specimens tested were inspected for sub-critical crack growth using the acquired image data. Arcan-type specimens tested at 0° (i.e. pure mode I) were observed to exhibit subcritical crack growth as critical failure was approached. Specimens loaded at 30° and above, i.e. approximately $K_{II}/K_I > 1$, all failed suddenly, with no subcritical crack growth. A small number of specimens loaded at 15° showed some signs of subcritical crack growth.

A benefit of the parameter extraction method is that it does not require the crack lengths or loading angles to be perfect since the stress intensity values are measured directly. The DICITAC method has been validated for modes I and II [112], and quantitatively assessed for the pure mode I case with the materials studied here (in chapter 5). Consequently the determination of stress intensity values from load

measurements was not a priority and so theoretical values were determined for a limited number of specimens.

The normal method to determine stress intensity factors involves using tabulated shape functions, almost always derived from finite element analyses. The tabulated shape functions for Arcan-style mixed-mode (I/II) specimens with edge cracks are generally tabulated for various values of a/w ; the crack length to specimen width ratio. In metallic specimens, where starter cracks tend to be applied by (pure mode I) fatigue loading, initial crack length can be closely controlled. In polymer specimens with razor-tapped cracks, this is not the case; values of a/w inherently vary between specimens. Normalised stress intensity factors from the literature for angled edge-cracked specimens loaded axially are reproduced in figure 7.3.

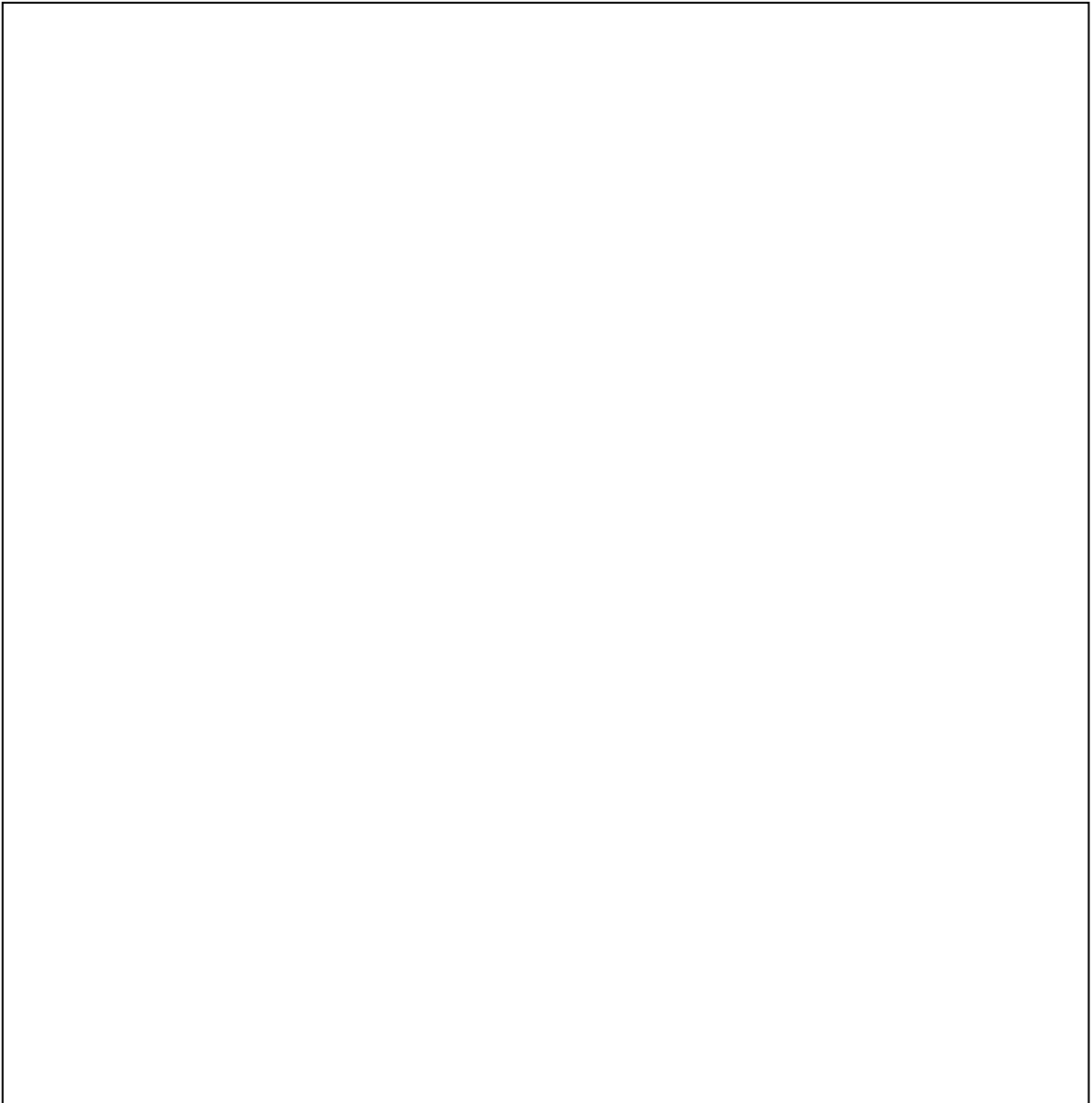


Figure 7.3 - Theoretical stress intensity values, varying with loading angle (and α) for the angled edge-cracked specimens subject to uniaxial loading (from [71])

The tabulated data from Richard [71] and Heydari *et al.* [130] both present the same values for mode I and mode II normalised stress intensity factors for angled cracks loaded in Compact shear and Arcan-type orientations. Using approximate shape functions from these studies, ‘theoretical’ stress intensity factors were determined for a small number of specimens. Results are presented in figure 7.4; the ‘theoretical’ values determined from approximate shape functions have been labelled as “LOAD” and have been compared with values determined using DICITAC. Details of the derivation of these values can be found in the appendix, section 11.3.

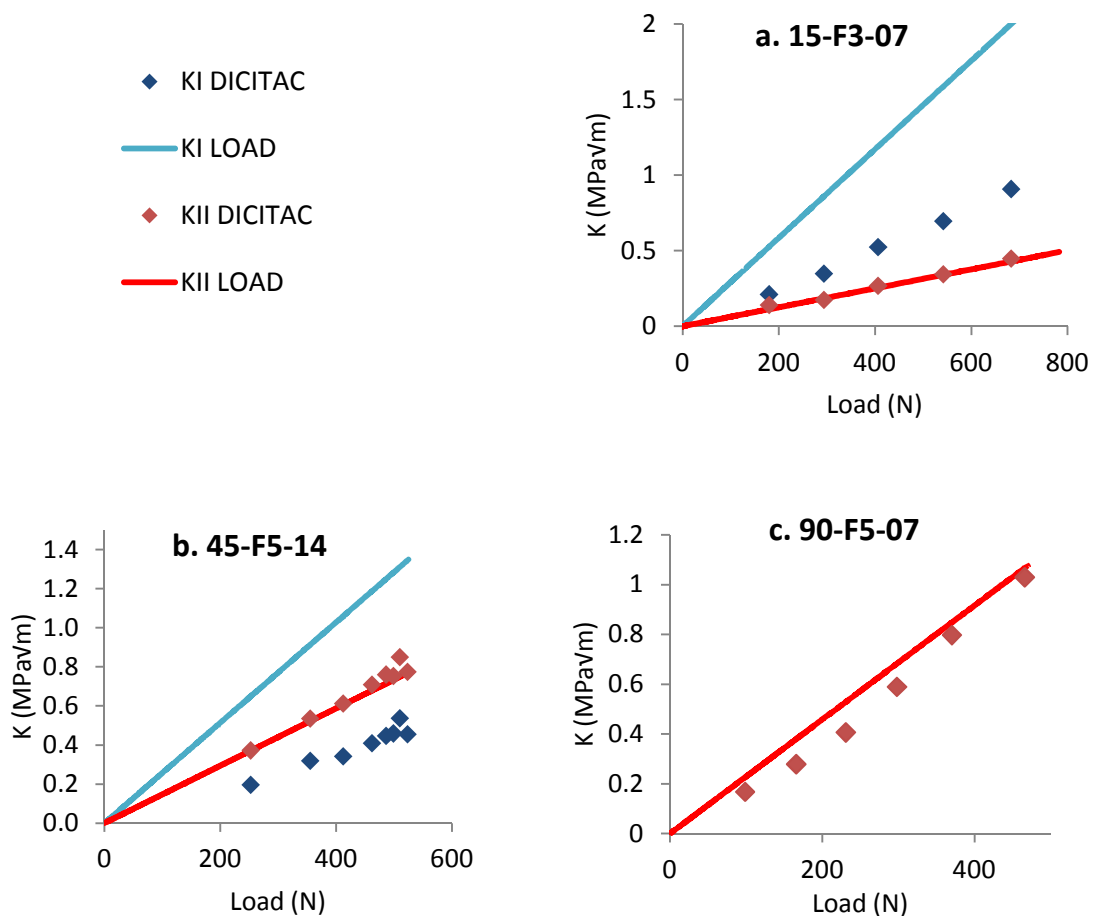


Figure 7.4 - Load based theoretical mixed-mode stress intensity factors against values measured using DICITAC for three specimens at a. 15°, b. 45° and c. 90° loading angles

Figure 7.4 shows mode II stress intensity factors for all specimens to be remarkably close to those predicted by the FE method, but shows significant disparity between

K_I values from the two methods for the 15° and 45° loading cases. The K_I values determined with the FE shape functions are consistently lower than those determined with DICITAC. DICITAC has been validated for both mode I and mode II stress intensity factor measurement [112] and no such problems were experienced, nor were they experienced in the validation in chapter 5. It was felt that any disparity between the theoretical and measured values in this case lies with the fault of the theory and not the direct measurements. As will be seen in chapter 8, the measured values of K_{II}/K_I strongly support the kink angles measured directly from individual broken specimens

The work of Sutton *et al.* [131] defines a remote mode mixity β as equation (7.1) thus:

$$\beta = \arctan\left(\frac{K_{II}}{K_I}\right) \quad (7.1)$$

where all terms have their usual meaning. The study finds the approximation that the remote mode mixity is equivalent to the local mode mixity (which they measure using a CTOD method), and also to the loading angle ϕ . Values determined using DICITAC for all the specimens tested in this study are presented in figure 7.5. Since the arctan function is periodic, where negative values of K_I have been measured, the resultant negative β values have been translated to show values of β greater than 90°. This has only been required when $K_I \approx 0$ but has been measured as a negative value; such as specimen 90-N-09 in which $K_I = -0.027$ and $K_{II} = 1.565$ as determined by DICITAC. Instead of an angle of $\arctan(1.565/-0.027) = -89.01$ being recorded, a more representative angle of 90.99° has been recorded for β instead. Negative values of K_I are not physically meaningful as stress intensity factors; instead they are related to \pm error at zero. Values that are any more negative than the inherent scatter of the technique (i.e. $\pm 0.03 \text{ MPa}\sqrt{\text{m}}$) are thought to be related to crack closure in some specimens.

Figure 7.5 shows mode mixity angles for all specimens fall close to the line $\beta = \phi$.

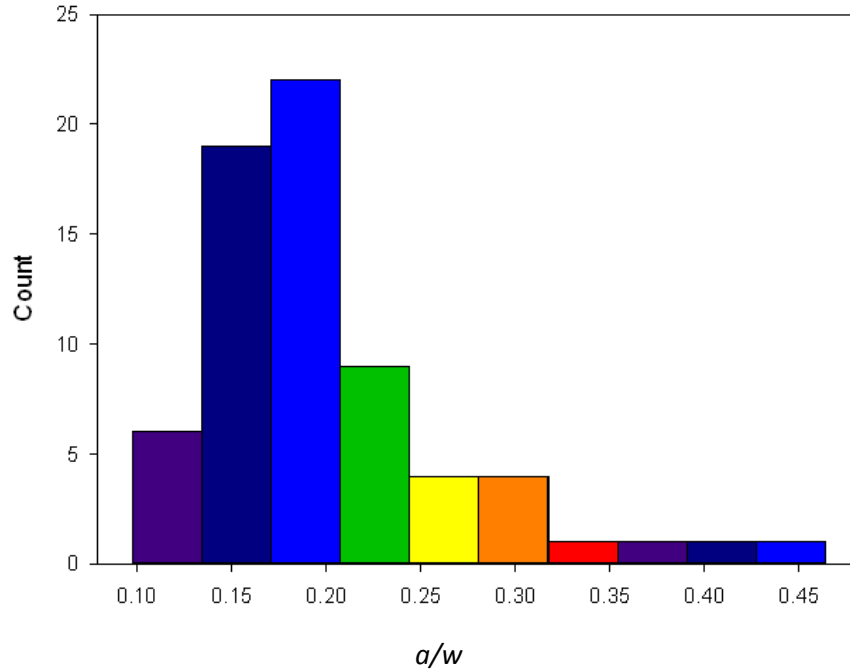


Figure 7.6 - Histogram illustrating a/w values across all specimens

K_I and K_{II} values at failure, K_{IQ} and K_{IIQ} , (the subscript Q referring to the value at failure load Q , not to be confused with subscript c referring to a material toughness value) were taken immediately prior to fracture and plotted against loading angle for all materials. These are presented in figures 7.7a-e.

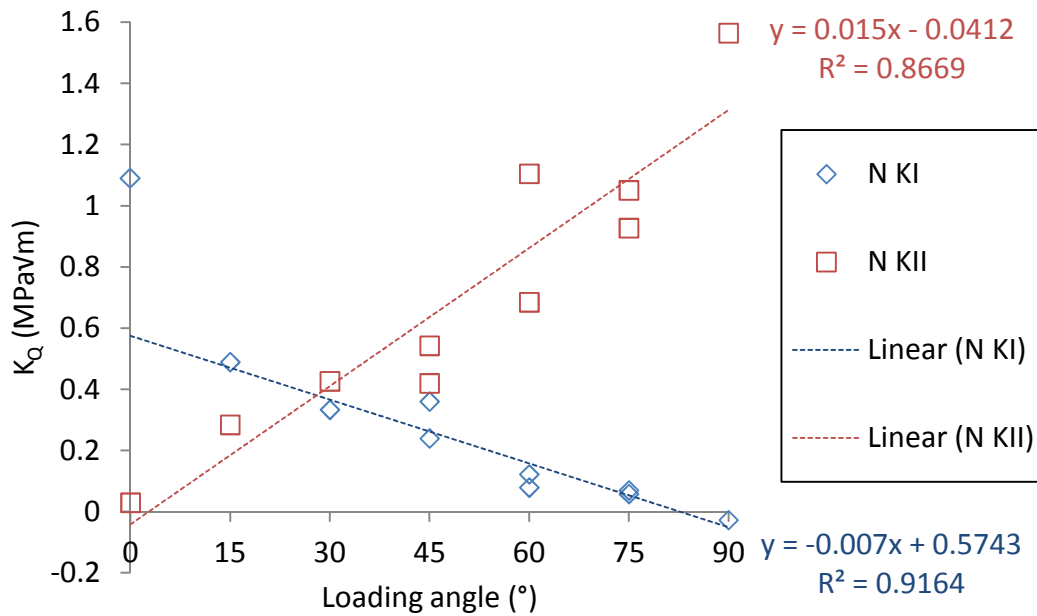
The data show a roughly linear relationship between loading angle and critical stress intensity factor. This is especially apparent for K_{IIQ} . Least-square linear regression lines have been applied to these data to aid statistical processing.

Failure values are naturally subject to scatter, especially so in the case of mixed-mode loading since failure is sudden and of a kinking nature.

Whilst normalised stress intensity factors at equivalent loads are expected to follow curves such as those reproduced in figures 7.3, failure points would not be expected to follow this behaviour. Instead, they are expected to follow a failure envelope based on the material mode I and II toughness values. Figures 7.7 show both mode I and II components to contribute toward failure, as expected. As loading angle is increased, there is a steady, apparently linear, increase in mode II stress intensity factor (at failure) and equivalently a reduction in mode I stress intensity factor.

Linear regression curves have been applied to the data for both mode I and II in all specimens, however the value of K_{IQ} at pure mode I loading (i.e. 0°) has been excluded from the regression curves. This is discussed in some detail in section 7.2.3.

a. NEAT



b. F2

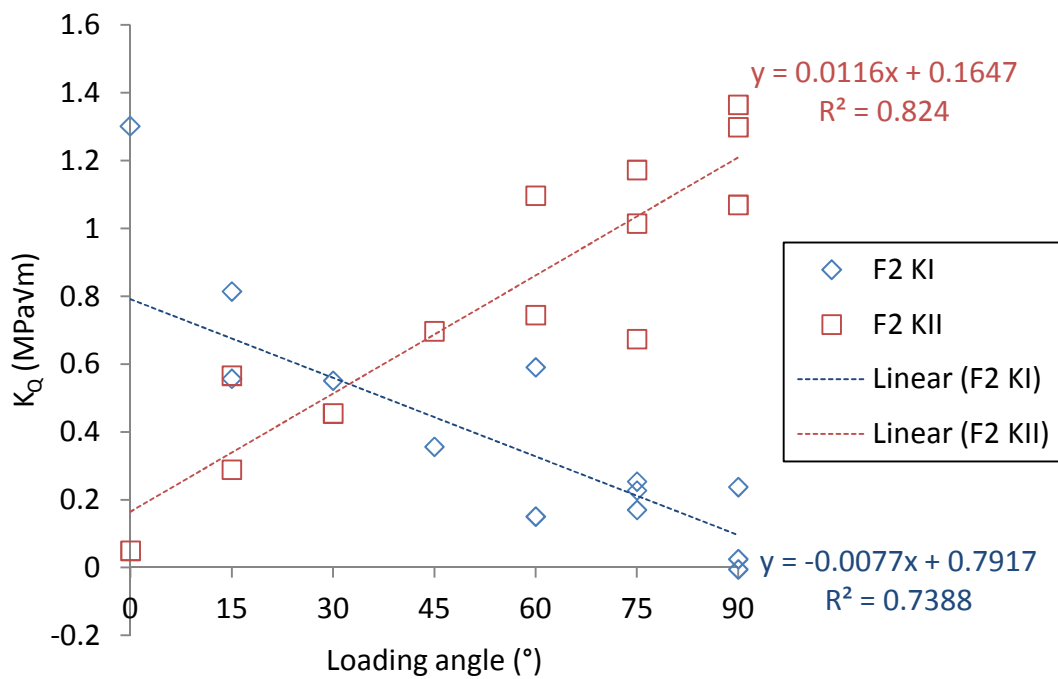


Figure 7.7 continued...

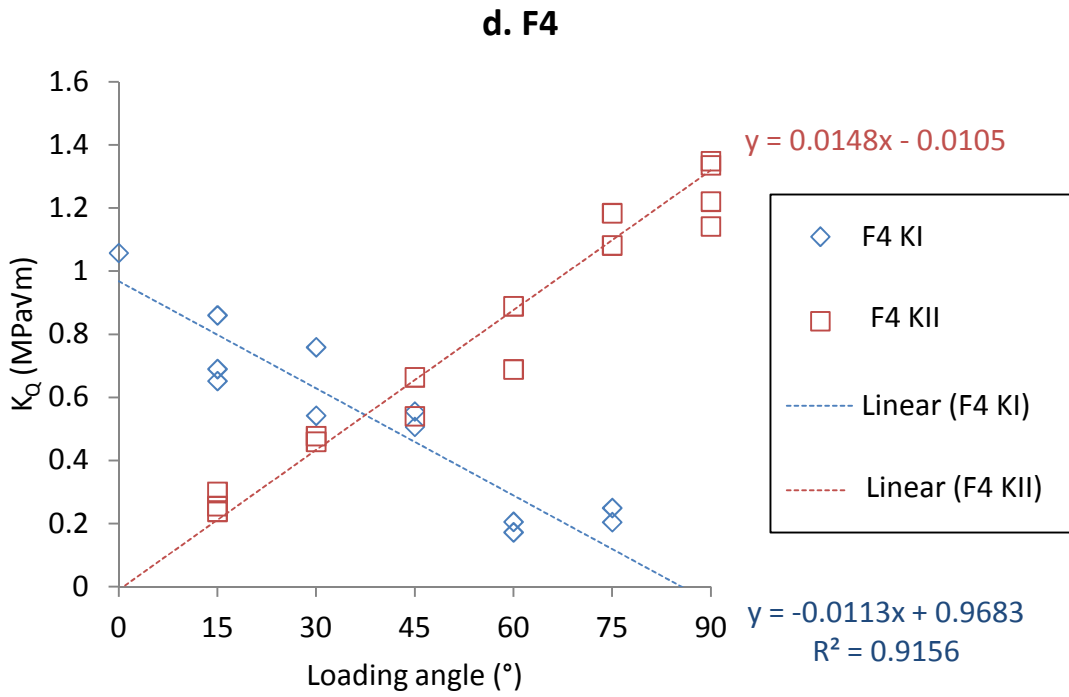
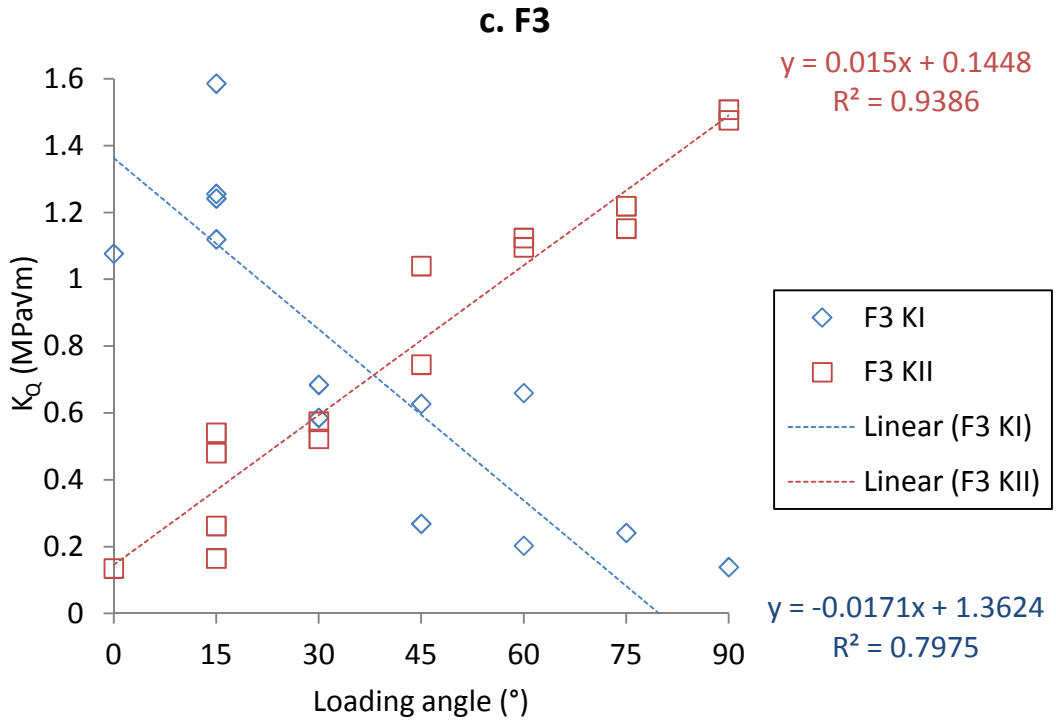


Figure 7.7 continued...

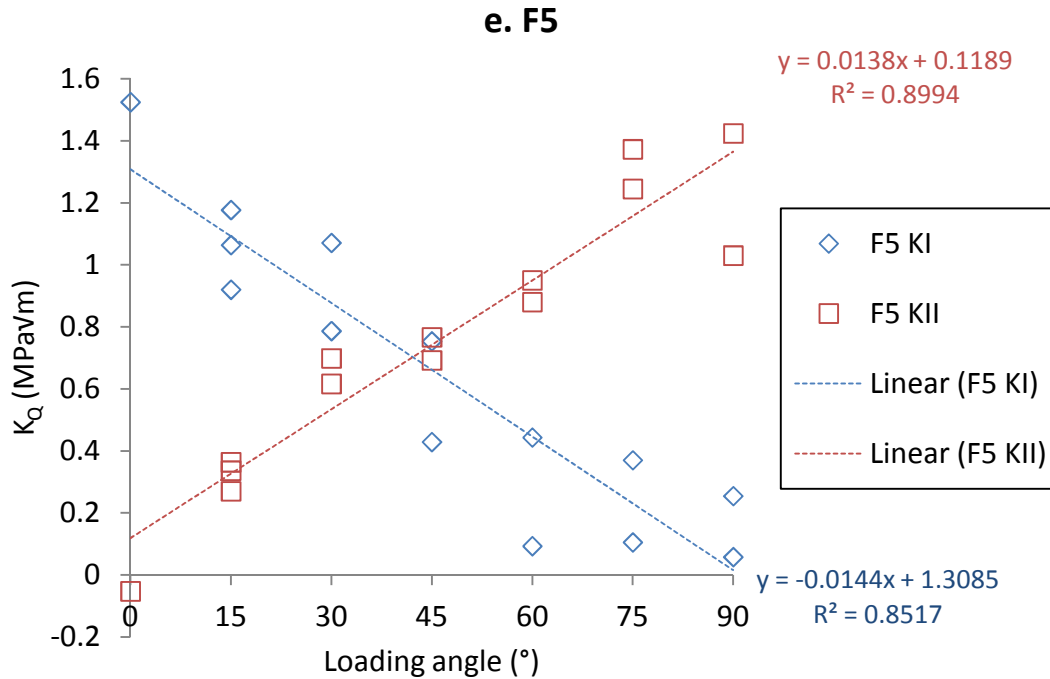


Figure 7.7 – Critical stress intensity factors for all specimens of each material against loading angle

7.2.2.1 Comments on the pure mode II specimens

As mentioned briefly in section 3.4, the Williams stress solutions are valid for traction-free cracks, which the specimens loaded at 90° are not necessarily. Additionally, it was noticed that the crack-tip locating algorithm sometimes failed to locate cracks in the 90° specimens. However, the stress intensity values from the 90° specimens appear consistent, but it is suspected that their results, especially in terms of K_{II}/K_I , could be less accurate than the other mixed-mode I/II and pure mode I data, especially in cases of significant negative measured K_{II} values.

7.2.3 Linear regression in K_{IQ} and K_{IIQ}

The empirical mixed-mode failure envelope describes failure occurring when the sum of the fraction of stress intensity over material toughness, i.e. the sum of K_I/K_{Ic} and K_{II}/K_{IIc} , is equal to one, where each fraction is to the power of an appropriate, empirically observed value. The fracture envelope is discussed further in section 7.3 but the equation is presented, thus:

$$\left(\frac{K_I}{K_{Ic}}\right)^m + \left(\frac{K_{II}}{K_{IIc}}\right)^n = 1 \quad (7.2)$$

Initial observation of the results in figures 7.7 show a strongly linear relationship between loading angle (and as explained earlier in this section, mode mixity β) and K_{IIQ} . This strongly suggests a power relationship of $n = 1$ for equation 7.2.

Whilst K_{IIQ} at pure mode I loading is around zero, and can be seen to linearly increase as loading angle increases to 90° , the mode I behaviour is less consistent. The value of K_{IQ} at a zero degree loading angle is equivalent in most cases to the mode I fracture toughness as measured previously in standard compact tension specimens. During initial tests of the specimen, the DICITAC K_{IQ} values were measured using DICITAC prior to testing the rest of the specimens, as a check of the suitability of the specimen. The first values tested were within experimental error of the standard CT specimen values and so whilst two or more specimens were tested for the mixed-mode specimens, only one specimen of each material was tested at zero degrees. The zero-degree test for F5 can be seen to be significantly higher than the compact tension measured K_{Ic} value.

The mode I critical data does not follow the same linear relationship as the mode II critical stress intensity factors. Examination of the mixed-mode failure envelope suggested two options be considered. The first is that the value of m in equation 7.2 varies between materials, perhaps equal to 0.5 for NEAT and F2 resins, and 1 for F4 and F5 resins. Powers used in the mixed-mode envelope method found in the literature are all integer values and are not seen to vary between different formulations of similar materials. The results from the F3 resin show behaviour that is inconsistent with the mixed-mode failure envelope; that measured K_{IQ} values for each of four specimens loaded at 15° were measured as being above the plane strain mode I fracture toughness, K_{Ic} of the material, despite non-zero values of K_{IIQ} . This behaviour leads into the second option; that under mixed-mode loading, the true plane-strain fracture toughness is not a good measure of fracture toughness.

It is thought that the multitude of different toughening mechanisms present in a particulate toughened thermoset (described in sections 2.6 and 5.8) contribute differently in pure mode I and mixed-mode I/II cracks. The kinking failure of cracks subjected to non-zero shear components is very different to the more progressive onset of crack-growth associated with failure in pure mode I specimens. Crack-pinning, particle bridging and crack-path deflection have all been attributed to providing improvements in toughness, and hence resistance to fracture, in particulate toughened materials under pure mode I loading. It is reasonable to deduce that the efficacy of each of these mechanisms is affected by shear loading. As a consequence of this, it is postulated that K_{Ic} does not represent the resistance to fracture by mode I loading when shear is present in materials of the types studied here. An alternative value is proposed in section 7.3.

7.2.4 Using K_{II}/K_I instead of loading angle

As a mode II component was introduced, the Arcan specimens stress intensity values at fracture (figures 7.7) were significantly more scattered than experienced in the pure mode I tests in section 5.3.5. This additional scatter is unsurprising considering the brittle nature of the material and the more sudden, crack kinking nature of failure, and also the way these data have been collated and presented ignoring differences in crack length ratio α .

Whilst the crack loading angle is a convenient measure of how the specimens were loaded, small variations in crack length or crack tip angle are not accounted for. Examining data relative to loading angle in some respects mirrors the feeling that the level of mode mixity can be determined from the net specimen geometry and loading angle. One of the findings of this study is that stress intensity factors and T -stresses, including the ratio of K_{II}/K_I , appear to be functions of more than the net geometry alone. As such, it seems sensible to present this data in terms of the measured K_{II}/K_I values, rather than the method by which we have applied them.

Measured values of K_{II}/K_I are plotted against loading angle in figure 7.8. It can be seen that there are considerable difference in K_{II}/K_I at each loading angle, in some cases spanning two magnitudes.

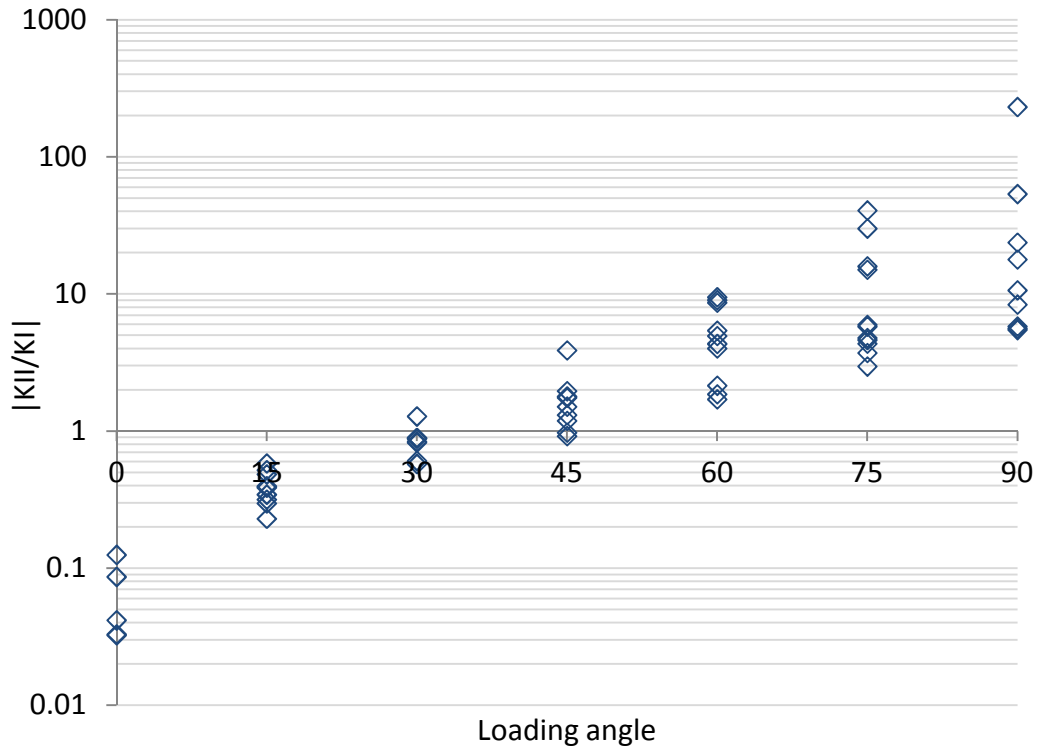
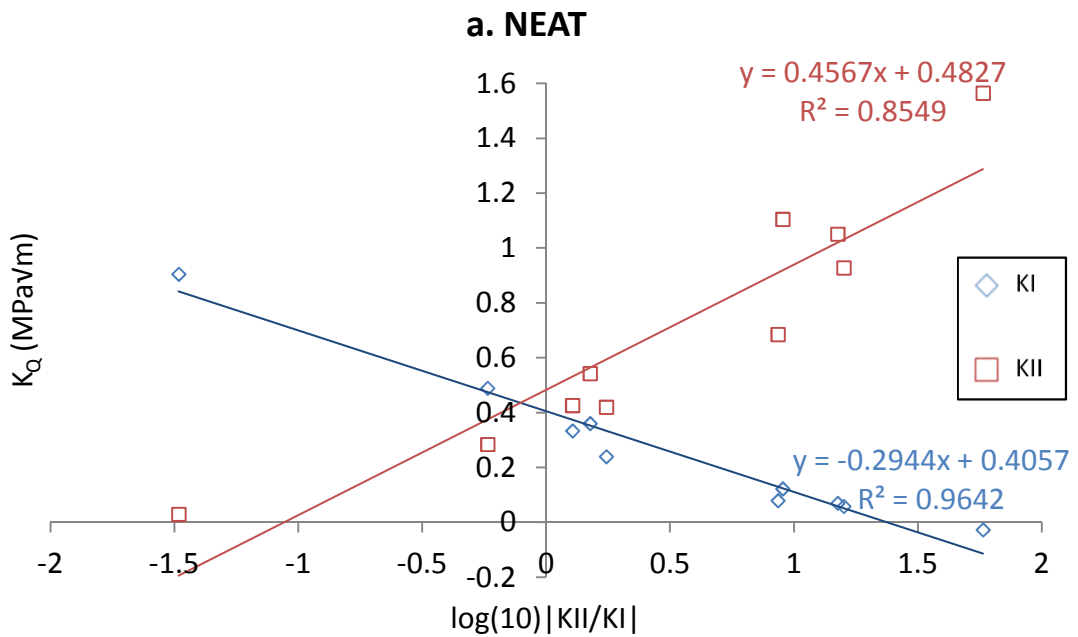
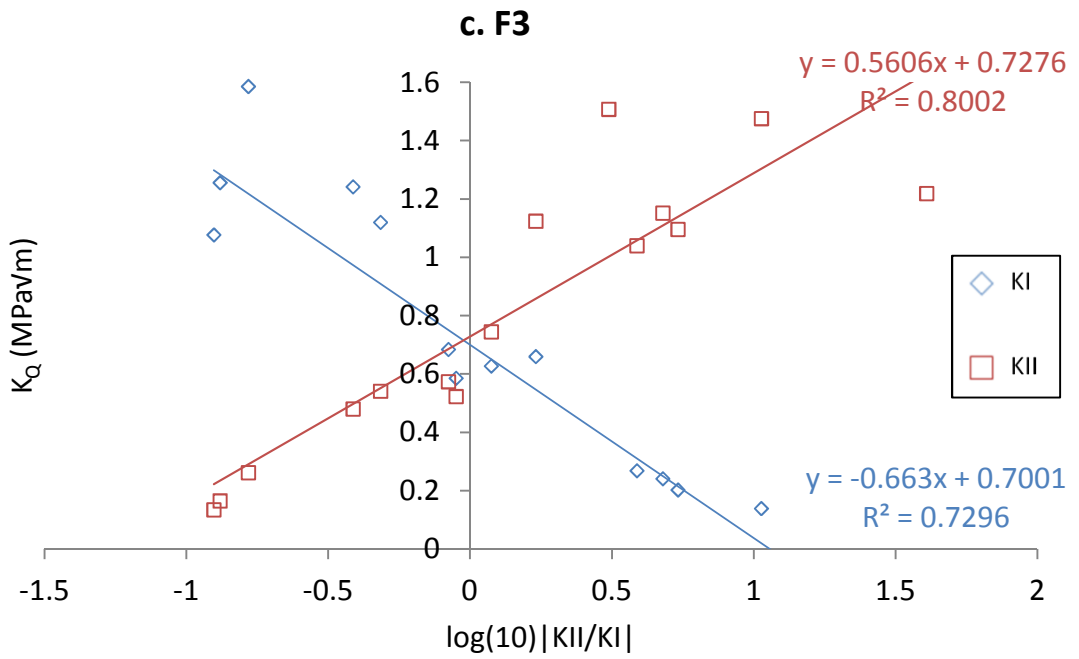
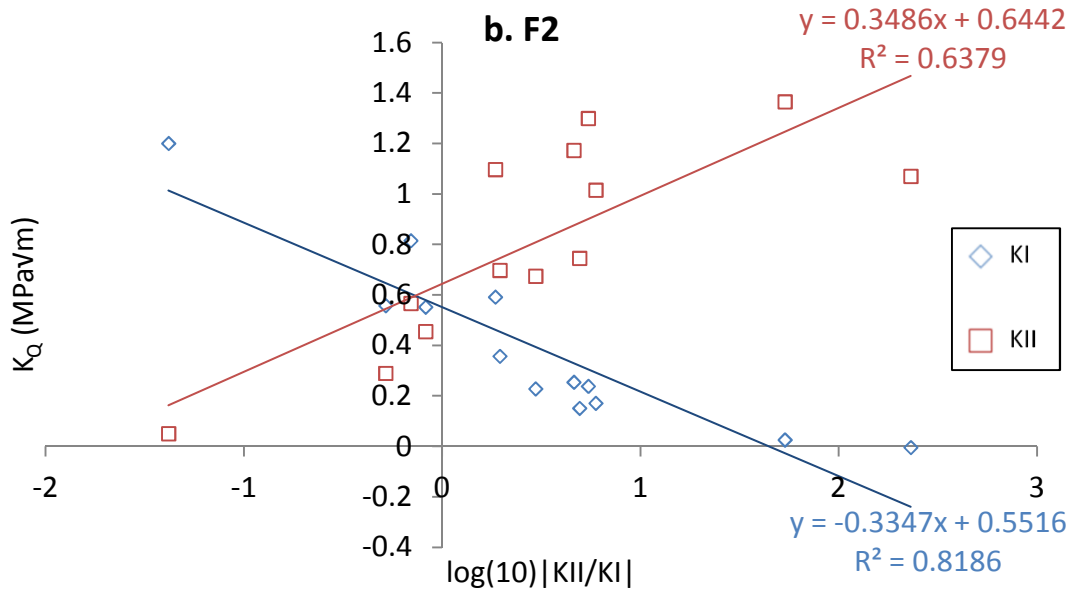


Figure 7.8 - Loading angle against measured K_{II}/K_I (logarithmic scale)

An unfortunate consequence of comparing failure values against K_{II}/K_I instead of loading angle is that +/- errors in K_I and K_{II} measurement become vastly increased. Despite this, K_{IQ} and K_{IIQ} against $\log_{10}|K_{IIQ}/K_{IQ}|$ are presented in figures 7.9a-e.





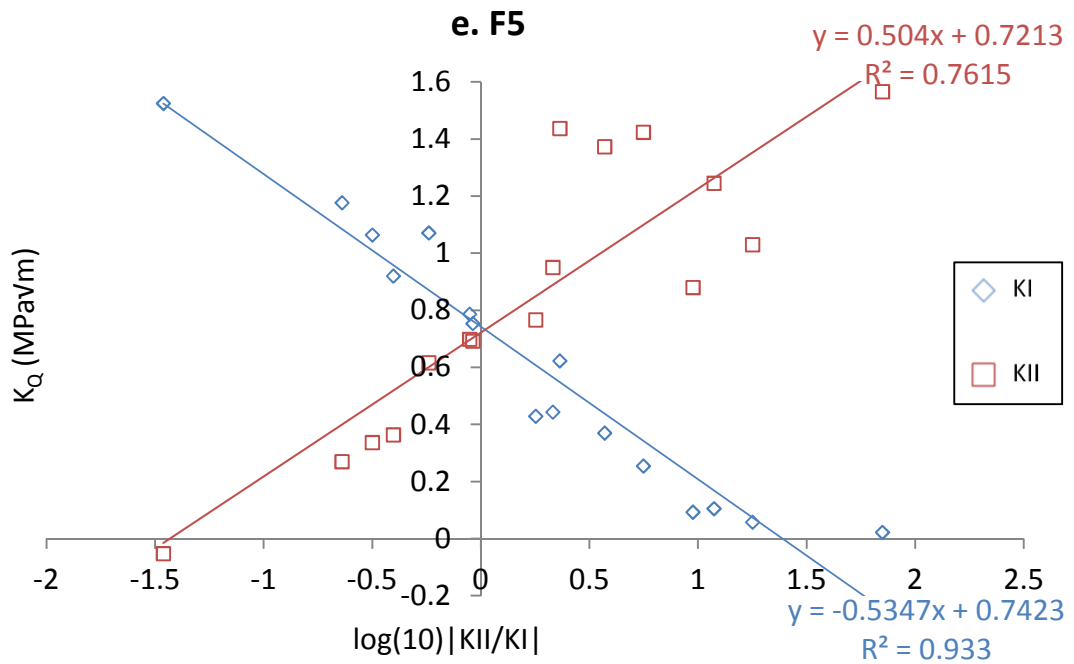
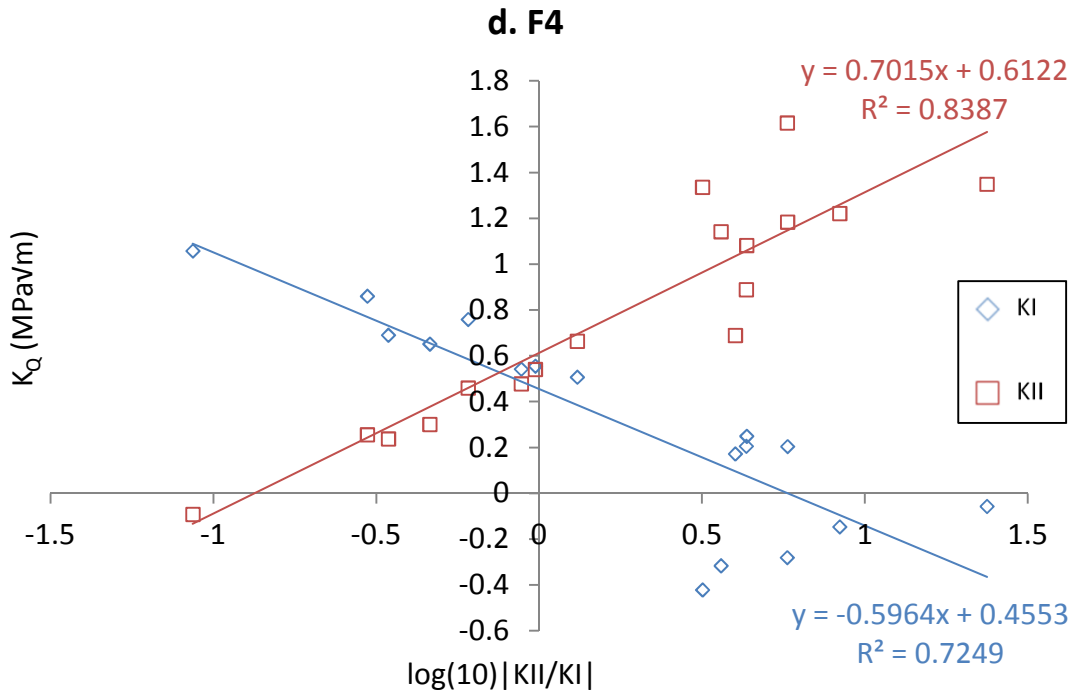


Figure 7.9 – Critical stress intensity values against $\log_{10}(K_{II}/K_I)$

Figures 7.9a-e show that the regression (albeit now logarithmic) trends are conserved when replacing loading angle with measured K_{II}/K_I , however there is a noticeable increase in scatter over the data presented in figures 7.7.

7.3 Determining K_{IIc} using an elliptical model for mixed-mode failure

As introduced in section 7.2.3, mixed-mode failure can be described by the elliptical function described in equation 7.3.

$$\left(\frac{K_{IQ}}{K_{Ic}}\right)^m + \left(\frac{K_{IIQ}}{K_{IIc}}\right)^n = 1 \quad (7.3)$$

Choosing appropriate power terms m and n gives an opportunity to determine K_{IIc} from mixed-mode results. As discussed in section 7.2.2.1 and will be further discussed in section 7.3.1, the mixed-mode tests performed here are not best-suited to measuring critical pure mode II values, and so the ability to determine a mode II toughness, K_{IIc} from all of the mixed-mode specimens is of great benefit.

As initial values, K_{IQ} , K_{Ic} (from compact tension tests), K_{IIQ} and an estimate of K_{IIc} , using the average K_{IIQ} at 90° loading, were input into equation 7.4 and the $1 + error$ term calculated for different values of m and n for all specimens. Likely values of m and n were taken from the literature as being 1 or 2. The $1 + error$ terms are plotted in figures 7.10. In addition to these figures being plotted, the average and standard deviations of the $1+error$ term across all specimens was calculated for each case. The closer these values are to 1, and the lower the standard deviation, the smaller the error and the better the fit of the powers. These results are shown in table 7.1.

$$\left(\frac{K_{IQ}}{K_{Ic}}\right)^m + \left(\frac{K_{IIQ}}{K_{IIc}}\right)^n = 1 + error \quad (7.4)$$

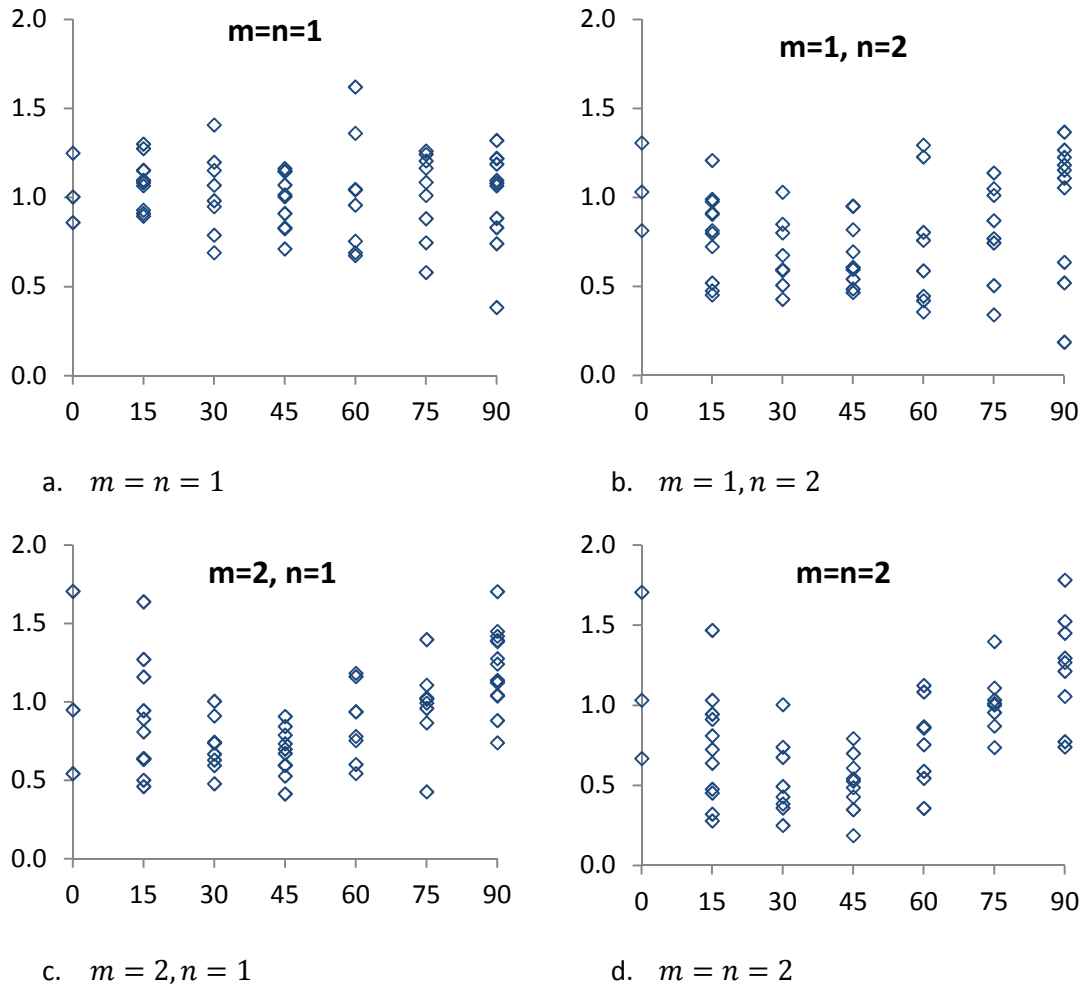


Figure 7.10 – 1+error plots for mixed mode fracture (equation 7.6) for different values of m and n

Table 7.1 - 1+error values

Values of m, n	Average (mean) 1+error	Standard deviation
$m=n=1$	0.96	0.211
$m=1, n=2$	0.86	0.370
$m=2, n=1$	0.86	0.431
$m=2, n=2$	0.92	0.321

The apparent linearity of the K_{I_Q} and K_{II_Q} data (against loading angle), and the minimum average and most consistent error values using $m = n = 1$ suggest these are the most appropriate values for consideration, and form the best description of the mixed-mode failure in the case of the tests performed.

Closer analysis of the K_{I_Q} and K_{II_Q} data and the mixed-mode failure envelope being analysed showed an interesting issue. As discussed in section 7.2.3, the K_{I_Q} linear

regression curves shown in figures 7.7a-e clearly do not all coincide with the mode I fracture toughness K_{Ic} at 0° loading. To describe the mixed-mode behaviour of the materials better, the concept of an alternative description of effective K_{Ic} will be introduced.

It has been established that the epoxies tested here kink toward tensile opening cracks when subjected to critical loading with a mode II component. To understand the materials' resistance to applied mode II loading, it is important to understand this crack kinking. It has been established that there is a large difference in fracture between the pure mode I case and when a small mode II component has been introduced. Furthermore, there are significant differences between different materials in this transition region. An effective mode I fracture toughness value for materials failing with stability-driven crack kinks when subjected to mixed-mode loading has been defined here as the value of the fitted K_{IQ} curves at a loading angle of 0° (pure mode I loading). This term has been coined $K_{IcMM-eff}$ (where MM-eff means 'mixed-mode effective'). This is illustrated in figure 7.11.

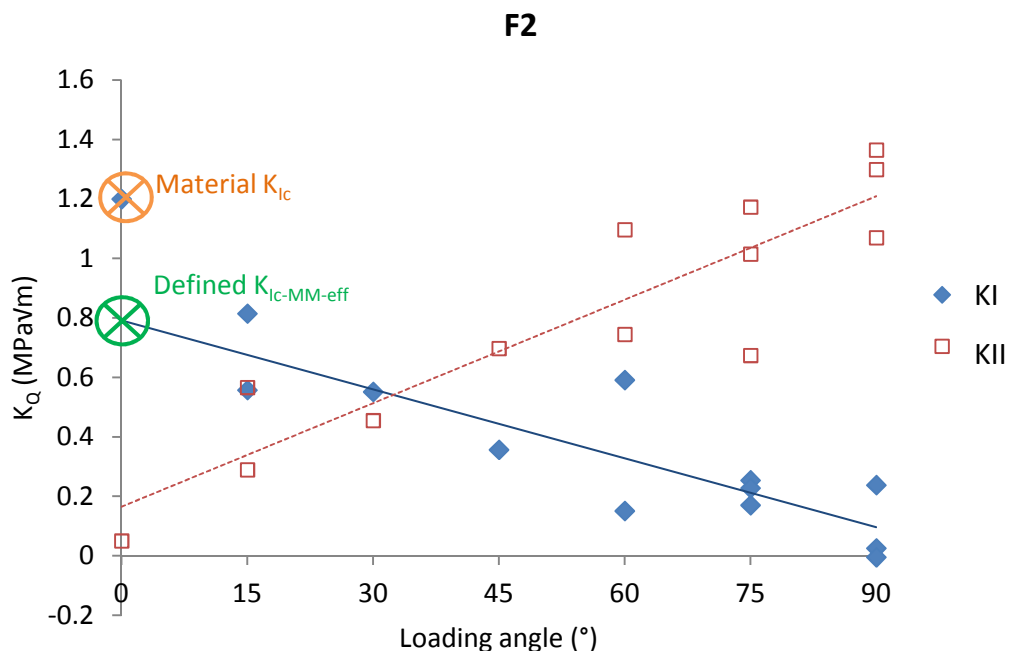


Figure 7.11 – Non linearity at pure mode I case highlighted. Illustrating the concept of effective mixed mode K_{Ic} , $K_{IcMM-eff}$ (mixed-mode) for materials with kink-related mixed-mode toughness

The multiple toughening mechanisms present in mode I cracks mentioned in section 5.8 are difficult to quantitatively attribute importance to. It is believed that these mechanisms behave differently when materials are subject to shear components. It is this that is thought to explain the lack of correlation between mode I bulk resin toughness and mode II composite toughness.

It is therefore thought that for mixed mode loading of relatively brittle kinking materials with significant microstructures and complex toughening mechanisms, equation 7.4 is not valid in its original form. Instead equation 7.5 is proposed in which K_{Ic} is replaced with $K_{IcMM-eff}$.

$$\left(\frac{K_{IQ}}{K_{IcMM-eff}}\right)^m + \left(\frac{K_{IIQ}}{K_{IIc}}\right)^n = 1 \quad (7.5)$$

Values of $K_{IcMM-eff}$ have been determined and are listed in table 7.2.

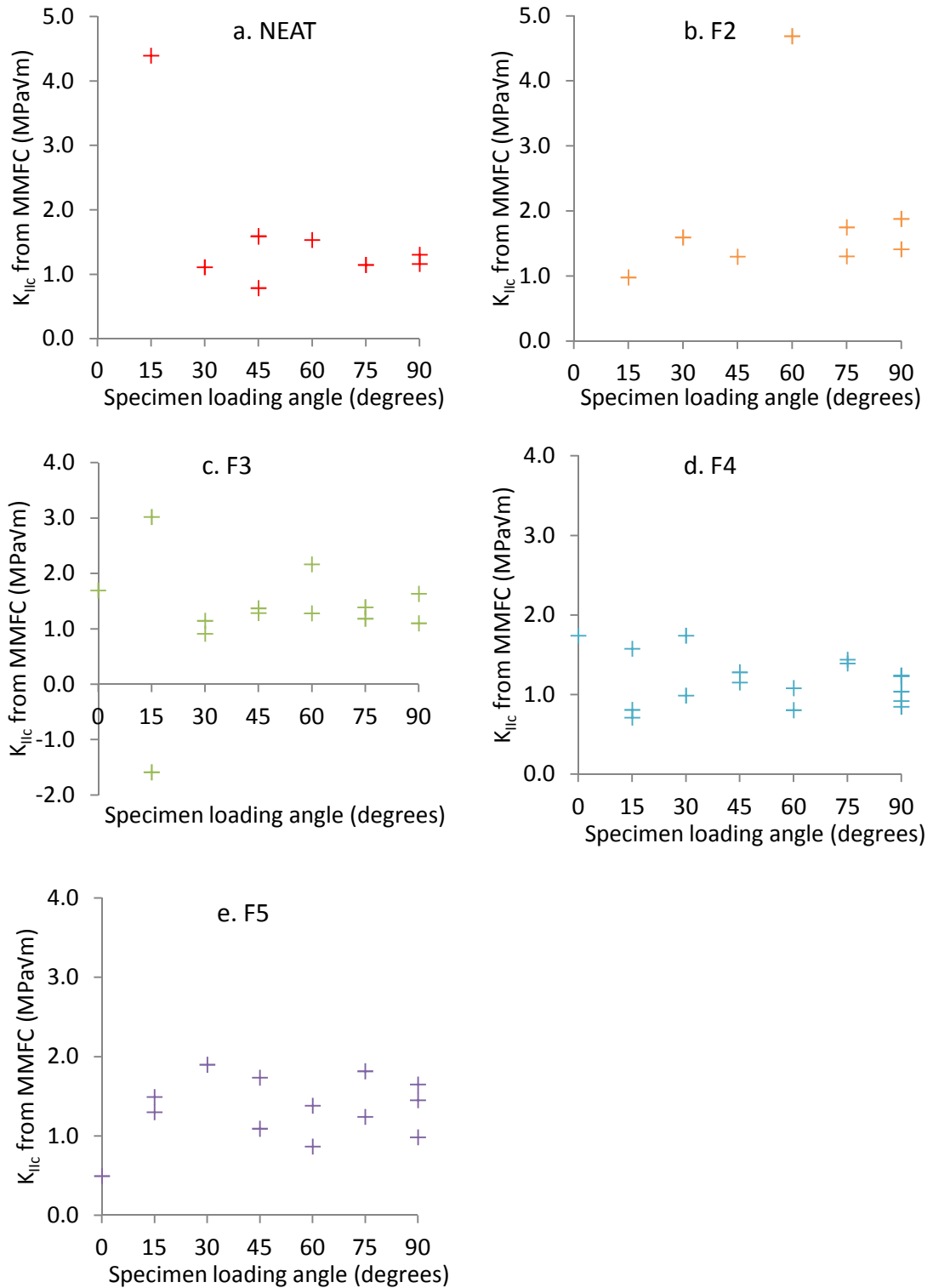
Table 7.2 - Effective mode I fracture toughness for mixed-mode loading; $K_{IcMM-eff}$

Material	K_{Ic} (MPa√m)	$K_{IcMM-eff}$ (MPa√m)
NEAT	0.95	0.626
F2	1.19	0.772
F3	1.33	1.354
F4	1.05	0.993
F5	1.25	1.075

Rearranging equation 7.5 (for $m = n = 1$) allows apparent values of K_{IIc} to be extrapolated from mixed-mode experiments, thus:

$$K_{IIc} = K_{IIQ} \left(1 - \left(\frac{K_{IQ}}{K_{IcMM-eff}}\right)\right)^{(-1)} \quad (7.6)$$

From this equation, replacing K_{Ic} with the new $K_{IcMM-eff}$ term, K_{IIc} values can be determined from each mixed mode specimen. These are shown in figures 7.12.



Figures 7.12 – K_{IIc} measured for each specimen from the Mixed-Mode Failure Criterion (MMFC).

As can be seen in figures 7.12a-e, lower loading angle specimens with low values of K_{IIQ} and high values of K_{IQ} the results are unsurprisingly more scattered due to the errors associated with dividing by small numbers. A spurious value in the F2 results

(figure 7.12-b) at 60° is apparent; since this specimen also exhibited an irregular shaped crack front this data point was excluded. Averaging values from 30° to 90° (excluding the aforementioned spurious value) give the following K_{IIc} values (table 7.3).

Table 7.3 - Apparent K_{IIc} values, as measured using mixed-mode technique

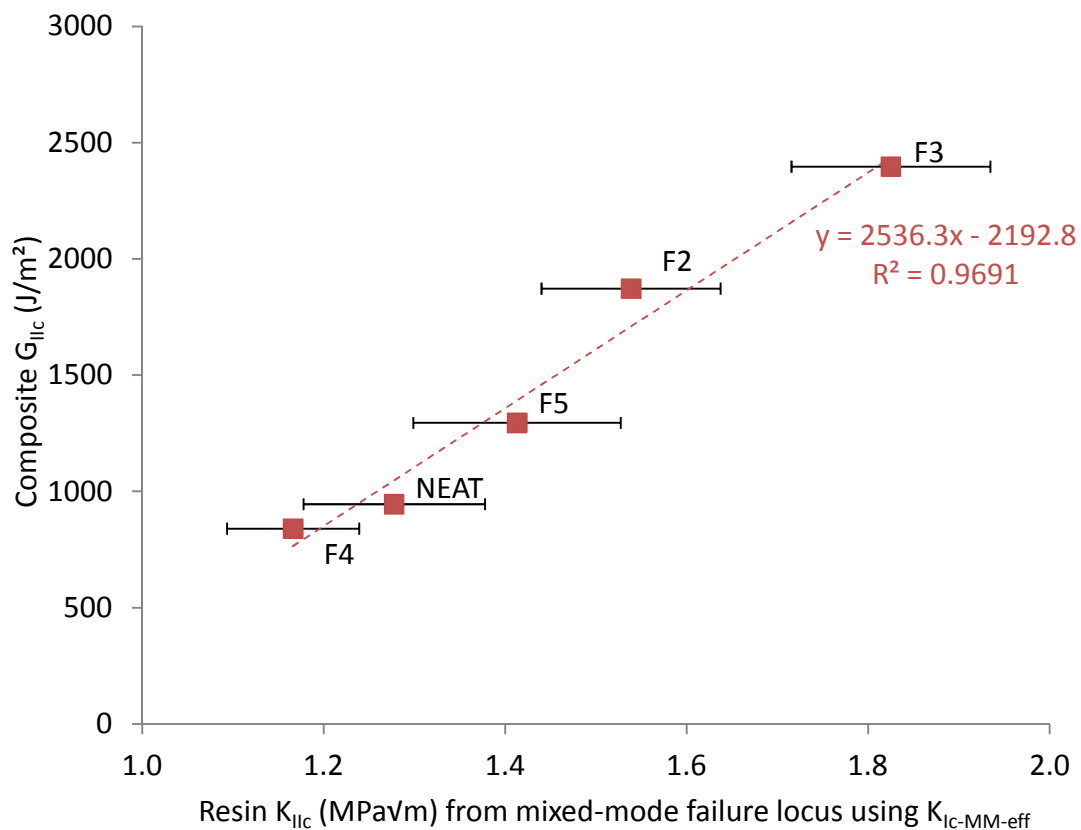
Material	Apparent K_{IIc} (MPa√m)	Standard deviation	Standard error: $SE_{\bar{x}} = s/\sqrt{n}$
NEAT	1.278	0.283	±0.100
F2	1.539	0.242	±0.099
F3	1.825	0.346	±0.110
F4	1.166	0.262	±0.073
F5	1.413	0.361	±0.114

7.3.1 K_{IIc} : Material property or ‘apparent’ value?

The values of K_{IIc} presented in table 7.3 have been introduced as ‘apparent’ values rather than true critical, material properties. Measured values of K_{IIc} have been found to be strongly dependent upon the T -stress caused by the specimen design [54, 55]. This is one reason why K_{IIc} is notoriously difficult to measure in bulk materials. Also, since the kinking failure of pre-cracked brittle materials under shear loading is not a shear sliding mechanism; consequently, K_{IIc} , the critical stress intensity factor at which in-plane shear crack growth will occur, is somewhat of a misnomer anyway. The consequence of these points is that whilst K_{IIc} values measured by one method are quantitatively comparative, values measured with different methods are not. It is for this reason that K_{IIc} values are often described as ‘apparent’ since they are not intrinsic material properties. It is felt that the apparent toughness values determined in this chapter are representative of the material fracture behaviour under shear loading.

7.4 Comparing mode II failure in composites with the resin tests

Comparing the values of K_{IIc} determined using the mixed-mode failure envelope (section 7.3) showed strong correlation between resin K_{IIc} and composite G_{IIc} (data supplied by Cytec Engineered Materials, some more details can be found in the appendix, section 11.4). This can be seen in figure 7.13.



K_{IIc} error bars: $SE_{\bar{x}} = \pm s/\sqrt{n}$ (see footnote for details)

Figure 7.13 - Measured values of resin K_{IIc} against composite G_{IIc} ¹²

It is accepted that there is not necessarily enough data here to categorically state that $K_{IIc_{resin}}$ is directly proportional to $G_{IIc_{composite}}$, however for the resin systems

¹² K_{IIc} error bars: Standard error of the mean, $SE_{\bar{x}} = \pm s/\sqrt{n}$; where s is the sample standard deviation and n is the sample size (i.e. the number of independent values of K_{IIc} averaged to find the mean value). G_{IIc} values are courtesy of Cytec Engineered Materials.

tested here, this appears to be the case. This is strongly analogous to the documented proportionality of $K_{Ic_{resin}} \propto G_{Ic_{composite}}$ discussed in section 2.4.5 and it is suspected that the reason this has not previously been shown to be valid for the mode II case is due to difficulties in measuring resin K_{IIc} (or more accurately, an appropriate value of apparent K_{IIc}) with sufficient precision. It can be seen that both the particulate/interlaminar toughened materials (F2-5) and the unmodified NEAT resin follow the same relationship, however it is cautiously anticipated that, due to the general difficulties associated in taking quantitative G_{IIc} measurements, that this method is qualitative. It is unknown how comparable toughened systems with differing resins, different particle sizes, volume fractions or distributions would be but it is hoped that the method would still give useful comparative data.

It is unknown whether average K_{IIQ} values at a 90° loading from a sufficiently large number of specimens would yield the same result. Performing large numbers of tests at 90° loading, and considering failure loads in addition to displacement field-derived stress intensity data could confirm the $K_{IIc_{resin}} \propto G_{IIc_{composite}}$ hypothesis, however as discussed in section 7.2.2.1, one of the limitations of the DICITAC method is that the pure mode II case pushes the limits of the assumptions of the crack-tip description used.

7.5 Concluding remarks

Mode I and mode II stress intensity factors have been determined for specimens of five epoxy formulations under mixed-mode loading, using the DIC and fracture parameter extraction techniques. Apparent values of mode II fracture toughness were determined from the mixed-mode data using a modified failure envelope and these were found to be closely proportional to composite mode II toughness values measured in an external laboratory in composites made from the formulations using the same resin batches.

Earlier attempts to link resin mode II behaviour to composite mode II behaviour have been unsuccessful, owing mostly to the lack of a true shear failure mode. A consequence of the kinking, tensile direction crack growth mechanism result in a

strong sensitivity to the mode I component. This can neither be measured nor controlled easily without the use of experimental mechanics techniques. It seems from this study that relatively small improvements in resin mode II toughness correspond to higher improvements in the composite, the opposite of the situation in mode I. This is thought to relate to the reduction in allowable process-zone size in a laminate for mode I, and an increase in the allowable process-zone size in a laminate for mode II loading, both due to the constraint caused by the fibres. This behaviour has not been observed before and goes some way to explain how seemingly small differences between particle materials and shapes can strongly affect the interlaminar mode II toughness performance of ILTP toughened systems.

The next chapter focuses on the kinking of the cracks in the mixed-mode specimens tested. Measurements, including crack kink angle, shear strain fields, and the stress intensity factors determined in this chapter, will be compared with a number of theoretical failure criteria. Part of the motivation for this is to assess the experimental mechanics method of this chapter against completely independent theoretical values.

Chapter 8

Mixed-mode results and discussion: Crack kinking

8.1 Kink angle measurement

Other than the pure mode I specimens, all specimens exhibited crack kinking. Cracks exhibiting curvature were measured at the initial kink of the crack, as illustrated in figure 8.1. Kink angles θ_k have been measured digitally using ImageJ [132] at an estimated accuracy of around $\pm 1^\circ$. This process is shown in figure 8.2; in this figure the measured angle is subtracted from 180° to obtain the kink angle θ . These kink angles are presented for all specimens against loading angle in figure 8.3 and separated by material, and shown against K_{II}/K_I in figures 8.4a-f. Two specimens with uneven starting crack-tips and unusually twisted, three-dimensional crack paths were excluded from the measurements.

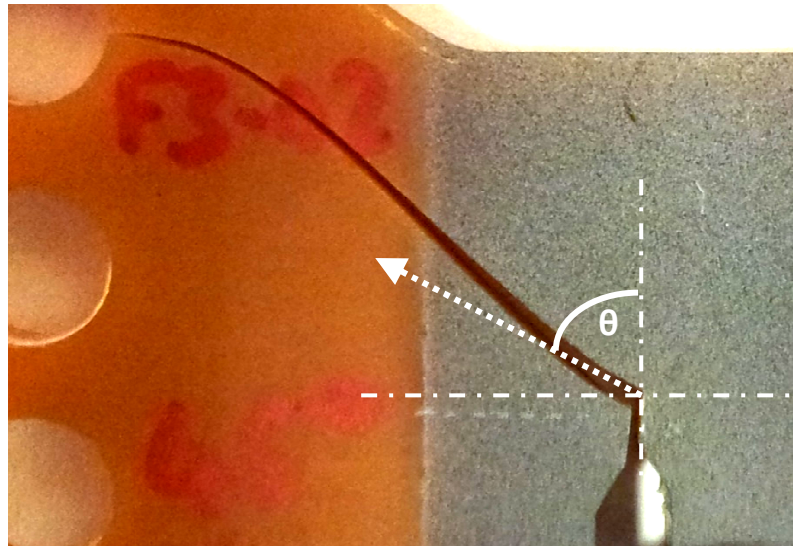


Figure 8.1 – Measuring instantaneous, absolute crack kink angle θ in a specimen

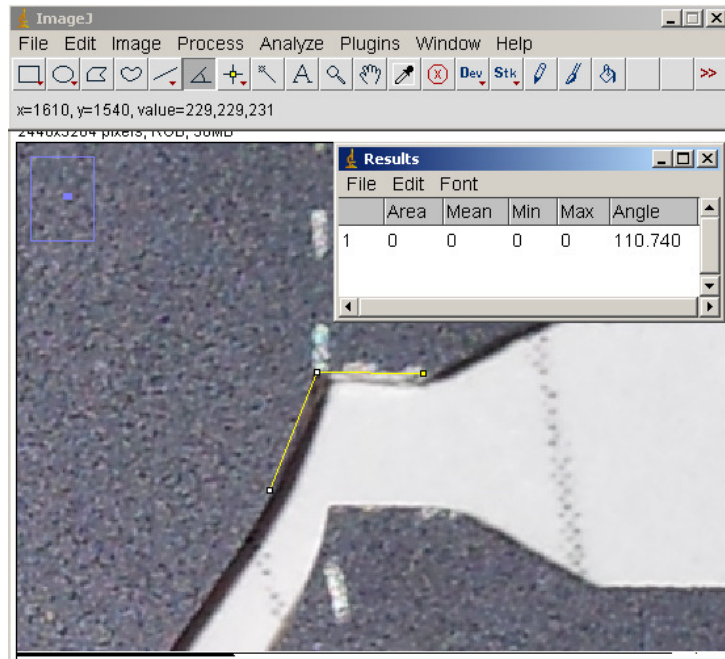


Figure 8.2 – Measuring initial kink angle θ using ImageJ

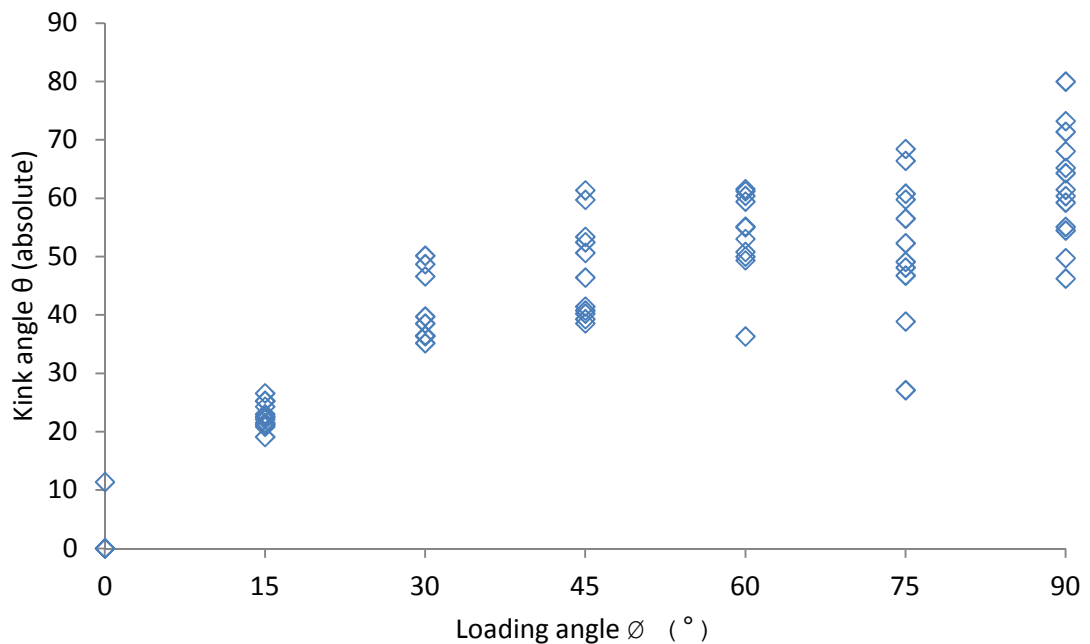
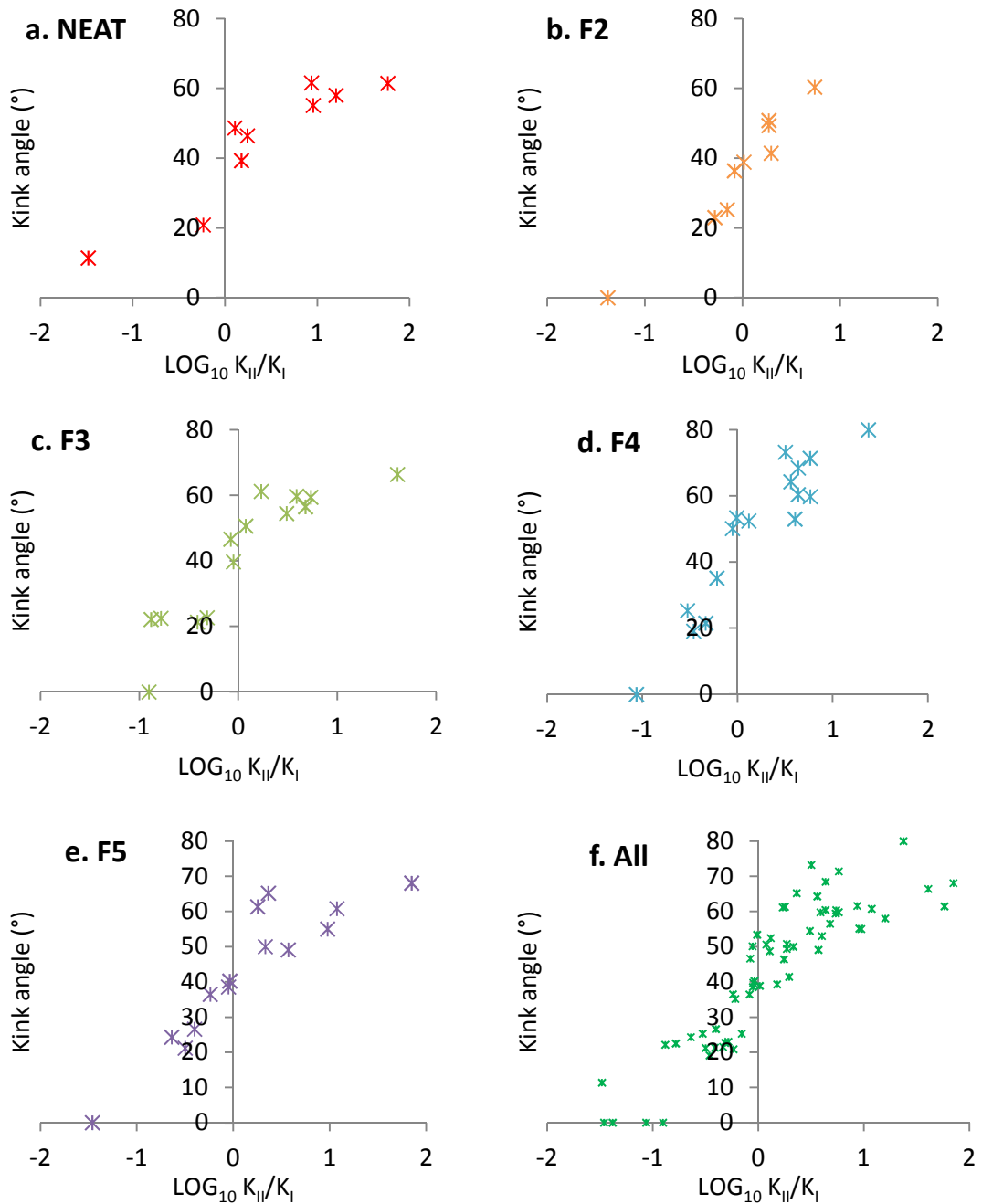


Figure 8.3 – Absolute kink angle α against loading angle for all specimens

Figure 8.3 shows the range of kink angles for all materials at different loading angles. There is a significant amount of scatter in kink angles in specimens loaded at higher loading angles. The amount of scatter in this figure is comparable to the scatter in DIC-measured K_{IIQ}/K_{IQ} against loading angle, shown in figure 7.8. Figure 8.4a-f show the kink angles against K_{II}/K_I , scatter is noticeably reduced.



Figures 8.4 – Kink angles against DICITAC-measured K_{II}/K_I values for each material (and for all specimens).

8.2 Using kink angle as an indicator of K_{II}/K_I

Figures 8.4a-f show no significant differences between kink angles at given loading angles for different formulations in the number of specimens tested. The figures do show reasonable correlation between measured mode mixity and kink angle. Comparing figure 8.4f (enlarged as figure 8.5) with measured values of K_{II}/K_I

against loading angle, reproduced as figure 8.6, it can be seen that the kink angle appears to be as good an indication of K_{II}/K_I as the loading angle is. For situations where DIC measurement is not available, it is suggested that the deduction of K_{II}/K_I could be made from the kink angle in addition to loading angle.

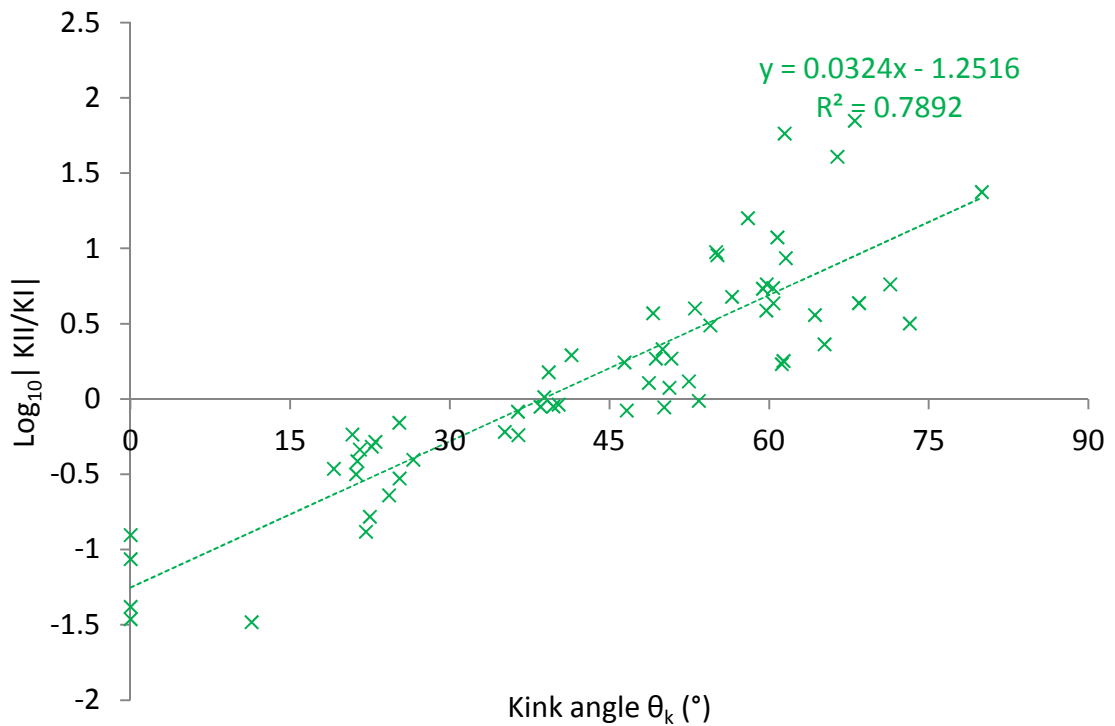


Figure 8.5 – K_{II}/K_I against kink angle

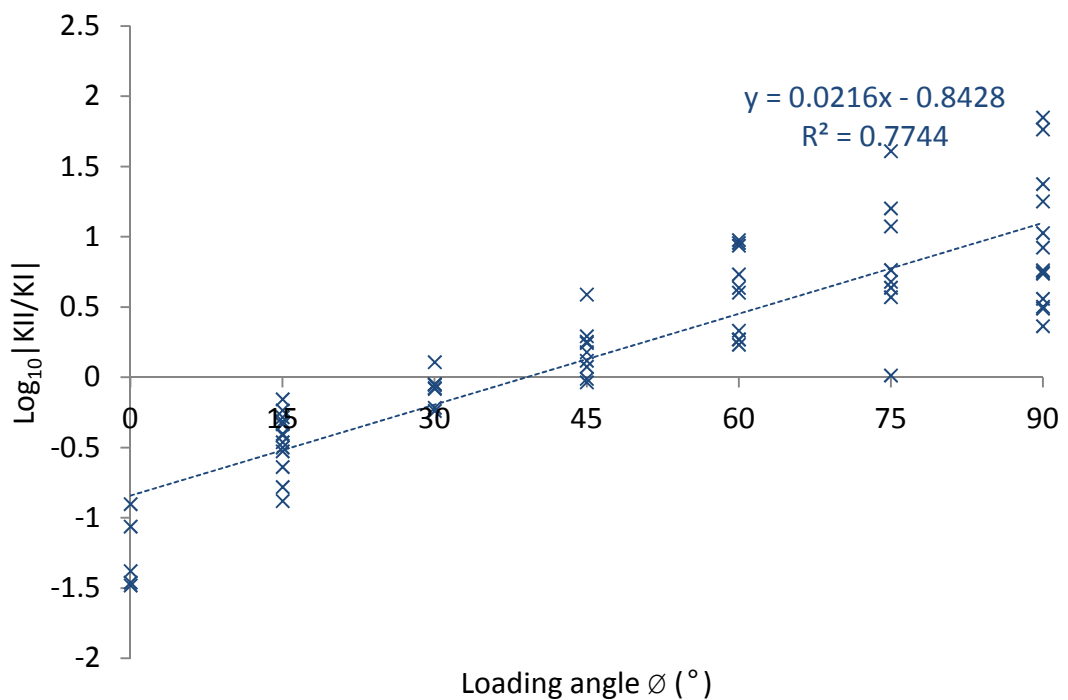


Figure 8.6 – K_{II}/K_I against loading angle

Whilst both figures 8.5 and 8.6 seem to have comparable correlation, each shows that using one alone gives a poor measure of K_{II}/K_I . When the two are combined, it is thought that a better estimate of K_{II}/K_I can be found, as shown in figure 8.7; note that at 75° loading (indicated with sky blue circular points), K_{II}/K_I values from 10^0 to $10^{1.6}$ were measured and both of these extremities correlate closely with the crack kink angle.

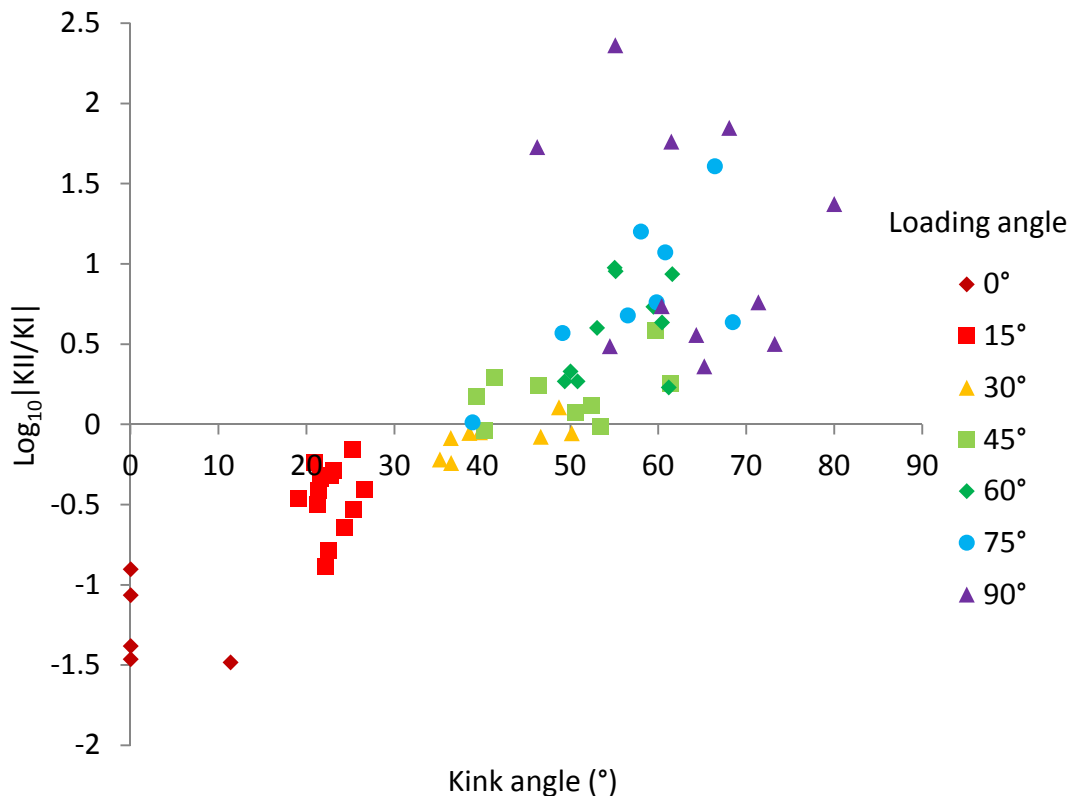


Figure 8.7 – K_{II}/K_I against kink angle, data separated by loading angle

Additionally, figure 8.7 shows the specimens loaded at 90° to be by far the most scattered; it is thought that this is a consequence of the reduction in accuracy of the technique at the 90° loading angle discussed in section 7.2.2.1. In these specimens the kink angles varied considerably and so it is suggested that using kink angle to infer K_{II}/K_I in the (almost) pure mode II loading cases could improve accuracy over the DICITAC technique.

8.3 Failure criteria

There are a number of fracture criteria to predict kink angle in brittle materials. The most popular two in the literature will be explored.

8.3.1 Maximum tangential stress criterion

Ergodan and Sih's [50] maximum tangential stress criterion, also referred to as the maximum hoop stress criterion (MHSC) predicts cracks to kink in the direction perpendicular to the maximum tangential stress (i.e. the maximum principal stress) at critical loading.

Ignoring second order terms, the hoop stress can be described thus [133]:

$$\sigma_{\theta\theta} = \frac{1}{\sqrt{2\pi r}} \left\{ K_I \left(\frac{3}{4} \cos \frac{\theta}{2} + \frac{1}{4} \cos \frac{3\theta}{2} \right) - K_{II} \left(\frac{3}{4} \sin \frac{\theta}{2} + \frac{3}{4} \sin \frac{3\theta}{2} \right) \right\} \quad (8.1)$$

This equation was solved for the average applied K_{II}/K_I at each loading angle (although any values of K_{II}/K_I could have been used) and a curve fitted through these points. The result is shown in figure 8.8.

8.3.2 Minimum strain energy density criterion

The minimum strain energy density criterion (MSEDC) predicts crack kinking to occur in the direction of minimum strain energy density at critical loading. Strain energy density can be described thus [133]:

$$\begin{aligned} S = & \frac{1}{16\pi\mu} (\kappa - \cos \theta)(1 + \cos \theta) K_I^2 \\ & + \frac{1}{8\pi\mu} \sin \theta \{ 2 \cos \theta - (\kappa - 1) \} K_I K_{II} \\ & + \frac{1}{16\pi\mu} \{ (\kappa + 1)(1 - \cos \theta) + (1 + \cos \theta) \\ & \times (3 \cos \theta - 1) \} K_{II}^2 \end{aligned} \quad (8.2)$$

Again, these equations were solved for the average K_{II}/K_I value at each loading angle. Results are plotted in figure 8.8.

8.3.3 Comparing the failure criteria

Figure 8.8 shows each of the failure criteria plotted for applied K_{II}/K_I . The average of the two failure criteria is also shown.

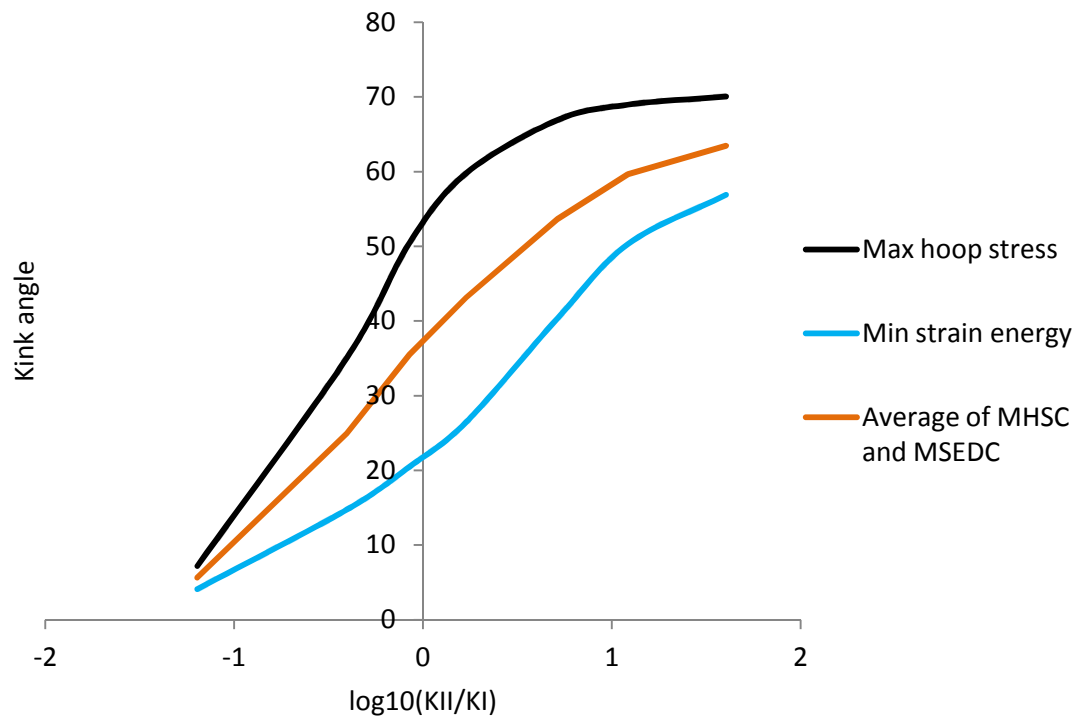


Figure 8.8 - Theoretical kink angles for two failure criteria

Figure 8.8 clearly shows significant differences in the kink angle predictions from the different criteria. The theoretical values are shown alongside the measured values in figure 8.9.

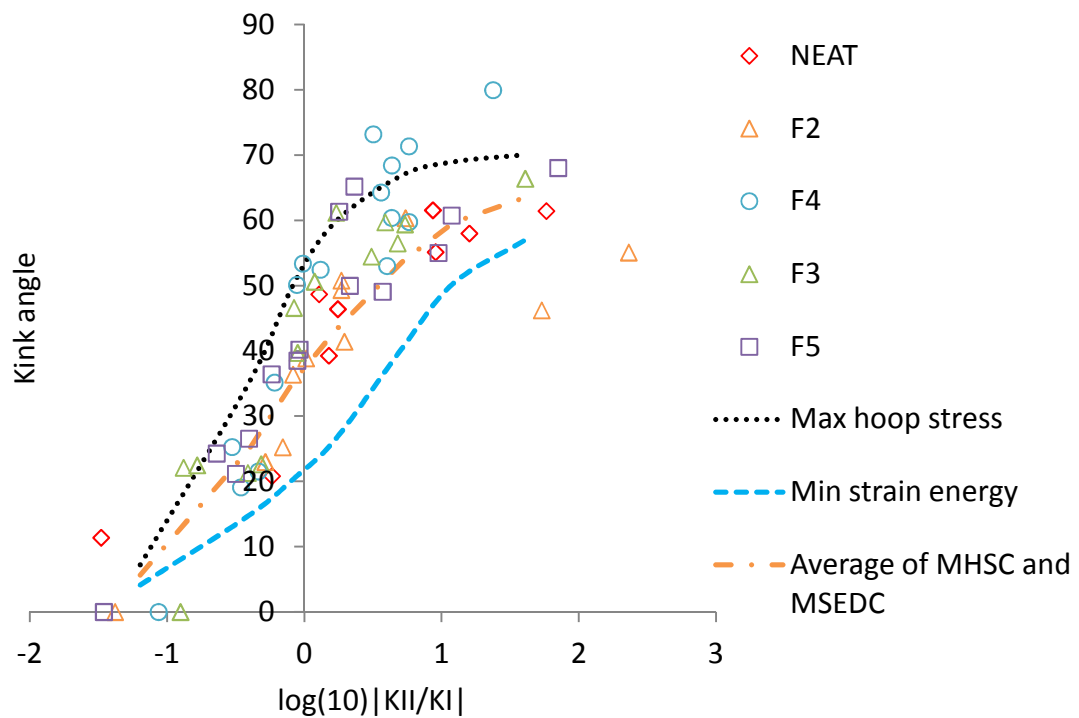
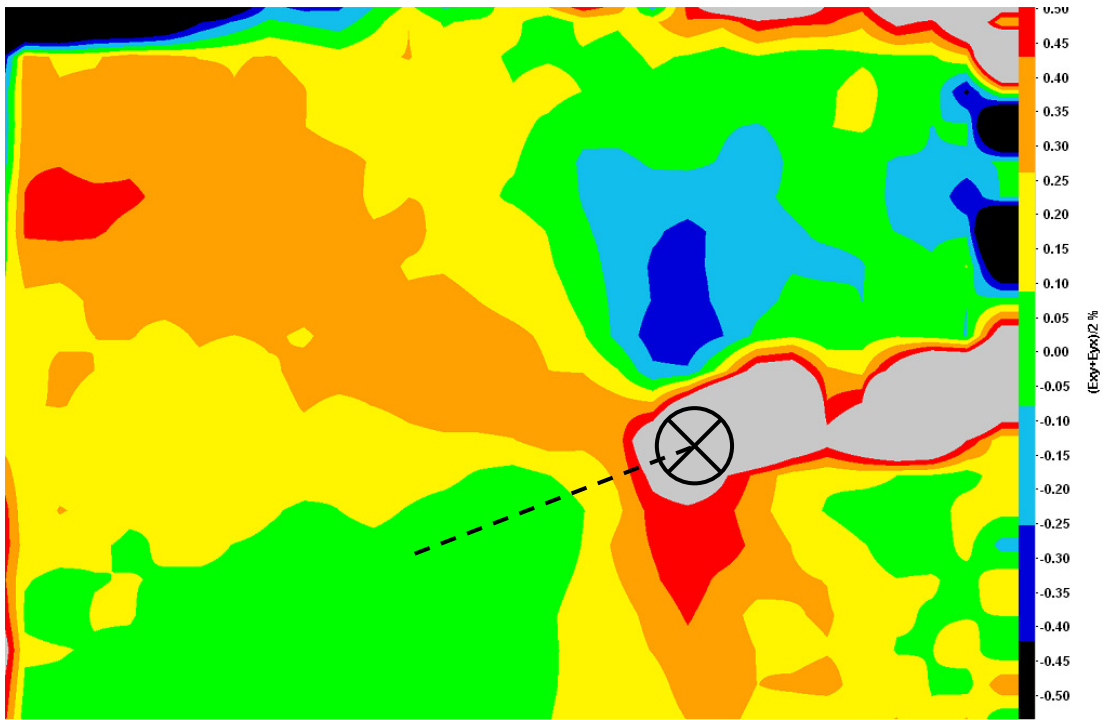


Figure 8.9 - comparing the measured kink angles with theoretical failure criteria

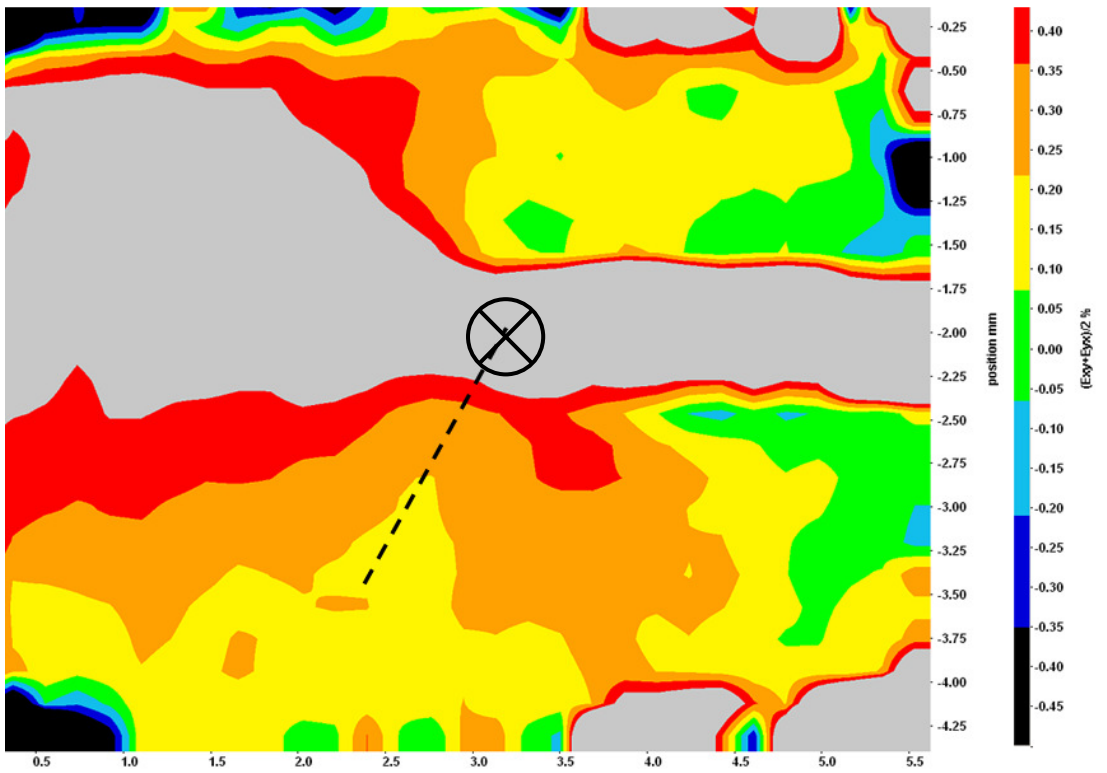
Figure 8.9 shows almost all of the measured results to fall directly between the two failure criteria. This strongly suggests that the measured K_{II}/K_I values have not been systematically under- or overestimated, especially in the mixed-mode region (see the comments in section 7.2.2.1 regarding accuracy of the results at 90° loading). At lower loading angles, measured values follow the theoretical values.

8.3.4 Comparing kink behaviour with strain map data

Shear strain fields for a number of specimens were determined using LaVision StrainMaster 7.1 software and these were compared with the kink angles measured for the specimens. Interestingly, whilst the theoretical minimum strain energy criterion (MSED) appears to consistently underestimate the kink angles measured in the experimental data (figure 8.9), there was found to be close agreement between direction of minimum shear strain energy and kink angle from DIC $\frac{1}{2}(\varepsilon_{xy} + \varepsilon_{yx})$ maps. A number of these are shown below with crack tip position and actual kink angles overlaid in figures 8.10a-h.

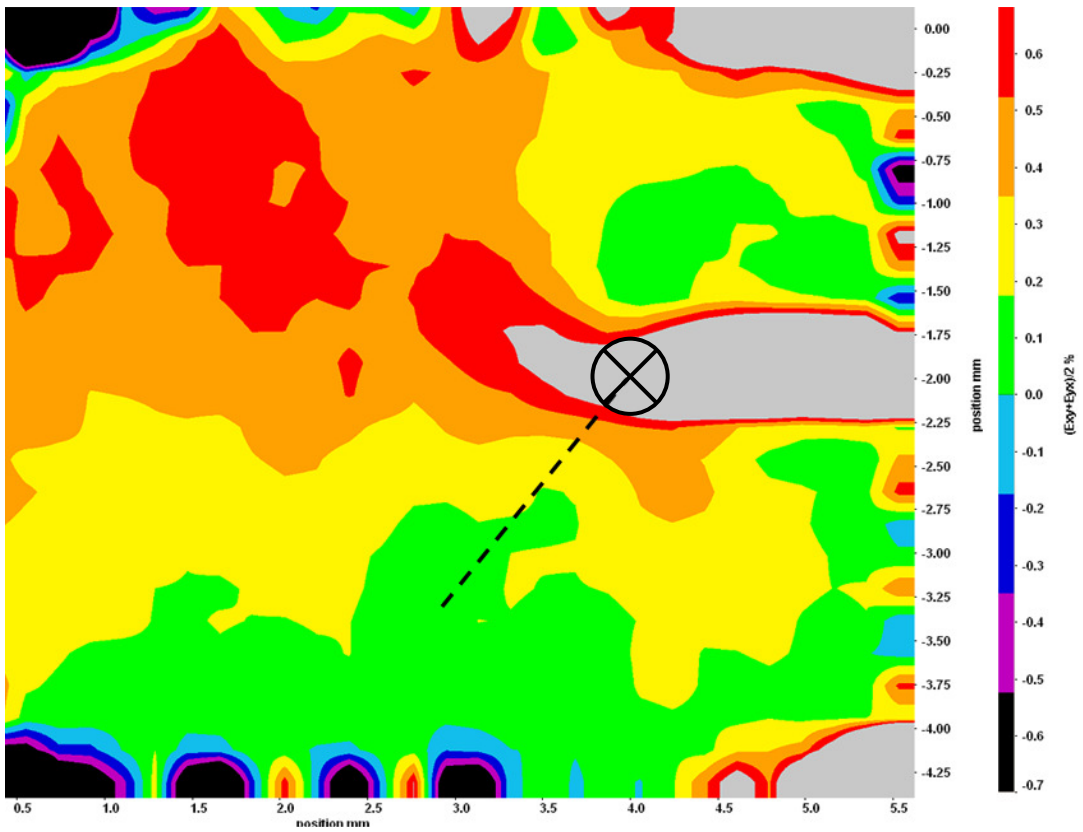


a. 15-F4-02, 21.3° kink angle

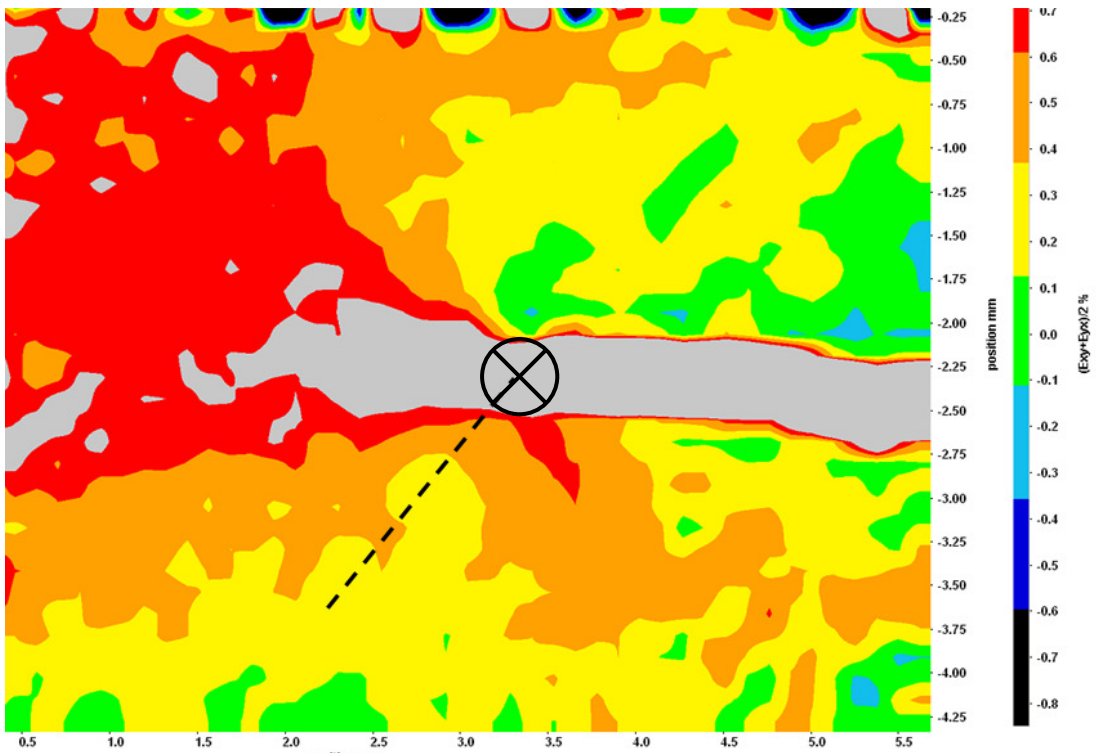


b. 45-F5-14, 61.3° kink angle

Figure 8.10 continued...

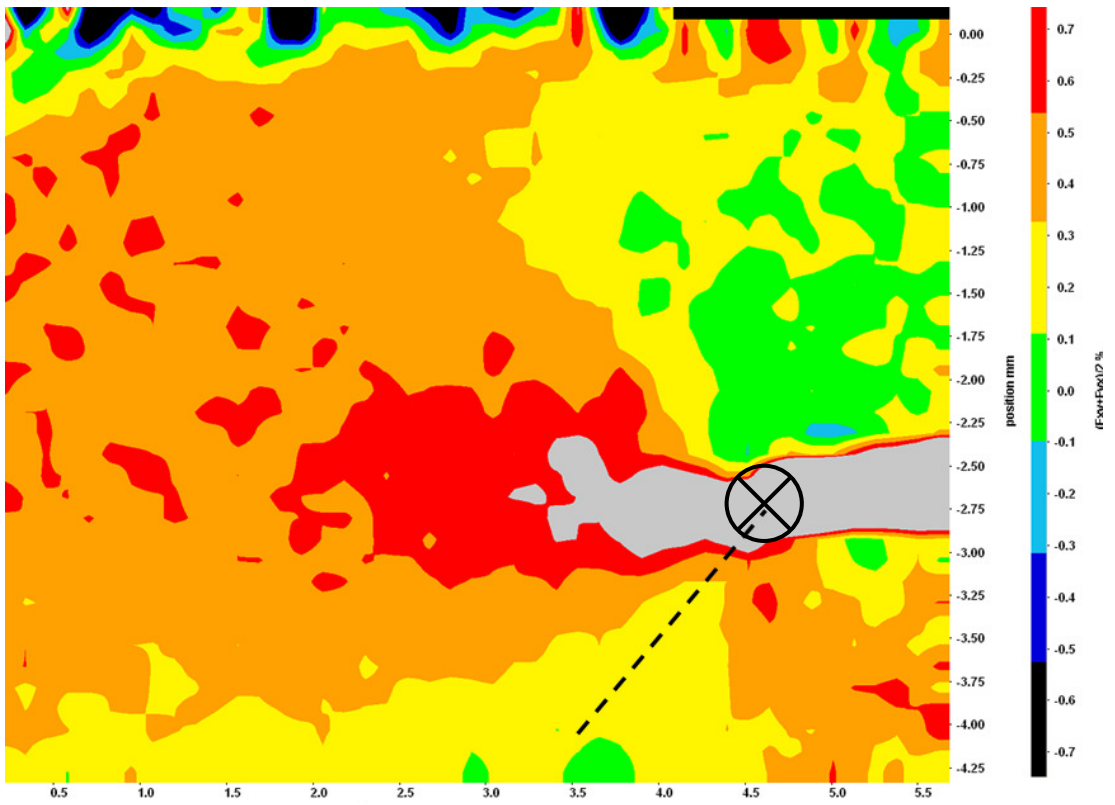


c. 45-F3-10, 50.6° kink angle

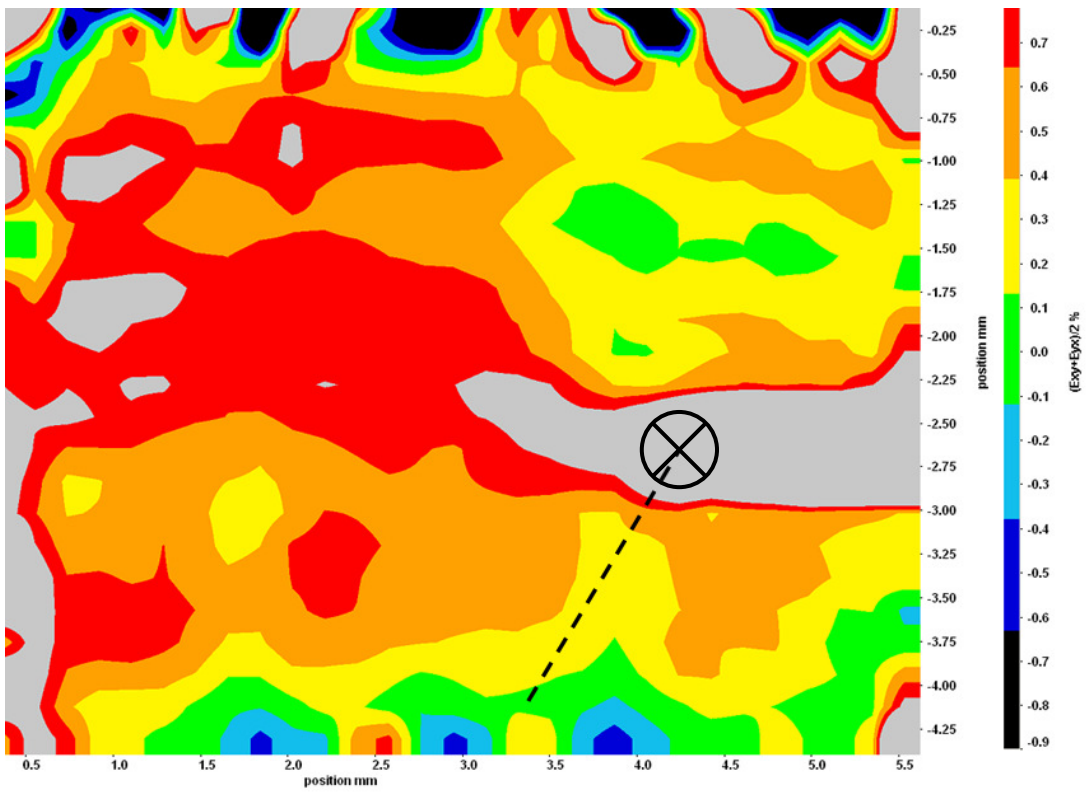


d. 60-F2-08, 50.8° kink angle

Figure 8.10 continued...

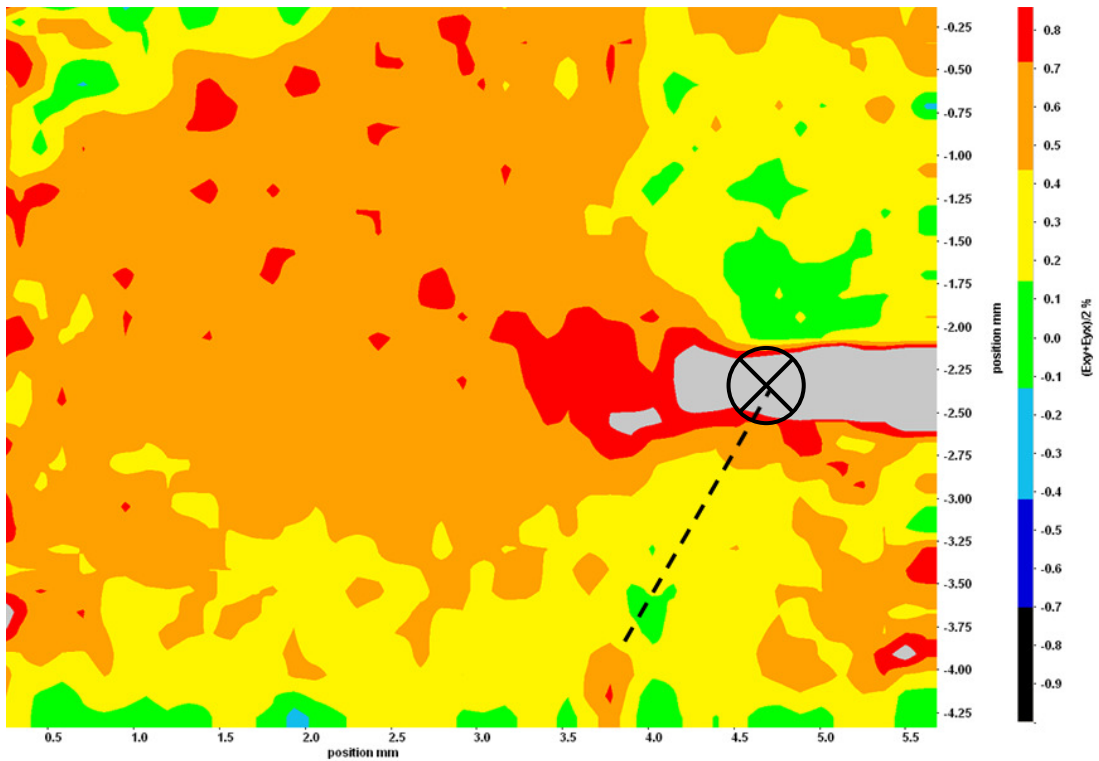


e. 60-F5-16, 50.0° kink angle

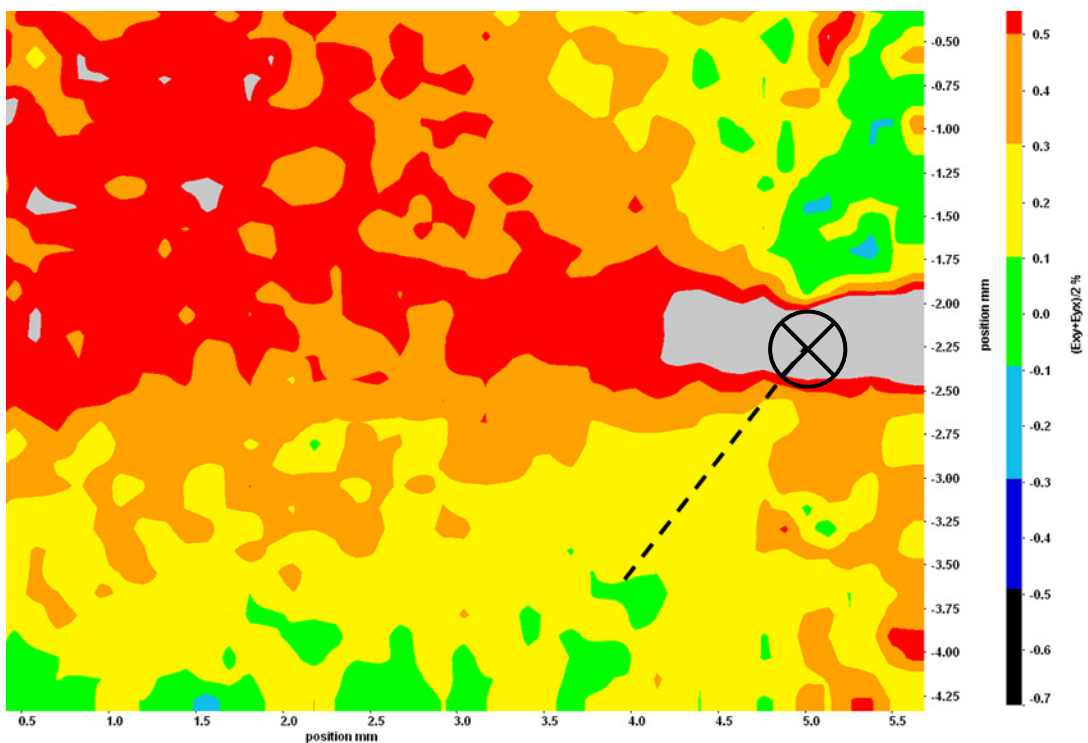


f. 60-F3-15, 59.4° kink angle

Figure 8.10 continued...



g. 75-F4-06, 59.8° kink angle



h. 75-N-05, 52.3° kink angle

Figure 8.10 – Average shear strain $(\epsilon_{xy} + \epsilon_{yx})/2$ in a number of specimens. Note scale bars; lime green is zero. Measured kink angles are overlaid in black. Crack tips are indicated by crosses (cracks are from right to left). Grey areas are areas of high measured strain that have been scaled out of range for clarity.

It is suggested that the analytical description for the MSEDG (equation 8.2) does not describe the direction of minimum strain energy as accurately as can be measured using full-field techniques. The inclusion of further terms (including non-singular terms) could improve the accuracy of the criterion but would clearly reduce the convenience of the criterion.

Concluding Remarks

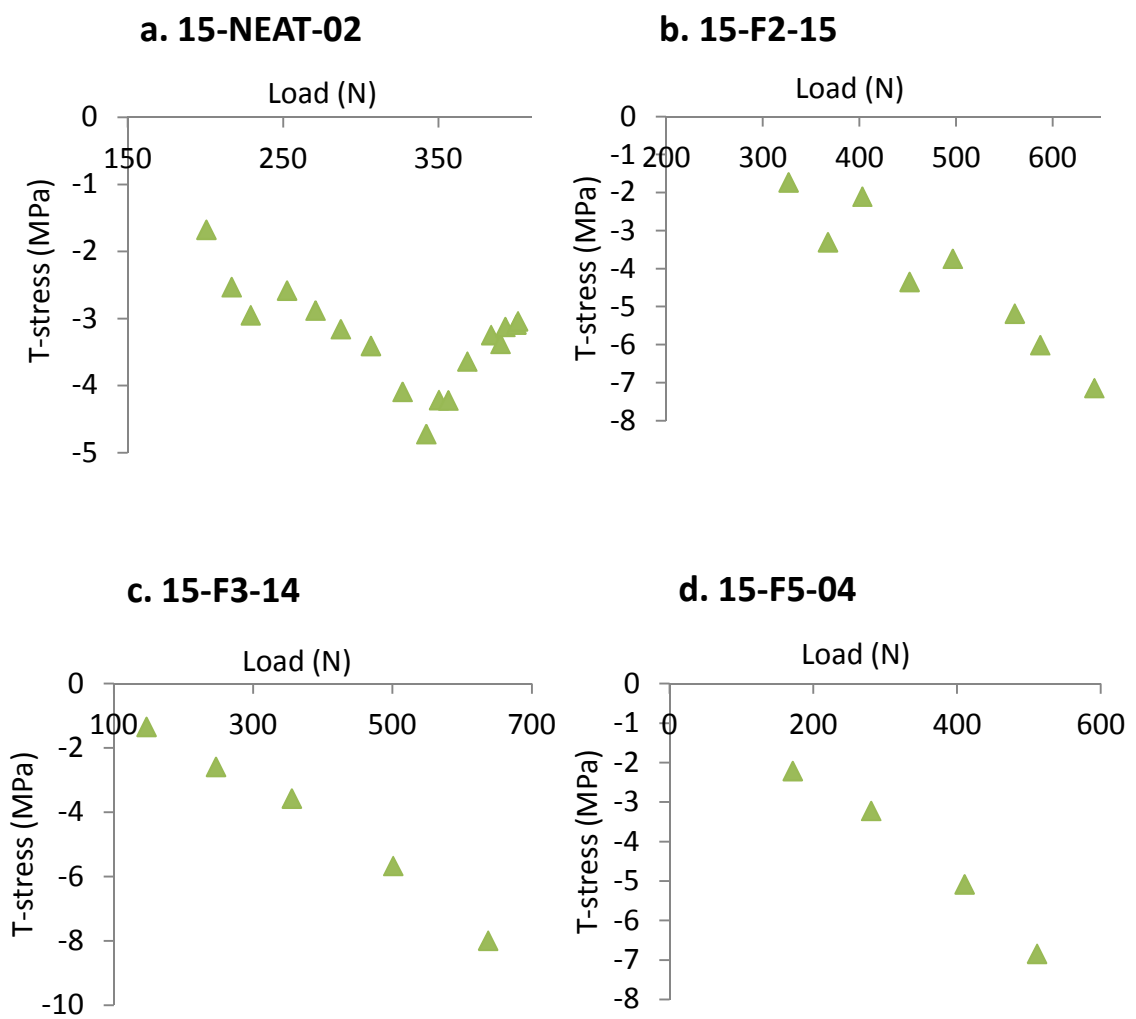
The crack kinking in the mixed-mode specimens has been shown to be a useful measurement to record. Significantly, the kink angles show that the mode mixity calculated from the stress intensity factors determined using DICITAC are in agreement with theoretical failure criteria. An underestimation of the kink angle predicted by the Minimum Shear Strain Energy equation was confirmed using DIC strain maps.

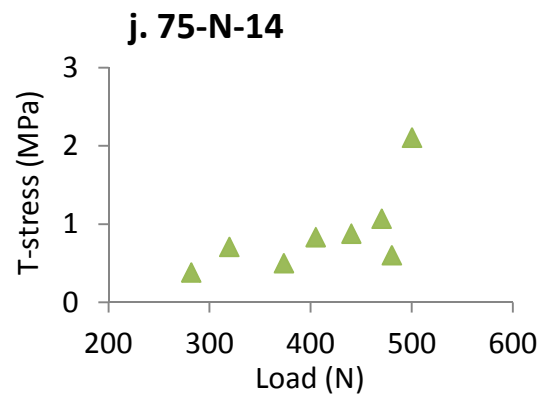
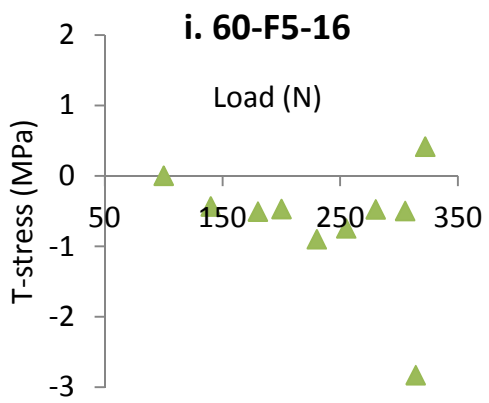
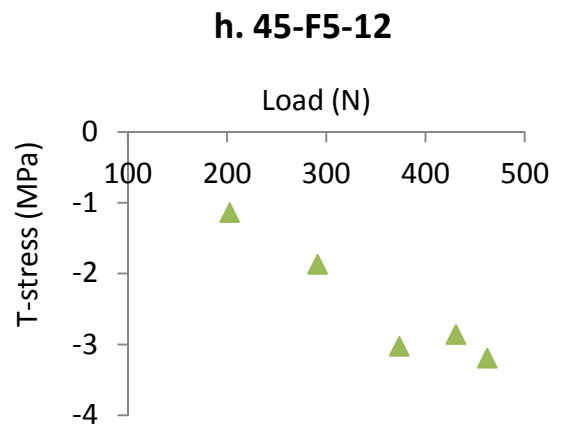
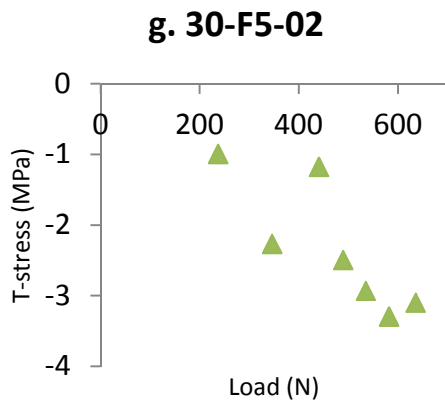
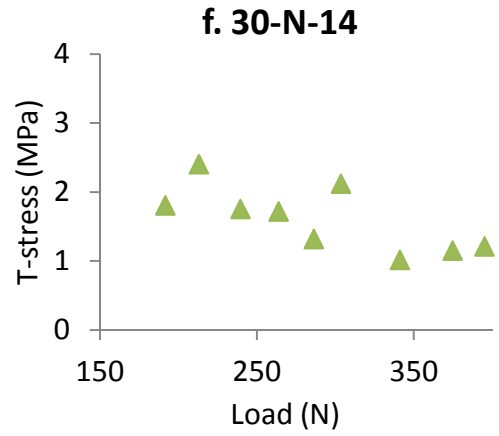
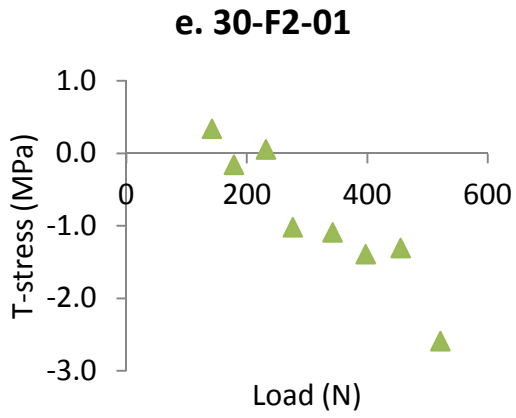
Chapter 9

Mixed-mode results and discussion: The T -stress

9.1 Introduction

The T -stress values extracted from the displacement field data at the same time as the stress intensity values are presented in figure 9.1a-l.





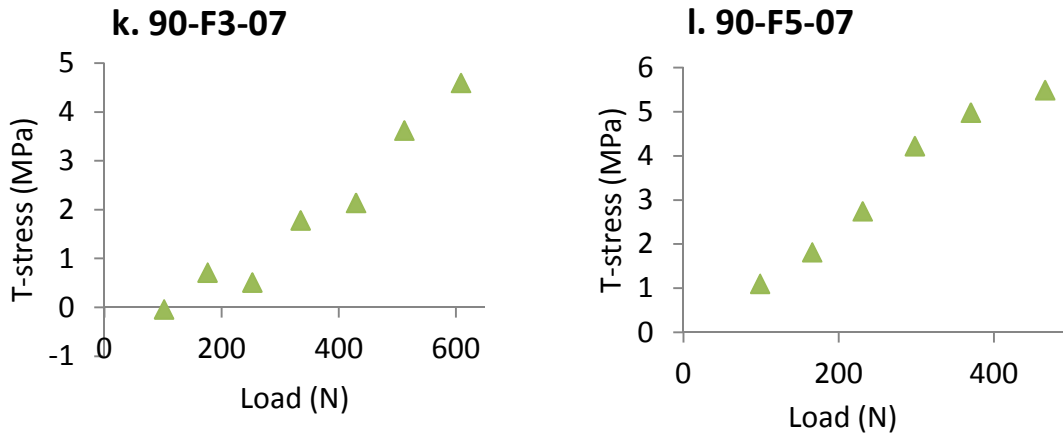


Figure 9.1 –T-stress values extracted throughout loading for a number of specimens

Figures 9.1a-l show some inconsistency in final T -stress values. In a small number of cases, the frame immediately prior to failure appears to have captured image data as the fracture process is beginning and the final-frame T -stress values are wildly different to those preceding them. In view of these results, critical values were determined by taking the last frame prior to fracture, and checking this against a point five frames earlier, to ensure that the measured critical value was representative of a pre-critical, rather than post-critical, crack tip state.

9.2 Critical T -stress values

T -stress values were determined using the Williams method in DICITAC at critical loading for all specimens. As with the stress intensity values, T -stresses were taken as the last stable value before failure; figure 9.1-l is a good example of a specimen exhibiting a final frame value which has been affected by near-critical damage processes and is not representative of the progression through loading.

Unlike most other specimens examined further, the 15° loading angle NEAT specimen 15-NEAT-02 in figure 9.2 shows a non-linearity in the T -stress. Upon further inspection of the recorded images, this specimen was the only specimen (other than those loaded in pure tension) that exhibited any crack growth prior to failure. All other specimens failed suddenly with kinked cracks. This crack growth can

be seen to occur over the ten frames prior to failure. Detail from the final, pre-failure frame is shown in figure 9.2.

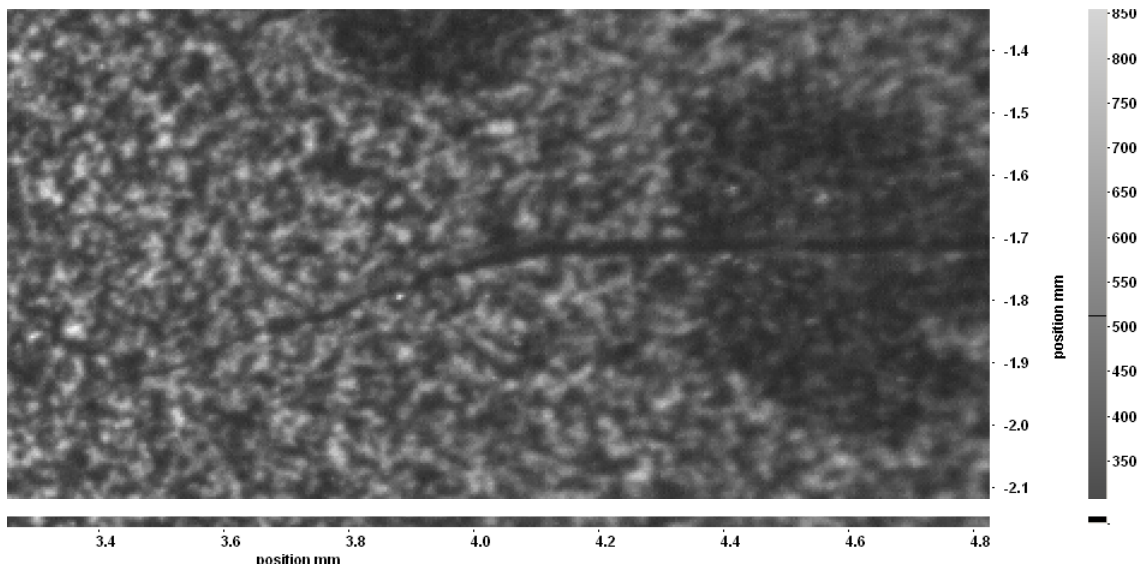
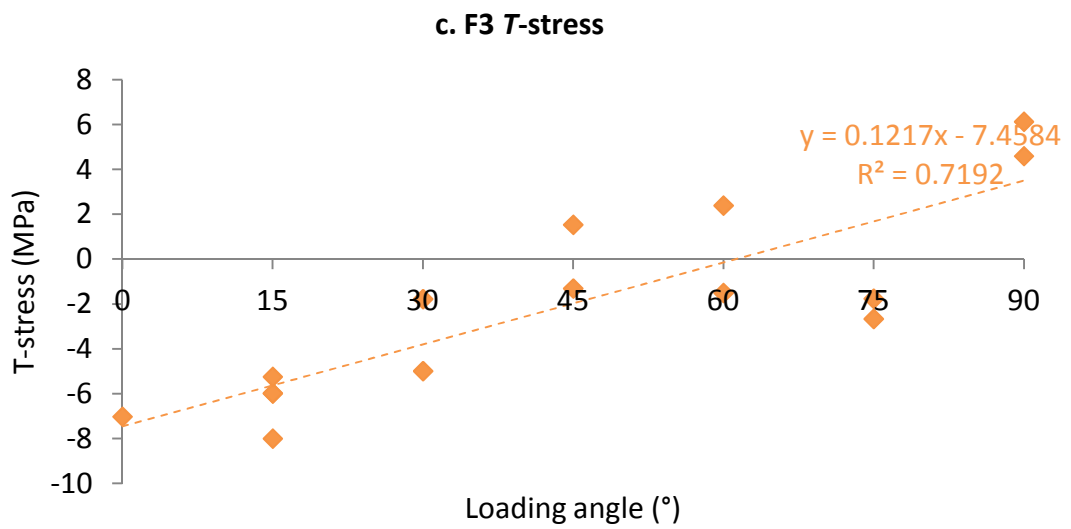
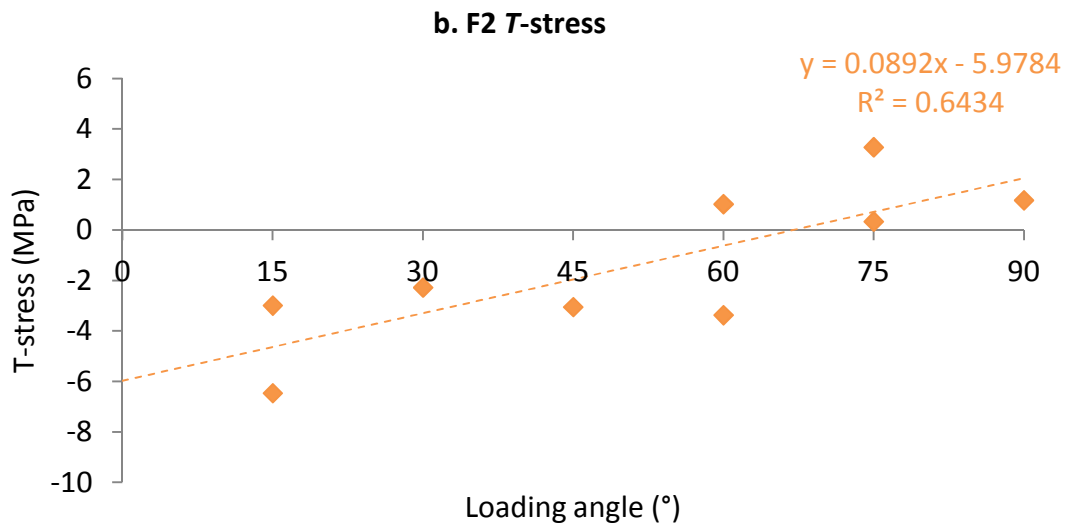
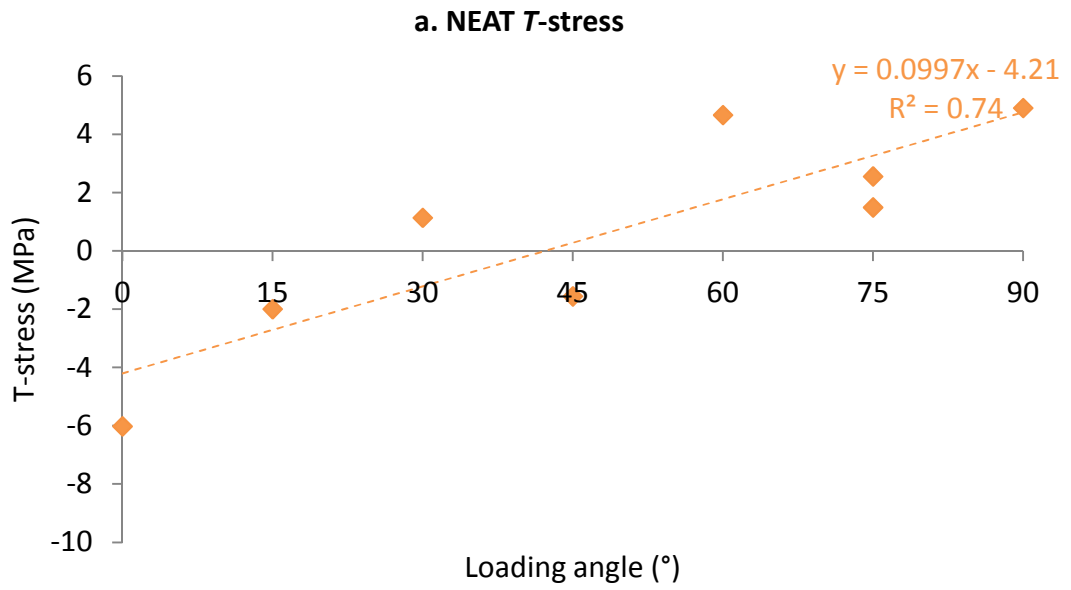


Figure 9.2 - Subcritical angled crack growth in 15-NEAT-02 specimen

Figures 9.3a-e show the critical T -stress data against loading angle for all specimens, separated by material. The data show an apparent linear relationship between loading angle and T -stress at failure. Whilst there is a significant amount of scatter, R^2 correlation values (1 minus mean square error over variance) are all reasonable; values range from 0.64 to 0.85 (simplistically, 1 is perfect regression data, 0 is noise).

It is worth reiterating that the T -stresses recorded here are for the outer-surface of the specimen and not for the centre-plane as typically discussed or calculated using FE methods [120]. All crack fronts in the mixed-mode tests were seen to be straight, not thumbnail shaped, thus cracks exhibited minimal crack tunnelling and so the external, plane-stress T -stresses legitimately can be assumed to be equivalent to the internal (plane strain) T -stresses.



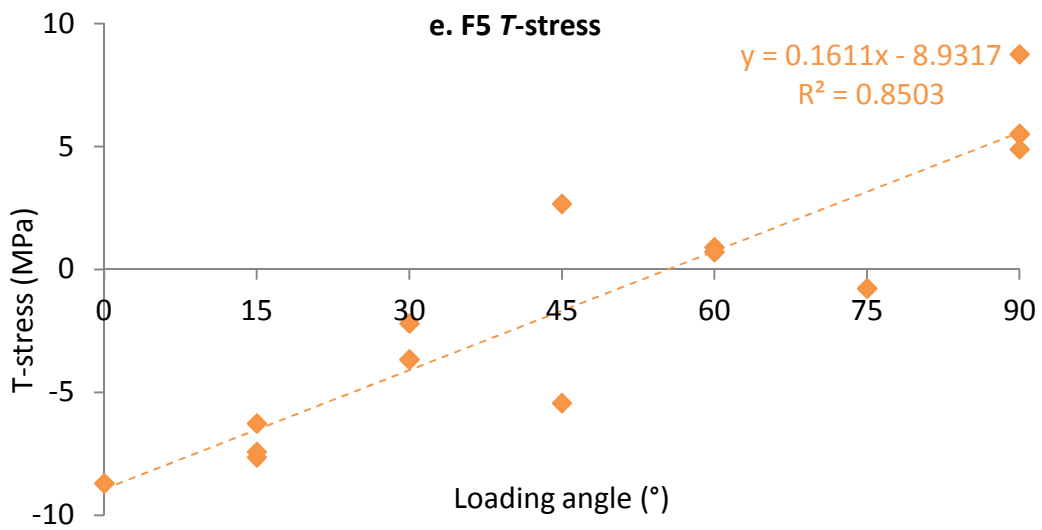
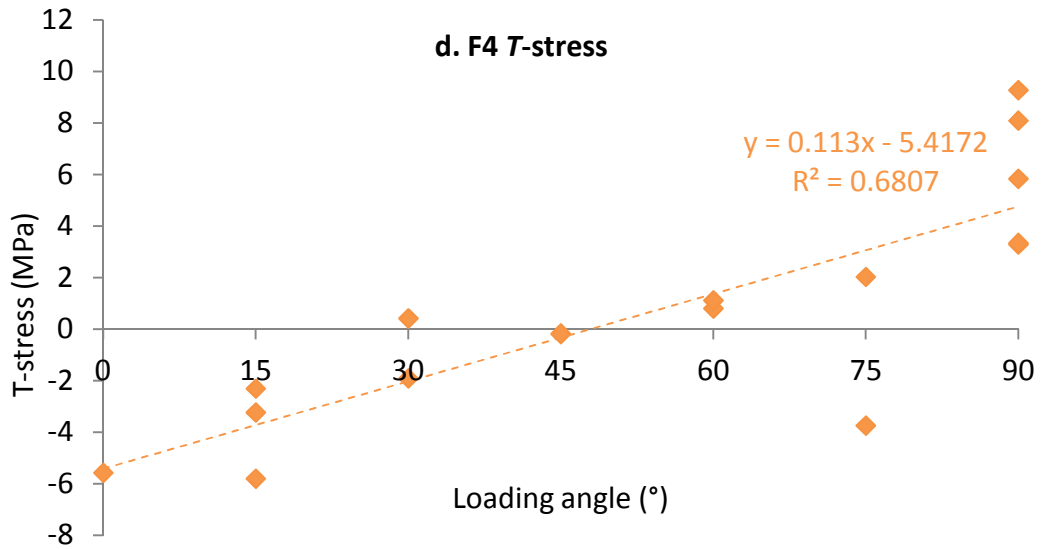


Figure 9.3 – *T*-stress measurements for all specimen, plotted against loading angle. Least-squares linear regression lines are included.

As discussed in section 2.5, a positive *T*-stress is known to result in an unstable crack path whereas a negative *T*-stress results in a stable crack path [47]. Thus, the point at which the *T*-stress changes from being negative to become positive can be considered a quantifiable limit of crack path stability. Figures 9.3a-e show this stability limit to vary between material with considerable difference in the loading angle at which the regression curves cut the x-axis. The loading angle at which this occurs has been termed here the *T*=0 loading angle. As discussed in section 8.2, loading angle has been shown to be a reasonable indicator of the level of shear present.

Despite crack-kinking being present in each loading case with any mode II component, negative T -stresses were still present throughout loading (figures 9.3a-e) at low loading angles. It is believed therefore that the T -stress is more indicative of crack path stability than a requirement for it. However, it is suggested that the point at which the regression lines cut the x-axis is still a useful relative measure of stability. The $T=0$ loading angles for each material are listed in table 9.1.

Table 9.1 - Showing the loading angle for which $T=0$ from linear regression

Material	Loading angle at $T=0$
NEAT	42.2°
F2	66.7°
F3	61.3°
F4	47.9°
F5	55.5°

9.2.1 T -stress quantifying material-induced crack-tip geometry

LEFM theory states that the T/σ is dependent upon geometry and independent of material properties [9, 125]. However, the T -stress values measured in this study suggest that material properties are capable of altering the T -stress. A possible explanation for this is that the presence of toughening particles modifies the crack tip geometry, as seen in section 5.8. Cracks in the LEFM model are considered as singularities, with a correction made for plasticity if required [9]. However, in the naturally 'sharp' cracks tested, crack fronts of the NEAT resin and the toughened F2, F3 and F5 resins varied tremendously. NEAT resin crack-fronts were extremely well defined by a mirror-like front, whilst the crack fronts of particulate toughened F2, F3 and F5 resins were rough and less well-defined due to the crack-pinning mechanisms. The material F4 contains diffuse-interphase/interface particles were significantly less rough but still noticeably rougher than the NEAT resin crack-fronts. These differences in crack-tip geometry could explain the difference in T -stress measurements. Also, since these measurements are critical values, difference in measured values will be heavily influenced by the toughnesses of the materials.

Interestingly, the differences in $T=0$ loading angle roughly follow the mode II toughness of the materials (and their composites) in that NEAT and F4 are the least tough, with F5 being tougher, and F2 and F3 having the highest toughness. This relationship is shown in figures 9.4 a-b.

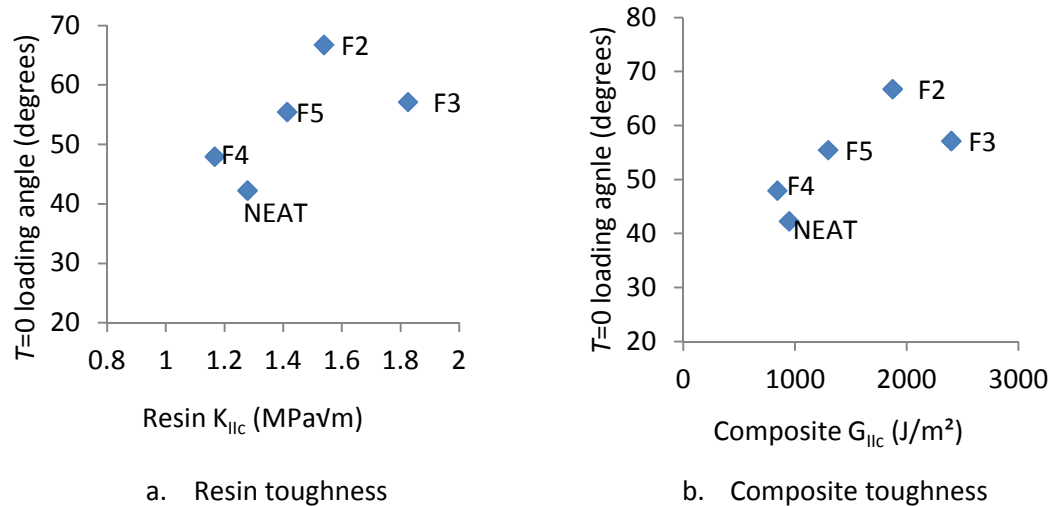


Figure 9.4 – $T=0$ loading angle against (a.) resin and (b.) composite mode II toughnesses

Whilst the data are clearly subject to significant levels of uncertainty, an apparent trend appears when all of the T -stress data is collated. It is thought that the materials' mode II toughness in both bulk resin and composite form is strongly driven by the directional stability of the stationary crack and that this can be modified by the presence of particulate toughening agents. It is also thought that T -stress measurements may be capable of qualitatively or quantitatively assessing this stability.

The same process can be applied by taking $T=0$ values for a value of K_{II}/K_I ; the variation in T -stress behaviour is as apparent and follows the same trend. As experienced with the stress intensity measurements (figures 7.9a-e), the level of scatter is inherently increased and consequently results are considerably less statistically significant. T -stress is plotted against measured K_{II}/K_I in figures 9.5, the $T=0$ points listed in table 9.2 and these plotted against toughness values in figures 9.6.

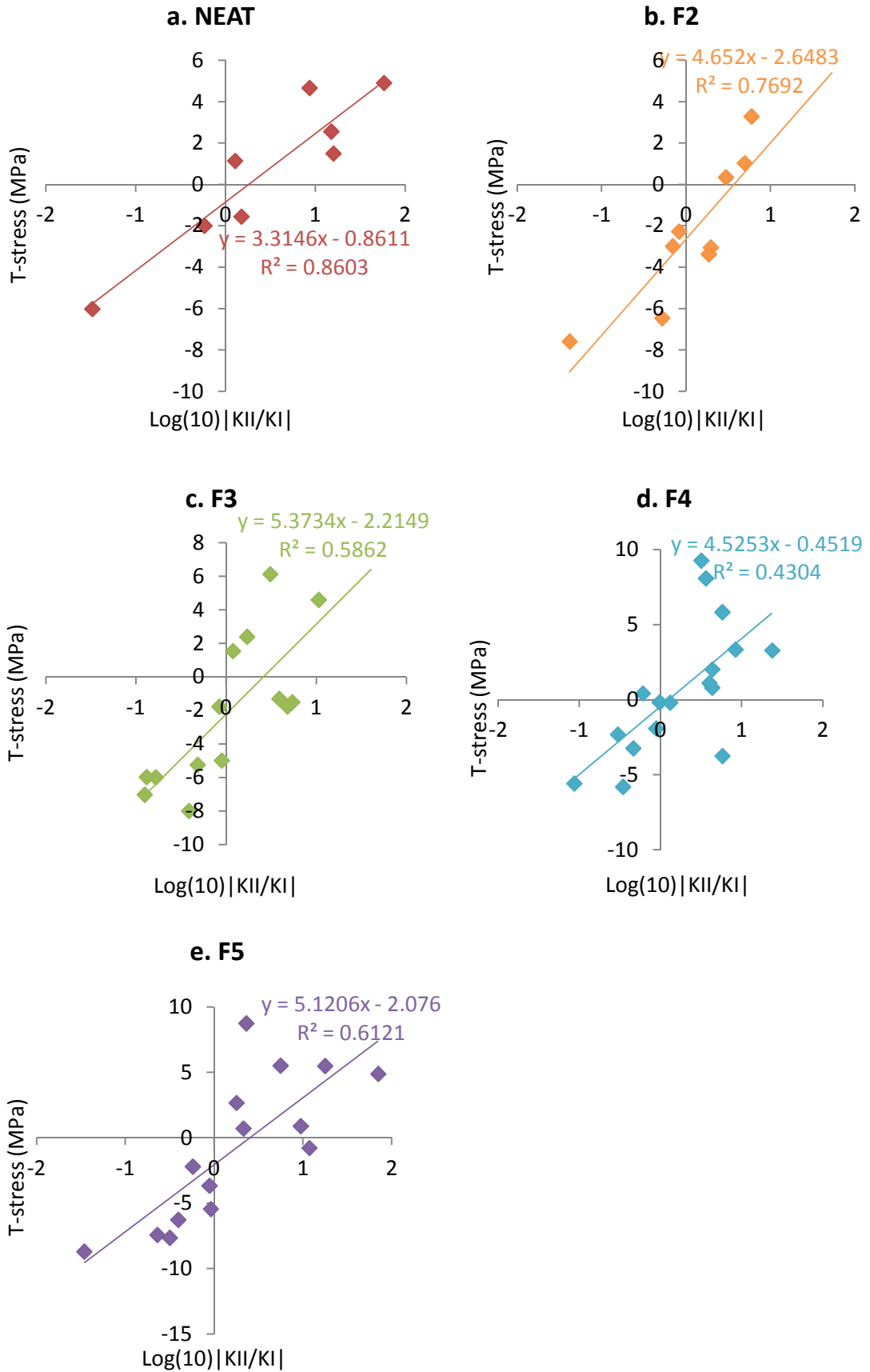


Figure 9.5 – T-stress measurements for all specimens, plotted against measured K_{II}/K_I . Least-squares linear regression lines are included.

Table 9.2 – Showing the value of K_{II}/K_I for which $T=0$ from linear regression

Material	K_{II}/K_I at $T=0$
NEAT	0.259
F2	0.569
F3	0.412
F4	0.100
F5	0.405

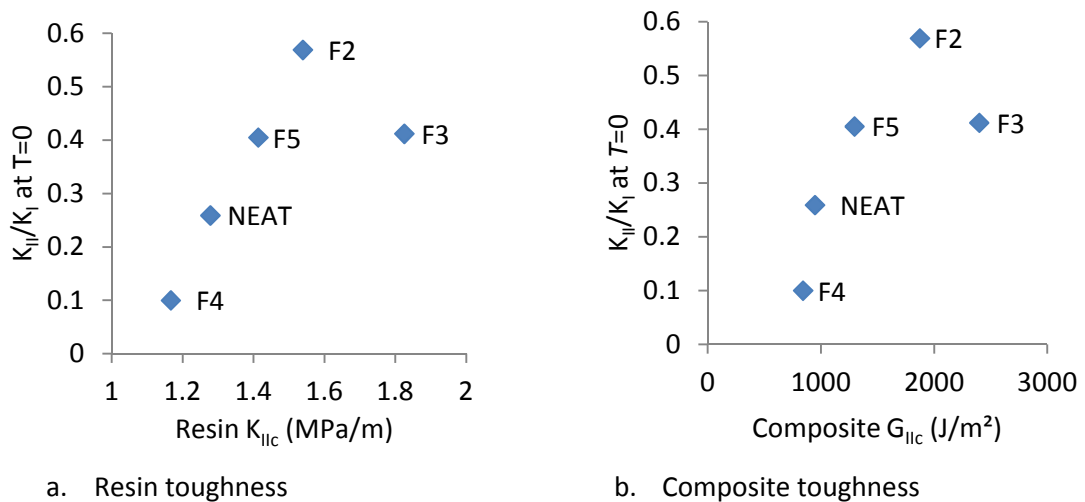


Figure 9.6 – K_{II}/K_I at $T=0$ against (a.) resin and (b.) composite mode II toughnesses

9.3 Concluding remarks

T -stress measurements displayed significant levels of scatter, however some interesting behaviours were identified. Treating the T -stress as a method of quantifying the crack-path stability *between materials* is thought to be novel, however, there is insufficient data and too much scatter to support any hypotheses in a statistically meaningful way.

It is thought that by taking steps to minimise the levels of scatter recorded, T -stress measurements will be more consistent and reliable. A key factor in reducing the scatter was identified in section 5.4 as being careful control over the levels of constraint in different specimens. In order to measure consistent T -stress values, it is advised that specimens with more controlled and quantifiable levels of constraint are used than those employed here.

Chapter 10

Conclusions

10.1 Conclusions

Stress intensity factors and the T -stress were successfully measured in a wide range of specimens by parameter extraction from DIC displacement fields using the Williams approach. After careful consideration of the specimen constraint, the T -stress was shown to be acceptably close to theoretical values. For the first time, a comprehensive sensitivity study was carried out to assess the effect of crack tip location definition, data collection window and the overall accuracy of the technique. It is expected that these studies will aid researchers in the use of tools such as DICITAC more effectively and efficiently in the future.

A large number of T -stress measurements in real specimens have been performed. Previously there were very few direct measurements in the literature and analytically derived solutions have been shown to be variable. The discontinuity in T -stress measurements immediately prior to fracture measured in this work was not found elsewhere in the literature. Another novelty of the T -stress results presented here is that they show for the first time the magnitude of the variation between nominally identical specimens. A study of compact tension specimens showed that there is a significant difference between the applied levels of constraint assumed by theory and standards, and those that can be created in laboratory conditions. Flexible fixtures, universal joints, and slack pins are commonplace in the testing of 'brittle' materials such as thermoset plastics. Whilst the results presented here, and the literature, show that the T -stress has limited effect on mode I toughness, it is a variable that should be controlled with more care.

Differences in behaviour were observed when a mode II component was introduced to a (mode I) opening crack. It was assessed that the toughening mechanisms present in pure mode I cracks have differing efficacies between pure mode I and mixed-mode loading. This is thought to be the reason why mode I toughness is a

poor predictor of mode II performance in structured materials such as particulate toughened epoxies. It is thought that this is the first time that these effects have been directly measured, and attributed to physical behaviour, in a bulk material.

Four particulate modified epoxy resins, toughened with equivalent volume-fractions of similarly sized and distributed thermoplastic materials (and an unmodified resin) were found to exhibit differing toughness properties and fracture behaviour. Resin fracture toughness and mixed-mode performance were measured in mode I, the mixed mode I/II region, and in (almost) pure mode II loading. Most significantly, a method of accurately measuring an appropriate mode II apparent toughness was developed and this was found to correlate strongly with the resin performance in a composite form. A thorough search of the literature did not find any other attempt, successful or otherwise, to characterise composite mode II toughness in interlaminar toughened or ordinary composites by a resin-only test. By utilising experimental mechanics techniques, this long-standing problem has taken a significant step forward. It is believed that this work is the first time a measurable property has been shown to correlate, with physical basis, with interlaminar toughened composite performance.

The consequences of the resin-to-composite mode II relationship are far-reaching; interlaminar toughened systems dominate the composites used in current and future aerospace programs. The benefits of being able to identify behaviours that are directly comparable to composite behaviour is of great significance to the development of composite materials. Prior to this project, the only method of selecting good materials with which to make ILTP, short of creating a batch of prepreg with each ILTP, was to form resin specimens and perform mode I toughness measurements. Toughening mechanisms would typically be identified using fractography. Neither resin-based result was able to predict how suitable a particle would be when in a composite form under shear loading. The results of this study have shown that, just as mode I toughness can be inferred from mode I resin tests, by identifying and performing the correct tests, mode II toughness and behaviour can also be inferred from resin tests in particulate toughened epoxies.

It is hoped that this study will enhance the understanding of interlaminar toughened materials. It is envisaged that the novel metrological methodologies explored here, and the material behaviours observed, can help drive the development of tougher, and equally importantly, better understood materials.

10.2 Recommendations for future work

There is much scope for further study in this topic. Most significantly, it is suggested that the proposed links between resin crack-path stability behaviour and composite interlaminar behaviour should be investigated further. The obvious starting place for this is to employ full-field experimental mechanics techniques in composites. Measuring behaviour in composites to verify and expand the conclusions of this study would be useful as well as prudent.

The method of measuring mixed-mode performance, K_{IIc} and the T -stress employed in this study are time-consuming and complex, but by controlling the identified sources of error to minimise scatter, it is suggested that it can be used to assess the potential of future toughened resin systems. Indeed, at the time of writing, the full-field parameter extraction technique described here is in the early stages of implementation at the project's sponsor company. A simpler alternative industrially applicable method would be a simple load-based system eliminating the requirement of relatively complex full-field measurement equipment and significant data processing steps. However, the use of full-field measurement techniques and parameter extraction has been shown to offer vastly increased insight into the quantifiable mechanisms in fracture.

A major issue in this work was the lack of provision of adequate mechanical testing frames. Four different frames were used; one of which was low accuracy and then suffered a load cell failure, one was too compliant and poorly aligned, one was out-of-service for over a year, and one was excessively large and had terrible load resolution at the loads used. For future work, in the absence of adequate strategic investment in such equipment, it is strongly advised that a small, custom, hand driven, instrumented test frame, such as a modified Hounsfield W-type test frame, is

made and used instead of relying upon antiquated and poorly instrumented electronic/hydraulic test frames.

The conclusions of this work suggest that developing a simplified testing methodology to assess the behaviour of cracks under shear-components in bulk resin materials gives useful data that can be directly related to composite performance and aid the development of tougher composites. There are two directions that this could take; either a simplified, more focused methodology of measuring parameters using full-field techniques could be developed, or alternatively, full-field techniques could be used to attempt to develop and verify a load-based measurement system.

With hindsight, the specimen geometry chosen for the mixed-mode testing involved a large number of machining steps and it is recommended, for the sake of efficiency, that future tests of this type adopt a simpler specimen. The canister type load cells employed in the majority of the tests presented in this work were less suited to compressive loading and so the asymmetric four-point bend specimen and related compression-based systems would have been less convenient. The simplicity of beam-type specimens over machined, pinned specimens make more sense in the case of repeated testing to destruction and it is suggested that they be considered more seriously in future.

A notable omission from this work is that of computational modelling. It was felt by the author that multiscale computational modelling would require knowing a lot about interface and interphase strengths, stiffnesses and other chemistry-related mechanical properties relating the particles and their interface with the epoxy matrix. Whilst these could be determined experimentally, and models tuned from macro-scale experimental studies, it was deemed to be better use of time to observe the influence of the particles on the fracture process as a whole. Thus, the measurement of properties and suitability of a formulation can be made without knowledge of the toughening system. For comparison of systems with equivalent spatial, but varying micromechanical properties (i.e. different particles, same volume fraction and particle size), this was considered the more sensible approach.

Finite element studies assessing the fracture behaviour around varying sizes and distributions of particles were found to be plentiful in the literature. This makes sense; models must be tuned for chemical-mechanical properties of the particles and interfaces/interphases only once if only one particle type is employed.

This study has focused entirely on measurements made in the linear-elastic region. A worthwhile direction that this study almost took is to look closer at the crack tip behaviour. Stereomicroscopic DIC techniques could feasibly be used to measure full-field data in the process-zone. With appropriate optics, speckle patterns and experimental technique, strain fields could be measured around and between particles, giving new insight into the effect inclusions have on cracks. The effect of inclusions is widely researched using finite element tools. Even in the plane tensile case, direct measurement in real materials with inclusions at a small scale would be groundbreaking.

Chapter 11

Appendix

11.1 Theoretical K and T -stress values for specimen 00-F5-06

Specimen 00-F5-06, frame 188. Load at this point is 360.1 N. Specimen thickness is 3.74 mm. Ligand length is 15.1 mm. Crack length is 4.03 mm.

Applied stress therefore is:

$$\sigma = 360.1 / (15.1 \times 10^{-3} \times 3.74 \times 10^{-3}) = 6.38 \text{ MPa}$$

Theoretical T/σ for crack under uniaxial tension is approximately -0.6 (see section 5.6). Therefore theoretical T -stress at frame 188 is:

$$T_{theoretical} = -0.6 \times 6.38 = -3.83 \text{ MPa}$$

Shape function for an edge-cracked finite plate is

$$Y = 1.12 - 0.23 \left(\frac{a}{w}\right) + 10.6 \left(\frac{a}{w}\right)^2 - 21.7 \left(\frac{a}{w}\right)^3 + 30.4 \left(\frac{a}{w}\right)^4$$

therefore, for crack length 4.03 mm and specimen width 15.1 mm, $a/w = 0.267$ and $Y = 1.55$. Using the equation,

$$K_I = Y\sigma\sqrt{\pi a}$$

theoretical K_I is therefore,

$$K_I = 1.55 \times 6.38 \times \sqrt{\pi \times 4.03 \times 10^{-3}} = 1.116 \text{ MPa}\sqrt{m}$$

The measured T -stress value using appropriate data ranges in 00-F5-06 at frame 188 was -5.0 MPa. A T -stress of -5.0 MPa in this case corresponds to a measured value of T/σ of -0.78 .

11.2 Details and data from tensile tests

NEAT and F2 tensile tests performed on an Instron 5801 hydraulic test frame with 50kN load cell, shown in figure 9.1. Strains were measured using 2D DIC. Tests were performed at a nominal speed of 1.8 mm/min.

F3, F4 and F5 tensile tests were performed by CEM.



Figure 11.1 – Instron 5801 test frame

Table 11.1 – Epoxy stiffness measurements

Specimen	<i>E</i> (0-1% strain) GPa	<i>E</i> (0-0.5% strain) GPa
NEAT-T02	3.152	3.468
NEAT-T03	3.141	3.534
NEAT AVERAGE	3.146	3.501
F2-T01	3.041	3.264
F2-T02	3.061	3.304
F2-T03	3.079	3.368
F2 AVERAGE	3.060	3.312
F3 (CEM)	3.18	-
F4 (CEM)	3.11	-
F5 (CEM)	2.91	-

11.3 Calculation of load-based SIFs from tabulated shape functions

Where:

$$K_I = Y_I \left(\frac{F}{wt} \right) \sqrt{\pi a}$$

$$K_{II} = Y_{II} \left(\frac{F}{wt} \right) \sqrt{\pi a}$$

Approximate shape functions Y_I and Y_{II} were determined from Richard's data. These are shown in table 11.2.

Table 11.2 – Analytical shape functions for three specimens

Specimen	a (mm)	w (mm)	a/w	t (mm)	Y_I	Y_{II}
15-F3-04	4.29	15.0	0.29	3.70	1.5	0.3
45-F5-14	3.42	15.1	0.23	3.74	1.4	0.8
90-F5-07	3.72	15.2	0.23	3.71	-0.1	1.2

11.4 Additional details of G_{IIc} tests

G_{IIc} tests were performed on the toughened resins using the end-notched-flexure method. Specimens were made from 190/34 grade prepreg (190gsm fibre, 34% by volume resin) using an IM carbon fibre. The measurement for the NEAT resin with the same test but with a 134/34 grade prepreg. Values were averaged across a number of tests. Data were supplied by Cytec Engineered Materials.

11.5 Out of plane (z) displacement fields measured using DIC

Figure 11.2 is a screenshot from a 3D-DIC test performed by Rob Wood of GOM as part of a site demonstration with the view to purchasing a system. The data shows rigid out-of-plane motion of the order of 5-10 μm , and out of plane displacement around the crack tip, caused by Poisson contraction of the specimen, of the order of

10 μm . These values are both within those analytically and experimentally predicted in the error analysis of section 5.6.

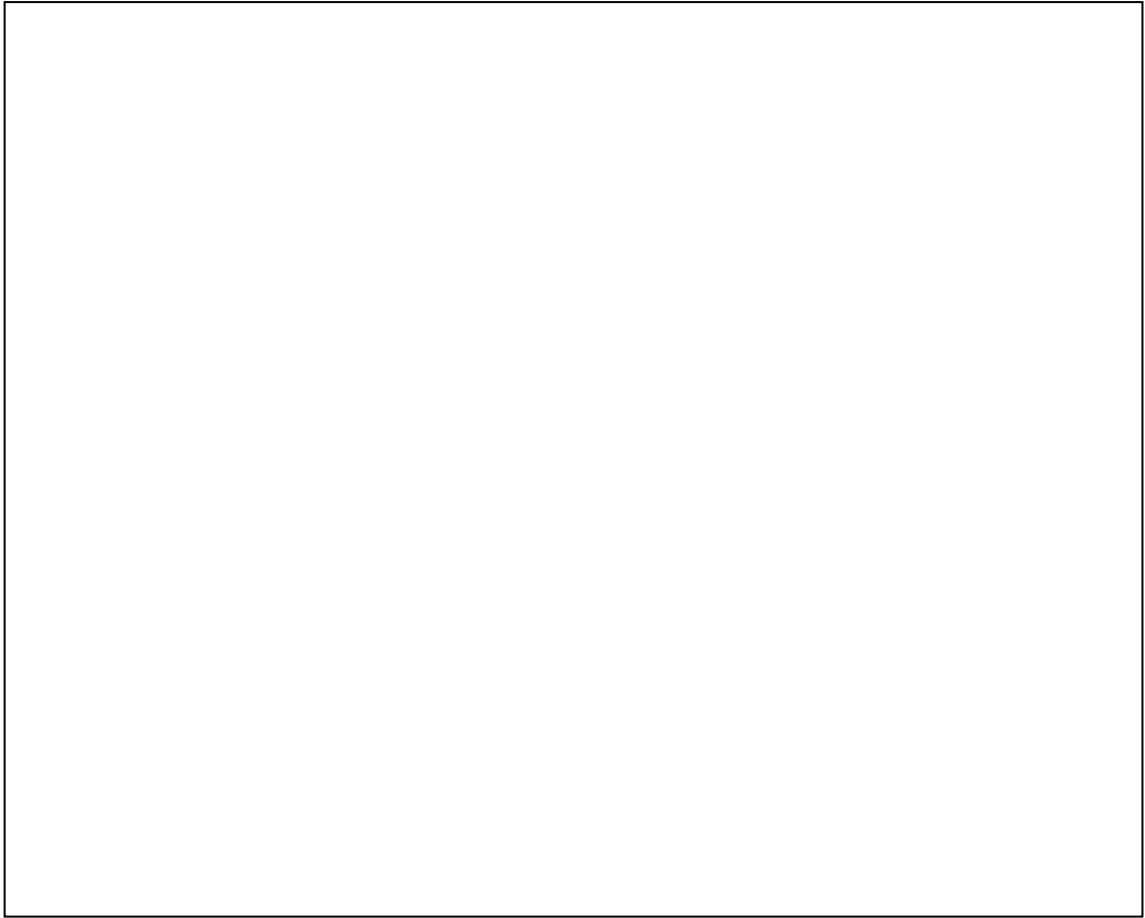


Figure 11.2 – z (out of plane) displacements. Length scale bar is approximate. (courtesy of Rob Wood, GOM)

References

1. British Standards Institution, *BS ISO 13586:2000, Plastics. Determinations of fracture toughness (G_{Ic} and K_{Ic}). Linear elastic fracture mechanics (LEFM) approach*. 2000, BSI
2. Boeing. *Boeing Commercial Airplanes - 787 Dreamliner - Background*. 2010 [Accessed 08/03/2010]; Available from: <http://www.boeing.com/commercial/787family/background.html>.
3. Airbus. *A350 XWB first composite lay-up manufactured in Nantes*. 2009 [Accessed 08/03/2010]; Available from: http://www.airbus.com/en/presscentre/pressreleases/pressreleases_items/09_12_04_a350xwb_first_composite.html.
4. Aerts, V., *Personal communication*. 2011, Cytec Engineered Materials
5. Groleau, M.R., *et al.*, *Mode II fracture of composites interlayered with nylon particles*. *Composites Science and Technology*, 1996. 56(11): p. 1223-1240.
6. Krueger, R., *The Virtual Crack Closure Technique: History, Approach and Applications*. NASA/ICASE Report No. 2002-10, 2002. NASA/CR-2002-211628.
7. Ramsteiner, F., *An approach towards understanding model II failure of poly(methyl methacrylate)*. *Polymer*, 1993. 34(2): p. 312-317.
8. Altstädt, V., *et al.*, *Interlaminar crack growth in third-generation thermoset prepreg systems*. *Polymer*, 1993. 34(4): p. 907-909.
9. Anderson, T.L., *Fracture Mechanics: Fundamentals and Applications*. 3rd ed. 2004: CRC Press.
10. Sultan, J.N., Laible, R.C., and McGarry, F.J., *Microstructure of two-phase polymers*. *Applied polymer symposium*, 1971(16): p. 127-136.
11. Yee, A.F. and Pearson, R.A., *Toughening mechanisms in elastomer-modified epoxies - Part 1 Mechanical studies*. *Journal of Materials Science*, 1986. 21(7): p. 2462-2474.
12. Pearson, R.A. and Yee, A.F., *Toughening mechanisms in thermoplastic-modified epoxies: 1. Modification using poly(phenylene oxide)*. *Polymer*, 1993. 34(17): p. 3658-3670.
13. Pearson, R.A., *Introduction to the Toughening of Polymers*, in *Toughening of Plastics*. 2000, American Chemical Society. p. 1-12.
14. McGrail, P.T. and Jenkins, S.D., *Some aspects of interlaminar toughening: reactively terminated thermoplastic particles in thermoset composites*. *Polymer*, 1993. 34(4): p. 677-683.
15. Kinloch, A.J., Yuen, M.L., and Jenkins, S.D., *Thermoplastic-toughened epoxy polymers*. *Journal of Materials Science*, 1994. 29(14): p. 3781-3790.
16. Dean, J.M., *et al.*, *Mechanical properties of block copolymer vesicle and micelle modified epoxies*. *Journal of Polymer Science Part B: Polymer Physics*, 2003. 41(20): p. 2444-2456.
17. Gerard, P., *et al.*, *Toughness properties of lightly crosslinked epoxies using block copolymers*. *Macromolecular Symposia*, 2007. 256: p. 55-64.
18. Hydro, R.M. and Pearson, R.A., *Epoxies toughened with triblock copolymers*. *Journal of Polymer Science Part B: Polymer Physics*, 2007. 45(12): p. 1470-1481.
19. Ruzette, A.V. and Leibler, L., *Block copolymers in tomorrow's plastics*. *Nature materials*, 2005. 4(1): p. 19-31.
20. Zhao, S., *et al.*, *Mechanisms leading to improved mechanical performance in nanoscale alumina filled epoxy*. *Composites Science and Technology*, 2008. 68(14): p. 2965-2975.

21. Balazs, A.C., Emrick, T., and Russell, T.P., *Nanoparticle Polymer Composites: Where Two Small Worlds Meet*. Science, 2006. 314(5802): p. 1107-1110.
22. Kim, B.C., Park, S.W., and Lee, D.G., *Fracture toughness of the nano-particle reinforced epoxy composite*. Composite Structures, 2008. 86(1-3): p. 69-77.
23. Blackman, B., et al., *The fracture and fatigue behaviour of nano-modified epoxy polymers*. Journal of Materials Science, 2007. 42(16): p. 7049-7051.
24. Johnsen, B.B., et al., *Toughening mechanisms of nanoparticle-modified epoxy polymers*. Polymer, 2007. 48(2): p. 530-541.
25. Ayatollahi, M.R., Shadlou, S., and Shokrieh, M.M., *Fracture toughness of epoxy/multi-walled carbon nanotube nano-composites under bending and shear loading conditions*. Materials & Design, 2011. 32(4): p. 2115-2124.
26. Ayatollahi, M.R., Shadlou, S., and Shokrieh, M.M., *Mixed mode brittle fracture in epoxy/multi-walled carbon nanotube nanocomposites*. Engineering Fracture Mechanics, 2011. 78(14): p. 2620-2632.
27. Boyer, F., et al., *Mechanical and electrical behavior of a PEEK/carbon nanotubes composite*, in *ECCM15 - 15th European Conference on Composite Materials*. 2012: Venice, Italy
28. Chen, B., *Polymer nanocomposite: preparation, structure and properties*, in *Composite Systems and Innovation Centre (CSIC) Seminar series*. 21st June 2012, The University of Sheffield
29. Ma, P.C., Kim, J.-K., and Tang, B.Z., *Effects of silane functionalization on the properties of carbon nanotube/epoxy nanocomposites*. Composites Science and Technology, 2007. 67(14): p. 2965-2972.
30. Shaffer, M. and Kinloch, I.A., *Prospects for nanotube and nanofibre composites*. Composites Science and Technology, 2004. 64(15): p. 2281-2282.
31. Chapartegui, M., et al., *Specific rheological and electrical features of carbon nanotube dispersions in an epoxy matrix*. Composites Science and Technology, 2010. 70(5): p. 879-884.
32. Fan, Z. and Advani, S.G., *Rheology of multiwall carbon nanotube suspensions*. Journal of Rheology, 2007. 51(4): p. 585-604.
33. Brooker, R.D., Kinloch, A.J., and Taylor, A.C., *The Morphology and Fracture Properties of Thermoplastic-Toughened Epoxy Polymers*. The Journal of Adhesion, 2010. 86(7): p. 726 - 741.
34. Takeda, N., et al., *Experimental characterization of microscopic damage progress in quasi-isotropic CFRP laminates: effect of interlaminar-toughened layers*. Advanced Composite Materials, 1998. 7(2): p. 183-199.
35. Kageyama, K., et al., *Mode I and mode II delamination growth of interlayer toughened carbon/epoxy (T800H/3900-2) composite system*, in *Composite materials: fatigue and fracture, fifth volume*, R.H. Martin, Editor. 1995, ASTM International.
36. Elber, W., *Toughening of graphite-epoxy composites by interlaminar perforated Mylar(R) Films*. NASA Technical Memorandum 78643, Langley Research Center, 1978.
37. Yadav, S.N., Kumar, V., and Verma, S.K., *Fracture toughness behaviour of carbon fibre epoxy composite with Kevlar reinforced interleave*. Materials Science and Engineering: B, 2006. 132(1-2): p. 108-112.
38. Hamer, S., et al., *Mode I interlaminar fracture toughness of Nylon 66 nanofibrilmat interleaved carbon/epoxy laminates*. Polymer Composites, 2011. 32(11): p. 1781-1789.
39. Arai, M., et al., *Mixed modes interlaminar fracture toughness of CFRP laminates toughened with CNF interlayer*. Acta Mechanica Solida Sinica, 2012. (Article in press).

40. Kuwata, M. and Hogg, P.J., *Interlaminar toughness of interleaved CFRP using non-woven veils: Part 2. Mode-II testing*. Composites Part A: Applied Science and Manufacturing, 2011. 42(10): p. 1560-1570.
41. Stevanovic, D., et al., *Numerical simulation of elastic-plastic interlaminar crack propagation in interlayer-toughened composite materials*. International Journal of Materials and Product Technology, 2002. 17: p. 99-107.
42. Stevanovic, D., et al., *Mode I and mode II delamination properties of glass/vinyl-ester composite toughened by particulate modified interlayers*. Composites Science and Technology, 2003. 63(13): p. 1949-1964.
43. Stevanovic, D., et al., *FEA of crack-particle interactions during delamination in interlayer toughened polymer composites*. Engineering Fracture Mechanics, 2005. 72(11): p. 1738-1769.
44. Cartié, D.D.R. and Irving, P.E., *Effect of resin and fibre properties on impact and compression after impact performance of CFRP*. Composites Part A: Applied Science and Manufacturing, 2002. 33(4): p. 483-493.
45. Tsotsis, T.K., *Interlayer toughening of composite materials*. Polymer Composites, 2009. 30(1): p. 70-86.
46. Kim, J., et al., *Fracture toughness of CFRP with modified epoxy resin matrices*. Composites Science and Technology, 1992. 43(3): p. 283-297.
47. Cotterell, B., *Notes on the paths and stability of cracks*. International Journal of Fracture, 1966. 2(3): p. 526-533.
48. Christopher, C.J., et al., *Towards a new model of crack tip stress fields*. International Journal of Fracture, 2007. 148(4): p. 361-371.
49. Nurse, A.D. and Patterson, E.A., *Experimental determination of stress intensity factors for cracks in turbine discs*. Fatigue & Fracture of Engineering Materials & Structures, 1993. 16(3): p. 315-325.
50. Erdogan, F. and Sih, G.C., *On the crack extension in plates under plane loading and transverse shear*. Journal of Basic Engineering, 1963. 85(4): p. 519-526.
51. Li, X.-F., Liu, G.-L., and Lee, K., *Effects of T-stresses on fracture initiation for a closed crack in compression with frictional crack faces*. International Journal of Fracture, 2009. 160(1): p. 19-30.
52. James, M.N., et al., *Guest Editorial: Special Issue on Characterisation of Crack Tip Stress Fields*. Fatigue & Fracture of Engineering Materials & Structures, 2012. (Article in press).
53. Sherry, A.H., France, C.C., and Goldthorpe, M.R., *Compendium of T-stress solutions for two and three dimensional cracked geometries*. Fatigue & Fracture of Engineering Materials & Structures, 1995. 18(1): p. 141-155.
54. Smith, D.J., Ayatollahi, M.R., and Pavier, M.J., *The role of T-stress in brittle fracture for linear elastic materials under mixed-mode loading*. Fatigue & Fracture of Engineering Materials & Structures, 2001. 24(2): p. 137-150.
55. Smith, D.J., Ayatollahi, M.R., and Pavier, M.J., *On the consequences of T-stress in elastic brittle fracture*. Proceedings of the Royal Society A: Mathematical, Physical and Engineering Science, 2006. 462(2072): p. 2415-2437.
56. Hsieh, T., et al., *The toughness of epoxy polymers and fibre composites modified with rubber microparticles and silica nanoparticles*. Journal of Materials Science, 2010. 45(5): p. 1193-1210.
57. Kinloch, A., et al., *The interlaminar toughness of carbon-fibre reinforced plastic composites using 'hybrid-toughened' matrices*. Journal of Materials Science, 2006. 41(15): p. 5043-5046.

58. Lee, J.J., Lim, J.O., and Huh, J.S., *Mode II interlaminar fracture behavior of carbon bead-filled epoxy/glass fiber hybrid composite*. *Polymer Composites*, 2000. 21(2): p. 343-352.
59. Lee, J.J. and Suh, C.M., *Interlaminar fracture toughness and associated fracture behaviour of bead-filled epoxy/glass fibre hybrid composites*. *Journal of Materials Science*, 1995. 30(24): p. 6179-6191.
60. ASTM, *ASTM D5045 - 99(2007)e1: Standard Test Methods for Plane-Strain Fracture Toughness and Strain Energy Release Rate of Plastic Materials*. 1999 (approved 2007)
61. Sato, N. *Novel test method for characterizing accurate intra-laminar fracture toughness of CFRP*. in *15th European Conference on Composite Materials*. 2012. Venice.
62. British Standards Institution, *BS ISO 15024:2001, Fibre-reinforced plastic composites - Determination of mode I interlaminar fracture toughness, G_{Ic} , for unidirectionally reinforced materials*. 2001, BSI
63. Carlsson, L.A., Gillespie, J.W., and Pipes, R.B., *On the analysis and design of the end notched flexure (ENF) specimen for mode II testing*. *Journal of Composite Materials*, 1986. 20(6): p. 594-604.
64. Davies, P., *et al. Development of a standard mode II shear fracture test procedure*. 1996.
65. Blackman, B.R.K., Brunner, A.J., and Williams, J.G., *Mode II fracture testing of composites: a new look at an old problem*. *Engineering Fracture Mechanics*, 2006. 73(16): p. 2443-2455.
66. ASTM, *ASTM D7078 / D7078M - 05 -- Standard Test Method for Shear Properties of Composite Materials by V-Notched Rail Shear Method*. 2005
67. Adams, D.F. and Walrath, D.E., *Current Status of the Iosipescu Shear Test Method*. *Journal of Composite Materials*, 1987. 21(6): p. 494-507.
68. Banks-Sills, L., Arcan, M., and Bui, H.D., *Toward a pure shear specimen for K_{IIc} determination*. *International Journal of Fracture*, 1983. 22(1): p. R9-R14.
69. Richard, H.A., *A new compact shear specimen*. *International Journal of Fracture*, 1981. 17(5): p. R105-R107.
70. Yuan, W.G., Lai, M.O., and Lee, K.H., *Evaluation of KII test specimens using J-integral*. *Finite Elements in Analysis and Design*, 1994. 18(1-3): p. 211-224.
71. Richard, H.A. and Benitz, K., *A loading device for the creation of mixed mode in fracture mechanics*. *International Journal of Fracture*, 1983. 22(2): p. R55-R58.
72. Ayatollahi, M.R. and Sedighiani, K., *A T-stress controlled specimen for mixed mode fracture experiments on brittle materials*. *European Journal of Mechanics - A/Solids*, 2012. 36(0): p. 83-93.
73. Ma, F., *et al., A CTOD-based mixed-mode fracture criterion*, in *ASTM STP 1359 Mixed-mode crack behaviour*, K.J. Miller and McDowell, Editors. 1999, ASTM Special Technical Publications.
74. Greer Jr, J.M., Galyon Dorman, S.E., and Hammond, M.J., *Some comments on the Arcan mixed-mode (I/II) test specimen*. *Engineering Fracture Mechanics*, 2011. 78(9): p. 2088-2094.
75. Ayatollahi, M.R. and Aliha, M.R.M., *Analysis of a new specimen for mixed mode fracture tests on brittle materials*. *Engineering Fracture Mechanics*, 2009. 76(11): p. 1563-1573.
76. Hashemi, S. and Williams, J.G., *Crack sharpness effects in fracture testing of polymers*. *Journal of Materials Science*, 1985. 20(3): p. 922-928.

77. O'Brien, T.K., *Composite interlaminar shear fracture toughness, GIIc: Shear measurement or sheer myth?* NASA Technical Memorandum, NASA-TM-110280, 1997.
78. Carpinteri, A., *et al.*, *Is mode II fracture energy a real material property?* Computers & Structures, 1993. 48(3): p. 397-413.
79. Liu, K. and Piggott, M.R., *Fracture failure processes in polymers. I: Mechanical tests and results.* Polymer Engineering & Science, 1998. 38(1): p. 60-68.
80. Piggott, M.R., *et al.*, *Why not replace shear evaluation of interfaces with tensile measurements,* in *5th International Conference on Deformation and Fracture of Composites.* 1999, IOM Communications, The Institute of Materials: London, UK. p. 111-119
81. Piggott, M.R., Liu, K., and Wang, J., *New experiments suggest that all shear and some tensile failure processes are inappropriate subjects for ASTM standards,* in *Composite structures: Theory and practice,* P. Grant and C.Q. Rousseau, Editors. 2001, ASTM STP 1383. p. 324-333.
82. Dally, J.W. and Riley, W.F., *Experimental Stress Analysis.* 2005, Knoxville, United States: College House Enterprises Llc.
83. Cloud, G., *Optical Methods of Engineering Analysis.* 1998, Cambridge, UK: Cambridge University Press.
84. Nurse, A.D. and Patterson, E.A., *Determination of predominantly mode II stress intensity factors from isochromatic data.* Fatigue & Fracture of Engineering Materials & Structures, 1993. 16(12): p. 1339-1354.
85. Zakeri, M., Ayatollahi, M.R., and Guagliano, M., *A Photoelastic Study of T-stress in Centrally Cracked Brazilian Disc Specimen Under Mode II Loading.* Strain, 2011. 47(3): p. 268-274.
86. Sharpe, W., ed. *Springer Handbook of Experimental Solid Mechanics.* 2008, Springer US.
87. Tomlinson, R.A., Du, Y., and Patterson, E.A., *Understanding crack tip plasticity - a multi-experimental approach.* Applied Mechanics and Materials, 2011. 70: p. 153-158.
88. Sutton, M.A., *et al.*, *Determination of displacements using an improved digital correlation method.* Image and Vision Computing, 1983. 1(3): p. 133-139.
89. Tschopp, M.A., *et al.*, *Microstructure-Dependent Local Strain Behavior in Polycrystals through In-Situ Scanning Electron Microscope Tensile Experiments.* Metallurgical and Materials Transactions A, 2009. 40(10): p. 2363-2368.
90. López-Crespo, P., *et al.*, *Study of a crack at a fastener hole by digital image correlation.* Experimental Mechanics, 2009. 49(4): p. 551-559.
91. LaVision. *StrainMaster Product Brochure.* 2007 [Accessed 08/03/2010]; Available from: <http://www.lavision.de/download/index.php?ObjectID=969>.
92. Sutton, M.A., Orteu, J., and Schreier, H., *Image Correlation for Shape, Motion and Deformation Measurements: Basic Concepts, Theory and Applications.* 2009: Springer.
93. Correlated Solutions. *Principle of Digital Image Correlation.* 2009 [Accessed 08/03/2010]; Available from: <http://www.correlatedsolutions.com/index.php/principle-of-digital-image-correlation>.
94. LaVision, *StrainMaster 2D 7.1, Getting Started.* 2005
95. Correlated Solutions, *Vic-3D 2007 Testing Guide.* 2007.
96. Correlated Solutions. *Vic-3D 2009.* 2009 [Accessed 08/03/2010]; Available from: <http://www.correlatedsolutions.com/index.php/products/vic-3d-2009/vic3d>.

97. Roux, S., et al., *Three-dimensional image correlation from X-ray computed tomography of solid foam*. Composites Part A: Applied Science and Manufacturing, 2008. 39(8): p. 1253-1265.
98. Roux, S., Rethore, J., and Hild, F., *Digital image correlation and fracture: an advanced technique for estimating stress intensity factors of 2D and 3D cracks*. Journal of Physics D: Applied Physics, 2009. 42(21): p. 214004.
99. Avril, S., Vautrin, A., and Surrel, Y., *Grid method: Application to the characterization of cracks*. Experimental Mechanics, 2004. 44(1): p. 37-43.
100. LaVision, *StrainMaster software manual for DaVis 7.0*. 2005
101. Crammond, G., Boyd, S.W., and Dulieu-Barton, J.M., *Speckle pattern characterisation for high resolution digital image correlation*, in *8th International Conference on Advances in Experimental Mechanics: Integrating Simulation and Experimentation for Validation*, R.L. Burguete, et al., Editors. 2011, Applied Mechanics and Materials: Edinburgh, UK
102. Reu, P.L. and Miller, T.J., *The application of high-speed digital image correlation*. Journal of Strain Analysis for Engineering Design, 2008. 43(8): p. 673-688.
103. Pan, B., Lu, Z., and Xie, H., *Mean intensity gradient: An effective global parameter for quality assessment of the speckle patterns used in digital image correlation*. Optics and Lasers in Engineering, 2010. 48(4): p. 469-477.
104. Pan, B., *Recent Progress in Digital Image Correlation*. Experimental Mechanics, 2011. 51(7): p. 1223-1235.
105. Zanganeh, M., Tomlinson, R.A., and Yates, J.R. *T-stress determination using digital image correlation*. in *11th International Congress and Exhibition on Experimental and Applied Mechanics*. 2008. Orlando, Florida.
106. Roux, S. and Hild, F., *Stress intensity factor measurements from digital image correlation: post-processing and integrated approaches*. International Journal of Fracture, 2006. 140(1): p. 141-157.
107. Kirugulige, M.S. and Tippur, H.V., *Measurement of fracture parameters for a mixed-mode crack driven by stress waves using image correlation technique and high-speed digital photography*. Strain, 2009. 45(2): p. 108-122.
108. Du, Y., et al., *Evaluation Using Digital Image Correlation of Stress Intensity Factors in an Aerospace Panel*. Experimental Mechanics, 2010. In Press, Corrected Proof.
109. Lopez-Crespo, P., et al., *The stress intensity of mixed mode cracks determined by digital image correlation*. The Journal of Strain Analysis for Engineering Design, 2008. 43(8): p. 769-780.
110. McNeill, S.R., Peters, W.H., and Sutton, M.A., *Estimation of stress intensity factor by digital image correlation*. Engineering Fracture Mechanics, 1987. 28(1): p. 101-112.
111. Muskhelishvili, N.I., *Some basic problems of the mathematical theory of elasticity*. Moscow, 1954: Noordhoff International Publishing, Leyden.
112. Zanganeh Gheshlaghi, M., *Experimental investigation of crack paths*, in *Mechanical Engineering*. 2008, University of Sheffield. PhD Thesis.
113. Zanganeh, M., Tomlinson, R.A., and Yates, J.R., *T-stress determination using thermoelastic stress analysis*. Journal of Strain Analysis for Engineering Design, 2008. 43(6): p. 529-537.
114. Sanford, R.J. and Dally, J.W., *Stress intensity factors in the third-stage fan disk of the TF-30 turbine engine*. 1978, Washington, D.C.: Naval Research Laboratory. FR-8202.
115. Cotterell, B., *On fracture path stability in the compact tension test*. International Journal of Fracture, 1970. 6(2): p. 189-192.
116. Tong, J., *T-stress and its implications for crack growth*. Engineering Fracture Mechanics, 2002. 69(12): p. 1325-1337.

117. Zakeri, M., Ayatollahi, M.R., and Guagliano, M., *A Photoelastic Study of T-stress in Centrally Cracked Brazilian Disc Specimen Under Mode II Loading*. Strain, 2010***. Article in press.
118. Roux, S. and Hild, F. *Toughness measurement in brittle materials from digital image correlation*. in *11th International Conference on Fracture*. 2005. Torino, Italy.
119. Hild, F. and Roux, S., *Measuring stress intensity factors with a camera: Integrated digital image correlation (I-DIC)*. Comptes Rendus Mécanique, 2006. 334(1): p. 8-12.
120. Yates, J.R., Zanganeh, M., and Tai, Y.H., *Quantifying crack tip displacement fields with DIC*. Engineering Fracture Mechanics, 2010. 77(11): p. 2063-2076.
121. Zanganeh, M., *DICITAC*. 2010, University of Sheffield
122. Navitar. *Precise Eye Performance Specifications* [Accessed 28/01/2011]; Available from: http://navitar.com/pdf/pe_performance_specs.pdf.
123. Williams, M.L., *On the stress distribution at the base of a stationary crack*. Journal of Applied Mechanics, 1957. 24: p. 109-114.
124. British Standards Institution, *BS EN ISO 527-1:1996, BS 2782-3:Method 321:1994, ISO 527-1:1993*. 1994
125. Fett, T., *Stress Intensity Factors, T-stresses, Weight Functions*. IKM 50. 2008: Institute of Ceramics in Mechanical Engineering (IKM).
126. Fett, T., *A compendium of T-stress solutions*. Vol. FZKA--6057. 1998: Forschungszentrum Karlsruhe GmbH Technik und Umwelt (Germany). Inst. fuer Materialforschung.
127. British Standards Institution, *BS 7448-1:1991, Fracture mechanics toughness tests - Part 1: Method for determination of K_{Ic}, critical CTOD and critical J values of metallic materials*. 1991
128. Sutton, M.A., et al., *The effect of out-of-plane motion on 2D and 3D digital image correlation measurements*. Optics and Lasers in Engineering, 2008. 46(10): p. 746-757.
129. *Fractography of Modern Engineering Materials, Composites and Metals - STP 948*. ASTM Special Technical Publications, ed. J.E. Masters and J.J. Au. 1987: ASTM.
130. Heydari, M., Choupani, N., and Shamel, M., *Experimental and Numerical Investigation of Mixed-Mode Interlaminar Fracture of Carbon-Polyester Laminated Woven Composite by Using Arcan Set-up*. Applied Composite Materials, 2011. 18(6): p. 499-511.
131. Sutton, M.A., et al., *Development and application of a crack tip opening displacement-based mixed mode fracture criterion*. International Journal of Solids and Structures, 2000. 37(26): p. 3591-3618.
132. Rasband, W.S., *ImageJ*. 1997-2012, U.S. National Institutes of Health: Bethesda, Maryland, USA, <http://imagej.nih.gov/ij/>
133. Araki, W., et al., *Fracture toughness for mixed mode I/II of epoxy resin*. Acta Materialia, 2005. 53(3): p. 869-875.